Tesis Doctoral

Búsqueda de partículas supersimétricas en estados finales con muchos jets y energía faltante

Reisin, Hernán Diego

2014

UNIVERSIDAD DE BUENOS AIRES
Facultad de Ciencias Exactas y Naturales
Departamento de Física

Búsqueda de partículas supersimétricas en estados finales con muchos jets y energía faltante

Tésis para optar por el título de
Doctor de la Universidad de Buenos Aires en el área Ciencias Físicas

Hernán Diego Reisin

Director de Tésis:	Dr. Gustavo Otero y Garzón
Consejero de Estudios:	Dr. Ricardo Piegaia
Lugar de Trabajo:	Departamento de Física, FCEyN, UBA

Buenos Aires, Marzo 2014

Búsqueda de partículas supersimétricas en estados finales con muchos jets y energía faltante

Resumen

Muchas extensiones del modelo estándar (ME) de física de partículas predicen la existencia de partículas con masas en la escala del TeV que interactúan por la fuerza fuerte y decaen a descendientes que interactúan débilemente. Supersymetría (SUSY) es una de las teorías más estudiada y un firme candidato para describir la física más allá del ME pues provee una explicación consistente a diversos conflictos teóricos como el problema de jerarquía del ME. En el contexto de ésta teoría, las partículas que interactúan fuertemente son los *super*compañeros de los quarks (squarks, $\tilde{q}$) y los gluones (gluinos, $\tilde{g}$). Si resultan ser accesibles cinemáticamente, los squarks y los gluinos podrían ser producidos en las interacciones protón-protón (pp) en el Gran Colisionador de Hadrones (LHC). Este trabajo de tésis presenta el resultado de la búsqueda de nuevas partículas que decaen a estados finales con un gran número (desde al menos 7 a al menos 10) jets junto con energía faltante en ausencia de electrones y muones aislados. El análisis se desarrolló con datos de colisiones pp a una energía en el centro de masa de $\sqrt{s} = 8$ TeV colectados por el detector ATLAS en el LHC, correspondientes a una luminosidad integrada total de 20.3 fb^{-1}. Se incrementó la sensibilidad de la búsqueda para identificar posibles eventos de SUSY al considerar regiones de señal definidas en función variables de subestructura de jets como el número de jets provenientes de quarks b y de la suma de las masas de jets de gran radio. La búsqueda no revela un exceso significativo respecto de los valores predichos por el ME. Los resultados son interpretados en el contexto de un modelo cMSSM y de varios modelos simplificados inspirados en SUSY. Los límites de exclusión extienden los resultados previos restringiendo varios modelos supersimétricos. Por ejemplo, en un modelo donde los gluinos producidos decaen vía $\tilde{g} \to t + \bar{t} + \tilde{\chi}_1^0$, se excluyen masas del gluino menores que 1,1 TeV para masas del neutralino ($\tilde{\chi}_1^0$) por debajo de 350 GeV.

Palabras clave: Supersymmetry, ATLAS, LHC, Jets, Jet substructure, gluinos, stops

Search of supersymmetric particles in multi-jet events with missing energy

Abstract

Many extensions of the Standard Model (SM) of particle physics predict the existence of TeV-scale strongly interacting particles that decay to weakly interacting descendants. Among them, Supersymmetry (Susy) is one of the most studied and a leading candidate theory for describing physics beyond SM since provides a consistent explanation to several theoretical concerns like the hierarchy problem of the SM. In the context of this theory, the strongly interacting parent particles are the partners of the quarks (squarks, $\tilde{q}$) and gluons (gluinos, $\tilde{g}$). If they are kinematically accessible, the squarks and gluinos could be produced in the proton-proton (pp) interactions at the Large Hadron Collider (LHC). This thesis presents the results of the search for new particles decaying to final states with large numbers (from at least 7 to at least 10) of jets together with significant missing transverse momentum and no isolated electrons or muons. The analysis is performed with a total integrated luminosity corresponding to 20.3 fb^{-1} of pp collision data at center-of-mass energy $\sqrt{s} = 8$ TeV collected by the Atlas experiment at the LHC. The sensitivity of the search to identify possible Susy-like event candidates is enhanced by considering signal regions defined in terms of the number of b-tagged jets and the scalar sum of masses of large-radius jets in an event. These searches found no significant excess over the Standard Model expectation. The results are interpreted in the context of an cMssm model and various simplified supersymmetry-inspired models. The exclusion limits substantially extend previous results constraining several supersymmetric models. For example, in a model where both of the pair-produced gluinos decay via $\tilde{g} \rightarrow t + \bar{t} + \tilde{\chi}_1^0$, gluino masses smaller than 1.1 TeV are excluded for neutralino ($\tilde{\chi}_1^0$) masses below 350 GeV.

Keywords: Supersymmetry, Atlas, LHC, Jets, Jet substructure, gluinos, stops

Acknowledgements

The span over which this doctorate was conducted not only forged and strengthened scientific and academic skills but was also unavoidably crossed by many aspects of the human condition. Because of this my appreciation to the following people exceeds the mere formality.

To Gustavo Otero y Garzón and 'Richard' Piegaia for your scientific guidance, training and infinite patience, but above all things for your kind understanding and support across the time of this thesis. To Ariel Schwartzman, whose devotion to the experiment echoed as a permanent beacon toward relevant subjects of study. To many members of the ATLAS Jet Substructure, Jet/ETmiss and SUSY multi-jet groups, from whom in many meetings and discussions I acquired an incredible amount knowledge, among which I recognize Anna Sfyrla, David Miller and Dag Gillbert for your valuable feedback. My special gratitude to Mireia Crispin Ortuzar, ∼24/7 co-analyst partner; you made the exhausting rush toward the deadlines a bearable task. To Max Swiatlowski and Bart Butler, because thanks to your aid with the parallel computing framework the results of this thesis could be produced within the demanded timescales. To dear friends, classmates, 'office-mates' and ATLAS colleagues gathered along the road, Yanncito, Orel, Javi, Lean, Laura, Sabrina, Gaston and Pablo, for the time shared. My acknowledgement extends to medical doctors of the Clinic and Nephrology departments of the Lanari Institute (UBA), because you have alleviated an otherwise complex issue that could have jeopardized the conclusion of this thesis. To Nacho and Inés, for directing me to this doctorate since the very beginnings of time. To the evergreen Melisa, por todo y a pesar de todo.

Contents

1 Introduction **1**

2 The Standard Model and beyond: Supersymmetry **5**

2.1 The Standard Model . . . 5

2.1.1 Sectors 5

2.1.2 Hadronic collisions 9

2.1.3 It's 'just' a model, after all 11

2.2 . . . and beyond: Supersymmetry 14

2.2.1 A symmetry called 'super' 15

2.2.2 Minimal Supersymmetric Standard Model (MSSM) 17

2.2.2.1 R-Parity 22

2.2.2.2 Mass spectrum of the MSSM 23

2.2.3 Simplified models 25

3 The experiment **31**

3.1 The Large Hadron Collider 31

3.1.1 Machine design 31

3.1.2 LHC operation during 2012 33

3.2 The ATLAS apparatus 37

3.2.1 Coordinate system 38

3.2.2 Tracking system 39

3.2.3 Calorimeter system 41

3.2.3.1 Liquid Argon calorimeters 42

3.2.3.2 Tile calorimeters 44

3.2.4 Muon spectrometer 45

3.2.5 Forward detectors 47

3.2.6 The solenoidal and toroidal magnet systems 48

3.2.7 Trigger and data acquisition 48

3.3 Object recontruction and identification in ATLAS 51

3.3.1 Track and vertex reconstruction 51

3.3.2 Electron reconstruction 53

3.3.3 Muon reconstruction 55

3.3.4 Jets 56

3.3.4.1 Topological clusters . . . 56
3.3.4.2 Jet energy calibration . . . 58
3.3.5 Missing transverse momentum . . . 60
3.3.6 b-jet tagging . . . 61
3.4 The analysis software . . . 64

4 Jets and their substructure **65**
4.1 Jet definitions . . . 66
4.2 Jets in the Boosted Regime . . . 68
4.2.1 Large-R ("fat") jets . . . 68
4.2.2 Jet mass . . . 70
4.2.3 Subjets . . . 71
4.2.3.1 Subjet performance . . . 72
4.2.3.2 Subjet energy scale (subJES) . . . 73
4.2.3.3 Ghost association of particles . . . 76
4.3 Jet grooming . . . 79
4.3.1 Jet grooming definitions . . . 79
4.3.2 Jet substructure and grooming in data and simulation . . . 81
4.3.2.1 Jet mass resolution . . . 82
4.3.2.2 Impact of pile-up on the jet mass scale and resolution . . . 85
4.4 Composite Jets . . . 87

5 Analysis strategy **91**
5.1 Motivation . . . 91
5.2 Data-set and Monte Carlo samples . . . 93
5.2.1 Recorded data . . . 93
5.2.2 Standard Model Monte Carlo . . . 93
5.2.3 Signal Models . . . 94
5.3 Definition of primary physics objects . . . 95
5.4 Off-line event selection . . . 97
5.4.1 Trigger . . . 97
5.4.2 Event cleaning . . . 99
5.4.3 Monte Carlo re-weighting . . . 102
5.4.3.1 Monte Carlo scale factors . . . 102
5.4.3.2 NLO k-factors . . . 104
5.5 Signal regions . . . 105
5.5.1 Inheritance . . . 105
5.5.2 The multi-jet + flavour stream . . . 105
5.5.3 The multi-jet + M_J^{Σ} stream . . . 106
5.5.4 Optimization . . . 107
5.5.4.1 b-jet stream . . . 108

5.5.4.2 M_{J}^{Σ} stream . . . 111
5.5.5 Sensitiveness to pile-up . . . 114
5.5.6 Summary of signal regions . . . 115
5.6 Glossary of phase space regions . . . 118
5.7 Statistical methods . . . 118
5.7.1 Profile likelihood function (PLL) . . . 120
5.7.1.1 Incorporating systematic uncertainties . . . 122
5.7.1.2 Incorporating statistical uncertainties . . . 123
5.7.1.3 Analysis specificities . . . 124
5.7.2 Profile likelihood test statistic . . . 125
5.7.3 Discovery significance and exclusion limits . . . 127

6 Background estimation **131**
6.1 Multi-Jet production . . . 133
6.1.1 Template method . . . 133
6.1.2 SoftTerm $E_{\mathrm{T}}^{\mathrm{miss}}$ correction . . . 136
6.2 'Leptonic' backgrounds . . . 138
6.2.1 Selection of $t\bar{t}$ and W+jets enriched background . . . 140
6.2.2 Selection of Z+jets enriched events . . . 143
6.2.3 $t\bar{t}$+(W,Z) and single tops . . . 145
6.3 Other Standard Model processes . . . 147
6.4 Summary of central background values . . . 147
6.5 Background uncertainties . . . 149
6.5.1 Multi-jet background uncertainties . . . 150
6.5.2 Non-multi-jet background uncertainties . . . 152
6.5.2.1 Detector Uncertainties . . . 153
6.5.2.2 Theoretical Uncertainties . . . 155
6.5.3 Other experimental uncertainties . . . 158

7 Results & Interpretations **159**
7.1 Results . . . 159
7.2 Model interpretations . . . 159

8 Summary & Conclusions **169**

A Event displays **191**

B Details of systematic uncertainties for the backgrounds **193**

1 Introduction

With the recent discovery of a new particle in the mass region around 125 GeV [1, 2] and having spin 0 [3], the Standard Model (SM) of particle physics is probably reaching to its zenith. Precision measurements of the couplings and rates of different decay channels are still needed to determine whether or not this novel particle has all the properties predicted for the long-awaited Higgs boson [4–6]. In either case, a superseding model is mandatory. If this new particle is not the Higgs boson, then a different model would be obviously required. If it is, then all the ingredients of the SM would be in place. Yet, and in spite the SM has proven to be the best description there is of the fundamental microscopic particles and their interactions, it is probably not the ultimate theory since it leaves unanswered several questions. A more general theory should –for instance– include the omnipresent gravity force, explain the mass of neutrinos (see chapter 13 of ref. [7]), predict at least one candidate for the non baryonic component of the galaxies referred to as *Dark Matter* [8], and provide a consistent explanation for the observed matter-antimatter asymmetry in the Universe [9].

The Large Hadron Collider (LHC) [10] and the main detectors therein [11–14] were built in order to expand the current frontier of knowledge and hopefully provide with sufficient information to construct the next generation of 'Standard Models'. *A theory of everything* [15] encompassing these and other unresolved issues is however experimentally unaccessible with the current technology, if it actually exists in the GUT or Planck scales ($\sim 10^{14} - 10^{17}$ GeV, where $1\,\text{GeV} = 10^9$ eV). In particle colliders we are restricted to test lower energy effective (and probably still incomplete) theories. Among the many possible extensions to the Standard Model, supersymmetric models [16–20] which postulate that for each particle with fractional spin there must exist a particle with integer spin (and viceversa) are specially favored theoretically [21]. They provide a simple and *elegant* solution to the naturalness problem of the SM [20] and predict (under reasonable assumptions) the existence of a massive stable weakly interacting particle (called LSP, for lightest supersymmetric particle) that may be the yet-unknown component of Dark Matter, among other properties.

Supersymmetric models conserving the R-parity symmetry (needed to assure the stability of protons [22–26]) and in particular the Minimal Supersymmetric Standard Model (MSSM) [27, 28] predict the existence of strongly interacting TeV-scale mass particles that may be kinematically accessible at the LHC. Such particles are expected to decay in cascades, the

nature of which depends on the mass hierarchy within the model. At the LHC events from these processes would be characterized by final states containing large numbers of hadronic jets (multi-jet) originating from emissions of quarks and/or gluons, in association with significant missing transverse momentum $E_{\mathrm{T}}^{\mathrm{miss}}$ from the unobserved weakly interacting descendants.

This thesis describes the study conducted to seek for supersymmetric particles in events characterized by the presence of multi-jet and $E_{\mathrm{T}}^{\mathrm{miss}}$ but no leptons in the final state [29], originating from proton–proton (pp) collisions recorded by the ATLAS experiment during the year 2012. The analysis uses the full 2012 dataset corresponding to $20.3\,\mathrm{fb}^{-1}$ of pp collision data at center-of-mass energy $\sqrt{s} = 8$ TeV. The search strategy follows closely that used in previous multi-jet searches [30–32] but introduces many improvements in order to enhance the sensitivity to new physics. Events are selected with large jet multiplicities, with requirements ranging from at least 7 to at least 10 jets, which implies a selection that explores more extremes regions of the phase space than previous analyses. Requiring a large jet multiplicity has the effect of increasing the sensitivity to models that predict many-body decays or sequential cascade decays of the strongly interacting parent particles. The sensitivity of the search is further enhanced by the subdivision of the selected sample into several categories using additional information. Event classification based on the number of jets containing b-quarks (b-jets) gives enhanced sensitivity to models which predict either more or fewer b-jets than the Standard Model background. In a complementary stream of the analysis, a novel jet definition ('composite' jets) is introduced and validated. Jets (with a large radius parameter) reconstructed with this approach are used to form an event variable, the sum of the masses of the composite jets, which gives additional discrimination in models with a large number of objects in the final state [33]. The results are interpreted in the context of several models and upper limits are provided.

The text is organized as follows. Chapter 2 begins with a brief overview of the Standard Model and some of its limitations. It follows with a friendly introduction of general aspects of supersymmetry and the description of the minimal supersymmetric model consistent with the SM, and finally describes additional 'simplified models' which facilitate the experimental evaluation of signal models. The LHC and the ATLAS detector and a summary of their performance during 2012 are described in chapter 3. In this chapter are also detailed the procedures used to acquire the data from collisions and to reconstruct and identify the primary physical objects of the analysis. Chapter 4 focus on different techniques used to reconstruct the rich hadronic phenomenology in the LHC. These encompass the description from standard jet algorithms to more sophisticated post-processing techniques that permit the use of jets and the information encoded in their internal structure (jet substructure) for the discrimination between signal and background in search analyses (jets, electrons, $E_{\mathrm{T}}^{\mathrm{miss}}$, etc.). Chapter 5 contains the bulk of the analysis strategy. It describes the rationale of the analysis, the target signatures to which the event selection is sensitive and the corresponding signal models of interest (for which reasonable accep-

tance and discrimination is expected), the details of the object and event selections, the definition and optimization of the signal regions, and a (hopefully) clear explanation of the statistical methods used to formally address the question: "is there new physics hidden in these data?". Chapter 6 presents a detailed description of the methods used to estimate the event yields (and their uncertainties) of the Standard Model background processes. The main results of the search including upper limits on visible cross sections and exclusion limits to several models are presented in chapter 7. Finally, chapter 8 presents a summary and the conclusions.

2
The Standard Model and beyond: Supersymmetry

The Standard Model (SM) of elementary particle physics constitutes the most accurate description of matter and their interactions. The exceptional agreement of its predictions to the colossal body of experimental evidence collected over the last century [7] is not only a triumph for the model itself or the perturbative calculation framework in which predictions rely. It is also a reinforcement for the role of symmetries in physics laws and for the two major current paradigms in physics: the quantum nature of matter and the Lorentz covariance of physical laws. In spite of this, it is not expected to be the ultimate model because leaves unanswered many questions, as for instance "why there exist three fermion families identical among each other except for their masses?". This chapter presents generalities about the SM and its limitations in section 2.1, and one superseding alternative (which is the subject of the search in this thesis): supersymmetry in section 2.2. The list of particular models used to interpret the results of this analysis is described in section 2.2.3.

2.1 The Standard Model ...

I don't pretend here to overwhelm the reader with an in depth description of all the SM properties and virtues, which are anyway perfectly well described elsewhere, from the seminal works [4–6, 34–38], or undergraduate/advanced textbooks [39–41], and dedicated reviews [7]. Nonetheless, I will present some key features with the aim to motivate a smooth transition to the Supersymmetric models considered for this search.

2.1.1 Sectors

Being a relativistic quantum field theory, information about the model is totally contained in the terms of the Lagrangian density, $\mathcal{L}_{SM}$. In this model *matter fields* are fermions described by half-integer spin Dirac spinors (ψ) and the interaction among these occurs via exchange of spin one bosonic *force-carriers*. Interactions emerge as the result of the Lagrangian invariance to the gauge symmetry group $\mathrm{SU}(3)_c \otimes \mathrm{SU}(2)_L \otimes \mathrm{U}(1)_Y$. This gauge symmetry in turn precludes the inclusion of naïve mass terms of the form $m\bar{\psi}\psi$ into $\mathcal{L}_{SM}$, a prohibition that is evaded by the electroweak symmetry breaking using the ingenious

Higgs mechanism [4–6].

$\mathcal{L}_{SM}$ is formed by the addition of several complementary terms representing the strong $\mathrm{SU}(3)_c$ subgroup, the electroweak $\mathrm{SU}(2)_L \otimes \mathrm{U}(1)_Y$ sector, and the Higgs sectors describing the masses for quarks, leptons and weak bosons.

The strong sector. The description of strong interactions originally developed by Gell-mann [34] and Zweig [35] to describe the prolific abundance of mesons and barions in the 1960's, evolved over the years into a renormalizable quantum field theory, referred to as Quantum Chromodynamics (QCD) [7]. The Lagrangian of QCD within the Standard Model is given by

$$\mathcal{L}_{QCD} = \sum_{\psi} \bar{\psi}_{q,a} \left[i\gamma^{\mu} \left(\delta_{ab}\partial_{\mu} + i g_s T^c_{ab} G^c_{\mu} \right) \right] \psi_{q,b} - \frac{1}{4} F^G_{\mu\nu} F^{G\mu\nu} \tag{2.1}$$

The sum runs over the $\psi_{q,a}$ quark fields (the only fermions carrying color charge) of flavour q with a color index $a = 1, 2, 3$. The rest of the terms are the strong coupling constant g_s, the Dirac matrices γ^{μ}, G^c_{μ} are eight (c=1,...,8) Lorentz vectors representing the massless gluon gauge bosons, and T^c_{ab} are the generators of $\mathrm{SU}(3)_c$ group. They encode the fact that a gluon's interaction with a quark rotates the quark's color in $\mathrm{SU}(3)_c$ space. No mass terms are included for the quarks as they arise from the Higgs-fermion sector as described later[1]. The last term is the kinetic energy of gluons, with $F^G_{\mu\nu}$ analogous to the electromagnetic field strength tensor, but at variance to photons (given that gluons carry color charge) it also produce gluon–gluon interactions. Quarks come in two types, 'Up' (with electric charge $+\frac{2}{3}$) and 'Down' (with electric charge $-\frac{1}{3}$), forming a pair structure that is replicated in three families (generations) of increasing mass formed by: up (u) and down (d) quarks, charm (c) and strange (s) quarks, and the heavier top (t) and bottom (b) quarks.

At the Large Hadron Collider this is the dominant interaction because colliding particles carry color charge and g_s is much larger that the electroweak coupling constants, g' and g. Observational phenomenology of the strong-sector (asymptotic freedom, confinement and hadronization) is deferred to section 2.1.2.

The electroweak (EW) sector. In the SM the electromagnetic and weak interactions are jointly described by the Glashow-Weinberg-Salam theory [36–38] in a unified electroweak interaction that satisfies the gauge $\mathrm{SU}(2)_L \otimes \mathrm{U}(1)_Y$ symmetry group. The theory proposes four massless vector gauge bosons, three W^a_{μ} (a=1,2,3) corresponding to the $\mathrm{SU}(2)_L$ symmetry subgroup and one B_{μ} associated to the $\mathrm{U}(1)_Y$ hypercharge symmetry. The coupling of EW bosons to fermions is not obvious —or at least not as simple as the coupling in

[1] The QCD Lagrangian actually has a mass term for the fermion fields of the form $\bar{\psi}_{q,a}\delta_{ab}m_q\psi_{q,b}$, that is incompatible with gauge invariance and therefore not included within the SM.

electromagnetism or QCD. The Lagrangian for the electroweak interactions is given by

$$\mathcal{L}_{EW} = \sum_{\Psi} \bar{\Psi} \left[i\gamma^{\mu} \left(\partial_{\mu} + igT_L^a W_{\mu}^a + ig' \frac{1}{2} T_Y B_{\mu} \right) \right] \Psi - \frac{1}{4} W_{\mu\nu}^a W_a^{\mu\nu} - \frac{1}{4} B_{\mu\nu} B^{\mu\nu} \tag{2.2}$$

with T_L^a the generators of the $\mathrm{SU}(2)_L$ group[1], T_Y the generator of the $\mathrm{U}(1)_Y$ group, and g and g' the coupling constants to the W_{μ}^a triplet and B_{μ} fields. The fields Ψ are fermion weak multiplets, either left doublets or right chirality singlets

$$\Psi : \begin{pmatrix} \nu_{\ell_i} \\ \ell_i \end{pmatrix}_L \text{ and } (\ell_i)_R \text{ for leptons, and } \begin{pmatrix} u_i \\ d'_i \end{pmatrix}_L, (u_i)_R \text{ and } (d_i)_R \text{ for quarks} \tag{2.3}$$

where the down elements d'_i are not flavor eigenstates but a mixture of them given by the Cabibbo-Kobayashi-Maskawa [42, 43] unitary rotation: $d'_i = \sum_j V_{ij} d_j$.

Higgs sector for EW bosons. Weak gauge bosons in equation 2.2 are massless; if these were the physical particles the weak interaction would have infinite range in conflict with experiments. The mass problem is tackled in the Standard Model by postulating an elementary spin zero Higgs boson, whose couplings to other particles determine their masses. The (minimal) solution is provided by the inclusion of four real scalar fields arranged into a complex scalar $\mathrm{SU}(2)_L$ isospin doublet $\phi = \begin{pmatrix} \phi^+ \\ \phi^0 \end{pmatrix}$ described by the dynamics

$$\mathcal{L}_{H-V} = \underbrace{\left| i \left(\partial_{\mu} + igT_L^a W_{\mu}^a + ig' \frac{1}{2} T_Y B_{\mu} \right) \phi \right|^2}_{|D_{\mu}\phi|^2} \underbrace{- \mu^2 \phi^{\dagger}\phi - \lambda \left(\phi^{\dagger}\phi \right)^2}_{-V(\phi)} \tag{2.4}$$

with $\mu^2 < 0$ and $\lambda > 0$ by construction to degenerate the minimum of the ϕ field potential. Upon breaking the symmetry of the vacuum expectation value of ϕ, mass terms for the physical weak bosons, $W^{\pm}$ and Z^0, arise from the kinetic part of the lagrangian $\mathcal{L}_{H-V}$. Thus, three out of the four real scalar fields are 'eaten' as longitudinal components by the weak bosons, which results in mass terms dependent solely on the gauge couplings (g and g') and the vacuum expectation value of ϕ. The remaining scalar field (technically fluctuations of it above its vacuum expectation value) is the massive electrically-neutral Higgs boson predicted in 1964 [4–6]. It is still early to be certain that the scalar boson announced nearly 50 years later on 2012 [44] is exactly Higgs boson of the minimal SM, but at any rate its discovery has convinced many people that the EW symmetry breaking is a fundamental mechanism to explain the origin of mass of subatomic particles [45].

Higgs-fermion sector. The last sector of the (minimal) Standard Model is responsible for the masses of the fermions. A rather miraculous property of the minimal SM is that the same Higgs isospin doublet necessary for the EW symmetry breaking is essential for the generation of fermion masses. The generic term is given by the gauge invariant Yukawa

[1] The subscript L indicates that they only act on left-handed fermions: $T_L^a = {}^1\!/_2 \tau^a P_L$, where τ^a are the usual Pauli matrices and P_L the projector to left chirality states

coupling of fermions with the Higgs doublet in the form: $y_{ij}\bar{\psi}_i\psi_j\phi$. The complete sector reads as

$$\mathcal{L}_{fermions} = -y_\ell \left(\bar{\nu}_\ell,\, \bar{\ell}\right)_L \begin{pmatrix}\phi^+\\ \phi^0\end{pmatrix} \ell_R - y_d^{ij} \left(\bar{u}_i,\, \bar{d'}_i\right)_L \begin{pmatrix}\phi^+\\ \phi^0\end{pmatrix} d_{jR} - y_u^{ij} \left(\bar{u}_i,\, \bar{d'}_i\right)_L \begin{pmatrix}-\phi^0\\ \phi^-\end{pmatrix} u_{jR} + \text{h.c.} \tag{2.5}$$

Expansion of the scalar doublet around its vacuum expectation value ($\phi^0 = \frac{v+h}{\sqrt{2}}$, $\phi^\pm = 0$) results immediately in two terms for the lepton *sub*sector

$$\mathcal{L}_{leptons} = -\frac{y_\ell v}{\sqrt{2}}\bar{\ell}\ell - \frac{y_\ell}{\sqrt{2}}\bar{\ell}\ell h \equiv -m_\ell\bar{\ell}\ell - \frac{m_\ell}{v}\bar{\ell}\ell h \tag{2.6}$$

representing the lepton mass term and its coupling to the Higgs boson h, upon identification of the lepton mass with the Yukawa constant through: $m_\ell = y_\ell v/\sqrt{2}$. The quark *sub*sector is slightly more complicated because of the CKM mixing of down-like quarks d'_i. Masses for the quarks and their interactions to h are similarly obtained but require prior diagonalization to the flavour quark base. Note that neutrinos are considered as massless here which –in spite of being experimentally false– it is a very good approximation for collider physics, and is therefore irrelevant for the phenomenology at LHC.

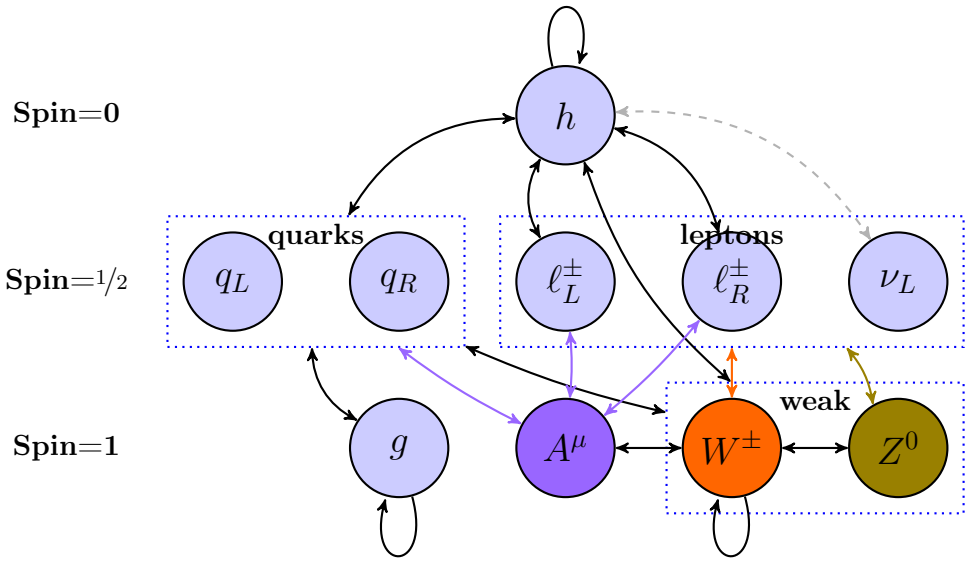

Figure 2.1: Pictorial representation of the particle content in the Standard Model and their interactions (fermion antiparticles are understood). Arrows connect particles that are directly coupled in the SM Lagrangian.

In summary, the overall set of particle content and interactions resulting from the Lagrangians in equations 2.1, 2.2, 2.4 and 2.5 is sketched in figure 2.1. Each sector of the standard model is intrinsically interesting an contains rich phenomenology. An extensive collection of measurements has been collected over the last decades for QCD, quantum electrodynamics and the weak sectors, while the Higgs-vector boson sector has started to be scrutinized in the view of novel experimental evidence [46] and hopefully precision measurements will be available soon for fermionic channels too [47]. Some aspects of the

strong sector that are relevant in the context of collider physics are described in the next section.

2.1.2 Hadronic collisions

At the LHC strong interaction scattering dominates the inclusive pp cross section. Some features of this processes are described here.

Hadrons are composite objects formed by point-like particles referred as partons [48, 49], as inferred from deep inelastic scattering experiments [50, 51]. Before their experimental discovery, partons had already been identified with the quark and gluon fields from equation 2.1 as the $SU(3)_c$ symmetry is extremely successful at accommodating the spectrum hadronic bound states

As color charged particles become closer the strong coupling among them becomes weaker and at sufficiently small scales (less than the size of the proton) parton dynamics is almost free, an effect called *asymptotic freedom*. Asymptotic freedom emerges as a consequence of the negative sign of the β function of QCD [52, 53] because predicts a region of energies in which the strength of the coupling constant (or of $\alpha_s = g_s^2/4\pi$) becomes small. At the electroweak scale $\alpha_s \approx 0.1$, which implies that perturbative calculations converge relatively fast and also provides a practical meaning to the use of Feynman diagrams in this regime. In particular, this permits the calculation of partonic cross sections for processes occurring at the LHC to leading-order (LO), next-to-leading order (NLO) or even higher orders with increasing precision.

Yet, colored particles have never been observed in isolation but always enclosed in the color-neutral hadrons, a phenomenon called color confinement. This means that partonic cross sections have to be embedded within the hadronic environment in order to provide an hadronic cross section, directly accessible for experiments. When viewed from a frame in which the proton has infinite momentum the basic inelastic scattering occurs as if partons were quasi-free within the proton [51]. This permits to consider the collision among hadrons as a rapid collision between two of their respective constituting partons occurring at a timescale much shorter than the typical timescale in which partons interact among each other within the hadron. This is known as the factorization theorem, and is extremely convenient since the hadron structure at low energy is non-perturbative precluding the use of perturbative technology. The factorization separates the hadronic cross section into two parts, a process dependent perturbative QCD calculable parton cross section $\hat{\sigma}_{ij}$, and universal functions that describe the partonic content within the hadrons. The hadronic cross section at some energy Q^2 can be written as

$$\sigma(p_1, p_2) = \sum_{i,j} \int dx_i dx_j \, \hat{\sigma}_{ij}(p_1, p_2, \alpha_s(\mu_R), Q^2/\mu_r^2, Q^2/\mu_f^2) f_i(x_1, \mu_f) f_j(x_2, \mu_f) \qquad (2.7)$$

Here, p_1, p_2 are the momenta of the incoming hadrons and $f_i(x_1, \mu_f)$ and $f_j(x_2, \mu_f)$ are the parton distribution functions (PDFs) where $f_i(x_1, \mu_F)dx_1$ gives the number of partons of type i that carry a fraction x_1 of the total hadron momentum p_1. The partonic cross section is calculated at some order in perturbation theory at some renormalization scale μ_r. The parton distribution functions are evaluated at the factorization scale μ_f, which defines an energy scale that separates the perturbative from the non-perturbative QCD regimes. In principle, any prediction of a cross section must be independent of the (arbitrary) choice of μ_r and μ_f, but finite order calculations are not. They are usually taken equal $\mu_r = \mu_f$, and close to the scale of the process Q^2. The sensitiveness of cross sections to these scales and to the particular choice of the PDFs are evaluated as theoretical systematic uncertainties, as mentioned in section 6.5.2.2.

When two of such partons (i, j) collide can undergo a large angle ('hard') scattering generating two (or more) final-state partons at large momemtum transverse to the initial beam direction (large transverse momentum, p_{T}). Partons at these states tend to radiate more partons (a process called *final state radiation*) and eventually evolve into an apparent 'spray' of hadrons that we label *jets*. As the parton shower evolves they loose momentum and at the scale of Λ_{QCD} (the mass of the proton) the strong interaction becomes dominant over the kinematics leading to a combination of the produced partons into hadrons. This mechanism is called *fragmentation* or *hadronization* and is consequence of the color confinement principle: partons fragment into hadrons before they could be directly detected. The totality of partons within the shower hadronize at the very neighborhood of the interaction point within a length of the size of the proton (1 fm).

It is important to note that the full final state contains another component consisting of particles with lower p_{T}, defined as *underlying event*. There are several additional processes that can lead to energy deposits at large transverse angles proceeding other than the hard scatter mentioned above. Partons can radiate mostly gluons and photons (less likely since $\alpha_s > \alpha \approx 1/137$) before the hard scattering takes place, a process called *initial state radiation* (ISR). An additional consequence of the composite nature of hadrons is that when two of these particles collide multiple simultaneous parton interactions (MPI) can occur. In this case the remaining partons within the hadrons are not mere spectators of the hard scatter but participate of a (generally softer) scattering process too. Even in the absence of a hard-scattering process, a collision involving only soft exchanges typically produces many particles, mostly of low p_{T} but populating all of the available phase space. From the experimental point of view all these processes are indistinguishable from the hard scatter and therefore introduce an uncertainty about the energy of the hard collision $\sqrt{\hat{s}}$.

A pictorial representation of an hadron–hadron collision and the main processes involved is shown in figure 2.2

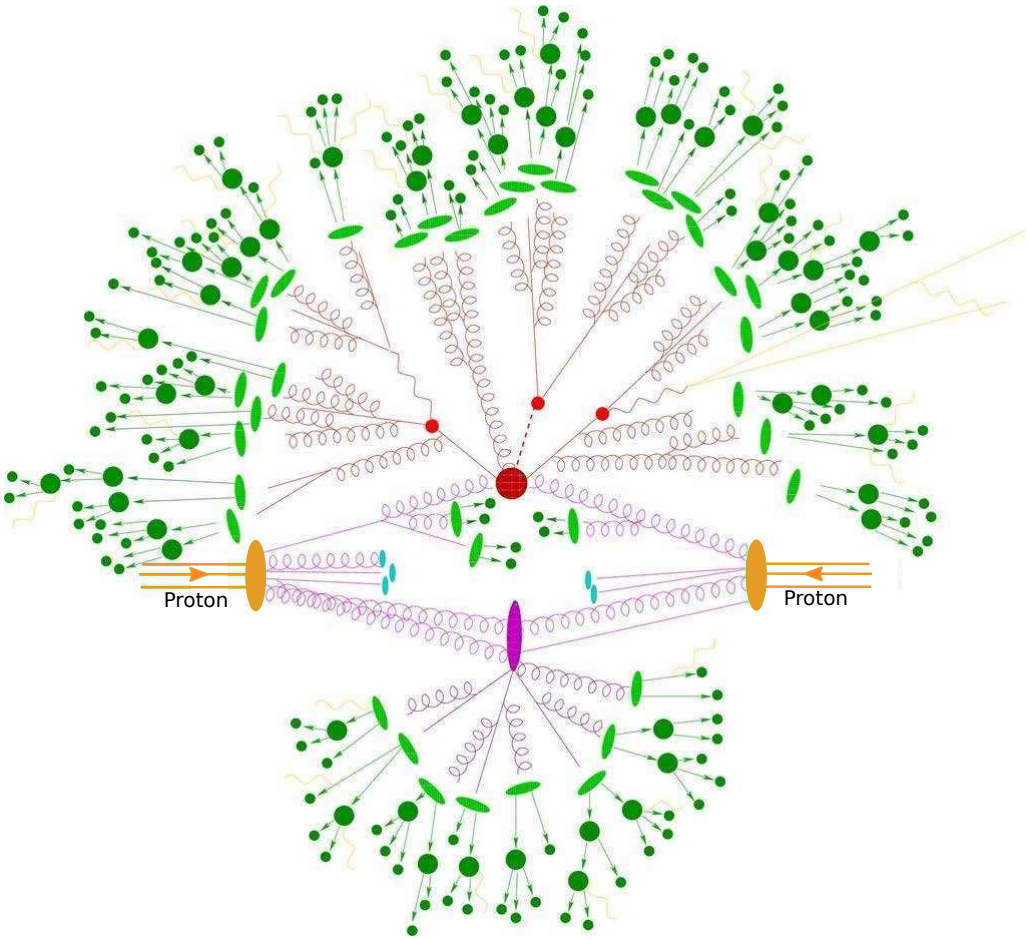

Figure 2.2: Sketch of the various phases of an hadron collision. The outer circles visualizes the event evolution driven by non-perturbative dynamics (depicted by the green and orange blobs) while the inner part shows the phases related to short-distance phenomena (depicted by the red and magenta objects). Protons (in orange) radiate gluon or quark partons (in magenta). They can interact in a hard collision (in red) which follows in a large parton shower or can interact softly (in magenta) leading to underlying events. Pile-up events (section 3.1.2) proceeding from additional pp interactions are not shown here.

2.1.3 It's 'just' a model, after all

One of the major ambitions of Physics is the entelechy of a Theory of Everything gathering in a single and coherent conceptual framework all physical aspects of the universe [15]. Regardless of whether such a theory is achievable or not, it is clear that the Standard Model —in spite of its extraordinary success— does not provide a *complete* description for all physical phenomena since, for instance, gravity is not a part of it [1]. The Standard Model agrees with all confirmed experimental data from accelerators so far, but this observed particle spectrum may not be enough to describe the matter composition of the visible Universe. Dark (i.e. non-luminous and non-absorbing) matter [8] forming $\sim$1/4 of the

[1]Gravity is non-essential for physics in collider experiments but may become mandatory to include its effects at the Planck scale ($M_P \simeq 10^{19}$ GeV) where its strength is comparable to the other microscopic interactions.

galaxies matter content may be composed of astrophysical objects (like primordial black holes) or the yet to be discovered axions, sterile neutrinos or weakly interacting massive particles (WIMPs) [7], none of which is predicted by the SM. Note that this is not an argument against the SM based on its impossibility to describe non-existing particles (an untenable argument), but points to the fact that does not provide a candidate for dark matter.

Besides inconsistencies with astrophysical evidence, strictly from the theoretical point of view the SM is very unsatisfactory to some theorists, e.g. [54, 55]. First of all, it does not explain particle quantum numbers such as the electric charge Q, weak isospin T_3, hypercharge Y and colour charges. From the brief overview in the last section it should remain clear that the values for the masses of the six quarks and the three 'electrons' are not provided by the theory as they depend on model's unknowns, the Yukawa couplings and the vacuum expectation value for ϕ. In fact, the Standard Model has a total of 19 (+9 if we take into consideration the mass of neutrinos responsible for neutrino-flavour oscillations) free parameters, that in addition to the fermion masses include also the three gauge coupling constants, the CKM mixing angles and the CP-violating Kobayashi-Maskawa phase, together with the Higgs and Z^0 masses. All parameters are constrained by experimental observations, but this number seems 'too large' as desired for an *elegant* theory, for which probably critical constants should come from the theory itself. There are however, other less subjective arguments than the aesthetic dislike for too many free parameters.

One non-trivial example of parameter arbitrariness in the SM is the EW symmetry breaking described in section 2.1.1, that tracing back the deduction relies in the quadratic factor of the scalar potential (equation 2.4) being $\mu^2 < 0$ and $\lambda > 0$, set *by hand* in order to obtain the well known 'mexican hat' potential. Yet, paraphrasing M. Peskin we are forced to accept that μ is a renormalizable parameter receiving large additive radiative corrections from loop diagrams that "can easily change the sign of μ^2" [20]. Perhaps, one of the most compelling arguments is the lack of naturalness within the Higgs sector. The renormalized squared mass of the Higgs is the bare mass plus self-mass corrections from higher order diagrams: $(m_h^2)_r = (m_h^2)_0 + \delta(m_h^2)$. The Higgs squared-mass receives quantum corrections due to loops from all fermions (as in figure 2.3(a), left diagram), but the leading term comes from the Higgs coupling to the top quark since the Yukawa coupling is proportional to the fermion mass (see equation 2.6). Considering only this contribution the leading order correction to the Higgs is quadratically divergent on the momentum cutoff of the loop integral Λ

$$\delta(m_h^2)_f = -\frac{{y_t}^2}{8\pi^2}\left[\Lambda^2 - 3m_t^2 \ln\left(\frac{\Lambda^2}{m_t^2}\right) + \dots\right] \tag{2.8}$$

where the ellipsis refers to terms which remain finite as $\Lambda \to \infty$ or are independent of the cutoff. Now that a scalar (spin=0) particle [3] was observed having a ('dressed') mass around 125 GeV [1, 2] we can face the naturalness criteria following K. Wilson's reasoning as done by L. Susskind in ref. [54] with 'realistic' numbers. Basically, if we assume that

no other physics exists up to the GUT ($\Lambda \sim 10^{14} - 10^{17}$ GeV [56]) or the Planck scale ($\Lambda = M_P \sim 10^{19}$ GeV [57]) then the bare mass of the Higgs is of $\mathcal{O}(\Lambda)$,

$$(m_h^2)_0 = (m_h^2)_r - \delta(m_h^2)_f \simeq \Lambda^2 \left(\frac{(m_h^2)_r}{\Lambda^2} - 1 \right) \simeq \Lambda^2 \left(10^{-24} - 1 \right) \tag{2.9}$$

where it was used a value of $\Lambda = 10^{14}$ and that the Yukawa coupling for the top quark is of $\mathcal{O}(1)$ [1]. The result is not a problem from the mathematical point of view of renormalization theory but triggers two intimately related issues. First, from a simple inspection the property m_h appears to have a value around the scale of the unknown high energy physics Λ, while in fact the observed Higgs mass is much smaller than this apparent *natural* scale. This constitutes a *naturalness problem* since the low energy observable is strongly sensitive to *minute* (much less than few percent) variations of the fundamental parameters (e.g. couplings, or even numerical constants) at the ultraviolet limit. And second, the need of a *fine-tunning* of these fundamental parameters to less than a part in $\sim 10^{12}$ in order to accommodate the precise cancellation between the correction and the bare mass to the level required for a 125 GeV Higgs. This fine-tuning problem would be much less severe if 'new physics' would appear at a scale much smaller than Λ.

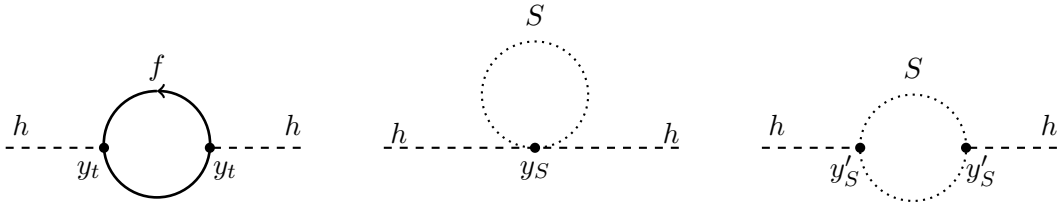

(a) loop correction to m_H^2

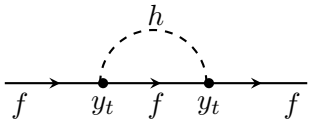

(b) fermion self energy

Figure 2.3: (a) One-loop self energy contributions to the squared mass parameter m_H, due to a Dirac fermion (left) and a scalar S (center and right) (to be described in section 2.2). and (b) to the fermion propagator due to the scalar boson.

The fine-tunning problem is unique for scalar particles like the Higgs since its mass is not prohibited by any symmetry of the Lagrangian as it does occur for the fermions for which terms of the form $m\bar{\psi}_R\psi_L$ are forbidden by the chiral symmetry, or for the gauge bosons protected by the gauge invariance that forbids terms like $m_A A_\mu A^\mu$ [39]. In particular, when including one-loop quantum corrections for the fermion mass due to the Higgs scalar (see figure 2.3(b)), it results that is only logarithmically divergent with the cutoff and

[1] At tree level the top mass is given by $m_t = y_t \frac{v}{\sqrt{2}} \approx y_t 173$ GeV where the vacuum expectation value at $v = 256$ GeV, very close to its physical mass $m_t^{obs} = 173.07 \pm 0.52^{(stat)} \pm 0.72^{(syst)}$ GeV [7].

proportional to the bare mass itself (see for instance equation 4 in ref. [58])

$$\delta(m_t) = -\frac{3y_t^2 m_t}{64\pi^2} \ln\left(\frac{\Lambda^2}{m_t^2}\right) + \dots \tag{2.10}$$

In the limit that the mass of the fermion vanishes ($m_t \to 0$), the correction also vanishes and therefore the fermion's renormalized mass is protected from large loop corrections relative to the bare mass. Even if $\Lambda \sim 10^{19}$ GeV, the correction is of the order of the bare mass $\delta(m_t) \sim m_t$ and no fine tunning is necessary after all. The fermion mass is said to be natural.

Alternatives to the Higgs mechanism have been proposed like the technicolor gauge couplings [59] or other possibilities for composite Higgses [60] that avoid the fine-tunning required for spin-zero fundamental particles. In this thesis, the analyzed models consider Higgs fields as fundamental (i.e. indivisible) particles and the naturalness problem of the scalar masses is confronted by an elegant solution: supersymmetry.

2.2 . . . and beyond: Supersymmetry

As discussed in the preceding section physics beyond the standard model (BSM) is motivated by experimental results and theoretical inferences. Any particle predicted by BSM theories that couple to the Higgs will contribute with virtual effects on the Higgs mass. Following an academic argument, if there would exist a heavy complex scalar particle S with mass m_S that couples to the Higgs through a quartic Lagrangian term $-y_S\,(\phi_S\phi_S^*)\,(hh^*)$ then the one-loop correction to the Higgs mass (figure 2.3(a) center) is [19],

$$\delta(m_h^2)_S = +\frac{y_S}{16\pi^2}\left[\Lambda^2 - m_S^2 \ln\left(\frac{\Lambda^2}{m_S^2}\right) + \dots\right] \tag{2.11}$$

As explicitly emphasized the scalar contribution is also quadratically divergent but –being a bosonic loop– it has the opposite sign compared to the fermionic one-loop correction in equation 2.8. A raw cancellation for the offending quadratic divergences occurs if the theory contains two complex scalars both assumed to couple the Higgs with a strength equal to $y_S = (y_t)^2$. After cancellation of the Λ^2 terms, the next most divergent contributions to the $\delta(m_h^2)_f$ term grows logarithmically with Λ, but even terms logarithmic in the cut-off can become unacceptably large. Cancellation of the logarithmic terms is ensured by the presence of an additional diagram (figure 2.3(a) right) induced by trilinear Higgs coupling $-y'_S\,(\phi_S\phi_S^*)\,h$,

$$\delta(m_h^2)_S = -\frac{{y'_S}^2}{16\pi^2}\left[\ln\left(\frac{\Lambda^2}{m_S^2}\right) + \dots\right] \tag{2.12}$$

From equations 2.8 and 2.11, cancellations needs in addition to $y_S = (y_t)^2$, that the trilinear coupling constant be $y'^2_S = 2y_S m_t^2$ and the scalar and fermion masses being equal $m_t = m_S$.

Thus, considering two complex scalar fields with the same mass than the fermion (and specific couplings) allows a *natural* bare mass for the Higgs close to the EW scale, and free from divergent quantum corrections. This solution to the Higgs mass relying on a precise relations between couplings and masses constitutes one of the most powerful motivations for models in which fermions and bosons are related by a symmetry: *supersymmetry*.

There is a colossal amount of features related to Supersymmetry in the literature spanning from its algebraic properties to the applications in string theory. In the next sections I will concentrate on two central aspects: a brief introduction of what supersymmetry is, and the description of minimal models derived consistently from it which provide the particle spectrum for the search described in this thesis.

2.2.1 A symmetry called 'super'

First of all, supersymmetry (Susy) is a symmetry –with a grandiose name– that if assumed as a symmetry of Nature has great implications for particle physics. Its interest relies in that 'supersymmetry algebra is the only graded Lie algebra of symmetries of the scattering matrix consistent with relativistic quantum field theory (QFT)', as demonstrated in ref. [21]. The expression is probably as accurate as is cryptic for a novice (and not so) reader, but in my opinion is an excellent starting point to introduce the mathematical substrate of this symmetry. The presentation here is far from being complete as it is not strictly demanded by the subject of the thesis, although a certain level of explanation is needed to set a common ground on the formal source for commonly used phrases like "a supersymmetry transformation turns a bosonic state into a fermion state" [19]. Excellent introductory and advanced reviews on the matter are suggested for further information in references [16–20].

Symmetries of a physical system impose stringent constraints (usually dubbed as "no-go" rules) on the formal elements used to describe the theory, either at the level of the Lagrangian, the action or the S-matrix[1]. Until the year 1974 [62] the golden rule for a particle model was that the only set of symmetry operators that could act on physical states and leave them invariant were the energy-momentum operator P_μ, the generators of the homogeneous Lorentz group $M_{\mu\nu}$, and a finite number of Lorentz-scalar charges, as established by the Coleman-Mandula theorem [63]. This is not new for us given that the Lagrangian of the Standard Model already described in section 2.1 is Poincare-invariant (i.e. invariant under the Lorentz transformations together with translations) and is also invariant under the gauge transformations generated by T^c_{ab} (from equation 2.1), T^a_L and T_Y (from equation 2.2). None of the gauge generators carry Lorentz indeces and therefore correspond to the Lorentz-scalars operators to which Coleman-Mandula theorem refers.

[1] Albeit it is common to introduce symmetries at the level of the Lagrangian, the scattering matrix –relating initial and final states undergoing a scattering interaction– is a more appropriate object of study as, from it, the scattering cross-section can be extracted [61].

Implicit in this golden rule is the conception that the generators of all the symmetries of the system must commute between each other[1] forming a Lie algebra. Again this is not a new concept as the most general description of a quantum system is provided by a Complete Set of *Commuting* Observables [64].

The limitation was evaded in ref. [21] by considering instead a "pseudo Lie algebra" (now called "graded Lie algebra") where symmetry generators can obey not only commuting rules but also commuting-anticommuting rules. The relaxation introduces new *super*symmetry operators carrying spinor indeces [18, 21] that have non-trivial commuting and anticommuting rules (see equations (1.6-1.8) in ref. [19]). It is known since long from QFT that Fermi-type operators (i.e. that have a spinorial index) satisfy anticommuting relations [61], but what is 'new' in supersymmetry is to have a symmetry generated by this kind of operator. Indeed, the generators of gauge symmetry which have spin zero when act on a state of definite spin j cannot alter that spin [17],

$$Q|j\rangle = |\text{same j, possibly a different projection of the multiplet}\rangle, \tag{2.13}$$

with $Q = T^c_{ab}, T^a_L, T_Y$. If we apply P_μ or the $M_{\mu\nu}$ or any general tensor of rank k –that are bosonic operators in the sense that they transform under Lorentz transformations as integer spin objects– the spin of the ket is changed by an integer amount n,

$$Q_{\mu\ldots\nu}|j\rangle = |j \pm n\rangle, \qquad \text{with } |j-k| \leq n \leq j+k \tag{2.14}$$

In both cases, a bosonic state remains bosonic and the same for the fermions; that is, the statistics remain the same. Whereas on the contrary, the generators of supersymmetry carrying spinorial indeces have fractional spin ($1/2$) and then change the spin of the state on which they act by $1/2$

$$Q_\alpha|j\rangle = |j \pm 1/2\rangle. \tag{2.15}$$

In other words, a supersymmetry transformation can turn a pure fermion state into a pure bosonic state and viceversa.

A mandatory consequence of this property is that supersymmetric multiplets must contain an equal number of fermionic and bosonic particle fields in order to be a closed system under supersymmetric operations. More precisely, there must be the same amount of fermionic and bosonic degrees of freedom. This provides a formal justification to the heuristic approach reproduced on section section 2.2, where two scalar fields where considered for each fermionic state in order to obtain a cancellation of quadratic and logarithmic divergences of the Higgs mass. Under general conditions, this cancellation turns from being a curious coincidence to be unavoidable within the context of a supersymmetric particle model.

There are many other technicalities which I won't include here as to when the supersymmetry increase or decreases by the spin of the state (e.g. why fermion superpartners of the

[1] For instance, $[T^c_{ab}, T_Y] = [T_Y, P_\mu] = 0$, where the commutator between operators is $[A, B] = AB - BA$.

Standard Model gauge boson are 1/2-spin fields and not 3/2-spin), the Grassman algebra needed to construct the continuous supersymmetry group, the analytic conditions upon the superpotential, what is the number of supersymmetric operators, or how supersymmetric models provide a consistent path toward Grand Unified Theories [56,65,66]. Necessary formal ingredients will be implicitly assumed when presenting the Minimal Supersymmetric Standard Model in the next section.

To close this section let's go back to the cryptic sentence at the beginning of this section. It should remain clear that it must be understood as that P_μ, $M_{\mu\nu}$, supersymmetric and scalar (for example, but not restricted to, the gauge symmetry) generators are the only set of operators that can simultaneously commute with the S-matrix, and then the only possible set of symmetries for any scattering model.

2.2.2 Minimal Supersymmetric Standard Model (MSSM)

The minimal Supersymmetric Standard Model, is the minimum set of fields and interactions necessary for a consistent supersymmetric theory that can reproduce the Standard Model phenomenology [19, 27].

Each Standard Model particle has a supersymmetric partner with spin differing by 1/2, called *sparticle* and symbolzied by a tilde ˜. Could any of the known particles in the Standard Model be paired up in supermultiplets? Or said differently, could any pair of the SM particles be each others sparticles? Unfortunately, not. The interactions among particles and sparticles in the MSSM are postulated to be the same as for the SM. This means that the Q_α operators must commute with the generators of the $\mathrm{SU}(3)_c \otimes \mathrm{SU}(2)_L \otimes \mathrm{U}(1)_Y$ gauge group, and in consequence the new sparticles must have the same gauge charges and couplings (not spin obviously) as the SM partners. None of the known fermions *quarks* and *leptons* can be paired with any of the known bosons $A_\mu, W^\pm, Z^0, g, H$, because their internal quantum numbers do not match. For example, quarks q live in triplet representations of colour, whereas the known bosons are either singlets or octets of colour. The only possibility is to introduce new supersymmetric partners for all the known particles.

Supersymmetric partners for SM fermions: sfermions. The SM fermions form chiral supermultiplets with their supersymmetric spin-0 partners. For future reference (section 2.2.2.2), in chiral supermultiplets 1/2-spin particles are described by two-component Weyl fermions, and 0-spin superpartners are complex scalar fields.

Supersymmetric partners for SM gauge bosons: gauginos. Gauge supermultiplets are formed by Standard Model gauge bosons and their half-spin superpartners, the gauginos. Gauge bosons must transform as the adjoint representation of the gauge group, so their fermionic partners, called gauginos, must also. Since the adjoint representation of a gauge group is always its own conjugate, the gaugino fermions must have the same gauge transformation properties for left-handed and for right-handed components [19].

The gauginos in the MSSM are Majorana fermions (i.e. they are theoir own anti-particles). The supermultiplet is then formed by gluons, the $SU(2)_L \otimes U(1)_Y$ vector bosons and their superpartners, the gluinos ($\tilde{g}$), the winos ($\tilde{W}$) and the bino ($\tilde{B}$).

Higgses and higgsinos. The higgs sector is not exactly replicated form the Standard Model. For the MSSM two distinct higgs complex doublets $H_{u,d}$ are introduced instead of just one:

$$H_u = \begin{pmatrix} H_u^+ \\ H_u^0 \end{pmatrix}, \qquad H_d = \begin{pmatrix} H_d^0 \\ H_d^- \end{pmatrix} \tag{2.16}$$

with opposite sign hypercharges. The reason to include two higgs fields is to cancel the axial-vector anomaly from the triangle diagram with two $SU(2)_L$ and one $U(1)_Y$ current (figure 2.4) that destroys the gauge invariance of the model [67]. Higgs bosons of equation 2.16 do not contribute to the fermion triangle-loop, but their spartners do and make a nonzero contribution to this anomaly. The anomaly is removed if two higgses with opposite sign hypercharge are included such that the contributions of their fermionic spartners, the higgsinos $\tilde{H}_{u,d}$, cancel each other. The vacuum expectations values acquired by the

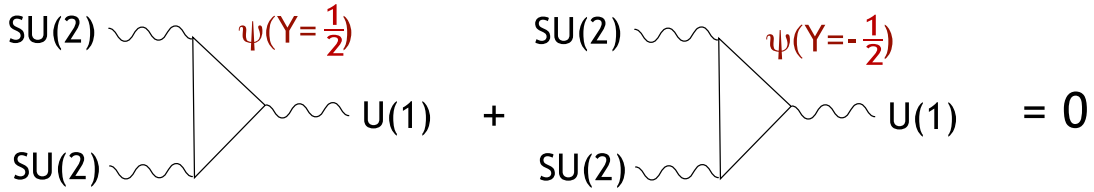

Figure 2.4: Vector-axial anomaly cancellation that requires two doubles of higgs fields in the MSSM, from [20] (there the convention for the hypercharge is $Y/2$).

electrically neutral component of these doublets are denoted by v_u and v_d, and their ratio is given by: $\tan\beta = v_u/v_d$. Upon electroweak symmetry breaking (EWSB), three of out of the eight scalar fields in equation 2.16 become the longitudinal component of the vector gauge bosons, while the remnants become two CP-even neutral scalars h^0 and H^0, one CP-odd neutral scalar A^0 and two charged scalars $H^\pm$. It may be obvious but worth mentioning that being fermions, all the components of the higgsinos (partners of higgses in equation 2.16) survive after EWSB, since none is 'lost' to give mass to the vector bosons. The particle content of the MSSM and the values of the gauge charges is summarized in table 2.1.

Before proceeding, it's worth to mention the evident, (a) none of the 'superpartners' has yet been seen experimentally, in particular they certainly cannot have the same mass as their SM partner states (as would normally be expected for a symmetry multiplet), so that (b) SUSY, as applied in the MSSM, must be (softly) broken somehow leading to more massive 'superpartners'. A less symmetrical model, however, does not make the natural argument impossible, as the cancellation of the quadratic divergence occurs whatever the values of m_f and m_S as seen from the expressions (2.8) and (2.11). But since these masses enter in the logarithmic divergence there will be a remaining correction to m_h^2 of the order $(m_S^2 - m_f^2)\ln\Lambda^2$. Softly broken SUSY may still solve the SM fine-tunning problem, provided

Name	Symbol	spin-0	spin-1/2	spin-1	$SU(3)_c$, $SU(2)_L$, $U(1)_Y$
Chiral supermultiplets					
squarks and quarks	Q	$(\tilde{u},\ \tilde{d})_{\rm L}$	$(u,\ d)_{\rm L}$		$(\mathbf{3},\ \mathbf{2},\ \frac{1}{3})$
($\times$3 families)	$\bar{u}$	$\tilde{u}^*_{\rm R}$	$u^\dagger_{\rm R}$		$(\bar{\mathbf{3}},\ \mathbf{1},\text{-}\frac{4}{3})$
	$\bar{d}$	$\tilde{d}^*_{\rm R}$	$d^\dagger_{\rm R}$		$(\bar{\mathbf{3}},\ \mathbf{1},\ \frac{2}{3})$
sleptons and leptons	L	$(\tilde{\nu},\ \tilde{e})_{\rm L}$	$(\nu,\ e)_{\rm L}$		$(\mathbf{1},\ \mathbf{2},\text{-}1)$
($\times$3 families)	$\bar{e}$	$\tilde{e}^*_{\rm R}$	$e^\dagger_{\rm R}$		$(\mathbf{1},\ \mathbf{1},\ 2)$
higgs and higgsinos	$H_u, \tilde{H}_u$	$(H^+_u,\ H^0_u)$	$(\tilde{H}^+_u,\ \tilde{H}^0_u)$		$(\mathbf{1},\ \mathbf{2},\ 1)$
	$H_d, \tilde{H}_d$	$(H^0_d,\ H^-_d)$	$(\tilde{H}^0_d,\ \tilde{H}^-_d)$		$(\mathbf{1},\ \mathbf{2},\text{-}1)$
Gauge supermultiplets					
gluino and gluon			$\tilde{g}$	g	$(\mathbf{8},\ \mathbf{1},\ 0)$
winos, W bosons			$\tilde{W}^\pm\ \tilde{W}^0$	$W^\pm\ W^0$	$(\mathbf{1},\ \mathbf{3},\ 0)$
bino, B boson			$\tilde{B}^0$	B^0	$(\mathbf{1},\ \mathbf{1},\ 0)$

Table 2.1: Chiral and gauge supermultiplets in the Minimal Supersymmetric Standard Model extending the particle spectrum of the Standard Model. The bar in $\bar{u}$, $\bar{d}$ and $\bar{e}$ is part of the name and does not denote any part of conjugation. The spin-0 are complex scalars, and the spin-1/2 are left handed two-component Weyl fermions.

that the new Susy superpartners are not to much heavier than the scale of electroweak symmetry breaking, such that the cutoff be somewhere in the range of the TeV scale (see chapter 9 of ref. [17] for a clear discussion).

The Mssm is based on a Lagrangian that contains a supersymmetric part and a soft supersymmetry-breaking part [68] introduced 'by hand' without spoiling the cancellation of quadratic divergences: $\mathcal{L}_{\rm MSSM} = \mathcal{L}_{\rm susy} + \mathcal{L}_{\rm soft}$. The supersymmetric part $\mathcal{L}_{\rm susy}$ has the same gauge interactions as the Standard Model; Yukawa fermion-scalar couplings needed to give mass to the quarks and leptons are contained in a superpotential $W_{\rm MSSM}$ that is a cubic function of chiral supermultiplets[1],

$$W_{\rm MSSM} = y_u^{ij}\bar{u}_{ai}Q^a_j \cdot H_u - y_d^{ij}\bar{d}_{ai}Q^a_j \cdot H_d - y_e^{ij}\bar{e}_i L_j \cdot H_d + \mu H_u \cdot H_d \qquad (2.17)$$

The first three terms yield masses for the charged leptons, up- and down-quarks, which are summed over colors ($a = 1, 2, 3$). All of the dimensionless Yukawa coupling parameters are 3×3 complex-valued matrices in the family space ($i, j = 1, 2, 3$) that determine the current masses and CKM mixing angles of the ordinary (i.e. SM) quarks and leptons, and are therefore constrained by precision measurements of the already known mass spectrum. Terms of the form $mH_uH_u^*$ are forbidden as the superpotential has to be an analytical function of the chiral superfields (but are included later to break Susy), so $\mu H_u \cdot H_d$ is the most general possible bilinear term. The '$\cdot$' notation means a SU(2)-invariant coupling of two doublets: $A \cdot B \equiv A_1B_1 - A_2B_2$, where 1, 2 are the weak isospin projections.

[1] In supersymmetric models the dynamical part of $\mathcal{L}_{\rm MSSM}$ is completely determined by the gauge symmetry group and by $W_{\rm MSSM}$, as described elsewhere (see e.g. section 4.6 in [19]).

The origin of the superymmetry-breaking piece $\mathcal{L}_{\text{soft}}$ is unclear and contains many unknown parameters not so constrained by measurements as it happens for $\mathcal{L}_{\text{susy}}$. Models breaking SUSY generally introduce extra terms in the MSSM Lagrangian with couplings of positive mass dimension (not dimensionless couplings) in order to naturally maintain a hierarchy between the electroweak scale and the Planck mass scale [69]. The candidates for such soft superymmetry breaking are gaugino masses for each of the gauge group factors in the Standard Model,

$$\mathcal{L}_{\text{soft}} = -\frac{1}{2}\left(M_1\tilde{B}\tilde{B} + M_2\tilde{W}^b\tilde{W}^b + M_3\tilde{g}^a\tilde{g}^a + h.c.\right) \tag{2.18}$$

where the index for the gluino runs $a = 1, \ldots, 8$, in the second (wino) term b runs from 1 to 3; these terms are admissible since gauginos in the MSSM are Majorana fermions and therefore explicit mass terms are not forbidden by the chiral symmetry. Trilinear scalar couplings (A-terms) for the scalars and the higgses

$$\mathcal{L}_{\text{soft}} = -\left(a_u^{ij}\,\tilde{\bar{u}}_{ai}\,\tilde{Q}_j^a H_u - a_d^{ij}\,\tilde{\bar{d}}_{ai}\,\tilde{Q}_j^a H_d - a_e^{ij}\,\tilde{\bar{e}}_i\,\tilde{L}_j H_d + h.c.\right) \tag{2.19}$$

where i and j are family labels. The a_u^{ij} coupling constants correspond to each of the Yukawa couplings of the superpotential equation 2.17. Squared mass m^2 terms for scalar sfermion fields (not prohibited by gauge invariance),

$$\mathcal{L}_{\text{soft}} = -{m^2_{\tilde{Q}}}^{ij}\,\tilde{Q}^\dagger_{ai}\,\tilde{Q}^a_j - {m^2_{\tilde{\bar{u}}}}^{ij}\,\tilde{\bar{u}}_{ai}\,\tilde{\bar{u}}^{a\dagger}_j - {m^2_{\tilde{\bar{d}}}}^{ij}\,\tilde{\bar{d}}_{ai}\,\tilde{\bar{d}}^{a\dagger}_j - {m^2_{\tilde{L}}}^{ij}\,\tilde{L}^\dagger_i\,\tilde{L}_j - {m^2_{\tilde{\bar{e}}}}^{ij}\,\tilde{\bar{e}}_i\,\tilde{\bar{e}}^\dagger_j \tag{2.20}$$

The five m^2 should be regarded as matrices in the flavour of the matter supermultiplets, are also in general complex but must be hermitian so that the Lagrangian remains real. Explicit higgs masses and (the only MSSM allowed) bilinear scalar mixing terms (B-term) are also incorporated,

$$\mathcal{L}_{\text{soft}} = -m^2_{H_u}H^*_u H_u - m^2_{H_d}H^*_d H_d - (bH_u H_d + h.c.)\,. \tag{2.21}$$

All the terms in equations (2.18)–(2.21) do respect gauge invariance symmetries but manifestly break SUSY, since they involve only the scalars and gauginos, and omit their respective superpartners. These terms also satisfy a constraint –in order to lead to a soft-breaking– that factors are not expected to have a characteristic mass scale in the order to 1 TeV. The bottom-line of these considerations is that mass terms which preserve electroweak symmetry can be written down for all the unobserved particles of the MSSM, whereas similar mass terms for the known particles of the SM would all break the electroweak symmetry explicitly, which is unacceptable. This fundamental difference between particles and sparticles is a common argument to say that, from the viewpoint of the MSSM, it is natural that the known particles have been found –since they are within the 'light' scale associated with electroweak symmetry breaking– while the masses of the undiscovered articles can be significantly higher.

Unlike the supersymmetry-preserving part of the Lagrangian, the above $\mathcal{L}_{\text{soft}}$s introduces more than 100 new parameters among phases and mixing angles in the MSSM Lagrangian that were not present in the ordinary Standard Model. Yet, because most of the new parameters imply flavour mixing or CP violating processes they are severely constrained by the existing results (see the list of references [78]-[103] in [19]). For example, if the matrix ${m_L^2}^{ij}$ in (2.20) has a non-supressed off-diagonal term such as ${m_L^2}^{e\mu}\tilde{e}_L^\dagger\tilde{\mu}_L$, then unacceptable large lepton flavour changing $\mu \to e$ would be generated for example through the loops in figure 2.5(a). Similarly, squark square-masses are bounded due to flavour mixing and

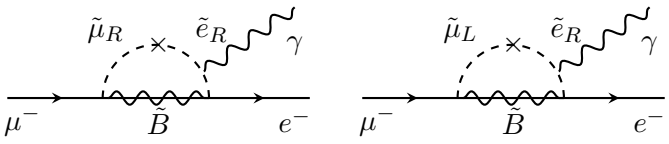

(a) constraint to $m^2_{\tilde{e}}$ (b) constraint to a_e^{ij}

Figure 2.5: Some diagrams that contribute to the process $\mu^- \to e^- + \gamma$ in models with lepton flavor violating soft supersymmetry breaking parameters (indicated by $\times$).

CP-violating constraints, from data on $K^0 \leftrightarrow \bar{K}^0$ mixing (see figure 6.7 in [19]) $D^0 \leftrightarrow \bar{D}^0$ and $B^0 \leftrightarrow \bar{B}^0$ mixing, and the decay $b \to s\gamma$ [68]. The number of free parameters in CP- and flavour-conserving MSSM is drastically reduced to 22, which include the ratio of the vacuum expectation values for the higgses ($\tan\beta$), but the number is still large

A further simplification known as constrained MSSM (cMSSM)[1] assumes universality of the gauge interactions at the GUT scale for all the gaugino masses (2.18), the scalar-squared masses are taken as diagonal in flavor having the same mass (m_0) at the ultraviolet limit (2.20), and the A-terms are taken proportional to the Yukawa couplings by a universal constant of proportionality (2.19):

$$\begin{aligned} &M_1 = M_2 = M_3 = m_{1/2} \\ &{m^2_{\tilde{Q}}}^{ij} = {m^2_{\tilde{u}}}^{ij} = {m^2_{\tilde{d}}}^{ij} = {m^2_{\tilde{L}}}^{ij} = {m^2_{\tilde{e}}}^{ij} = m_0^2\delta^{ij} \\ &a_u^{ij} = A\, y_u^{ij}, \quad a_d^{ij} = A\, y_d^{ij}, \quad a_e^{ij} = A\, y_e^{ij} \end{aligned} \tag{2.22}$$

The set of four parameters $(m_{1/2}, m_0, A, \tan\beta)$ and the sign of μ (2.17) constitute an extremely more manageable SUSY phase subspace over the full 100+ parameter space of the (unconstrained) MSSM. This parametrization is extensibly used in the literature to express the allowed/exclusion regions of SUSY models. Conditions on the A-terms equation 2.22 assure that only the squarks and sleptons of the third family can have large triple scalar couplings. If $m_{1/2}$, m_0 and b in equation 2.21 all have the same complex phase, the only CP-violating phase in the theory will be the usual CKM one (leaving aside CP-violation in the neutrino sector).

[1] cMSSM is often also referred as mSUGRA (standing for minimal SUpersymmetric GRAvity) although in the last case the symmetry breaking is explicitly driven by a hidden sector through gravity interactions [18].

2.2.2.1 R-Parity

There was an omission when writing the superpotential (2.17) since there are other gauge-invariant terms (like three-quark vertices $\lambda^{ijk}\bar{u}_i\bar{d}_j\bar{d}_k$ among others) that could have been added and still preserve the renormalizability of the theory. The reason to not include them is because they violate either baryon number (B) or total lepton number (L) [70]. Interactions in the Standard Model conserve the B and L (per family), although these symmetries were not postulated at the outset of its construction. Whether or not the MSSM must satisfy these symmetries too depends on whether or not the Nature has decided to conserve their associated charges. The empirical results point in that direction as the lightest baryon (proton) mean lifetime is of at least $\sim 10^{31}$ years [7] and can therefore be considered fairly stable, while lepton number violation has not been observed in any reaction so far (e.g. no double beta decays in absense of neutrinos: $0\nu2\beta$). Even so, B and L are known to be violated in principle albeit the effect is negligible for experiments at ordinary energies [71]. To immunize the MSSM from interactions that produce visible violations of these numbers an additional symmetry operator referred as R-parity [27] is defined for each particle as

$$P_R = (-1)^{3(B-L)+2s} \tag{2.23}$$

where s corresponds to the particle spin. The R-symmetry principle veto a Lagrangian term if the product of P_R for all the fields in it is -1. The advantage of R-parity is that it can in principle be an exact and fundamental symmetry, which B and L themselves cannot while still preventing terms with an odd number of leptons of quarks. There is a subsidiary phenomenological consequence because all of the Standard Model particles and the higgs bosons of the MSSM have even R-parity ($P_R = +1$), while all of the 'supersymmetric particles': sfermions, gauginos, and higgsinos have odd R-parity ($P_R = -1$). If R-parity is exactly conserved there cannot be any interaction vertex in the theory containing an odd number of $P_R = -1$ sparticles, which has remarkable observational consequences:

- In experiments colliding ordinary matter R-parity conservation demands that sparticles can only be created (or annihilated) in even numbers, given that $P_R = 1$ for the initial state. In particular, at the available energy of the Large Hadron Collider, heavy sparticles –if exist– would be created in pairs.
- In analogy with what happens with the proton stability if B would be conserved, the lightest supersymmetric particle (LSP) having $P_R = -1$ must be stable. Therefore, conservation of R-parity would also demand that any decay chain starting on a sparticle must eventually finish in a state that contains an odd number (probably one) of LSPs.

Connected with these comments, the MSSM mass spectrum is normally adjusted such that the LSP be an electrically neutral sparticle, so it can be considered as a promising particle candidate for Dark Matter (section 2.1.3) that only interacts weakly (and gravitationally).

2.2.2.2 Mass spectrum of the MSSM

In the MSSM several mechanisms co-exist to turn the gauge eigenstates mentioned so far (table 2.1) into physical mass eigenstates. Massive gauge bosons and SM ordinary fermions can only acquire mass by means of electroweak symmetry breaking, although the mechanism itself is more complicated than for the case of the SM since here there are two complex higgs doublets. Massive supersymmetric particles, on the contrary, can also have a Lagrangian mass term in the absence of electroweak symmetry breaking, as was already shown in the $\mathcal{L}_{\text{soft}}$ SUSY-breaking terms (2.18)–(2.21). A mass term $m^2|\phi|^2$ is allowed by all gauge symmetries for complex scalar fields like squarks, sleptons (2.20), and higgs scalars (2.21). Higgsino (2.18) and gaugino (2.21) mass terms are not forbidden by chiral symmetry, since both have the same gauge transformation properties for left-handed and right-handed components (are Majorana fermions).

Upon electroweak symmetry breaking and with the inclusion of supersymmetry breaking terms, there can be mixing between the electroweak gauginos and the higgsinos, and between particles/sparticles sharing the same quantum numbers. What follows is a qualitative presentation about the mass eigenstates of the MSSM, which is fundamental to predict the possible final states accessible for current collider experiments.

Charginos ($\tilde{\chi}^{\pm}_{1,2}$). Electrically charged higgsinos ($\tilde{H}^+_u$ and $\tilde{H}^-_d$) are mixed with electrically charged gauginos ($\tilde{W}^+$ and $\tilde{W}^-$) because of the effects of electroweak symmetry breaking to form mass eigenstates called *charginos*. Higgsinos receive a direct contribution from the μ term in the Higgs potential (2.17), the charged winos from the M_2 parameter in equation 2.18. Because of Higgs-higgsino-gaugino vertices –proceeding from the kinetic part of $\mathcal{L}_{\text{SUSY}}$ not shown here– these fields are coupled; if this coupling would not exist charged higgsinos and gauginos could have been independently diagonalized. Diagonalizing the system results in two pairs of electrically charged mass eigenstates denoted by $\tilde{\chi}^{\pm}_1$ and $\tilde{\chi}^{\pm}_2$. Each pair is degenerate in mass and the naming convention is such that $m_{\tilde{\chi}^{\pm}_1} \leq m_{\tilde{\chi}^{\pm}_2}$.

Neutralinos ($\tilde{\chi}^0_{1,2,3,4}$). The situation is similar for neutral higgsinos ($\tilde{H}^0_u$ and $\tilde{H}^0_d$) and the neutral gauginos ($\tilde{B}$ and $\tilde{W}^0$), except that here M_1 and M_2 are involved (equation 2.18). They combine to form four mass eigenstates called *neutralinos*, denoted by $\tilde{\chi}^0_1$, $\tilde{\chi}^0_2$, $\tilde{\chi}^0_3$, $\tilde{\chi}^0_4$, with increasing masses respectively. The lightest neutralino, $\tilde{\chi}^0_1$, is usually assumed to be the LSP since it is the only supersymmetric neutral particle light enough as to make a good dark matter candidate.

Gluinos. The gluino, being a color-octet fermion, cannot mix with any other particle in the MSSM, as the only remaining particles carrying color (in the adjoint representation) are the 1-spin gluons. The source for gluino mass is the SUSY-breaking mass M_3 in equation 2.18. A gross prediction based on renormalization group evolution [19] relates the gluino mass parameter with the bino and wino mass parameters (M_1 and M_2) by

$$M_3 \colon M_2 \colon M_1 \approx 6 \colon 2 \colon 1 \ , \tag{2.24}$$

at a Q scale near the TeV. This establishes a rough hierarchy between gluinos, and the binos+higgsinos mass eigenstates, with the gluinos being considerably heavier that the lighter neutralinos and charginos.

Squarks and sleptons. In principle, any collection of scalars with the same charges (electric, color, R-parity)[1] can mix with each other. This means that with completely arbitrary soft terms, the mass eigenstates of the squarks and sleptons of the MSSM should be obtained by diagonalizing three 6×6 squared-mass matrices for up-type squarks ($\tilde{u}_L$, $\tilde{c}_L$, $\tilde{t}_L$, $\tilde{u}_R$, $\tilde{c}_R$, $\tilde{t}_R$), down-type squarks ($\tilde{d}_L$, $\tilde{s}_L$, $\tilde{b}_L$, $\tilde{d}_R$, $\tilde{s}_R$, $\tilde{b}_R$), and charged sleptons ($\tilde{e}_L$, $\tilde{\mu}_L$, $\tilde{\tau}_L$, $\tilde{e}_R$, $\tilde{\mu}_R$, $\tilde{\tau}_R$), and one 3×3 matrix for sneutrinos ($\tilde{\nu}_e$, $\tilde{\nu}_\mu$, $\tilde{\nu}_\tau$). Fortunately, the strong assumptions taken for the constrained MSSM in equations (2.22) predict that most of these mixing angles are very small:

- For the first two generations of fermions, the Yukawa couplings are small and therefore the contributions to the first and second generation sfermion masses which are proportional to the Yukawa couplings can be neglected.
- The A-terms for the first and second generations are also assumed to be small due to flavour-changing contraints.

The first- and second-family squarks and sleptons end up in 7 very nearly degenerate, unmixed pairs $(\tilde{e}_R, \tilde{\mu}_R)$, $(\tilde{\nu}_e, \tilde{\nu}_\mu)$, $(\tilde{e}_L, \tilde{\mu}_L)$, $(\tilde{u}_R, \tilde{c}_R)$, $(\tilde{d}_R, \tilde{s}_R)$, $(\tilde{u}_L, \tilde{c}_L)$, $(\tilde{d}_L, \tilde{s}_L)$. The squarks of the first and second families are nearly degenerate and much heavier than the sleptons. This is because each squark mass gets the same large positive-definite radiative corrections from loops involving the gluino.

In contrast, the third-family squarks and sleptons can have substantial mixing in pairs ($\tilde{t}_L$, $\tilde{t}_R$), ($\tilde{b}_L$, $\tilde{b}_R$) and ($\tilde{\tau}_L$, $\tilde{\tau}_R$), because of the effects of large Yukawa (y_t, y_b, y_τ) and soft (a_t, a_b, a_τ). For the top squarks, there are several non-negligible contributions for the left-right mixing of the top squarks described by a Hermitian 2×2 mass matrix, which in the basis ($\tilde{t}_L$, $\tilde{t}_R$) reads [72]

$$\begin{pmatrix} (m^2_{\tilde{Q}})^{33} + m_t^2 + \Delta_{\tilde{t}_L} & m_t \left(a_d^{33} - \mu \tan\beta\right) \\ m_t \left(a_d^{33} - \mu^* \tan\beta\right) & (m^2_{\tilde{\bar{u}}})^{33} + m_t^2 + \Delta_{\tilde{t}_R} \end{pmatrix} \tag{2.25}$$

where $\Delta_{\tilde{t}_R}$ and $\Delta_{\tilde{t}_L}$ are of the order $\mathcal{O}(m_Z)$. Upon diagonalization, the resulting mass eigenvalues are

$$m^2_{\tilde{t}_{1,2}} = m_t^2 + \frac{1}{2}\left[m^2_{\tilde{t}_\mathrm{L}} + m^2_{\tilde{t}_\mathrm{R}} \mp \sqrt{\left(m^2_{\tilde{t}_\mathrm{L}} - m^2_{\tilde{t}_\mathrm{R}}\right)^2 + 4\left|m_t\left(a_d^{33} - \mu\tan\beta\right)\right|^2}\right] \tag{2.26}$$

where $m^2_{\tilde{t}_\mathrm{L}}$ and $m^2_{\tilde{t}_\mathrm{R}}$ are the diagonal elements in equation 2.25. Due to the large value of m_t, the mixing is particularly strong in the stop sector which ends in highly non-degenerate

[1] Note that the weak charge is not included here as 0-spin particles don't have two chirality states; the R or L 'handedness' in the name of scalar fermions refers to the chirality of their SM partners.

mass eigenstates, unlike with what happens for unmixed sfermions of the first- and second-families. In particular, the lightest top squark $\tilde{t}_1$ (or the lightest sbottom $\tilde{b}_1$) is probably lighter than the other squarks.

The argumental lines are similar for sbottoms and staus, and similar relations stand for the sbottom (stau) replacing $t \to b$ and a_u^{33} ($t \to \tau$ and a_e^{33}).

Higgs sector. As mentioned before, following EWSB five scalar degrees of freedom remain from the two complex Higgs doublets (2.16). Two charged mass-degenerate bosons $H^{\pm}$ with mass given at tree level by

$$m_{H^{\pm}}^2 = m_{A^0}^2 + m_W^2 \tag{2.27}$$

and three electrically neutral scalars, from which one is CP-odd called A^0

$$m_{A^0}^2 = 2b/\sin(2\beta) \tag{2.28}$$

(where b is the quadratic SUSY-breaking term quadratic in the Higgs fields from equation 2.21) and the other two are CP-even named h^0 and H^0 with masses

$$m_{h^0,H^0}^2 = \frac{1}{2}\left(m_{A^0}^2 + m_Z^2 \mp \sqrt{(m_{A^0}^2 - m_Z^2)^2 + 4m_Z^2 m_{A^0}^2 \sin^2(2\beta)}\right). \tag{2.29}$$

The h^0 boson is the lighter particle by convention and behaves almost similar to the SM Higgs although it has very different couplings. In principle the masses of A^0, H^0 and $H^{\pm}$ can be arbitrarily large but the mass of h^0 is upper bounded. Including top-squark loops and assuming that all of the sparticles that can contribute to $m_{h^0}^2$ in loops have masses that do not exceed 1 TeV, the upper limit is $m_{h^0} \lesssim 150$ GeV [19]. It's still too early to determine if the SM-consistent scalar boson discovered at 125 GeV in the LHC [1,2] could be the lighter MSSM Higgs h^0.

In the next section the practicality of MSSM for actual searches is discussed and additional models are also introduced.

2.2.3 Simplified models

The general MSSM has too many parameters to be practically scanned at any experiment. On the other end, an extremely constrained model like cMSSM have only five free parameters providing a more attackable phase space but introduce theory prejudice, that is the specific set of assumed SUSY-breaking terms in $\mathcal{L}_{\text{soft}}$ and their behaviour at the GUT scale (2.22). Results presented using values at the ultraviolet scale like m_0 or $m_{1/2}$ make difficult the comparison of among alternative theories: results must be reinterpreted in terms of parameters at EW scale and these low energy limits must be translated back –through renormalization group (RG) evolution– to the UV scale parameters of the alternate model. Given the complexity of RG evolution the approach is anything but straightforward. Also,

there are often many production modes and decay channels contributing to the same experimental final phenomenology (see e.g. figure 2.6(a)). Relative production rates, branching ratios and mass splittings affecting those processes are highly dependent on the specific choice of model parameters and the particular mechanism of SUSY-breaking. Therefore analyses optimized to a given signature for a set of parameters may not be effective for the same final state topology if Nature (in case supersymmetric particles exist) 'had chosen' other configuration.

A different approach called *simplified model* [73, 74] is to focus on one or few production processes and decay chains with fixed branching ratio (BR). A simplified model is specifically designed to involve only the minimal particle content and few interactions necessary to produce SUSY-like final states contributing to the channels of interest. Therefore a simplified model is not a fully SUSY model since only the parameters relevant to the single decay chain are considered.

Some of these models are limits of more general new-physics scenarios, where all but a few particles are integrated out. For instance, consider a direct three-body gluino decay into an electroweak gaugino and two light-flavored quarks, $\tilde{g} \to q\bar{q}'\tilde{\chi}_1^0$. This decay mode occurs in supersymmetric models where the squarks are significantly heavier than the gluino; it proceeds through the interaction term $\mathcal{L}_{\text{int}} = \frac{\lambda}{M^2}\tilde{g}q\bar{q}'\tilde{\chi}_1^0 + h.c.$, where λ is the *same* Yukawa coupling for the quark-squark-neutralino vertex. The simplified decay chain for the assumed mass spectra is shown in figure 2.6(b).

Although, the simplified model is clearly model dependent (e.g. it depends on the couplings of the full theory), it does avoid some pitfalls of full-model dependence. The dimensionality of the theoretical parameter space is reduced to a handful of sparticle mass parameters and relevant branching ratios, allowing for the commonalities between different models to become apparent. The sensitivity or upper limits for any new-physics search is presented using parameters directly related to collider physics observables: the masses at the weak-scale of the new particles, production cross-sections, and branching fractions. Varying the few model parameters gives a complete survey of the final state configurations produced by the decay chain of interest and exposes transparently the sensitiveness of a given analysis.

In practice, it is necessary first to postulate relevant particles of the search for which the simplified models will be constructed. Although, generally $m_{sleptons} < m_{squarks}$, at a hadron collider like the LHC the most copiously produced SUSY particles are expected to be the strongly-interacting in inclusive squark and gluino pair-production, and squark-gluino figure 2.7. Direct third-generation pair production channel has a smaller relative rate but is also considered relevant here as it tends to produce many jets in their final state. Therefore, simplified models considered here have gluinos or squarks as outgoing sparticles in the matrix elements.

What follows is a list of models used to interpret results, in addition to the full cMSSM described before. With the sole exception of the last model presented next, all processes

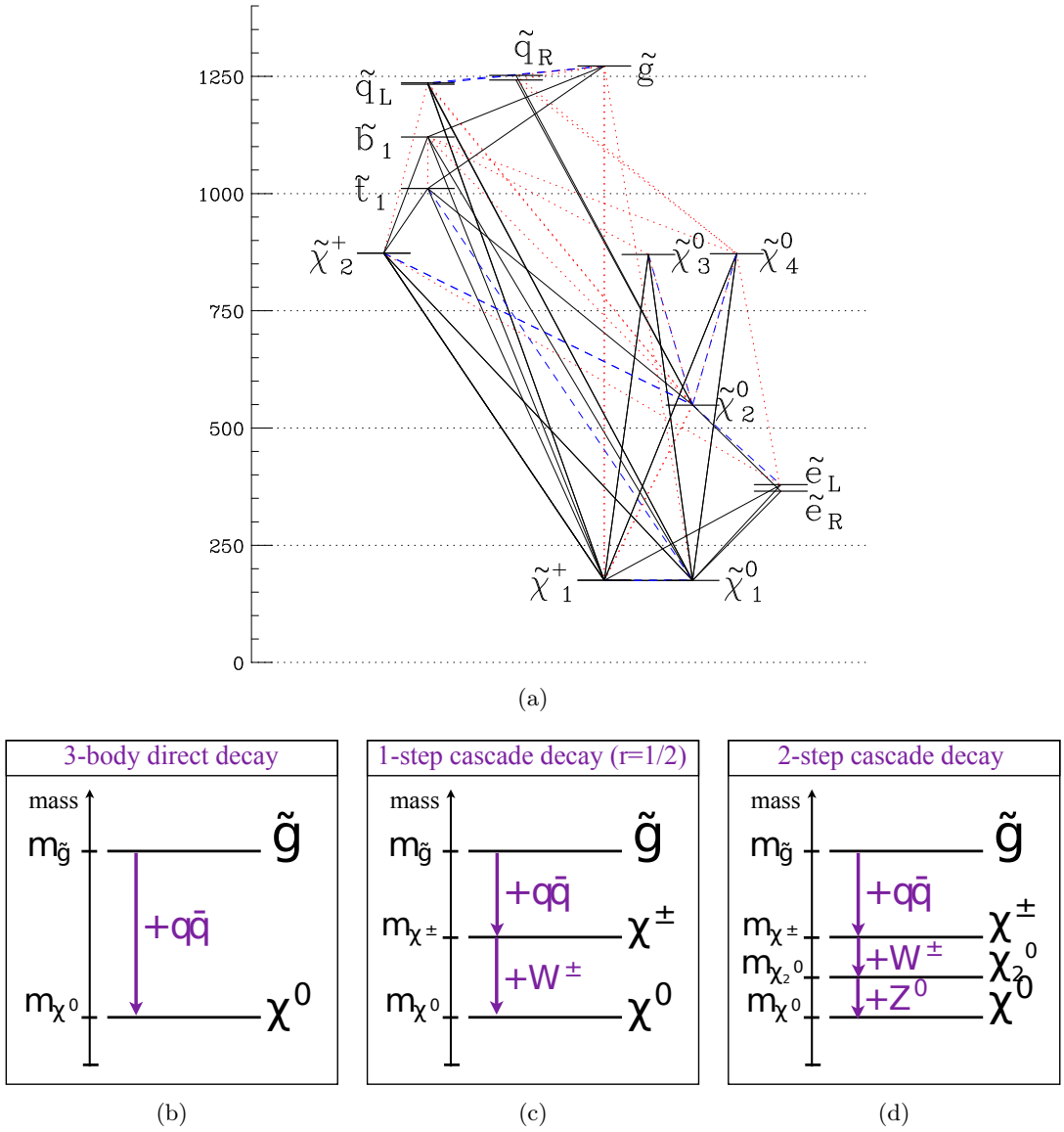

(a) (b) (c) (d)

Figure 2.6: (a) Sample schematic mass spectra for MSSM undiscovered sparticles included here to illustrate the complexity of decay chains involved in full models, from [75]. Spectra and decay modes for *Gtt* (b), one-step (c) and two-steps (d) simplified models considered in this thesis. The masses of the intermediate states in the decay chains are held at a fixed distance from $m_{\tilde{g}}$ and $m_{\tilde{\chi}^0_1}$, corresponding to slices through the mass parameter space that are representative of all the kinematical configurations. From [76].

conserve R-parity (called RPC processes), and therefore conserve baryon- and lepton-numbers. All have in common that many coloured particles in the final state and a neutral LSP for R-parity conserved models.

'Gluino–stop (off-shell)' model. This model is characterized by the pair production of gluinos followed by their decay with 100% branching ratio to $t\bar{t} + \tilde{\chi}^0_1$ ($\tilde{g} \to t\bar{t}\tilde{\chi}^0_1$), through a virtual stop particle. Current constraints allow gluinos to be too heavy to be produced at visible rates in the LHC, or it could be relatively light. Naturalness arguments for supersymmetry favour light gluinos and stop particles (also higgsinos) so it is very natural

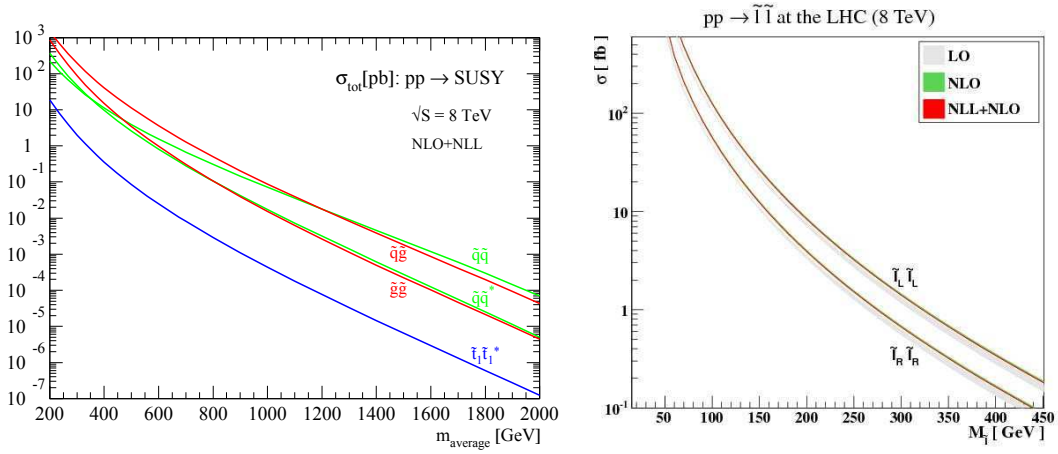

(a) squark and gluino production

(b) slepton production

Figure 2.7: (a) Cross sections for squark and gluino hadroproduction including next-to-leading order supersymmetric QCD corrections, computed using NLL-fast [77]. The dominant process for squark-squark production is $gg \to \tilde{q}\bar{\tilde{q}}$, through the gluon s-channel, squark t- and u-channels, and through the four-point interaction. The gluino pair production is produced principally from $gg \to \tilde{g}\tilde{g}$ in the gluon s-channel, the gluino t- and u-channels, and the gluon s-channel in the $q\bar{q} \to \tilde{q}\bar{\tilde{q}}$ process. (b) Cross sections for slepton pair production taken from [78].

to consider this decay pattern.

Here, squark masses are assumed to be high enough, so that gluino decay via a virtual (off-shell) squark looks like 3-body decay as shown in figure 2.8(a). In such cases, the final state of gluino-mediated squark production has 4 quarks in the final states. For the target phenomenology, the four associated jets (plus those produced by initial or final state radiation) may not be enough to our multi-jet signal regions. In the case of third-generation, each final state top can lead to up to five jets if the $W^{\pm}$ and the b both decay fully hadronically.

Implicit here (and also for the remaining models) is that this process must satisfy simple relations between the masses of the particles in the decay chain (due to basic conservation of energy). In this case, the process can only occur if the gluino mass is larger than: $m_{\tilde{g}} > 2m_t + m_{\tilde{\chi}_1^0}$. The production threshold is drawn as a line in the exclusion plots indicating the kinematical limit of the model.

'Gluino–stop (on-shell)' model. This is similar to the previous 'Gtt' model but the stop squark is now assumed to be lighter than the gluino so the gluino decays through a on-mass-shell stop rather than a virtual one, as shown in figure 2.8(b). The on-shell constraint affects the kinematics, dominantly through the p_{T} spectrum of the four tops produced in the decays. Here the kinematics depend on three parameters; the masses of the gluino, of the squark and of the LSP. The masses of colored $\tilde{g}$ and of the invisible LSP are varied over the range from $[400, 1500] \times [0, 1000]$ in GeV at representative steps to cover the phase space of masses. Only gluino pair production is considered.

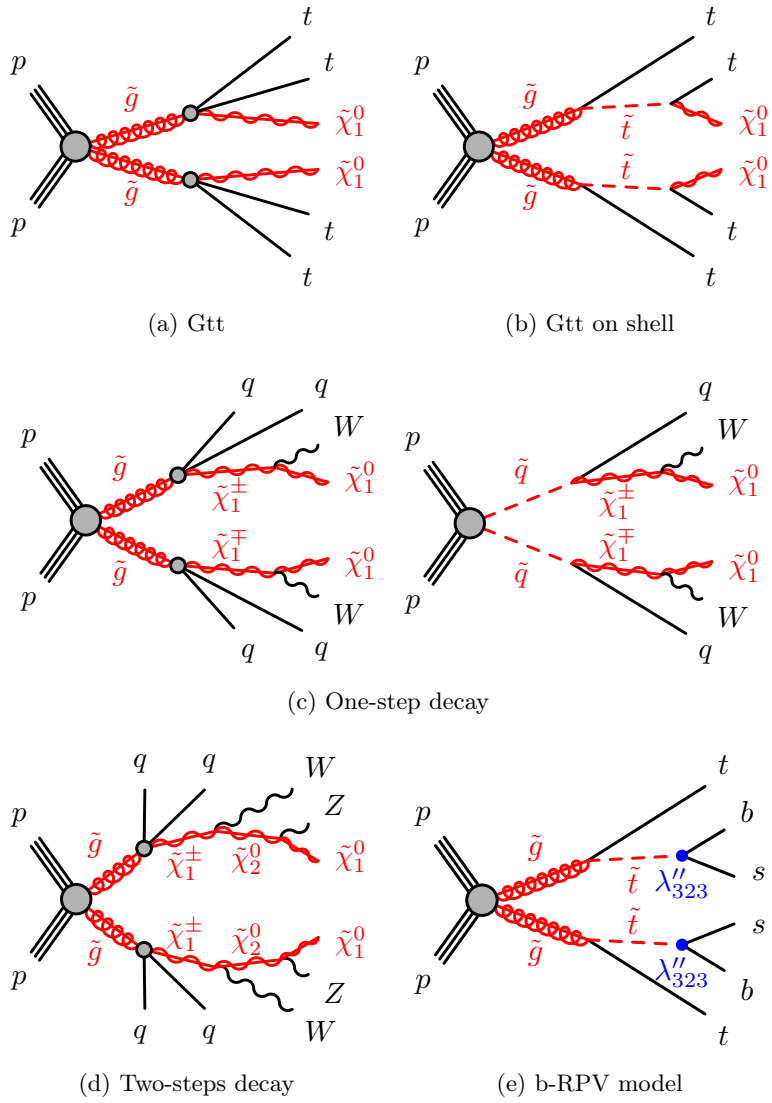

(a) Gtt (b) Gtt on shell

(c) One-step decay

(d) Two-steps decay (e) b-RPV model

Figure 2.8: Decay chains for the different simplified models predicting many jets and missing energy in the final state (from the weakly-interacting LSP). These are used to interpret results in this thesis.

'Gluino–squark (via $\tilde{\chi}_1^\pm$)' one-step model. Two varieties of sequential decay models are considered, starting with either pair-production of gluinos or pair-production of squarks as represented inn figure 2.8(c). Decays are defined by an intermediate decay:

$$\tilde{g} \to q\bar{q}\tilde{\chi}_1^\pm, \text{ or } \quad \tilde{q} \to q\tilde{\chi}_1^\pm,$$

Remember that charginos are and addmixture of the electroweak gauginos, so the chargino inherits $\mathrm{SU}(2)_L$ gaugino-gaugino-vector boson couplings of its components. Therefore, one possible decay of the chargino is into a lighter neutralino or chargino plus an electroweak gauge boson. In this model, the light chargino subsequently decay with 100% branching

ratio to

$$\tilde{\chi}_1^{\pm} \rightarrow W^{\pm}\tilde{\chi}_1^0.$$

The decay chain "gluino → heavy chargino → LSP" is preferred in many supersymmetric scenarios, including cMSSM [73]. When the intermediate particle is a chargino, all events have two $W^{\pm}$ bosons in the final state.

There are three free parameters in these systems; the mass of the coloured particle, the mass of the chargino and the mass of the neutralino. As it is desirable to pick two variables such that results can be shown in 2-D plots (where the axes are whatever two free masses), two choices are considered. In one case the mass of the LSP is fixed at 60 GeV

$$m_{\tilde{\chi}_1^0} = 60 \text{ GeV},$$

and in the other case the mass of the chargino is set exactly in between the masses of the mother sparticle and the LSP:

$$m_{\tilde{\chi}_1^{\pm}} = \frac{m_{\tilde{g},\tilde{q}} + m_{\tilde{\chi}_1^0}}{2}.$$

The gluino-gluino simplified models are of more interest for this analysis as they have higher jet multiplicities as shown in figure 2.8(c).

'Gluino–squark (via $\tilde{\chi}_1^{\pm}$ and $\tilde{\chi}_2^0$)' two-steps model. In this simplified model, each gluino of a pair decays as $\tilde{g} \rightarrow q + \tilde{q}$. Two intermediate steps occur in the cascade until the LSP is finally produced. In the first step the gluino decay in an effective three body decay to $qq' + \tilde{\chi}_1^{\pm}$ and in a second step the heavy neutralino ($\tilde{\chi}_2^{\pm}$) produced in the chargino decay leads to the lighter neutralino. The final state contains two quarks, two vector bosons, and an LSP per each gluino as indicated in figure 2.8(d). The intermediate particle masses $m_{\tilde{\chi}_1^{\pm}}$ and $m_{\tilde{\chi}_2^0}$, are set to $(m_{\tilde{g}} + m_{\tilde{\chi}_1^0})/2$ and $(m_{\tilde{\chi}_1^{\pm}} + m_{\tilde{\chi}_1^0})/2$, respectively. The sensitivity to squark-squark initiated cascades is smaller than for the gluino-gluino case since two less quarks are produced in the final state, so that process is not evaluated in this search.

Gluino–stop (b-RPV) model. In this simplified model, each gluino of a pair decays as $\tilde{g} \rightarrow \tilde{t} + \bar{t}$; and the $\tilde{t}$-squark decays via the R-parity- and baryon-number-violating decay $\tilde{t} \rightarrow s + b$. The psedudo-diagram is presented in figure 2.8(e).

cMSSM (Higgs aware) Plane. In spite of the comparative practical advantages simplified models have over full models, the SUSY program in ATLAS continues providing exclusions limits in cMSSM planes. Following the discovery of the Higgs boson at about 125 GeV, the cMSSM plane that had been used in previous searches is excluded due to the Higgs mass being lighter than its observed value across the whole plane. A benchmark point has been generated in this model assuming the following parameters; $\tan\beta = 30$, $A_0 = -2m_0$, $\mu > 0$, which satisfies the Higgs mass constraint across much of the space. cMSSM completes the set of models considered to set upper limits on visible cross sections to supersymmetric processes as described in section 7.2.

3
The experiment

3.1 The Large Hadron Collider

Since the pioneering work lead by E. Rutherford the exploration of the subatomic structure has been primarily conducted through the bombardment and collision of particles and the analysis of scattering angles and rates. The Large Hadron Collider (LHC) [10] is the most advanced and powerful source for the particle collisions ever built. The LHC is a synchrotron built by the European Organization for Nuclear Research (CERN), installed in the 27-kilometer circular tunnel previously occupied by the Large Electron Positron collider at approximately 100 metres underground below the border between France and Swizerland. It is a precision instrument capable of colliding energetic beams of protons (or heavier nuclei) at rates upward of millions per second in interaction 'points' (IPs) of the size of microns. The precision and high beam energy make of the LHC an extraordinary tool to explore the tera-electronvolt (TeV) scale, an energy range never before achieved in controlled collider experiments for elementary particle physics.

The ATLAS detector, one of the multipurpose experiments in the LHC assigned to analyze the collision outputs, will be described in section 3.2.

3.1.1 Machine design

The LHC has been originally designed to produce head-on collisions between beams of protons at a center-of-mass energy, $\sqrt{s}$, of 14 TeV. An unexpected technical incident occurred on September 2008[1] delayed the LHC's physics program and obligated to operate below the design specifications at $\sqrt{s} = 7$ TeV during the first years 2010–2011 and at $\sqrt{s} = 8$ TeV in the 2012 period. Since March 2013 the LHC is in a long shutdown period for maintenance and improvement that will allow to operate the machine at 6.5 or 7 TeV per beam in 2015.

In either case, TeV energies are not achieved from protons at rest in the LHC. This ring is actually the last shackle in a series of several intermediate accelerators –some of which have been operating for decades– that successively increase their energy. The whole chain is illustrated in figure 3.1(a). Protons extracted from ionized Hydrogen atoms are feed to

[1] A short-circuit in a connection between superconductors in the tunnel burned a hole in a vessel containing liquid helium, with catastrophic consequences for the LHC mechanics.

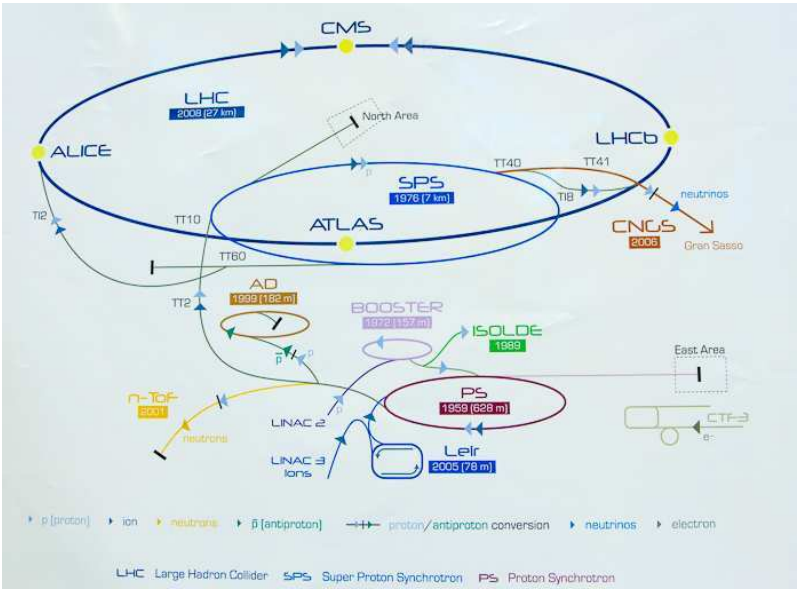

(a)

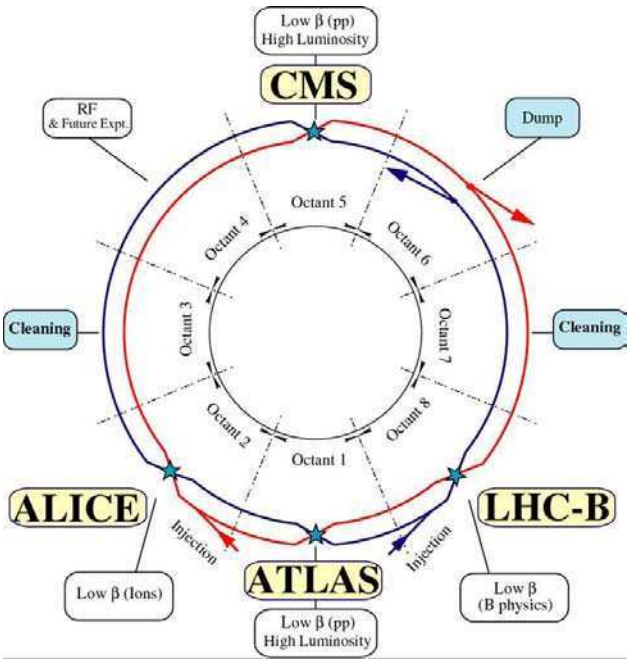

(b)

Figure 3.1: (a) The CERN accelerator complex © encompassing several accelerators (the length of each is included between parenthesis). CERN operates in parallel other non-LHC particle physics program like neutrino beams sent to Gran Sasso, which are also included in this picture. See text for more details. (b) LHC layout with four interaction points at the site of the detectors, the beam injection points at TI2 and TI8 transfer lines, and the dump site.

the linear particle accelerator Linac 2 where proton energy is raised to 50 MeV. These are then catered to the Proton Synchrotron Booster (PSB), where protons are further *boosted* to 1.4 GeV and injected then into the Proton Synchrotron (PS) hat increases the energy

up to 25 GeV. The Super Proton Synchrotron (SPS) is the last pre-LHC ring that further increases proton energy to 450 GeV. Prior injection into the LHC all protons in each stage flow in the same direction. Injection occurs in two different points (TI2 and TI8 transfer lines) such that contra-rotating beams result in the larger ring, as schematically shown in figure 3.1(b).

The LHC contains two adjacent, high-vacuum beam pipes (maintained at a pressure of 10^{-13} atm) running in parallel throughout all the ring, except mandatory discontinuities in the vicinity of the interaction points where the beams are allowed to cross. Each pipe directs a proton beam that is bent into a nearly circular trajectory by a large variety of superconducting magnets cooled to 1.9 K by liquid-helium vessels for proper operation of the magnets at the superconducting state. Bending is primarily driven by 1232 dipole magnets designed to operate at 11.85 kA, generating a magnetic field of 8.4 Tesla necessary for 7 TeV proton beams. A large series of smaller quadrupole, sextupole, octupole, and decapole magnets provide beam shaping to counteract Coulomb repulsion of the proton aggregate by squeezing the beam in its transverse plane. Beam acceleration within the LHC occurs in eight radiofrequency (RF) resonant cavities per beam where the electromagnetic field oscillates at a frequency that is a multiple of the protons revolution frequency (f_{rev}). Charged particles passing through the cavity are accelerated or decelerated by the electromagnetic force until become synchronized to the oscillating field in the cavity. The net effect is that protons tend to be grouped in tight bunches of tens of centimetres long each. During 2012 each bunch contained approximately 10^{11} protons, that ensured high instantaneous luminosity at the collision points and hence maximize the number of collisions. It should be noted that not all stationary regions of the RF potential (called buckets) are occupied but –as a consequence of the SPS and LHC injection strategy– a "bunch-train" consisting of a group of filled buckets separated by a time $\tau_{\text{bunch}} = 50$ ns, is in turn separated from other bunch-train by several empty buckets. In addition to organize protons longitudinally along the beam, once a stable time structure has been achieved the frequency of the cavities is slowly increased to transfer power to push the protons forward along the accelerator. This is the process called synchrotron acceleration. Each cavity delivers 2 MV (an accelerating field of 5 MV/m) at 400 MHz, and is kept at 4.5 K. Plateau energy is reached in around 15 minutes.

Both beams traveling in opposite directions are squeezed and focused at four intersect points (IP) where the detectors are placed: the multipurpose detectors of the ATLAS [11] and CMS [12] experiments, and two other dedicated detectors ALICE [13] and LHCb [14] for heavy ion and B-physics experiments, respectively 3.1(a).

3.1.2 LHC operation during 2012

The rate of production of a certain process i is directly related to the cross-section of such process $\sigma_{pp\to i}$ and the LHC capability to put the protons into close contact, as encoded by

the instantaneous luminosity L_0. Formally the rate is expressed by

$$\mathcal{R}_i = L_0 \sigma_{pp \to i} \tag{3.1}$$

where the cross-section is a purely physical magnitude (calculable from scattering amplitudes), whereas the luminosity depends exclusively on the beams optics an can be expressed by

$$L_0 = n_c f_{rev} \frac{N_1 N_2}{4\pi \sigma_x^* \sigma_y^*} \tag{3.2}$$

where n_c is the number of colliding bunch pairs, N_b is the number of protons per bunch in beam b, and $\sigma_{x,y}^*$ are the transverse sizes of the beam at the interaction point. Clearly the luminosity –and by inheritance the production rate– increases as bunches have more protons, more bunches crossings occur (either because there are more filled bunches in the pipe or the crossings are more frequent) or if the beams are more collimated at the IP as to reduce the transverse spread of protons. As a consequence, the observation of unlikely scattering processes with small cross sections requires to maximize the delivered instantaneous luminosity, which is turn limited by the machine performance and protection-thresholds. The timeline of peak luminosity as measured on-line during data taking is shown in figure 3.2(a). The time integrated luminosity $L_0^{int} = \int L_0 \, dt$, is shown underneath in figure 3.2(b).

A pp collision is in essence a stochastic process. As such the high luminosity not only enhances the probability of a single pp scattering but also increases the likelihood for multiple pp collisions per bunch crossing. The average expected number of inelastic collisions is refered to as $\langle \mu \rangle$. This variable follows a poisson distribution whose mean is dependent on L_0 by virtue of equation 3.1. Beam optics and bunch parameters at the IP can change across different periods of data-taking resulting in clear changes of the luminosity of the machine. Therefore, the underlying poisson distribution can be shifted towards higher or lower values of $\langle \mu \rangle$ as shown in figure 3.3 for 2011 and 2012 data.

In general, in each bunch crossing there is only one hard-scatter process that usually triggers the event (see section 3.2.7), while the remaining inelastic interactions contribute to soft additional deposition of energy in the detector that blur the resolution of the hard process of interest. This phenomenon called pile-up can occur in two forms. The first form coming from the multiple pp collisions happening in the same bunch crossing is referred as in-time pile-up. In-time pile-up conditions can be reasonably estimated by the number of primary vertices N_{PV}, as measured using the tracking system in ATLAS (section 3.2.2). The second form is a consequence of the short time separation between subsequent bunches ($\tau_{bunch} = 50$ ns in 2012). Due to the long time taken to produce and read-out the electronic signal in some sub-detectors (see section 3.2.4) pp scatterings from a given bunch crossing can affect the signal shape of future bunch crossings. This case is called out-of-time pile-up.

The 2012 pp program started effectively on 5 April when the LHC shift crew declared

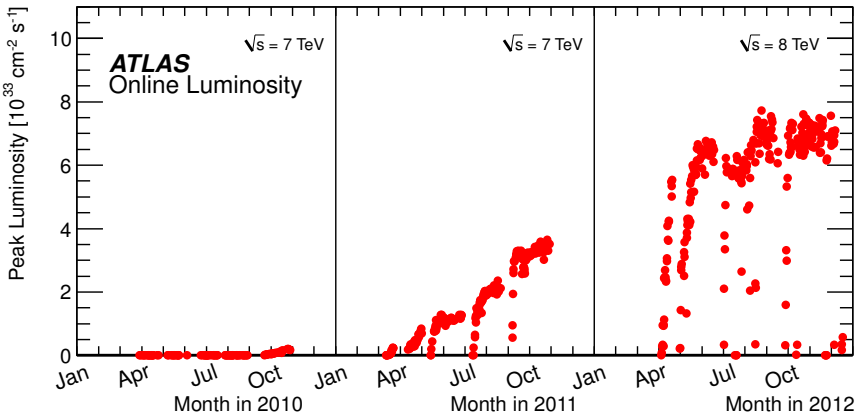

(a)

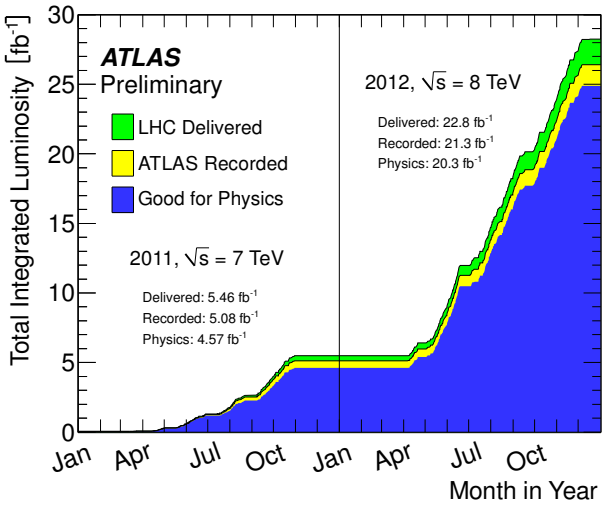

(b)

Figure 3.2: (a) The peak instantaneous luminosity delivered to ATLAS per day versus time during the *pp* runs of 2010,2011 and 2012. (b) Integrated Luminosity and Data Quality in 2011 and 2012 Cumulative luminosity versus time delivered to (green), recorded by ATLAS (yellow), and certified to be good quality data (blue) during stable beams and for pp collisions at 7 and 8 TeV center-of-mass energy in 2011 and 2012.

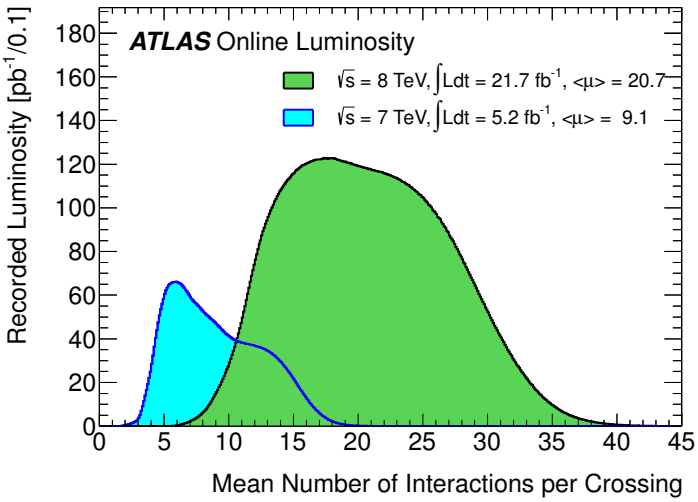

Figure 3.3: Number of Interactions per Crossing Shown is the luminosity-weighted distribution of the mean number of interactions per crossing for the 2011 and 2012 pp-collision data. The mean number of interactions per crossing corresponds the mean of the poisson distribution on the number of interactions per crossing calculated for each bunch. The different LHC configuration conditions over the year result in overlaping poissonian distributions with different means. More details on this can be found in ref. [79].

"stable beams" as two 4 TeV proton beams were brought into collision at the LHC's four interaction points. The pp data-taking continued until December 17. As mentioned before the instantaneous luminosity was on average higher during 2012 than in previous years as depicted in figure 3.2(a) peaking at $7.7 \times 10^{33}\, cm^{-2}s^{-1}$, close to the design value $1 \times 10^{34}\, cm^{-2}s^{-1}$ [80]. The average number of pp collisions per bunch crossing was 20.7, and peaked at more than 40 simultaneous crossings (figure 3.3).

The data-taking in ATLAS had an average efficiency of 93.5% (in rought terms corresponds to the yellow area divided the green area from figure 3.2(b)), where the loss of efficiency accounts for the turn-on of the high voltage of the Pixel, SCT and some of the muon detectors at the beginning of an LHC fill and any inefficiencies due to deadtime or due to individual problems with a given subdetector that prevent the ATLAS data taking to proceed. The overall integrated luminosity nearly quadrupled the accumulated during 2011 at $\sqrt{s} = 7$ TeV, and in fact each day of data-taking during 2012 was equivalent (at least) to the amount of data collected during the whole 2010 ($L^{int}_{2010} = 35$ pb^{-1}) [80]. Its uncertainty as measured using van der Meer scans [81] was 0.6 fb^{-1}.

The analysis presented in this thesis is based on the total sample of proton-proton collisions at $\sqrt{s} = 8$ TeV collected by the ATLAS experiment during 2012. Only data collected during stable beam periods in which all sub-detectors were fully operational are used. A brief description of the ATLAS detector and its sub-systems with which events resulting from proton collisions are measured and recorded is included in the next section.

3.2 The ATLAS apparatus

The ambitious CERN's physics program mounted around the Large Hadron Collider demands detectors capable of coping with its extraordinary conditions of operation. ATLAS, an ingenious acronym for "A Toroidal LHC ApparatuS", is one of the multi-purpose detectors built to meet this challenging demand. It spans over 44 m length and 25 m height, is located at Interaction Point 1 (figure 3.1(b)) and is composed of many sub-systems as illustrated by a computer simulated cut-view in figure 3.4. The ATLAS layout is forward-

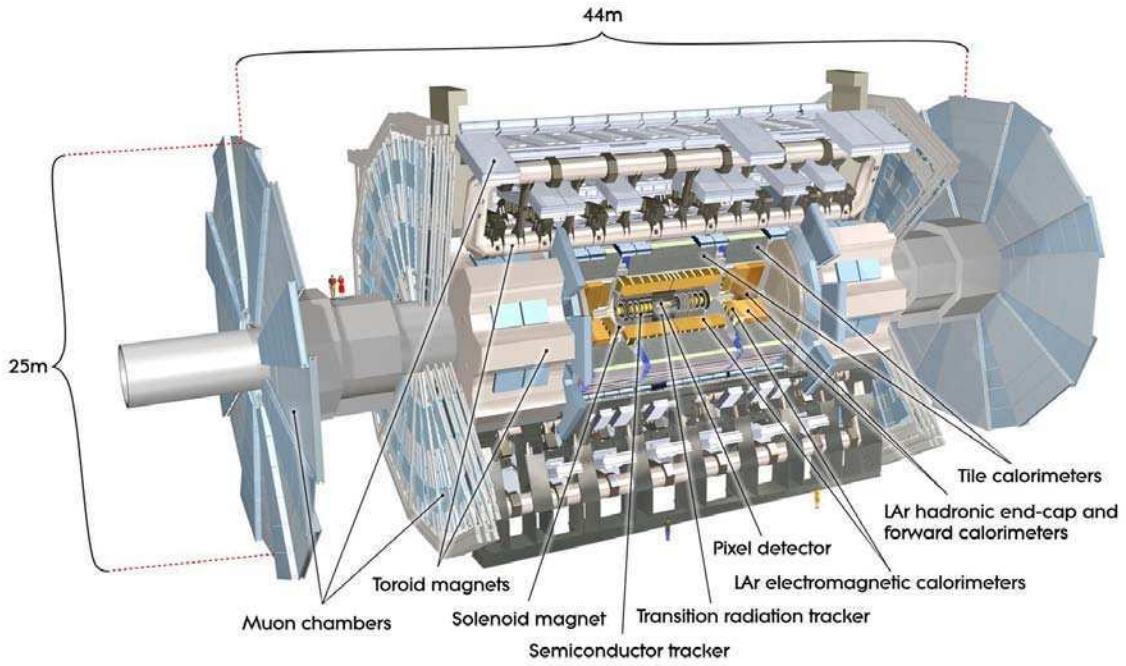

Figure 3.4: Computer generated image of the ATLAS experiment © 2012 CERN. The dimensions of the whole detector are 25m in height and 44m in length. The overall weight of the detector is approximately 7000 tonnes.

backward symmetric with respect to the interaction point, and consists of three primary detection systems layered radially upon each other: a central inner tracker (section 3.2.2) embedded in a 2 T solenoidal magnetic (section 3.2.6) field for measurement of position and momentum of charged particles, a calorimeter system for energy measurement of both neutral and electrically charged particles (section 3.2.3), and a muon spectrometer located within a large toroidal magnetic field to measure the position and momentum of muons (section 3.2.4). The organizational principle behind this architecture can be described by simple concepts. Vertex identification requires high resolution track reconstruction; to minimize large extrapolations the tracking system is inserted as close as possible to the interaction point. The energy of charged and neutral particles (with the exception of the muons) is measured in the second layer, the calorimeter system. These have large volume and are made of materials that guaranteed a large number of radiation lengths for

the incoming particles. Ideally particles are completely absorbed within the calorimeter(s) volume and their initial energy is thus measured as the sum of the deposited energy by the showered products of the original particle. This is the opposite case of the tracking system which is designed to not alter (too much) the original trajectory of the particles. Muons usually transverse the calorimeter without loosing a large amount of their original energy, and then their momentum can be measured with improved precision using the outermost muon tracking system (in general in combination with the inner tracker). A common factor to all sub-systems forming ATLAS is that they have to resolve physics signals and correctly identify different fundamental particles emerging from the collision spot at enormous rates, and be radiation resistant to survive the harsh environment [82]. The design performance for all main sub-systems is summarized in table 3.1.

Detector component	Design resolution	η coverage	
		for measurement	for trigger
Tracking	$\sigma_{p_T}/p_T = 0.05\% p_T \oplus 1\%$	$\|\eta\| < 2.5$	—
EM calorimetry	$\sigma_E/E = 10\%/\sqrt{E} \oplus 0.7\%$	$\|\eta\| < 3.2$	$\|\eta\| < 2.5$
Hadronic calorimetry	$\sigma_E/E = 50\%/\sqrt{E} \oplus 3\%$	$\|\eta\| < 3.2$	$\|\eta\| < 3.2$
Forward calorimeter	$\sigma_E/E = 100\%/\sqrt{E} \oplus 10\%$	$3.1 < \|\eta\| < 4.9$	$3.1 < \|\eta\| < 4.9$
Muon Spectrometer	$\sigma_{p_T}/p_T = 10\%$ at $p_T = 1$ TeV	$\|\eta\| < 2.7$	$\|\eta\| < 2.4$

Table 3.1: General performance goals of the ATLAS detector. Energy (E) and transverse momentum (p_T) are in [GeV]. Taken from ref. [11].

Another difficulty –consequence of the huge amount of collisions per second– is the computing power and network speeds needed to transfer the information collected at the detector, convert the measured electric pulses into physical entities (reconstructed jets, electrons, photons, etc.) and storage the information permanently in disks. The following sections are intended to provide a brief overview of the ATLAS detector and of its trigger and acquisition system (TDAQ). For further details the reader is kindly deferred to the original source of all this information in ref. [11].

3.2.1 Coordinate system

The coordinate system used in ATLAS is a right-handed Cartesian system centered at the nominal interaction point (the geometric center of the detector). The z-axis lies along the beam line, while the transverse x-y plane is defined with x pointing toward the center of the LHC ring and y points upwards. The direction of positive z (counter-clockwise in the LHC ring when viewed from above) is denoted as side-A of the detector and side-C is that with negative z. The azimuthal angle ϕ is measured around the beam axis, and the polar angle θ is obtained from the beam axis. The rapidity of a particle

$$y = \frac{1}{2} \ln \left(\frac{E + p_z}{E - p_Z} \right) \tag{3.3}$$

is defined in terms of energy (E) and momentum projection along the z-axis (p_z). The pseudorapidity

$$\eta = -\ln\tan(\theta/2), \tag{3.4}$$

is equal to the rapidity for massless particles, but in a general case is only a function of a geometrical variable which is really practical to immediately match the position of a particle with a given sub-detector in the same η range. The distance between two points (either calorimeter cells, of reconstructed objects) in the rapidity-azimuthal angle space is defined as

$$\Delta R(1,2) = \sqrt{(\eta_1 - \eta_2)^2 + (\phi_1 - \phi_2)^2} \tag{3.5}$$

The subscript T is used to indicate the magnitude in the transverse plane: $A_{\mathrm{T}} = \sqrt{A_x^2 + A_y^2}$.

3.2.2 Tracking system

The Inner Detector (ID), or central tracking system, is responsible of reconstructing the path of charged particles via high-resolution position measurements. Tracks are used for vertex reconstruction and identification. Combined with a solenoidal magnetic field of 2 T aligned with the beam line, tracks are used to measure the direction and momentum for particles having nominally $p_{\mathrm{T}} \gtrsim 500$ GeV within the acceptance pseudorapidity range $|\eta| < 2.5$ (table 3.1). The impact parameter can be measured with 10 μm resolution. The measurements are conducted by the combined use of three different technologies: the Pixel detector (Pixel), the SemiConductor Tracker (SCT) and the Transition Radiation Tracker (TRT). Diagrams of the inner detector components shown in figure 3.5 and described next.

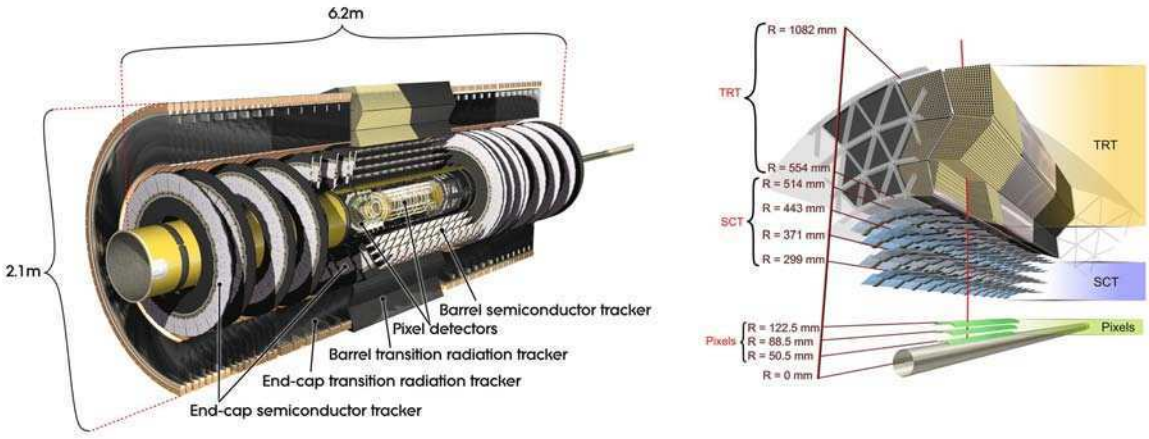

(a) (b)

Figure 3.5: Scheme of the ATLAS Inner Detector. ATLAS experiment © 2012 CERN.

Silicon pixel detector. The silicon pixel tracker is the innermost part of the tracking system formed by three concentric barrel layers built with semiconductor materials. Three additional disks at each end-cap are settled at distances of 495, 580 and 650 mm from

the IP along the beam direction. Pixels have 50 μm by 400 μm in size each, and are organized in modules, 1744 in total, each covering an active area of 16.4 mm $\times$ 60.8 mm and readout by 16 radiation-hard front-end chips. This results in a total of 80 million silicon pixels. In the barrel section, the pixel modules are oriented parallel to the beam line and have resolutions of 10 μm in r-ϕ and 115 μm in z. In the end caps, the modules are arranged radially providing a resolution of 10 μm in r-ϕ and 115 μm in r. The most central layer located at $\sim$5 cm from the pipe center (as shown in figure 3.5(b)) is subject to 160 kGy of ionizing radiation per year. This layer is referred as b-layer as is fundamental to the reconstruction of secondary vertices used in the identification of jets derived from heavy-flavour quarks (bottom and charm quarks).

Silicon strip tracker. The SemiConductor Tracker (SCT) implements long, narrow silicon strips making the coverage of a larger area more economical in terms of the number of channels. The physical principle is the same as for the Pixel detector; ionizing particles traversing the semiconductor produce electron-hole pairs whose currents are readout by the front-end chips, providing a binary response: a "hit" is registered only if the pulse height in a channel exceeds a preset threshold. There are 4088 SCT modules, each composed of two single-sided 64 mm silicon strip sensors attached to one another with a 40-mrad angular pitch to provide two-dimensional hit localization. The hit resolution in the transverse direction (r-ϕ) is 17 μm, while the longitudinal hit resolution (z in the barrel, r in the end caps) is 580 μm. The SCT operates in the same environmental conditions as the pixel detector at approximately -10°C to reduce the leakage current. The SCT is divided into four concentric barrel layers ($|\eta| < 1.1$) and nine end-cap disks ($1.1 < |\eta| < 2.5$) at each side. The disks are placed at a distance between 934 and 2720 mm from the interaction point along the beam direction. This system provides a total of approximately 6.3 million channels.

Transition radiation tracker. The Transition Radiation Tracker (TRT) surrounds the silicon detectors providing measurements of charged particles up to $|\eta| < 2.0$. It consists of proportional drift gaseous tubes (straws) 4 mm in diameter arranged longitudinally in up to 73 layers in the barrel ($|\eta| \lesssim 1.0$) and 160 radial straw planes in each end-cap ($1.0 \lesssim |\eta| \lesssim 2.0$). The barrel straws span 1440 mm in length and are further arranged into three cylindrical groups divided in 32 ϕ sector. There are 52544 axially oriented tubes in the barrel. End-cap TRTs have 122880 straws, each of 370 mm long. In total there are 350848 readout channels. Drift tubes are filled with a Xenon-CO_2-O_2 gas mixture that is ionized upon the passage of charged particles. Ions within the gas drift to the straw wall (acting as a cathode) and towards a tungsten (gold-coated) wire running inside the tube (that acts as an anode) due to a large electric potential of -1530 V applied between the wall and the wire. Under normal operating conditions, the maximum electron collection time is $\sim$48 ns. Particles with $p_{\mathrm{T}} > 500$ MeV within the η acceptance typically transverse more than 30 tubes. The large number of hits compensate for the relative low r-ϕ resolution of the TRT compared to the silicon trackers, 130 μm. In addition, the barrel drift tubes are embedded

in a matrix of polypropylene fibers that aid in electron identification via transition X-rays produced when charged particles cross inhomogeneous materials. In the end caps, the transition radiation is generated by foil interleaved between the straws. Electrons are differentiated from pions by the radiation characteristics. At the same energy, being lighter the electrons are faster than pions which results in more transition radiation and therefore a stronger signal. TR photons have ∼6 keV compared to the few hundred eV produced by a ionizing particle. The accompanying photons are measured by a radiation-hard higher threshold discriminator in the front-end electronics.

3.2.3 Calorimeter system

In the LHC (or any hadronic collider) the value of $\sqrt{s}$ is an indication of the initial energy at the hadronic level but the energy of the actual partonic process is honestly unknown beforehand. The energy of a given event is determined *ex post facto* by the calorimeter system. The ATLAS calorimeter system is a non-compensating sampling calorimeter composed by different sub-detectors spanning full ϕ-symmetry and pseudorapidity range up to $|\eta| < 4.9$ ($0.5° \lesssim \theta \lesssim 179.5°$). Broad η coverage is mandatory for an adequate event reconstruction, specially for accurate determination of the missing energy in physic processes where weakly interacting particles are expected (see section 3.3.5). The term "sampling" denotes the design approach that utilizes intercalated layers of absorber material and active medium. The readout signal is proportional to the energy deposited in each layer of the active media. "Non-compensation" means that part of the energy of nuclear collisions between the high-energy particles from the event and the detector material nuclei remains "invisible" to the active readout as is lost in the form of nuclear recoil or fission[1]. A consequence of non-compensation is that the energy response for hadronic particles (interacting strongly with the nuclei) is smaller than for particles of the same energy that interact predominantly by electromagnetic forces: $R(h)/R(e) < 1$.

In ATLAS, two calorimeter technologies are utilized. The innermost calorimeters use sampling technology with liquid argon (LAr) as the active detector medium. These are housed in three cryostats, one barrel and two end-caps, held at 80 K using liquid nitrogen. The barrel cryostat contains the Pb/LAr electromagnetic barrel calorimeter (EMB), whereas the two end-cap cryostats each contain the Pb/LAr electromagnetic end-cap calorimeter (EMEC), the Cu/LAr hadronic end-cap calorimeter (HEC), and the copper-tungsten/LAr forward calorimeter (FCal), as illustrated in figure 3.6. The outermost sampling detector, the hadronic calorimeter, uses steel as absorber and plastic scintillator-tiles as the active component, and is cooled with water. It is divided in three parts: the central barrel (Tile) and the two extended barrels (Extended Tile), see figure 3.6. This second construction approach provides high opacity to hadrons (9.7 nuclear interaction lengths at $\eta = 0$) at a

[1] A compensating calorimeter like the Dzero calorimeter at the Tevatron, had a fissionable material as absorber such that the energy lost due to nuclear interaction is *compensated* by the energy released by fissioned atom.

lower cost as compared to liquid argon calorimeters.

Charged particles are either produced in the partonic shower, from photon conversion ($\gamma \rightarrow e^- e^+$) or from hadronic showers initiated upon their interaction with the dense material of the absorber layers. Showers initiated by hadrons and mesons produce primarily pions and kaons. Neutral pions decay 'instantaneously' (within less than 30 nm) to two photons yielding an electromagnetic shower characterized by electron bremsstrahlung and e^+e^- pair production, whereas the remaining charged hadrons evolve in a hadronic shower molded by nuclear reactions. Construction details are described next.

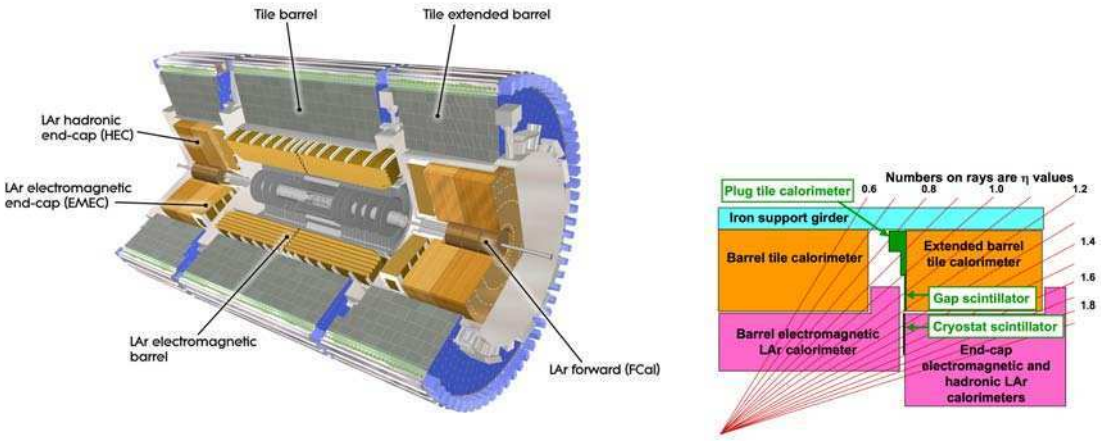

(a) (b)

Figure 3.6: (a) Computer simulated view of the ATLAS calorimeter system. (b) Schematic showing the angular coverage of different sub-detectors.

3.2.3.1 Liquid Argon calorimeters

Charged particles crossing a region filled with liquid argon ionize the liquid and the resulting charge is driven by a high bias voltage towards readout electrodes.

LAr electromagnetic calorimeters. The lead (laminated with stainless steel)/LAr electromagnetic calorimeter implements an accordion geometry that provides high azimuthal uniformity and minimize gaps in the ϕ direction, as shown in figure 3.7. The readout electrodes are located in the gaps between the absorbers and consist of three conductive copper layers separated by insulating polyimide sheets. The two outer cooper layers are at the high-voltage potential and the inner one is used for reading out the signal via capacitive coupling, as shown in figure 3.7(b).

The primary layer of the EMB is formed by a fine laterally and longitudinally segmentation ($\Delta\eta \times \Delta\phi = 0.003 \times 0.1$) that permits a discrimination between prompt photons and neutral pions (leading to two photons whose showers can be confused with photons), for showers within $|\eta| < 2.5$, as seen in figure 3.7(a). A second layer collects the largest fraction of the energy of the electromagnetic shower (around 80%), and is finely segmented in

square towers of $\Delta\phi \times \Delta\eta = 0.025 \times 0.025$ in the transverse plane ($\sim 4 \times 4$ cm^2 for $\eta = 0$) which permits a detailed reconstruction of the electromagnetic and hadronic showers in the calorimeter. The third layer has half the granularity of the previous layer and measures the tail of the electromagnetic shower. A presampler (not shown here) covers the region $|\eta| < < 1.8$ to improve the energy measurement for particles that start showering before entering the calorimeter. The whole volume of the EMB covers the region $|\eta| < 1.475$, and consists of two identical half-barrels each of 3.2 m length and inner (outer) diameter of 2.8 m (4 m) and formed by 1024 accordion-shaped absorbers. The EMB is housed inside the same cryostat that holds the inner detector's solenoid magnet. In the region $|\eta|$ < 1.8 a presampler calorimeter corrects for the energy lost in the cryostat material.This arrangement provides a total thickness ranging between 22 and 38 radiation lengths (X_0 in figure 3.7(a)) depending on η as shown in figure 5.1 from [11].

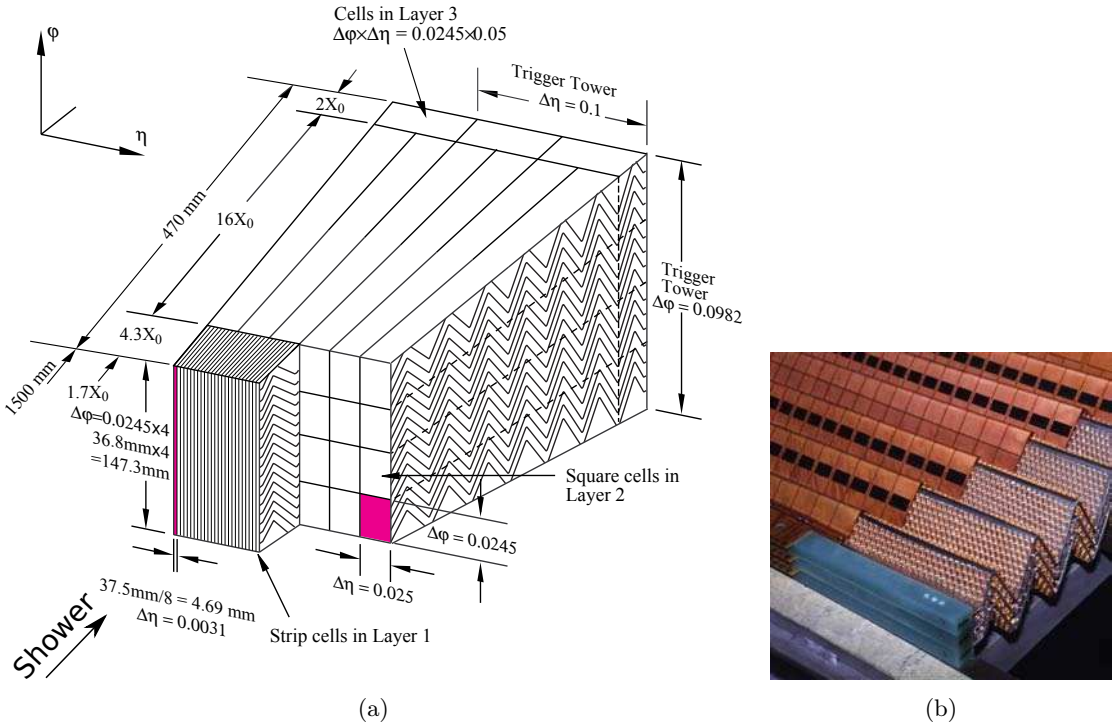

(a) (b)

Figure 3.7: (a) Sketch of a barrel module where the different layers are clearly visible with the ganging of electrodes in ϕ. The granularity in η and ϕ of the cells of each of the three layers and of the trigger towers is also shown, from [11]. (b) A detail of the accordion electrodes and of the spacers made of honeycomb polyimide sheets.

In the two electromagnetic end-cap components (EMEC) the accordion waves are parallel to the radial direction and run axially covering a region between $1.375 < |\eta| < 3.2$. The thickness of this subsystem is at least 27 radiation lengths but again vary as a function of the rapidity.

Geometrical groups of cells called *trigger towers* defined by the analogue sum of the read-outs from channels within $\Delta\phi \times \Delta\eta = 0.1 \times 0.1$ (see figure 3.7(a)) are practical as inputs for rapid trigger evaluation (but without resolution along the direction in which the shower

develops), as described later in section 3.2.7.

LAr hadronic calorimeters. The design of calorimeters at high $|\eta|$ is influenced by their proximity to the beam where the high energy detritus from the hard scatter can be harmful for the detectors. The hadronic end cap (HEC) is located at $1.5 < |\eta| < 3.2$ (figure 3.6) and implements a flat-plate design (at variance with the accordion of the EMB or the EMEC) which also uses liquid argon as an active medium but has cooper as the absorber material. The absorbers provide a depth of ∼12 nuclear interaction lengths (see figure 5.2 from [11] for more details). The liquid argon is recycled so the effects of radiation damage are attenuated over time.

The forward calorimeters (FCal) are located at each end-cap cryostat covering the high pseudorapidity region between $3.1 < |\eta| < 4.9$. Tubes of liquid argon running parallel to the beam have a central copper electrode and are embedded within an absorber matrix. The forward calorimeters at each side is split into three modules of 45 cm depth in z: an innermost electromagnetic layer is composed by copper/LAr modules (FCal1), and two outermost hadronic layers are made of cooper-tungsten/LAr modules. Cooper plates facilitate heat interchange, while the tungsten absorbers minimize the lateral spread of hadronic showers. The overall depth of this detector is approximately 10 nuclear interaction lengths.

3.2.3.2 Tile calorimeters

The tile hadronic calorimeter (Tile) consists of a central barrel section covering the region $|\eta| < 1.0$ and two extended barrels covering the region $0.8 < |\eta| < 1.7$ which use a polystyrene scintillator tile as the active material and steel plates as the absorber medium. The cell sizes in the hadronic calorimeters are larger than in the electromagnetic calorimeters; ranging from 0.1×0.1 to 0.2×0.2. The Tile is segmented in 64 wedges, each spanning $\Delta\phi \sim 0.1$ for full 2π azimuthal coverage and span longitudinally from 200 mm to 400 mm (that is 2 meters in the radial direction). A scheme of one of these wedges is shown figure 3.8. The total interaction length of the Tile calorimeter in the central barrel is $\lambda = 7.4$.

Ionizing particles produce ultraviolet scintillation light in the active material which is collected and transmitted to photomultiplier tubes (PMTs) via wavelength-shifting 1 mm-diameter fibres. The fibres coupled to each edge of the scintillating tiles are read out by two different PMTs to provide redundancy and sufficient information to partially equalise signals produced by particles entering the scintillating tiles at different impact positions. As it occurs with the EMB, the tile calorimeter is also capable to provide with analogue sums of subsets of its different electronic channels, to form trigger towers used at Level 1 trigger section 3.2.7.

The gap regions between the barrel and the extended ones are occupied with additional steel/scintillator modules which correct for energy losses in the inactive material in the

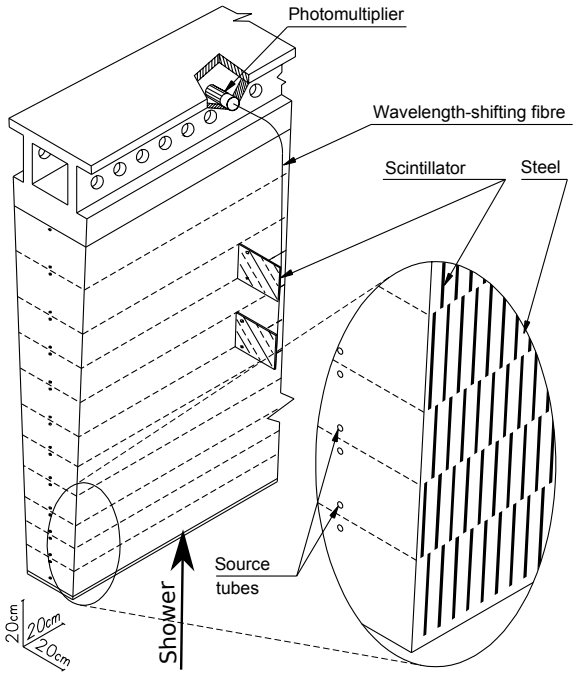

Figure 3.8: Schematic of the mechanical assembly of a single module of the Tile calorimeter showing the tile scintillators, the wavelength-shifting fibers and the photomultipliers for optical readout.

gap (see figure 3.6(b)).

3.2.4 Muon spectrometer

The muon spectrometer (MS) is responsible for the momentum-measurement of charged particles exiting the barrel and end-cap calorimeters in the pseudorapidity range $|\eta| < 2.7$ and select events of interest in the region $|\eta| < 2.4$. It also defines the characteristic shape, the enormous size and even the name of the ATLAS detector. The magnetic field for the muon spectrometer is produced by the barrel and end-cap air-core toroid magnets. The air-core magnet concept for the muon spectrometer minimises the amount of material traversed by the muons after exiting the calorimeters. The layout of the muon system and of the magnets is shown in figure 3.9. It consists of four primary subsystems. Two precision muon trackers: the monitored drift tubes (MDT) and cathode strip chambers (CSC), and two triggering subsystems: resistive plate chambers (RPC) and thin gap chambers (TGC), that are briefly described next.

Prescision subsystems. The MDT chambers are used in the central region $|\eta| < 2.7$, except in the innermost end-cap layer where their coverage is limited to $|\eta| < 2.0$. The basic element of the monitored drift tube chambers is a pressurised drift tube with a diameter of ∼30 mm, operating with Ar/CO2 gas (93/7 %) at 3 bar pressure (this mixture was selected for its aging properties and small likelihood of forming deposits within the tube). The electrons resulting from ionisation due to crossing muons are collected at the central

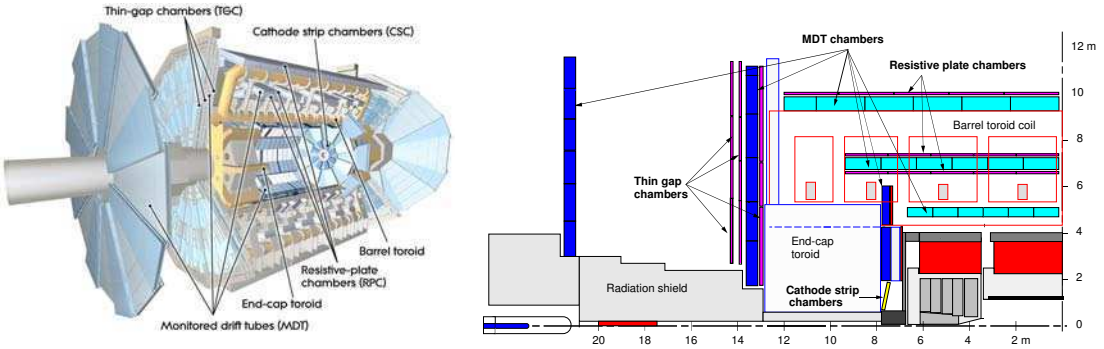

(a) (b)

Figure 3.9: (a) Overview of the ATLAS muon spectrometer components © 2012 CERN. (b) Cross-section of the muon system in a plane containing the beam axis (bending plane), from ref. [83].

(gold plated) tungsten-rhenium wire acting as an anode. The maximum drift time from the wall to the wire of about 700 ns, when operated at a nominal potential of 3080 V. The direction of the tubes in the barrel and end-caps is along ϕ. Signal transmission to the electronics and connection to the HV supply system are at opposite ends.

The limit for safe operation of the MDTs is at counting rates of about 150 Hz/cm^2, is exceeded in the region $|\eta| > 2$ for the first layer of the end-cap. In this η region of the first layer, the MDT's are replaced by CSCs which are safe up to counting rates of about 1000 Hz/cm^2, which is sufficient up to the forward boundary of the muon system at $|\eta| = 2.7$. The CSC's are multiwire proportional chambers with the wires oriented in the radial direction. To either side of the wire plane are cathode strip planes separated from the anode by 2.5 mm. Both cathodes are segmented, one with the strips perpendicular to the wires providing a spatial resolution of 60 μm in the bending plane r-z, and the other cathode has strips parallel to the wires providing resolution of 5 mm in the transverse coordinate. The readout is performed on the cathodes. Both subsystems are located between the eight coils of the superconducting barrel toroid magnet, while the end-cap chambers are in front and behind the two end-cap toroid magnets.

Trigger chambers. An essential design criterion of the muon system was the capability to trigger on muon tracks. The precision-tracking chambers have therefore been complemented by a system of fast trigger chambers capable of delivering track information within a few tens of nanoseconds after the passage of the particle, between 1.5 and 4 ns. In the barrel region ($|\eta| < 1.05$), Resistive Plate Chambers (RPC) were selected for this purpose, while in the end-cap ($1.05 < |\eta| < 2.4$) Thin Gap Chambers (TGC) were chosen. Both chamber types deliver signals within 15-25 ns, thus providing the ability to tag the beam-crossing and allowing the Level 1 trigger logic to recognise muon multiplicity and approximate energy range. The trigger chambers measure both coordinates of the track, one in the bending (η) plane and one in the non-bending (ϕ) plane. The RPC is a gaseous parallel electrode-plate (i.e. no wire) detector, formed by two resistive plates, kept parallel

at a distance of 2 mm by insulating spacers. The electric field between the plates of about 4.9 kV/mm allows avalanches to form along the ionising tracks towards the anode. The signal is read out via capacitive coupling to metallic strips, which are mounted on the outer faces of the resistive plates.

TGCs provide two functions in the end-cap muon spectrometer: the muon trigger capability and the determination of the second, azimuthal coordinate to complement the measurement of the MDTs in the bending (radial) direction. TGCs are multi-wire proportional chambers with the characteristic that the wire-to-cathode distance of 1.4 mm is smaller than the wire-to-wire distance of 1.8 mm. The high electric field around the TGC wires and the small wire-to-wire distance lead to very good time resolution of 4 ns. Only tracks at normal incidence passing midway between two wires have much longer drift times due to the vanishing drift field in this region. This high electric field necessitates a quenching gas mixture of 55% carbon dioxide and 45% n-pentane.

The trigger detectors, forming circular disks, are mounted in two concentric rings, an outer (end-cap) one covering the rapidity range $1.05 \leq |\eta| < 1.92$ and an inner (forward) one covering the rapidity range $1.92 < |\eta| \leq 2.4$.

3.2.5 Forward detectors

The forward detectors are responsible for the measurement of luminosity and beam conditions, and are often located at the limits or outside the main detector volume, but form part of the ATLAS subsystems. The Beam Condition Monitor (BCM), and Luminosity Cherenkov Integrating Detectors (LUCID) are two of such detectors.

BCM detectors are placed symmetrically around the interaction point at $z = \pm 184$ cm and 5.5 cm away from the beam-line, which corresponds to a $|\eta| = 4.2$. It provides ATLAS and the LHC operators measurements of the ATLAS collision rate as well as notification should a beam incident occur. For instance, one of the worst-case scenarios during LHC operation arises if several proton bunches hit the collimators in front of the detectors. While the accumulated radiation dose from such unlikely accidents corresponds to that acquired during a few days of normal operation, and as such provides no major contribution to the integrated dose, the enormous instantaneous rate might cause detector damage. BCM system detects such incidents and trigger an abort in time to prevent serious damage to the detector. The BCM system consists of two stations, each with four modules. Each module, includes two radiation-hard diamond sensors. The difference in time-of-flight between the two stations, distinguishes particles from normal collisions ($\Delta t = 0$, 25, 50 ns, etc.) from those arising from stray protons ($\Delta t = 12.5$, 37.5 ns, etc.).

LUCID detector is designed to detect inelastic pp scattering in the forward direction, in order to both measure the integrated luminosity and to provide on-line monitoring of the instantaneous luminosity and beam conditions. One LUCID module is located at 17 m

from the interaction point in z (and 10 cm apart from the beam-line) covering the range $|\eta|$ ∼5.8. They each consist of twenty aluminum tubes which surround the beam-pipe and point toward the interaction point. The tubes are filled with C_4F_{10} at a constant pressure of 1.2–1.4 bar, providing a Cherenkov threshold of 2.8 GeV for pions and 10 MeV for electrons. Cherenkov light created whenever particles go through them is reflected in the inner tube walls until it is measured by a PMT.

3.2.6 The solenoidal and toroidal magnet systems

The magnetic field responsible for bending the trajectory of charged particles is provided by the ATLAS magnet system. Thus, the momentum of particles can be measured via the radius of curvature of the tracks left within the detector systems. This magnetic system is 22 m in diameter and 26 m in length, with a stored energy of 1.6 GJ. ATLAS features a unique hybrid system of four large superconducting magnets, as shown in figure 3.10.

The central solenoid has an inner radius of 1.23 m, a total length of 5.8 m and sits just outside and surrounding the inner detector cavity 3.2.2. It shares the cryostat with the LAr EMB calorimeter, but in a separate vessel as the superconducting solenoid is kept at 4.5 K. A 2 T axial field is generated with 7.73 kA flowing through a single-layer aluminum coil wound by a niobium-titanium (NbTi) conductor. The flux is returned by the steel of the ATLAS hadronic calorimeter and its girder structure.

Three large superconducting toroids (one barrel and two end-caps), arranged with an eight-fold azimuthal symmetry around the calorimeters, which provide bending power for the muon spectrometer 3.2.4. The barrel toroids extend 25.3 m along the z axis whereas the end-cap toroids have 5 m lenght. The toroidal magnet implements coils consisting of a conductor made of a mixture of aluminum, copper and an alloy of NbTi and, that at 20.5 kA provides 0.2–2.5 T in the barrel and 0.2–3.5 T in the endcap.

3.2.7 Trigger and data acquisition

The data reconstructed on-line from the calorimeter and muon system is utilized by the trigger and data acquisition system (TDAQ) [83] to select potentially interesting events. There are several reasons to select/discard events. First, the vast majority of processes of interest have smaller relative cross sections (see for example figure 6.1) than the inclusive collisions and therefore there is no practical reason to save the information of events which do not provide interesting physics. Second, the bunch crossing rate at the LHC during 2012 was 20 MHz ($1/\tau_{bunch}$). So, even if all the events would be of interest, the information coming from the ∼100 million readout channels from all subsystems constitute ∼1.5 MB of data per event, meaning an impossible quantity of computer data storage needed for such amount of information. At any rate, in the eventuality that all events could be saved, every analyst performing a study would have to run his/her analysis over this huge dataset,

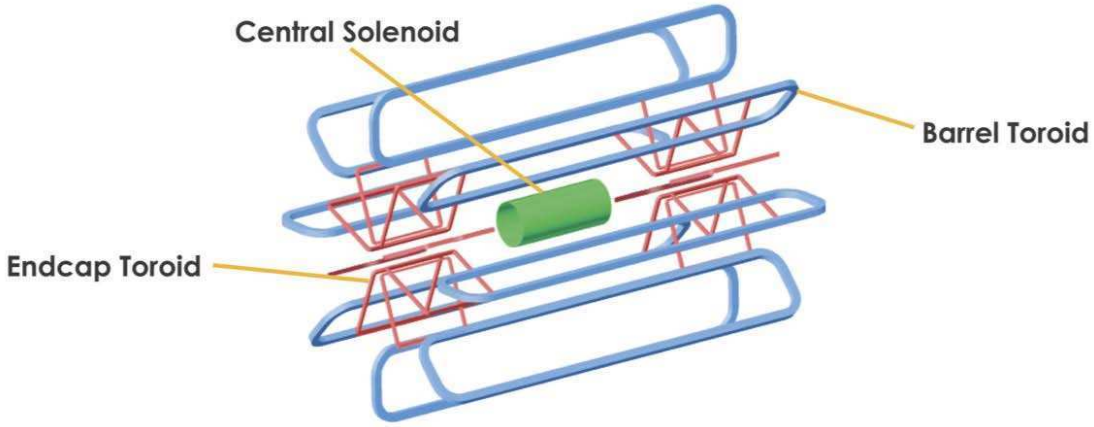

Figure 3.10: Geometry of magnet windings and tile calorimeter steel. The eight barrel toroid coils, with the end-cap coils interleaved are visible. The solenoid winding lies inside the calorimeter volume. The tile calorimeter is modelled by four layers with different magnetic properties, plus an outside return yoke.

which may become and endless task. Clearly, an educated on-line selection is mandatory. It has to be 'educated' since it has to maximize the rejection of unwanted event while minimizing the rejection of interesting events.

In ATLAS the trigger system is comprised of three levels of increasing refinement: a hardware-based Level-1 (L1), and two software-based instances called Level-2 (L2) and Event Filter (EF). The last two form together the so-called High-Level Trigger (HLT). The decision chain is sequential meaning that only events accepted at L1 are feed to L2[1]. There are many trigger-chains being analyzed simultaneously for each event. Each trigger chain looks for a particular event feature or topology, for example there is a trigger chain that looks for events having at least 4 jets having a p_{T} of at least of 50 GeV, and other trigger-chain that look for events containing at least one energetic electron. An event is kept is there is at least one accepted trigger chain (i.e. one topology of interest) for that event.

Level-1 trigger is primarily designed to decide within a 2.5 μm time-window whether a given event passes or not to L2. The actual event rate at the outflow of L1 is 75 kHz. The selection is based on information from the calorimeter and muon sub-systems, L1Calo and L1Muon. The L1Calo receives input from all calorimeters (EMB, HEC, EMEC, Tile, FCal) and looks for high-transverse energy (E_{T}) objects, such as electrons, photons, jets, and τ-leptons decaying into hadrons, or jets, as well as events with large missing and total transverse energy. Isolation can be required for these objects such that identified electrons, photons or taus are more likely to be prompt instead of secondary to parton showers. The L1 muon trigger (L1Muon) is based on signals originated in the muon trigger chambers (RPCs at the central region and TGCs at the forward region). L1Muon searches for

[1]The is a tiny fraction of *pass-through* events, that are stored regardless of the trigger decision. These events are used as an unbiased sample for trigger reference, and for minimum bias studies.

patterns of hits consistent with low-p_{T} muons triggered using at least 3 hits in the 4 inner layers, or high-p_{T} muons which require and additional hit in the outer station. At this level low-granularity calorimeter trigger towers (see section 3.2.3) are used to reconsruct L1 objects.

The overall decision of acceptance/rejection the event is made by the Central Trigger Processor (CTP), which combines the information for different object types and thresholds. The CTP has a trigger menu with up to 256 distinct signatures, most of which combine information from L1Calo and/or L1Muon. If a positive decision is taken for any of the 256 possible signatures, the detector buffers are readout into the data acquisition (DAQ) system.

High level trigger Upon the event is accepted by the L1 trigger, the information about the geometric location of L1 trigger objects (retained in the muon and calorimeter trigger processors) is sent to the next level as Regions-of-Interest (RoI). These RoIs consist of sub-regions of the detector where the L1 trigger has identified a possible trigger objects, and correspond to 1–2 % of the full channels of an event. In spite of the small fraction of data, these RoIs permit the L2 to request the DAQ the full granularity detail for these sub-regions. The RoI information is used to construct objects such as tracks and showers to be used in L2 decisions. If the L2 decision is negative the DAQ buffer is flushed, otherwise the final decision is taken by the EF. The EF is the more refined and latest level. Unlike the L2 trigger, the EF reconstructs the full event (not only the regions marked by L1 as interesting, i.e. the RoI). This stage applies standard ATLAS algorithms for tracking and jet reconstruction as those used off-line (where speed processing is not as limiting). The EF selects the events and classiffies them to streams according to the satisfied signatures. Events are accepted by the EF at a limiting rate of 600 Hz, and if so the full information of the event is transferred to sub-farm outputs for definitive storage[1]

A comment regarding the processing speed of the trigger decision chain. Given the limited bandwidth for processing at each stage L1/L2/EF, events can be discarded before even being analyzed if the input rate is larger than the computing capability of any of such stages. For example if L1 would accept events at 150 kHz, then 1/2 of these events have to be dropped out in order to cope with the 75 kHz input limit of L2. In this case it is said that L2 is *pre-scaled* (PS) by a factor of 2. Pre-scales reduce trigger output rate for given stage. In general, if a given trigger element of a given chain has a $PS = n$, means that $n - 1$ out of n events are randomly discarded whatever the decision of the previous trigger element was (i.e. 1 out of n is considered for trigger evaluation). Pre-scales are set independently for L1/L2/EF and for each of the 256 trigger signatures, and can be dynamically modified on-line in response to changes in the instantaneous luminosity.

In the same line, a trigger is said to be *unprescaled* if $PS = 1$. In practice, an unprescaled

[1] There are however a lot of events by-passing this dataflow. 200 MHz out of the 600 MHz that are stored, where not fully processed by the HLT but went directly to disk, for later reconstruction when computing resources be available. These events form the *delayed stream*.

trigger means that the trigger is evaluated for all events, and the events are kept or not based only on the trigger decision.

One last comment regarding the convention used to name the trigger element is `L_ipX_Y`, where `L` stands for the trigger level, `i` the multiplicity, `p` the particle or signature, `X` the minimum p_{T} required, and `Y` corresponds to information related to the identification of the object of interest. In case of combined signatures, the respective blocks `L_ipX_Y` are concatenated. This is the rule to understand the naming of the trigger names in table 5.1, for example.

3.3 Object recontruction and identification in ATLAS

The enormous technical complexity of the accelerator and of the detector –of which the previous section are only a very partial and rough description– should not shadow that were built to study (and discover) fundamental particles and their interactions. What actually happens at the femtoscopic level ('microscopic' is such a huge scale in this context) can only be inferred by studying the kinematics and nature of the particles that leave the collision. These particles, however, are not always directly observed or measured. For instance, a reconstructed object that we may identify with an 'electron' (or more properly a 'reconstructed electron candidate') is actually a measurement of a shower of particles that hit the detector and has some likelihood of being initiated by an electron decay. With this limitation in mind what follows in this section is the rough description of how experimental observables are reconstructed from the information provided by the ATLAS sub-systems, into objects that can be identified with physical particles. Further details can be found in the original sources [11, 83].

3.3.1 Track and vertex reconstruction

Tracks are reconstructed using information of the inner detector 3.2.2 for charged particles having $|\eta| < 2.5$ (the tracking system acceptance) and $p_{\mathrm{T}} \gtrsim 400$ MeV below which the tracking algorithms becomes inefficient. The ID tracking algorithms covers two stages, the main track reconstruction, and the second stage of pattern recognition for the finding of primary vertices, kink objects due to bremsstrahlung and their associated tracks [84, 85].

The first step in track reconstruction is the creation of three-dimensional representations of 'hits' (space-points) in the silicon and the transition radiation tracker sub-systems. Pixel measurements provide a natural high resolution two-dimensional local measurement that together with the corresponding location of the Pixel module in the ID define the spatial position of the hit. To construct the three-dimensional hit from measurements on an SCT (remember the module is a long strip not a point-like detector) it is used the stereo angle information from the two silicon modules glued together at a slanted angle. The timing

information from the TRT is translated into calibrated drift circles.

In a second step, track seeds are formed from a combination of two or three space-points in the three pixel layers (one point per layer), where the combination must be consistent with the interaction point. These seeds are then extended outside throughout the SCT to form track candidates; a strategy called inside-out. This results in a very high number of track candidates, many of which share hits, are incomplete or describe fake tracks (i.e. where hits are mixed into a track by combinatorial effects but do not originate from one single particle trajectory). Track candidates are refitted and ranked according to their likelihood to describe the real trajectories of particles, the fit quality (χ^2/DoF, which is in most cases not enough to decide whether a track is a good or fake track) and scores for different sub-detectors (preferring the precision measurements). Low ranked track candidates are neglected for further processing and the selected track candidates are extended into the TRT to associate drift-circle information in a road around the extrapolation. Extended tracks are refitted with the full information of all three sub-systems. Space-points that are close to the extrapolation from the SCT but are excluded in this last fit that includes TRT, are labeled as 'outliers'. Outliers provide a quality criteria to select electrons and muons, see tables 3.2 and 3.3.

A complementary strategy –called 'back-tracking' or 'outside-in'– searches for track segments in the TRT that were not included in the inside-out track-finding. Such segments are extended into the SCT and pixel detectors to improve the tracking efficiency for tracks coming from secondary vertices associated to decays of long-lived particles (e.g. K_s decays)

In the post-processing, primary vertices are reconstructed using an *iterative vertex finder* algoritm [86]. Tracks are selected with a small transverse impact parameter $|d_0| < 4$ mm, well-measured transverse and longitudinal impact parameters $\sigma(d_0) < 5$ mm, and $\sigma(z_0) < 10$ mm ($|d_0|$ and $|z_0|$ are the projections in $r-\phi$ and z of the point of closest approach of the track to the center of the luminous region of the beams), among with a minimum amount of hits in the SCT (4) and all the silicon detectors combined (6) [87]. The iterative vertex finder is applied to selected tracks. The first vertex seed is found by looking for the global maximum in the distribution of z_0. The iterative fit process takes as input the seed position and the tracks around it, and progressively down-weights the contribution of outlying tracks the overall vertex. Tracks incompatible with the vertex by more than 7 σ are used to seed a new vertex. The process continues until no unassociated tracks remain or no additional vertices can be found. Each vertex contains a minimum of two tracks.

Among all the reconstructed primary vertices (PV), the one with the highest $\sum(p_{\mathrm{T}}^{tracks})^2$ is chosen as the event vertex. The remaining, softer, PVs are considered pile-up collisions. The number of primary vertices is a measure of the additional activity of the event which is complementary to the average number of pp colissions μ described in section 3.1.2. See, for example, appendix A for a picture of vertices reconstructed in real events.

3.3.2 Electron reconstruction

Electrons and photons are reconstructed and identified following a procedure common to both [88, 89]. Since photons are not of interest to this thesis the description is focused on electrons. Electron reconstruction begins with the creation of a preliminary set of seed clusters formed by summing calorimeter cell towers (along the radial direction) within a fixed-size rectangular window of 3×5 cells in the $\eta \times \phi$ space. Each cell has size 0.025×0.025, see figure 3.7(a). Seed clusters with energies above 2.5 GeV are scanned by sliding the summing window over the detector acceptance [90]. In the region of the tracker detectors ($|\eta| < 2.5$), reconstructed tracks are matched to seed clusters by extrapolating them from their last measurement point to the second layer of the calorimeter[1]. If more than one track matches the seed cluster the one having the minimum ΔR distance (equation 3.5) is considered as the best match. After track matching the electromagnetic cluster is then recomputed using a 3×7 (5×5) sliding window in η/ϕ middle layer cell units in the barrel (end caps). The window size restricts electron identification to within a pseudo-rapidity range $|\eta| < 2.47$ ($= 2.5$ of ID acceptance, minus 0.025 of the cell size). Finally, the electron four-momentum is computed using in addition the track information from the best track matched to the original seed cluster. The energy is computed as a weighted average between the cluster energy and the track momentum. The ϕ and η directions are taken from the corresponding track parameters at the vertex unless the track contains no silicon hits, in which case η is provided by the cluster η-pointing. In cases where the track has only TRT hits, the ϕ position is taken from the track and the η is provided by cluster η-pointing.

There is an inherent ambiguity in this reconstruction between a prompt electron and a converted photon, since both objects are characterized by the existence of tracks pointing to an electromagnetic cluster. The reconstruction is not very selective such that ensures a high electron reconstruction efficiency. The particle identification criteria described next solves the ambiguity between these two cases.

The electron identification within $|\eta| < 2.47$ relies on a cut-based selection using calorimeter, tracking and combined variables aimed to reject contributions of the main backgrounds to prompt electrons: electrons from heavy flavors and from Dalitz decays (a meson decaying into two electrons and a photon) or photon conversions ($\gamma + X \rightarrow e^- + e^+ + X$, where X is the detector material) originating from neutral pion decays and jets. Three sets of cuts with increasing background rejection power are defined: loose, medium and tight [88] with an expected jet rejection of about 500, 5000 and 50000, respectively. The cuts are

[1] In contrast to the central electrons, reconstruction in the forward region ($2.5 < |\eta| < 4.9$) uses only the information from the calorimeters as the tracking system is limited to $|\eta| < 2.5$, which turns impossible to distinguish between electrons and photons from electric charge considerations. The selection criteria for high η electrons are based on cluster moments and shower shapes which provide efficient identification due to the good transverse and longitudinal segmentation of the calorimeters. In this case, clusters are not cell towers but three dimensional groupings of cells, called 'topological clusters', as those used for jets (section 3.3.4.1).

inclusive meaning e.g. that 'medium' cuts are applied on top of 'loose' cuts (see table 1 in ref. [89]). Loose selection involves shower shape variables like the cuts on how much energy is spread longitudinally (a longer shower tail characteristic to hadronic showers) and laterally (the width of the shower). The medium selection has stringent criteria on the shower shape and track quality (at least one/seven hits in the pixel/SCT detector and $|d_0| < 5$ mm for all tracks) and a good track-to-cluster matching: $\Delta\eta < 0.01$. The tight selection imposes even more stringent cuts to the tracks, a minimum number of hits in the TRT, an additional requirements on the energy/momentum ratio of the electron track and has a better rejection of converted photon candidates as requires at least one hit in the b-layer with which secondary vertices are better identified. The energy calibration and efficiency of electron identification has been studied by combining measurements of $Z \to e^+e^-$, $W \to e\nu_e$ and $J/\psi \to e^+e^-$ processes [89]. Strictly the efficiency is p_{T}–η and sample dependent, but in general a medium (tight) selection is about ∼94% (∼77%) efficient for electrons originating in W/Z boson decays.

Cut	Value
	Baseline Electrons
Acceptance	$E_{\mathrm{T}} > 10$ GeV, $\lvert\eta^{clust}\rvert < 2.47$
Quality	Medium
Overlap	$\Delta R(e, \mathrm{jet}) < 0.2$ or $0.4 < \Delta R(e, \mathrm{jet})$
	Signal Electrons (includes baseline selection)
Acceptance	$E_{\mathrm{T}} > 25$ GeV, $\lvert\eta^{clust}\rvert < 2.47$
Quality	Tight
Track Isolation	TrackPtCone30/$E_T < 0.16$
Calo Isolation	`CaloIso`/$E_T < 0.18$, where
	`CaloIso` = `CaloEtCone30` - 0.02015 × `vx_nTracks` (Data)
	`CaloIso` = `CaloEtCone30` - 0.01794 × `vx_nTracks` (MC)
Longitudinal IP	$\lvert z_0 \sin\theta\rvert < 0.4$ mm
Transverse IP	$\lvert d_0/\sigma(d_0)\rvert < 5.0$

Table 3.2: Summary of the electron definition cuts. For signal electrons a tight isolation is required. Here, `vx_nTracks` stands for the number of tracks defining the primary vertex.

For the analysis two definitions of electrons are used, a 'baseline' selection used to veto events, and a tighter selection referred as 'signal' electrons. The several additional cuts are applied to the electron candidates to define these two classes, which are summarized in table 3.2. A good quality of the electron is also required by removing electrons if they fall into the so-called LAr hole region (i.e. dead areas in the LAr calorimeter that affect the object reconstruction). In addition, the $E_{\mathrm{T}} = E^{clust}/\cosh(\eta)$ of electrons should exceed 10 GeV (for the baseline selection), where η is taken to be η^{track} (defined using the tracks pointing to the reconstructed electron); for Monte Carlo events, a smearing procedure needs to be applied to the electron energy to mimic the resolution in data. Furthermore, $|\eta^{calo}|$ should be less than 2.47.

Signal electrons are required to satisfy the tighter criteria definition and a minimum p_{T} of 25 GeV. These electrons must be isolated to further discriminate prompt electrons from secondary electrons coming from jets. The idea is that for isolated electrons the distribution of radiation in the cone surrounding it, is expected to peak at values close to zero, with a width that is sensitive to electronic noise, shower leakage, underlying event and pile-up contributions. Conversely, for electrons coming from within a jet, the annulus surrounding an electron is expected to be contaminated with radiation from the jet, and therefore the energy in it should be larger than zero. In consistence with this, a *track isolation* is quantified by the requirement that the scalar sum of the tracks p_{T} within a cone of radius of 0.3 (excluding those matching the electron towers) divided by the electron transverse energy E_{T}, must be less than a certain cut. A *calorimetric isolation* requires that the transverse energies of all EM and hadronic calorimeter cells around 0.3 the electron barycentre (except for those towers forming the electron) be less than a certain fraction of the electron E_{T}.

3.3.3 Muon reconstruction

Muon with momenta ranging from approximately 3 GeV to 3 TeV are reconstructed through the combination of accurate measurements in the muon spectrometer and in the inner detector which improves the muon identification efficiency and momentum resolution. The inner detector provides the best measurement at low to intermediate momenta, whereas the muon spectrometer takes over above 30 GeV. The muon spectrometer (3.2.4) also efficiently triggers on muons over a wide range of energies and within $|\eta| < 2.4$. This is the η range used to define muon control regions in section 6.2. ATLAS employs several track-reconstruction strategies for identifying muons (leading to different muon 'types'), according to the available information from the ID, the MS, and the calorimeter sub-detector systems [83, 91]

Stand-alone muons proceed from a direct track reconstruction based solely on the muon spectrometer data over the range $|\eta| < 2.7$, defined by the spectrometer acceptance. The toroidal field guarantees momentum resolution even at the highest values of η. These tracks are extrapolated to the beam line, taking into consideration both multiple scattering and energy loss in the calorimeter. Since these muon objects don't require a match to the inner tracker, muons produced in the calorimeter, e.g. from pion and kaon decays, are likely to be found by this approach and serve as a background of 'fake' muons for most physics analyses. One disadvantage of this approach is that very low momentum muons (around a few GeV) may be difficult to reconstruct because they do not penetrate to the outermost modules of the muon-spectrometer.

Combined muons are a combination of a muon-spectrometer track with an inner detector track over a smaller range $|\eta| < 2.5$, defined by the ID detector acceptance. Combination algorithms pair tracks from the two sub-systems and calculate a match chi-square, χ^2_{match}

that weights a distance between parameters of the tracks at the point of closest approach to the beam line. ATLAS uses two different algorithms, STACO (for STAtistical COmbinatorial) and Muid, to combined tracks that basically evaluate differently χ^2_{match}. STACO does a statistical combination of the inner and outer track vectors to obtain a combined track, where the track from each sub-system is weighted by the covariance of its reconstruction.

Segmented tagged muons are found by extrapolating inner detector tracks with sufficient momentum out to the first station of the muon spectrometer and search for nearby hits. A tag chi-square is define using the difference between any nearby segment and its prediction from the extrapolated track.

Calorimeter-tagged muons are reconstructed if a track in the ID can be associated to an energy deposit in the calorimeter as expected from a minimum ionizing particle. This type has the lowest purity of all the muon types but it recovers acceptance in the uninstrumented region of the muon spectrometer.

Similarly to the quality cuts applied to electrons, several additional cuts are applied once the STACO muon candidates are identified, as summarized in table 3.3. These cuts refine the number of track hits and fix the transverse and longitudinal impact parameters in order to minimize the missidentification of background muons. In particular, also tend to remove fake muons coming from jets at very high transverse momentum for which a part of the energy is not deposited in the calorimeter, but leaks out to the muon system and can be mistakenly reconstructed as muons. Prior to these cuts the transverse momenta of muons in Monte Carlo simulation are smeared to match the observed p_{T} resolution in data. Furthermore, signal muons must be isolated to minimize background muons from leptonic decays of b quarks.

3.3.4 Jets

Jets are the experimental realization of the partonic showering and subsequent hadronization of particles carrying color charge. Chapter 4 is devoted to describe the performance of algorithms used to reconstruct jets and how can be used to improve physics analyses. Here, a brief description is given of what are the inputs used to build the experimental jets an how jets are calibrated in ATLAS. Details of the recombination algorithms are left to that chapter.

3.3.4.1 Topological clusters

As is described in chapter 4, a jet algorithm receives a set of inputs and iteratively combines them to returns a set of four-momenta characterizing the final jets. A possible choice for inputs to the jet reconstruction algorithm is the set of high-granularity calorimeter cells, or of towers of cells running longitudinally along the calorimeter (like the sliding window used

Cut	Value
	Baseline Muons
Algorithm	STACO, combined or segment-tagged muon
Acceptance	$p_{\mathrm{T}} > 10$ GeV, $\lvert\eta\rvert < 2.5$
Quality	Loose
ID track quality	$\geqslant 1$ b-layer hit when it is expected
	$\geqslant 1$ pixel hit or crossed dead pixel sensor
	$\geqslant 5$ SCT hits or crossed dead SCT sensor
	Pixel holes + SCT holes < 3
	If $0.1 < \lvert\eta\rvert < 1.9$: $n_{\mathrm{TRT}} \geqslant 6$ or $n_{\mathrm{TRT}}^{\mathrm{outliers}} < 0.9\, n_{\mathrm{TRT}}$
	If $\lvert\eta\rvert \geqslant 1.9$ and $n_{\mathrm{TRT}} \geqslant 6$: $n_{\mathrm{TRT}}^{\mathrm{outliers}} < 0.9\, n_{\mathrm{TRT}}$
Overlap	$\Delta R(\mu, \mathrm{jet}) > 0.4$
	Signal Muons (includes baseline selection)
Acceptance	$p_{\mathrm{T}} > 25$ GeV, $\lvert\eta\rvert < 2.4$
Quality	Medium
Track Isolation	TrackPtCone30$/p_{\mathrm{T}} < 0.12$
Calo Isolation	`CaloIso`$/p_{\mathrm{T}} < 0.12$, where
	`CaloIso` = `CaloEtCone30` - 0.0648 × `vx_nTracks` - 0.00098 × (`vx_nTracks`)^2 (Data)
	`CaloIso` = `CaloEtCone30` - 0.0692 × `vx_nTracks` - 0.00076 × (`vx_nTracks`)^2 (MC)
Longitudinal IP	$\lvert z_0 \sin\theta\rvert < 0.4$ mm
Transverse IP	$\lvert d_0/\sigma(d_0)\rvert < 5.0$

Table 3.3: Summary of the muon definition cuts used in the analysis of this thesis. For signal muons a tight isolation is required. Here, `vx_nTracks` stands for the number of tracks defining the primary vertex. A 'hole' in the inner detector is a space-point were a measurement is expected based on the track reconstruction but no hit was registered (a track passing through an inactive module is not counted as a hole).

for electron reconstruction, 3.3.2). These however don't reproduce the actual shape of the particle cascade and are more susceptible to stochastic fluctuations of the detector state. Noise in the calorimeter comes from two principal sources. The first is from the readout electronics. The second is due to pile-up arising from extra interactions that can either be overlaid in the same beam crossing with the primary interaction (in-time) or occur during bunch crossings that are close in time to that of the primary interaction (out-of-time) as the response time of the calorimeter is longer than the 50 ns interval between crossings.

Jets used in this thesis use as inputs three-dimensional calorimeter topological clusters [90]. Topological clusters (topoclusters) are the primary input for jet reconstruction and also an important component of the missing transverse energy (section 3.3.5). The basic idea of topological clustering is to group into clusters neighboring cells that have significant energies compared to the expected noise. Topological clusters are built using a 4-2-0 clustering scheme optimized to find efficiently low energy clusters without being overwhelmed by noise [90]. The topocluster formation algorithm starts from a seed cell, whose signal-to-noise (S/N) ratio is above a threshold of $S/N = 4$. The noise is estimated as the absolute value of the energy deposited in the calorimeter cell divided by the RMS of the energy distribution measured in events triggered at random events. Cells neighboring (laterally and longitudinally) the seed which have a signal-to-noise ratio of at least $S/N = 2$ are then iteratively added. Finally, all nearest neighbor cells are added without any threshold to the cluster (this this was shown to increase single pion energy resolution). The topocluster algorithm efficiently suppresses the calorimeter noise. 'Hot' or particularly noisy cells are excluded entirely from topocluster formation, resulting in a minor loss of cells ($\sim$0.1%) of all calorimeter cells. Topoclusters having negative energy are rejected entirely from the jet reconstruction[1].

Incoming particles usually deposit their energy in many calorimeter cells, both in the lateral and longitudinal directions. Consequently topoclusters are of variable size and have a variable number of cells depending mostly on the energy of the incoming particle: more energetic particles produce larger showers and thus larger clusters. A topocluster ends up formed in average by approximately 250 calorimeter cells.

3.3.4.2 Jet energy calibration

Atlas has several jet calibration schemes [83], with different levels of complexity and different sensitivity to systematic effects. Jets reconstructed in the calorimeter system are formed from calorimeter energy depositions calibrated at the *electromagnetic energy scale* (EM) or from energy depositions that are corrected for the lower detector response to hadrons due to non-compensating calorimetry (see section 3.2.3) [92].

[1] The signal pulse shape from the liquid-argon cells is bipolar with a long undershoot. Thresholds for each calorimeter cell are based on the cell's particular noise characteristics to suppress both electronic noise and noise from out-of-time and multiple interactions. This combination can lead to an artifactual measurements of negative energy.

For the first family, the cell energy scale was established using test-beam measurements for electrons in the barrel and the endcap calorimeters. The absolute calorimeter response to energy deposited via electromagnetic processes was validated in the hadronic calorimeters using muons, both from test-beams and produced in situ by cosmic rays. This calibration is accurate only for electromagnetic showers. A posterior calibration is needed though to correct for several detector effects that affect the jet energy measurement. These effects are the calorimeter non-compensation that gives a lower response to hadrons than to electrons or photons, energy losses in un-instrumented parts of the detector occupied by support structure, cables, cryogenic vessels or other services (called *dead material*), leakage of particles reaching outside the calorimeters and thus not fully reconstructed, energy deposits of particles inside the truth jet entering the detector but that are not included in the reconstructed jet (referred as *out of calorimeter jet cone*), or for noise thresholds and particle reconstruction efficiency.

A more sophisticated scheme exploits the topology of the calorimeter energy depositions to correct for calorimeter non-compensation and the other jet reconstruction effects. The local cluster calibration (LCW) [93] improves the jet energy resolution by weighting differently energy deposits proceeding from electromagnetic and hadronic showers. The LCW calibration method classifies topoclusters as being mostly electromagnetic or hadronic on their origin based on cluster shape variables [90, 93]:

1. the energy density in cells in topoclusters is a good indicator since the radiation length X_0 is much smaller than the hadronic interaction length λ,
2. the cluster energy fraction deposited in different calorimeter layers,
3. the isolation variable characterising the energy around the cluster,
4. the depth of the cluster barycentre in the calorimeter.

These variables are used to calculate a classification weight that denotes the probability p for a cluster to stem from a hadronic interaction. Most topoclusters classified as electromagnetic have their center in the electromagnetic calorimeter, as expected; topoclusters classified as mostly hadronic are very often in the electromagnetic calorimeter too, since low p_{T} jets do not penetrate far into the hadronic calorimeter. However, a structure is observed, related to the position of the different longitudinal layers in the hadronic calorimeter that indicates and hadronic origin. Topoclusters receive calorimeter cell correction weights derived from detailed Monte Carlo simulations of charged pions. The applied weight is $\mathcal{W}_{HAD} \cdot p + \mathcal{W}_{EM} \cdot (1-p)$, where $\mathcal{W}_{EM} = 1$ and $\mathcal{W}_{HAD}$ is the weight for a purely hadronic beam derived from the Monte Carlo simulation.

Jets are then reconstructed directly from hadronically calibrated topoclusters. Final jet energy scale corrections also need to be applied to the LCW calibrated jets, but they are numerically smaller than the ones for the EM calibration scheme. Since this calibration scheme uses cluster-by-cluster and jet-by-jet information some of the sources of fluctuations

in the jet energy response are reduced, thereby improving the jet energy resolution. The overall uncertainty of the jet energy scale is smaller too. For all these reasons, this second scheme is used for the jets in the thesis.

Then the jet energy and direction as reconstructed in the calorimeters are corrected to restore the true jet energy. The *true* jet energy is defined by the energy of a jet formed by stable particles (excluding non interacting muons and neutrinos) as given from Monte Carlo simulation. The simulated response to jets at the LCW energy scale with respect to the truth jet energy $\mathcal{R}(p_{\mathrm{T}}) = \langle p_{\mathrm{T}}^{jet}/p_{\mathrm{T}}^{truth}\rangle_{MC}$, is used to calibrate the jets as the inverse of the response is equal to the average jet energy scale correction: $p_{\mathrm{T}}^{calibrated} = p_{\mathrm{T}}^{jet}/\mathcal{R}$. There is a final step where the extra energy due to additional pp collisions (pile-up) is partially removed by subtracting an amount of energy that is proportional to the *catchment area* of the jet and to the (median) density of energy of the event [94, 95].

The uncertainty of this calibration is tested on many experimental samples using jet-photon balance, di-jet and multi-jet balance, and jet-track association.

3.3.5 Missing transverse momentum

Observables described so far in this section are defined to measure the signatures of hadrons and fundamental particles. All electrically charged and/or strongly interacting particles are detected by some or a combination of the ATLAS sub-systems. The sole exception are electrically neutral color singlets like standard model neutrinos and MSSM neutralinos which being only weakly interacting can transverse the whole volume of the detector without notice.

Missing transverse momentum is used to infer the existence of these otherwise invisible particles. It is defined by the momentum imbalance in the plane transverse to the beam axis, where momentum conservation is expected. The vector momentum imbalance in the particles is obtained from the negative vector sum of the momenta of all particles detected in a pp collision:

$$\vec{E}_{\mathrm{T}}^{\mathrm{miss}} = -\sum_{\substack{i=\text{calorimeter cells,}\\ \text{tracks, muons}}} \vec{p}_{\mathrm{T}}^{\,i} \tag{3.6}$$

where its magnitude is denoted by $E_{\mathrm{T}}^{\mathrm{miss}}$. This sum runs over high granularity objects to improve the angular resolution. To enhance the energy resolution of energy deposits the reconstruction strategy of these well localized measurements are calibrated according to the reconstructed physics object to which they are associated. Since a calorimeter cell may belong to a reconstructed electron and also to a topocluster part of a jet, a hierarchy is set to avoid double countings. Calorimeter cells are associated with a reconstructed and identified high-p_{T} parent object in a chosen order: electrons, photons, jets and muons. For instance a calorimeter cell matched to a reconstructed photon and also to a jet, but not to an electron, is labeled as a being part of a photon [96]. Once the cells have been assigned

to their parent particle type the $\vec{E}_{\mathrm{T}}^{\mathrm{miss}}$ symbolically reads as a sum

$$E_{\mathrm{x(y)}}^{\mathrm{miss}} = E_{\mathrm{x(y)}}^{\mathrm{miss,e}} + E_{\mathrm{x(y)}}^{\mathrm{miss},\gamma} + E_{\mathrm{x(y)}}^{\mathrm{miss,jets}} + E_{\mathrm{x(y)}}^{\mathrm{miss,calo},\mu} + E_{\mathrm{x(y)}}^{\mathrm{miss},\mu} + E_{\mathrm{x(y)}}^{\mathrm{miss,Cellout}} \tag{3.7}$$

where the various terms have the following properties

- $E_{\mathrm{x(y)}}^{\mathrm{miss,e}}$, $E_{\mathrm{x(y)}}^{\mathrm{miss},\gamma}$, are reconstructed from cells in clusters associated the electrons and photons, following these criteria:
  - $E_{\mathrm{x(y)}}^{\mathrm{miss,e}}$ is calculated from reconstructed electrons passing the 'medium' electron identification requirements, with $p_{\mathrm{T}} > 10$ GeV and calibrated with the default electron calibration.
  - $E_{\mathrm{x(y)}}^{\mathrm{miss},\gamma}$ is calculated from photons reconstructed from photons with $p_{\mathrm{T}} > 10$ GeV at the EM scale as described in ref. [97].
- $E_{\mathrm{x(y)}}^{\mathrm{miss,jets}}$ is reconstructed from cells in clusters associated to jets with calibrated $p_{\mathrm{T}} > 20$ GeV with the LCW calibration (section 3.3.4.2).
- $E_{\mathrm{x(y)}}^{\mathrm{miss,calo},\mu}$ is the contribution to $E_{\mathrm{x(y)}}^{\mathrm{miss}}$ originating from the energy lost by muons in the calorimeter.
- $E_{\mathrm{x(y)}}^{\mathrm{miss},\mu}$ is calculated from the momenta of muon tracks reconstructed with $|\eta| < 2.7$. If a muon is isolated (i.e. there is no jet within $\Delta R = 0.3$ around the muon), then the term $E_{\mathrm{x(y)}}^{\mathrm{miss,calo},\mu}$ is not included in the sum.
- $E_{\mathrm{x(y)}}^{\mathrm{miss,Cellout}}$ is calculated from the cells in topoclusters which are not included in any of the above mentioned reconstructed objects. For tracks not associated to a topocluster nor to a reconstructed object, their transverse momentum is added to recover the contribution from low-p_{T} particles which do not reach the calorimeter or do not seed a topocluster.

Is clear from equation 3.7 that mismeasurements and uncertainties of the physical objects impact on the resolution of the missing energy. In general, jets are the dominant source for $E_{\mathrm{T}}^{\mathrm{miss}}$ uncertainty as electrons, photons and muons have better angular and energy resolutions. This property is exploited in section 6.1 to derive the QCD background contribution to this analysis.

3.3.6 *b*-jet tagging

Top and bottom-quarks are expected in many final states of supersymmetric models (see figure 2.8) and therefore the ability to identify jets originating or containing those quarks is important for the discrimination of signal events against uninteresting backgrounds. As shown in figure 3.11 for a given efficiency *b*-tagging algorithms are in generally much better at rejecting background that their top-tagger counterparts. This doesn't prevent from seeking final states with top quarks since they predominantly decay into bottom quarks

so identification of b-quark jets with high efficiency and high background rejection can improve any study targeting at either top or bottom quarks in the final state.

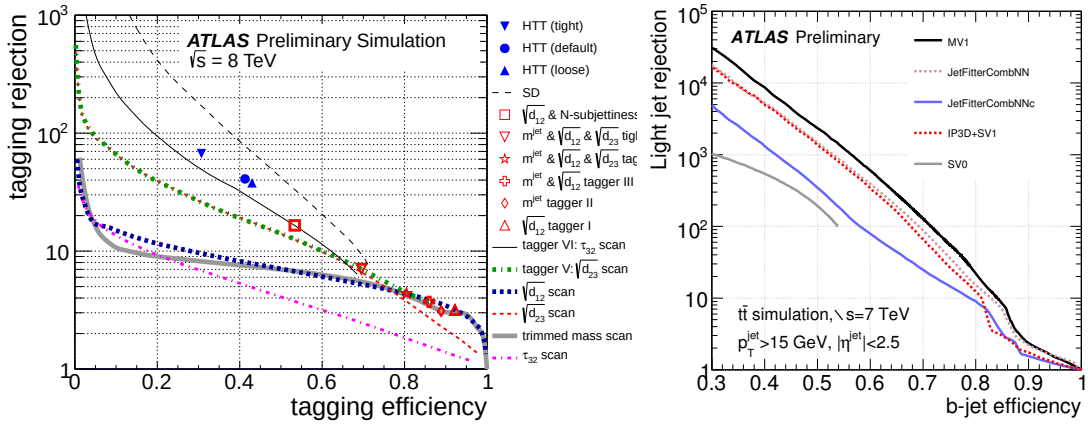

(a) top-jet tagging

(b) b-jet tagging

Figure 3.11: (a) Comparison of expected top jet tagging efficiency and light quark/gluon jet rejection. All substructure taggers and scans use trimmed anti-k_t (R = 1.0) jets, except the HEPTopTagger (HTT) that uses R = 1.2. The same $Z' \to t\bar{t}$, $m_{Z'} = 1.75$ TeV signal samples and multi-jet background samples and selection are used for all taggers. From ref. [98]. (b) Light-jet rejection as a function of the b-tag efficiency for several b-tagging algorithms, based on simulated $t\bar{t}$ events. From ref. [99].

A b-quark, once produced, fragments inevitably into a b-hadron. b-hadrons can be produced at ground state or at an excited state that decays rapidly through strong or electromagnetic interaction to a ground state b-hadron. Ground state b-hadrons can only decay weakly, with a typical proper timescale of ~ 1.5 ps. Considering time-dilation, a boosted b-hadron can travel few millimeters in the laboratory frame before decaying. Given the relatively high mass of B-hadrons their decay products tend to form a non-negligible decay angle (see equation 4.2) which leads to tracks with large impact parameters (passing far away from the interaction point). This signatures are exploited by b-tagging algorithms, which depend either on the presence of significantly displaced tracks (impact parameter taggers) or on the reconstruction of the b-hadron decay secondary vertex (vertex taggers).

The main b-tagging algorithm used in ATLAS is called Multi-Variate 1 (MV1), a neural network combination of three separate taggers known as IP3D, SV1, and JetFitter [100, 101]. The performance of the combined tagger is better than the individual taggers as shown in figure 3.11(b). For the analysis in this thesis the operating point at 70% tagging efficiency for MV1 is used. The rationale behind each of the taggers that serve as inputs for MV1 is described next.

All b-tagging algorithms takes as input the three-momenta of the jets, and matches to each jet all tracks that lay within a cone of radius R (the same R parameter of the jet) around the jet axis. Tracks are filtered to remove tracks with bad quality or that proceed

from electromagnetic interactions in the detector material (photon conversion) or those which can identified as secondary tracks from decays of even longer lived particles, like K_s^0 ($c\tau \approx 2.7\ cm$) and Λ baryons ($c\tau \approx 7.9\ cm$). The minimum track p_{T} is 1 GeV for the impact parameter taggers, and 400–500 MeV for the vertex taggers. These selections vary depending on the tagger. The minimum number of precision hits required is typically 7, for both approaches. For the vertex taggers, at least one of these hits must be in the pixel detector. For the impact parameter taggers, the track selection needs to be tighter since without the requirement of a vertex badly measured tracks affect directly the performance. In this case at least two of these hits must be in the pixel detector with one in the b-layer. In addition, the transverse and longitudinal impact parameters must satisfy $|d_0| < 1$ mm and $|z_0| \sin\theta < 1.5$ mm. Whereas for in the case of the algorithms relying on the reconstruction of secondary vertices a looser cut $|d_0| < 3.5$ mm is applied.

IP3D is an Impact Parameter b-tagger that looks for the transverse and longitudinal signed impact parameter significances, $IP/\sigma(IP)$. This ratio gives more relevance to well measured tracks. The sign of the impact parameter is defined as positive (negative) if the track intersects the jet axis in front (behind) of the primary vertex. The charged particle tracks originating from b-hadrons are expected to have significantly higher transverse and longitudinal impact parameters compared to prompt tracks originating directly from fragmentation. Tracks from secondary decays will have predominantly positive sign, while tracks from the fragmentation in light-jets tend to have a signed impact parameter distribution which is symmetric around 0, since they have no correlation with the jet direction. The IP3D tagger works by constructing a likelihood ratio between the b- and the c- or the light-jet hypotheses using two-dimensional distributions of the two impact parameter.

SV1 is a vertex algorithm that combines several variables. The typical topology of a b-hadron decay has two vertices, one stemming from the b-hadron decay and at least one more from the charm-hadron decay. SV1 makes no distinction between these two vertices. SV1 starts by forming two-track vertices from the tracks associated to the jet. Two-track vertices that are compatible with a b-hadron decay are kept and their tracks are combined into a global fit under the assumption of a single (inclusive) geometrical vertex. A iterative procedure is then used to remove the most inconsistent tracks until the inclusive vertex χ^2 of the fit is good. Discrimination between the light and b hypotheses is achieved via a likelihood ratio based on three variables: the invariant mass of all the tracks associated to the vertex, the ratio between the sum of the p_{T} of tracks in the vertex to the sum of track p_{T} for all the tracks associated with the jet, and the number of good two-track vertices. The first two variables have significant correlations and thus a two-dimensional distribution is used.

JetFitter is also a secondary vertex algorithm but uses a different hypothesis [101]. In this case, the b-hadron and the c-hadron decays are assumed to produce two separated vertices, aligned to the primary vertex at the interaction point, following the b-hadron flight path.

All charged particle tracks stemming from either the b- or c-hadron decay thus intersect this b-hadron flight axis, but not need to meet in a single point as happened for the SV1. Discrimination between b-, c- and light jets is based on a likelihood ratio constructed from the same variables as for SV1 with the addition of the flight length significances of the reconstructed secondary vertices.

3.4 The analysis software

The analysis codes produced for this thesis are written in C++ language and adapted for ProofAna (see appendix C of ref. [102]), an analysis framework based on Proof [103] a computer package for parallel computing. Most 'jobs' were run on the Tier3 computing facility from the Particle Physics and Astrophysics department at SLAC. This cluster was (at the time the this analysis was conducted) composed out of 225 cores, which allowed to process in parallel TeraByte(s) of data and simulation datasets within several hours. The analysis scripts were written in parallel by two separate groups (from Universities of Buenos Aires and Oxford) and the selections were mutually crosschecked to have perfect agreement, providing additional robustness and reliability on the results. Plots were produced using ROOT [104, 105], a C++ set of libraries oriented for analyses in high energy physics.

4
Jets and their substructure

"Jet algorithms do not find pre-existing jets, they define them."

– [106]

The dominant feature of high-energy hadron–hadron colliders such as the LHC is the production of highly collimated 'sprays' of energetic hadrons originated from the showering and decay of outgoing quarks and gluons in the large angle ('hard') collisions (see section 2.1.2). These bundles of particles, that we label *jets*, have historically been utilized as proxies for the quarks and gluons produced in the primary hard interaction.

It should be noted however that in practice the "one jet ↔ one parton" bijection is not possible. For example one parton may be reconstructed as multiple experimentally observed jets, or vice-versa multiple parton showers/decays may end up forming part of a single jet. Quoting S. Ellis [107]:

> "The constraints arising from the conservation of energy-momentum, colour, etc, guarantee that
>
> - a jet is NOT the remnant of a single parton;
> - a jet is NOT the result of a single parton shower;
> - a jet is NOT uniquely defined;
> - the properties of a jet will, in general, depend on how the jet is defined."

A *jet definition* to which he refers in the last item is a "recipe" –usually in the form of an algorithm– with which the four momenta of the final state partons, the resulting parton shower products, stable hadrons, or experimentally measured calorimeter energy deposits, may be compared on an equal footing. For this purpose, a jet algorithm must be able to define and identify jets using as inputs the information (four-momentum) corresponding to any stage of the evolution from the final state partons (*parton*-jets) to the final state hadrons (*particle*-jets) to energy depositions in the detector (*calorimeter*-jets).

Although the intuitive definition of a jet as "a large amount of hadronic energy in a small angular region" is sufficient to account for many qualitative features of hadron production, any detailed quantitative analysis requires a precise jet definition.

In the following sections it will be described the set of standard jet definitions most widely used in collider experiments, some of the most recent techniques to improve the measure-

ment of jet observables, and some characteristics of the jet internal structure.

4.1 Jet definitions

It is important to recognize that there is no fundamental, quantitatively unique definition of a jet. The jet definition may be adapted for a specific application (i.e. particular signatures) or experimental condition (high/low luminosity, high/low center-of-mass energy, etc.) in order to reconstruct more closely the hard scattering process. This flexibility is an accepted practice in many searches, as long as the same definition is consistently used when comparing data to expectations from theory and Monte Carlo (MC) programs. Nonetheless, to ensure stable definitions jet algorithms must satisfy a reasonable criteria:

- simple to implement in an experimental analysis and theoretical calculations;
- yield reliable (finite) results at all orders in perturbation theory;
- relatively insensitive to hadronization;
- infrared and collinear (IRC) 'safe' (see below);
- experimentally 'safe': not strongly affected by contamination from hadron remnants and other underlying soft events (pileup), or detector conditions (e.g., noise).

This list is an extension of the 'Snowmass accord' [108, 109] originally aimed to facilitate the comparison among jet physics results, that still provides a common ground for the development of modern jet algorithms.

Among the existing jet definitions ATLAS has adopted as its standard [106] the family of *sequential recombination* algorithms [109, 109–111]. These algorithms were specifically designed to be well-behaved (i.e. insensitive) in the presence of soft (infrared) and collinear gluon emission, and are thus usable for calculations done to any order in perturbation theory. They are referred to as being IRC safe (for a comparison between IRC safe and unsafe jet algorithms see table 6 in ref. [112]). Recombination algorithms work iteratively trying to reverse the pattern of QCD parton showers and multi-gluon radiations characterized by softer emissions as the shower evolves [113]. For this, the algorithm defines a distance d_{ij} between entities (particles or energy deposits in the calorimeter) and between entity i and the 'beam' d_{iB}:

$$d_{ij} = \min(p_{\mathrm{T},i}^{2p}, p_{\mathrm{T},j}^{2p}) \frac{\Delta R_{ij}^2}{R^2} \tag{4.1a}$$

$$d_{iB} = p_{\mathrm{T},i}^{2p} \tag{4.1b}$$

where ΔR_{ij}^2 is defined in equation 3.5, $p_{\mathrm{T},i}$ is the transverse momentum of particle i, and parameters p and R regulate the evolution of the clustering. The algorithm identifies the smallest of the distances and if it is a d_{ij} then combines[1] entities i and j, while if it is d_{iB}

[1]There exist many prescriptions as to how to *merge* entities i and j [109]. Throughout this thesis the covariant 'E-scheme' is used, which defines the four-moment (p^μ) of the combined pair by $p_{i+j}^\mu = p_i^\mu + p_j^\mu$.

defines entity i as a jet and removes it from the list of entities. Then, distances for the set of remaining entities are calculated and the procedure is repeated until all jets are found (i.e., no entities are left). The rationale behind this operation relies on the experimental conditions of the scattering process: $p + p \to h_1 + \ldots + h_n + X$, where h_i are the hadrons detected in the final state and X stands for hadrons that escape in the beam direction unnoticed for the detector (it has $y = \infty$). The above mentioned procedure prevents the admixture of measured and undetected entities into the same jet, thus providing *observable* jets. The use of a metric in (y–ϕ) space guarantees that the algorithm is invariant under longitudinal (along the beam) Lorentz boosts [109,113], which is a mandatory requirement for hadron–hadron collisions where the partonic center-of-mass energy isn't fixed.

Two examples that aim to reverse the shower history are the k_t algorithm for $p = 1$ [109] and the Cambridge-Aachen (C/A) algorithm for $p = 0$ [110,111]. The distance used for the k_t algorithm induces soft particles to be merged first, which introduces a strong sensitivity to small fluctuations of the energy density of the parton shower. The C/A algorithm relies solely on angular ordering of emissions in order to reconstruct the shower by omitting the transverse momentum from d_{ij}, which again results in a strong dependence to the experimental conditions. A case of particular interest corresponds to $p = -1$, referred as the 'anti-k_t' jet-clustering algorithm [114]. The metric d_{ij} for this algorithm implies that soft particles will tend to cluster with hard ones long before they cluster among themselves, effectively reducing the sensitivity to fluctuations of the parton shower or energy aggregates from UE. If a hard particle has no hard neighbors within a distance $2R$, then it will simply accumulate all the soft particles within a circle of radius R, resulting in a perfectly conical jet in the (y–ϕ) plane. More complex boundaries can occur for busy environments composed by many close-by showers. Still, the key feature of this algorithm is that the form of the jet (technically known as *catchment area* [115]) is extraordinarily resilient to soft fluctuations of the energy. The stability of the jet area facilitates the experimental calibration of jets (see section 3.3.4.2), eliminating some parts of the momentum-resolution loss caused by underlying-event and pile-up contamination [95]. From now on (unless stated otherwise) jets are built with anti-k_t algorithm.

The other free parameter in equation 4.1 is the radius R that sets a characteristic scale in the (y–ϕ) space, and generally speaking defines the area of the jet: $a^{jet} = \pi R^2$ for highly energetic and isolated jets. There is no strict recommendation for the choice of R, but as general guidance for values between 0.4 and 1.2 effects of hadronization and the influence of the underlying event are minimized [116] (see also figure 38 of ref. [112]). As the radius increases less energy is 'splashed out' of the jet, a phenomena known as out-of-cone energy, but the influence of underlying event also increases as the area of the jet growths (more about this particular aspect in section 4.3). The common values for anti-k_t jets in ATLAS are $R = \{0.4, 0.6, 1.0\}$ [106, 117]. In the next section section 4.2, I will describe some techniques developed in recent years to cope with energetic jets. These techniques use *large-R* jets that constitute a central ingredient of the search presented in this thesis.

4.2 Jets in the Boosted Regime

The high center-of-mass energy achieved at the LHC has opened new kinematic regimes to experimental study. The new phase space available for the production of SM particles with significant Lorentz boosts –or hypothetical new massive particles that decay to highly boosted SM particles– translates phenomenologically into novel experimental signatures. This, in turn forces the development and implementation of novel techniques, as described in the following sections.

4.2.1 Large-R ("fat") jets

When sufficiently boosted, heavy particles can be produced with transverse momenta that greatly exceeds their rest mass. As a consequence, the decay products of W bosons [118], top quarks [119, 120], and Higgs bosons [121] can become collimated to the point that standard reconstruction techniques begin to fail, and necessitates new ones to conduct measurements of these novel final states. One example of a new physics process that may

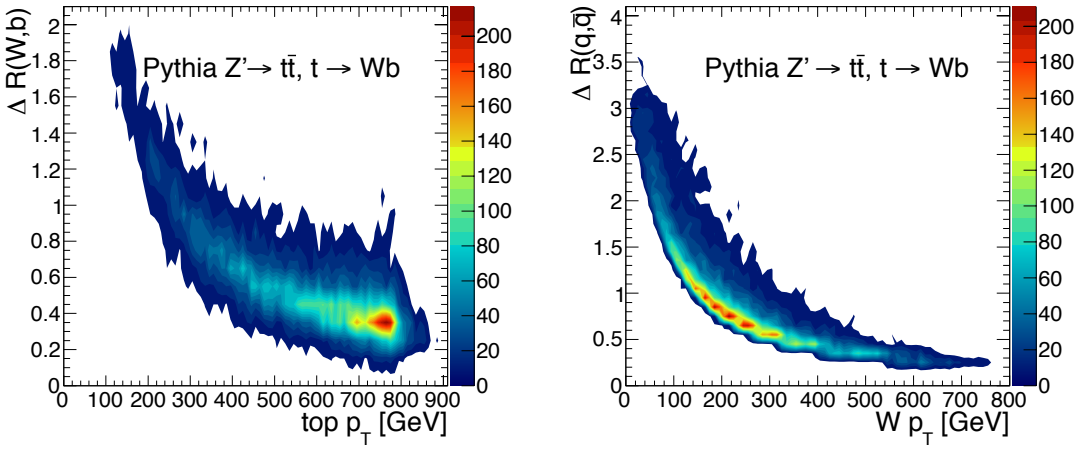

(a) $t \to Wb$ (b) $W \to qq'$

Figure 4.1: (a) The angular separation between the W boson and b-quark in top decays, $t \to Wb$, as a function of the top-quark transverse momentum (p_{T}^{t}) in simulated PYTHIA [122] $Z' \to t\bar{t}$ ($m_{Z'} = 1.6$ TeV) events. (b) The angular distance between the light quark and anti-quark from a W in $t \to Wb$ decays as a function of the p_{T} of the W boson (p_{T}^{W}). Both distributions are at the generator level and do not include effects due to initial and final-state radiation, or the underlying event. The color scale indicates number of events (arbitrary normalization) [117].

produce heavy objects with a significant Lorentz boost is the decay of the hypothetical heavy gauge boson, the Z', to top-quark pairs. Figure 4.1 shows the angular separation between the W and b decay products of a top quark in simulated $Z' \to t\bar{t}$ ($m_{Z'} = 1.6$ TeV) events, as well as the separation between the light quarks of the subsequent hadronic decay

of the W boson. For heavy particle decays the angular separation of the decay products is approximately[1]

$$\Delta R \simeq \frac{2m}{p_{\mathrm{T}}}, \tag{4.2}$$

where ΔR is the angular distance between the decay children, and p_{T} and m are the transverse momentum and the mass, respectively, of the decaying particle. For $p_{\mathrm{T}}^{W} > 200$ GeV, the ability to resolve the individual hadronic decay products using standard narrow-radius jet algorithms begins to degrade, and when p_{T}^{t} is greater than 300 GeV, the decay products of the top quark tend to overlap with a separation $\Delta R < 1.0$. Figure 4.2 shows the probability that the partons from a hadronic top decay are found within a given ΔR distance of 0.8, for a broad kinematic range of top production ($2m_t \leq m_{tt} \leq 2.5$ TeV). For top quarks produced at rest or close to the production threshold ($m_{tt} \approx 2m_t$) the decay products are typically well separated, and partons are resolved into individual jets. For more massive Z' the excess of energy excess is transferred to the tops momenta and a larger fraction of jets tends to collect more than just one decay parton. Techniques designed to recover sensitiv-

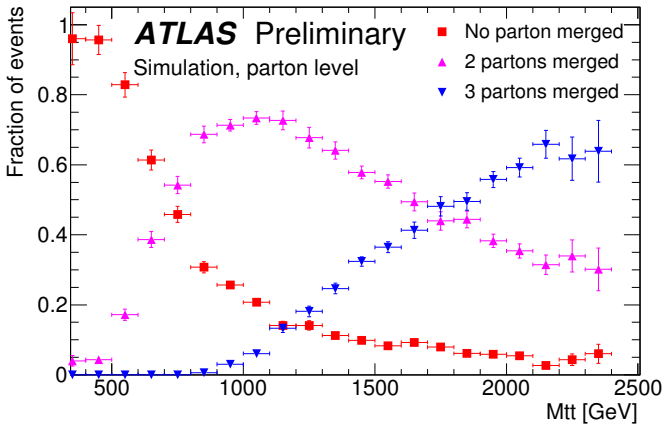

Figure 4.2: Top pair production from the decay of Z' (generated with ATLAS *fast* simulation [123]). Probability that the three partons from a hadronic top decay are found within a ΔR distance of 0.8. The red squares indicate the probability that no partons merge, the green triangles that two partons merge, but the third remains well separated, and the blue triangles that all three partons merge [124].

ity in such cases focus on large radius (large-R) jets. Large-R jets typically have $R \geq 1.0$ such that maximize the likelihood to harvest all the components of heavy particle decays or collect most part of the QCD shower. Note that there is nothing essentially prohibitive

[1] Consider the decay of a massive particle V to two massless particles 1 and 2, $V \to 1 + 2$. The invariant mass of V is $m^2 = (p_1 + p_2)^2 = 2\left[|\vec{p}_1||\vec{p}_2| - \vec{p}_1 \cdot \vec{p}_2\right]$, where $\vec{p}_i = p_{T,i}(\cos(\phi_i), \sin(\phi_i), \sinh(\eta_i))$ is the tri-momentum of the child i. Simplifying, the square mass is $m^2 = {p_T}^2 z(1-z)\Delta R^2$, where $z = p_{T,1}/p_T$, $1 - z = p_{T,2}/p_T$ are the momentum fractions carried by the two children and $\Delta R^2 = 2\left[\cosh(\eta_1 - \eta_2) - \cos(\phi_1 - \phi_2)\right] \simeq (\eta_1 - \eta_2)^2 + (\phi_1 - \phi_2)^2$ is an alternative definition of the square angular distance (see equation 11 in ref. [109]). The useful relation equation 4.2 results immediately for symmetric decays ($z = 1/2$).

about having two or more partons contained in the same jet. On the contrary, large-R jets at the *boosted* regime tend to extend the "one parton $\leftrightarrow$ one jet" idealized topology previously assigned to light partons (u, d, s, c and b quarks) also to the heavy particles of the SM (W, Z, Higgs boson and top quark). The characteristic two-body or three-body decays of a high p_{T} vector boson or top quark, can be distinguished by hard, wide-angle components representative of the individual decay products that result in a large reconstructed jet mass, as well as typical kinematic relationships among the hard components of the jet [118, 121, 125–129]. In contrast, jets formed from gluons and light quarks are characterized primarily by a single dense core of energy surrounded by soft radiation from the parton shower, hadronization, and underlying event (UE) remnants [130–132]. Many jet substructure techniques based on the examination of these distinct topologies were developed in recent years [133, 134] with the double purpose of i. improving the resolution of jet related measurements [135, 136], and ii. enhance the identification of vector [137] and Higgs [121] bosons, top quarks [138] or supersymmetric [33, 139] candidates. These techniques are classified in two categories. **Jet or event shapes** that characterize properties of the jet like its mass [140], radial extent (or width) and eccentricity [141], the angular correlations between its constituents [142], the pattern of inner energy distribution [132], the number of hard lobes of energy [125], or the color connection to other jets [126], among many others. New jet algorithms, referred to as **jet grooming**, refine the definition of a jet in a high-luminosity environment and potentiate the strength of jet shapes to be more effective as discriminants between signal and background candidates. The common strategy for these two variants starts from building large-R jets and then define an observable as a smooth functional of the energy flow within individual jets, which in practice is calculable using the discrete set of entities (constituents) that where merged to form the jet. This *top-down* strategy has the advantage that any jet observable can be compared against a hard scale of the problem: the energy and/or mass of the "parent" jet under consideration.

4.2.2 Jet mass

Preliminary studies were conducted for several jet shapes [33, 125, 126, 143]. Here, a particular interest is put on the jet mass, since it will be used as a discriminant variable in the search analysis (section 5.5.3). With the exception of heavy quarks, partons are essentially massless in the context of high energy collisions. Jets are not, in particular those with significant substructure. The jet mass m_j, is calculated from the energies and momenta of its constituents (clusters or stable particles) as

$$(m_j)^2 = \left(\sum_i p_i^\mu\right)^2 = \left(\sum_i E_i\right)^2 - \left(\sum_i \vec{p}_i\right)^2 \tag{4.3}$$

where a 4-vector-addition recombination scheme is clearly assumed. The standard ATLAS reconstruction procedure [141] considers the calorimeter clusters as massless ($E_i = |p_i|$),

while Monte Carlo particles are assigned their correct masses ($E_i > |p_i|$).

When a jet is formed via a parton shower, gluons may be radiated beyond the reach of the jet definition ('splash-out') and thus reduce the jet's energy compared to that of the parton, or alternatively it may be radiated within the reach of the jet definition and then generate a mass for the jet. The squared invariant mass of a jet to first non-trivial order is [144, 145]

$$\langle m_j^2 \rangle = C\,\alpha_s\,p_{\mathrm{T}}^2\,R^2 \tag{4.4}$$

where C is a coefficient that depends on the relative fraction of quarks and gluons and on the type of jet algorithm ($C = 0.16$ for quark-initiated jets and $C = 0.37$ for gluon-initiated jets). A consequence of this formula is the larger probability to see high mass jets initiated from a gluon as opposed to a light-quark. When a jet is formed from independent hadronic decays of very high-p_{T} top quarks and electroweak bosons the mean squared invariant mass is [33]

$$\langle m_j^2 \rangle = \mathcal{O}(1)\,p_{\mathrm{T}}^2\,R^2 \tag{4.5}$$

where α_s does not play any role. Note that, at the electroweak scale $\alpha_s \approx 0.1$ (see section 2.1.2) so the mass for these jets is larger. This difference, however is hard to exploit directly in hadron colliders as the jet mass is susceptible to contaminations from underlying event and pile-up [145] which induce variations $\langle \delta m_j^2 \rangle \simeq \rho\,p_{\mathrm{T}}\,R^4/4$ (with ρ the energy density per unit rapidity induced by UE/pile-up). With the use of grooming techniques (to be discussed later), jet mass has become a more 'profitable' variable for discriminating new heavy objects decaying into a single jet from the QCD background in high-multiplicity final states.

The organization of the text is as follows. Next we shift to the intimately related topic of subjets within a large-R jet in section 4.2.3. Finally, present the description of jet grooming algorithms in section 4.3 as a natural preamble to the introduction of *composite* jets used for this search in section 4.4.

4.2.3 Subjets

Jets have a substructure that can be interpreted as formed by sub-units or energy blobs in the hierarchy of the partonic shower/decay. These are called subjets. Subjets are ubiquitous objects in many substructure analyses [121, 126, 128]. They appear naturally in the hadronic decay of Z bosons (or top quarks) as a two-(three-)pronged structure observed in the detector. Each (not necessarily resolved) lobe can be associated with a given subset of the jet constituents comprising a single identifiable object called *subjet*. Within each jet, subjets are defined re-clustering the jet constituents using a jet algorithm[1] and a characteristic radius R_{sub} smaller than that of the parent jet. Usually $R_{sub} \lesssim R/2$ [136]. General aspects are shown next.

[1]The reclustering algorithm used to build the subjets is independent of the algorithm used for the jet.

4.2.3.1 Subjet performance

Figure 4.3 shows the ability of subjets to reconstruct parton level kinematics in a two-pronged topology. A simulated sample $Z + jets$ events with hadronically decaying Z bosons is used (generated using the HERWIG v6.510 [146] event generator interfaced with JIMMY v4.31 [147] for the UE). Reconstructed large-R jets (anti-k_t, $R = 1.0$) jets are labelled as a Z jet if the Z boson is contained within the jet and if its mass is within the mass of the Z boson ($70 \leq m_Z \leq 100$ GeV). Z jets were reclustered to form k_t subjets with $R_{sub} = 0.3$ [1] and the angular distance between the two leading (ordered by their p_{T}) subjets compared against the separation of the hadronic decays of the Z ($\Delta R(q, \bar{q})$) as shown in figure 4.3(a). Most jets have an angular separation that peaks at $\Delta R(q, \bar{q}) \approx 0.6$, as expected for $p_{\mathrm{T}}^{Z} \approx 200$ GeV (figure 4.1(b)). These variables are fairly correlated ($\rho = 0.808$) although the distance systematically tends to be smaller for the quarks than for the subjets. This is not mis-modeling but a consequence of the finite size of subjets. The edge of close-by subjets becomes distorted in the region where they are in contact pulling apart their centroids, which doesn't happen for point-like particles. At this energy $\sim 92\%$ of the Z jets have its leading subjets associated unequivocally to only one decay particle as indicated in figure 4.3(b). In the majority of the remaining cases the matching occurs for the lead subjet and one of the softer subjets. For more energetic jets the decay quarks and the associated subjets tend to be closer (figure 4.3(c)) and the particle $\leftrightarrow$ subjet assignment improves up to $\sim 95\%$ of the jets (figure 4.3(d)). Also a non negligible fraction ($\sim 2\%$) of jets have both quarks contained within the lead subjet, which means that –at this boost– subjets of this size ($R_{sub} = 0.3$) start to fail to resolve individual partons.

Subjets also reproduce the general features of parton QCD radiation. Large-R jets from dijet events are typically characterized by a highly energetic leading-$p_{\mathrm{T}}^{\mathrm{subjet}}$ subjet located close to the parent jet axis as shown in figure 4.4. These leading subjets carry a large fraction of the parent jet energy, and this fraction increases with the parent jet p_{T}: $\sim$ 71% for $100 \leq p_{\mathrm{T}}^{\mathrm{jet}} < 150$ GeV and $\sim$ 86% for $400 \leq p_{\mathrm{T}}^{\mathrm{jet}} < 500$ GeV. The second leading subjets are less energetic and have approximately 10% of the energy of the parent jet for 400 GeV $\leq p_{\mathrm{T}}^{\mathrm{jet}} < 500$ GeV. The leading-p_{T} subjet is located in average at $\Delta R \leq 0.07$ from the axis of the parent jet, while less energetic subjets are more distant from the axis of the parent jet: $\Delta R \geq 0.5$. These observations are consistent with the expected energy flow for QCD jets where a hard core is surrounded by isotropically distributed soft radiation [132]. Therefore, the subjet structure of jets from dijet events can be characterized by looking only to the leading and sub-leading subjets.

[1] As described in section 4.1, k_t algorithm reverses the shower history by merging soft particles first and is therefore the one of the standard choices to build subjets.

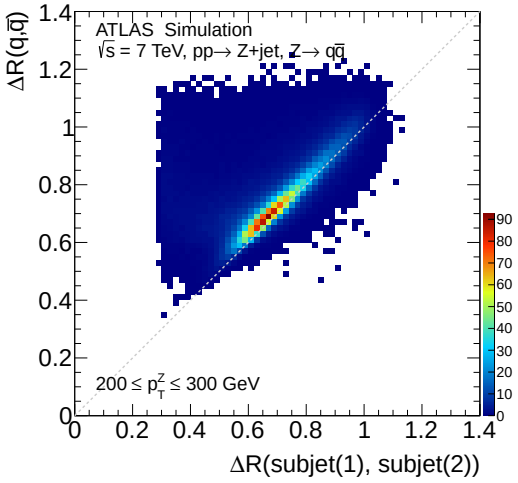

(a) angular separation, $200 \leq p_{\mathrm{T}}^{Z} \leq 300$ GeV

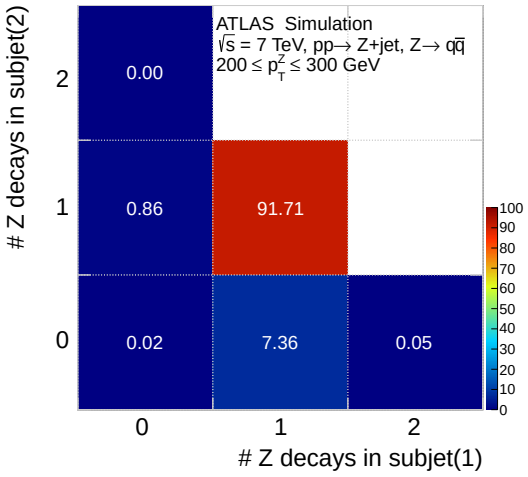

(b) subjet–parton match, $200 \leq p_{\mathrm{T}}^{Z} \leq 300$ GeV

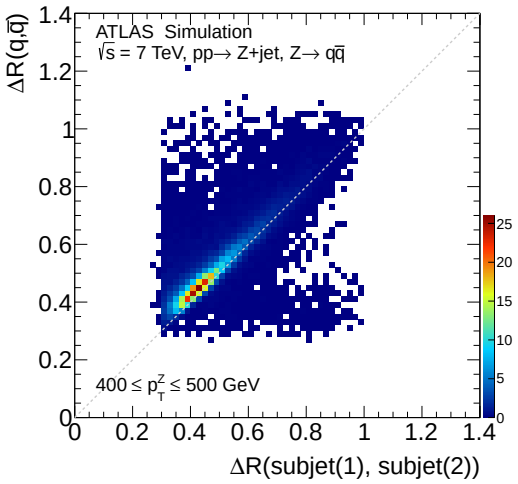

(c) angular separation, $400 \leq p_{\mathrm{T}}^{Z} \leq 500$ GeV

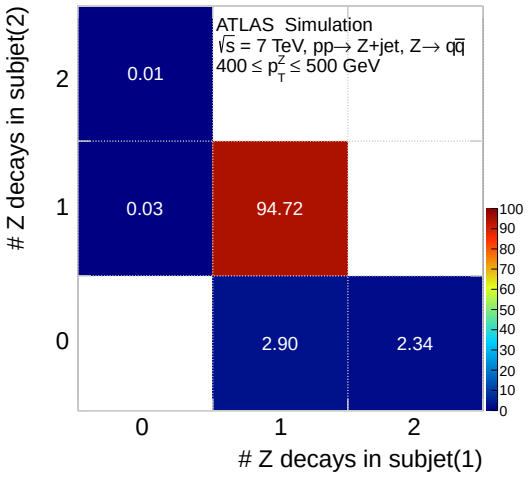

(d) subjet–parton match, $400 \leq p_{\mathrm{T}}^{Z} \leq 500$ GeV

Figure 4.3: (a) The correlation of angular separation between the decays of a Z boson ($\Delta R(q, \bar{q})$) and the angular separation between the hardest (subjet(1)) and second hardest (subjet(2)) subjets of the Z jet, for $200 \leq p_{\mathrm{T}}^{Z} \leq 300$ GeV. Subjets are constructed using the k_t algorithm with $R_{sub} = 0.3$, from anti-k_t ($R = 1.0$) jets. (b) The number of Z boson decays contained in subjet(2), as a function of the number of decays contained in subjet(1). The distribution is normalized to percentages. (c) same as (a) but for higher p_{T}^{Z}. (d) same as (b) but for higher p_{T}^{Z}.

4.2.3.2 Subjet energy scale (subJES)

Several grooming and tagging procedures rely heavily on the energy scale of subjets [121, 126, 136]. To this respect a proper understanding of their energy scale is mandatory to reduce the associated uncertainties. Studies were conducted using data from the entire 2011 ATLAS data-taking period, corresponding to $4.7 \pm 0.1\mathrm{fb}^{-1}$ of integrated luminosity [148].

In order to validate the subjet energy scale made for the calorimeter-subjets, these are com-

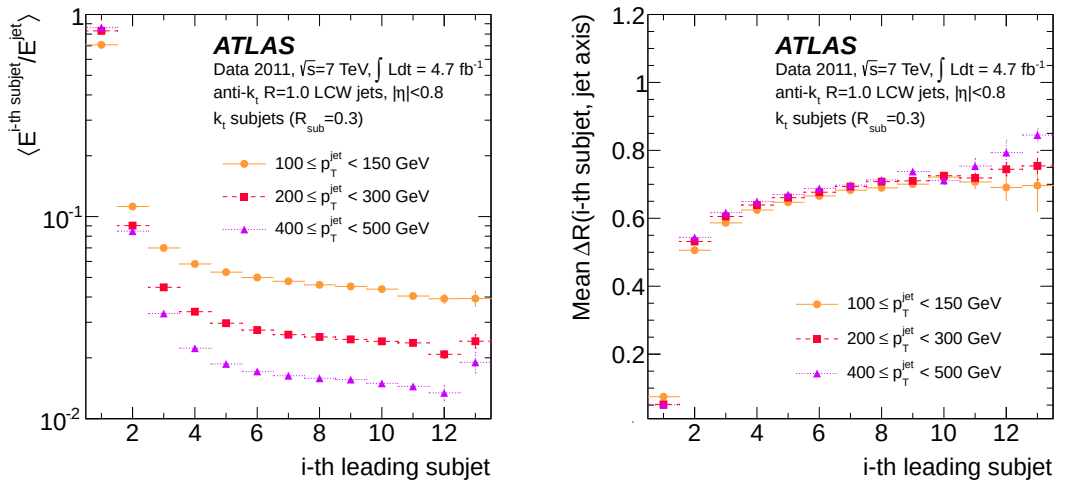

(a) Mean energy fraction carried by subjets

(b) Mean radial position of subjets within the parent jet

Figure 4.4: (a) Mean subjet energy fraction and (b) mean distance of subjets to the axis of the parent jet for different subjets in the jet.

pared to the energy of tracks. This is done in replacement of the direct ratio $p_{\mathrm{T}}^{\mathrm{jet}}(\mathrm{data})/p_{\mathrm{T}}^{\mathrm{jet}}(\mathrm{MC})$ that is sensitive to the mismodelling of jets at the hadron level. The inner detector and the calorimeter have largely uncorrelated instrumental systematic effects, and so a comparison of variables such as jet mass and energy between the two systems allows a separation of physics (correlated) and detector (uncorrelated) effects. Performance studies [149] have showed that there is excellent agreement between the measured positions of clusters and tracks in data, indicating no systematic misalignment between the calorimeter and the inner detector. The use of tracks also reduces or eliminates the impact of additional pp collisions by requiring the tracks to come from the hard-scattering vertex (see section 3.3.1). This approach was used extensively in the measurement of the jet mass and substructure properties of jets in the 2010 data [140].

The relative uncertainty is determined using the ratio of the transverse momentum of the calorimeter subjet (p_{T}^{subjet}) and the track p_{T} (p_{T}^{trk}) associated[1] to each subjet:

$$r_{\mathrm{trk}}^{\mathrm{subjet}} = \frac{\sum_{tracks} p_{\mathrm{T}}^{trk}}{p_{\mathrm{T}}^{subjet}} \tag{4.6}$$

The mean value of this ratio is expected to be well described by the detector simulation if detector effects are well modelled. That is to say, even if some underlying physics process is unaccounted for in the simulation, as long as this process affects both the tracks and calorimeter-subjet p_{T} in a similar way, then the ratio of data to simulation should be

[1]The association between tracks and subjets is done using the novel ghost-association technique described in section 4.2.3.3.

relatively unaffected when averaged over many events. A double ratio of r_{trk} is constructed in order to evaluate this agreement as

$$R_{trk} = \frac{\langle r_{\mathrm{trk}}^{\mathrm{subjet}} \rangle_{data}}{\langle r_{\mathrm{trk}}^{\mathrm{subjet}} \rangle_{MC}} \tag{4.7}$$

The dependence of R_{trk} on p_{T}^{subjet} provides a test of the deviation of simulation from data, thus allowing an estimate of the uncertainty associated with the Monte Carlo derived calibration.

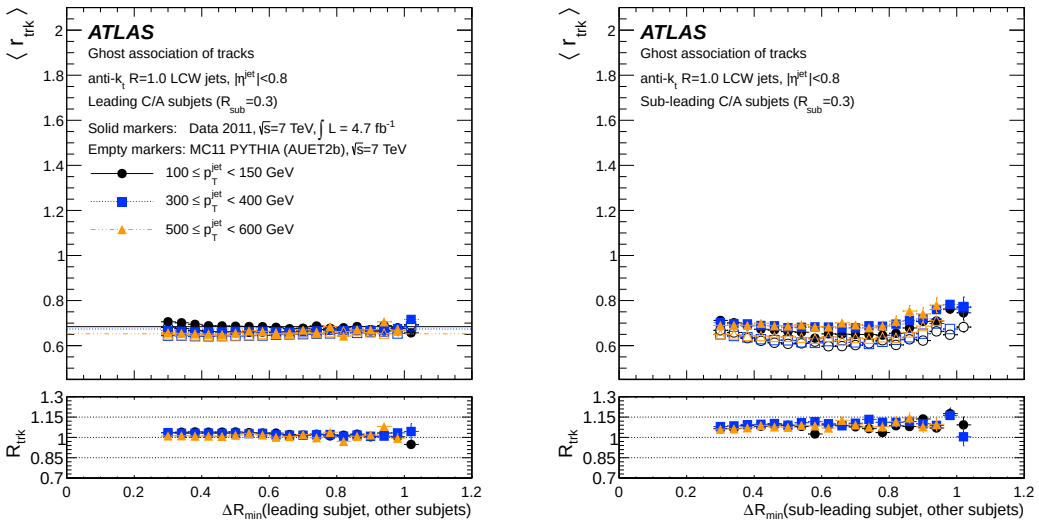

(a) Lead subjets (b) Second lead subjets

Figure 4.5: Mean ratio of calorimeter p_{T} to track p_{T} for leading (a) and second-leading (b) subjets as a function of the distance of the subjet to the nearest subjet within the jet. The horizontal lines in (a) indicate the p_{T} ratio for jets containing only one subjet, i.e. absolutely isolated subjets. Bottom panel shows the double ratio R_{trk}. Tracks are associated to subjets using 'ghost matching'.

Figure 4.5 shows the mean ratio $r_{\mathrm{trk}}^{\mathrm{subjet}}$ as a function of the distance between the subjet and its closest neighbor subjet in the $\eta - \phi$ plane. Some large-R jets are composed by a single isolated subjet that provide a standard with which to compare the impact of the proximity for non-isolated subjets. Isolated subjets have $r_{trk} \approx 0.7$ (horizontal lines in figure 4.5(a)), a value that is consistent to the expected charged-to-total fraction of particles by calorimeter and tracking detectors respectively ($n_{ch}/n_{tot} \simeq 2/3$). This value agrees within errors to the mean r_{trk} for non-isolated subjets, for both data and MC, independently of the parent jet p_{T}. For the uncalibrated subjets shown in figure 4.5(a), any difference between data and simulation is well within 5% for the leading-p_{T} subjet and 15% for the second leading subjet.

This uncertainty is reduced to 3.5% for calibrated subjets with some variations depending on the radii, from 2% for $R_{sub} = 0.4$ to 4% for $R_{sub} = 0.2$. Figure 4.6 shows the average

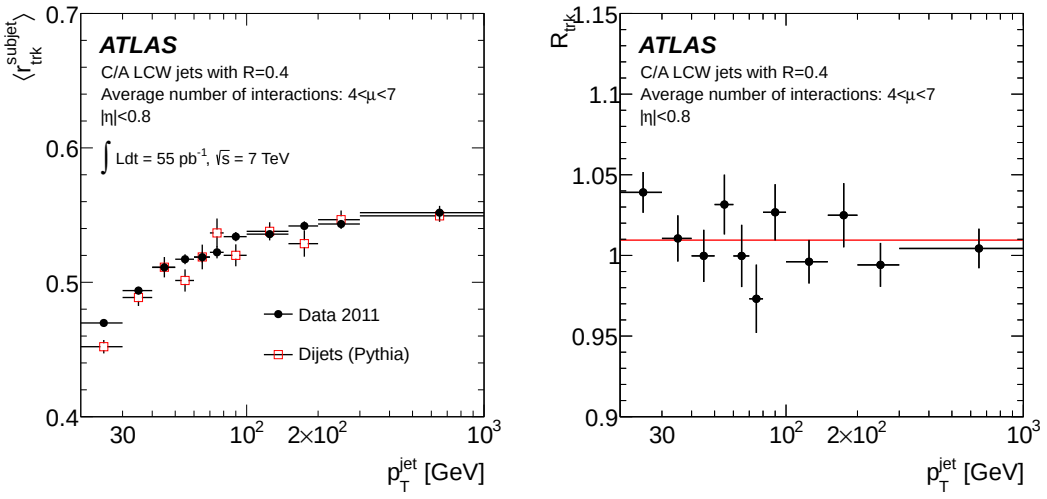

(a) (b)

Figure 4.6: Comparison of the calibrated C/A $R = 0.4$ calorimeter subjet p_{T} with the p_{T} of tracks matched to the subjet for ATLAS data recorded in 2011 and for dijet simulations with PYTHIA. The average number of interactions per bunch crossing (μ) ranges from 4 to 7. (a) The average ratio $\langle r_{\mathrm{trk}}^{\mathrm{subjet}} \rangle$ as a function of the calibrated jet p_{T}. (b) Deviations of the double ratio R_{trk} from unity serve as an estimate of the uncertainty of the MC calibrated calorimeter-jet p_{T}. The horizontal line indicates the uncertainty-weighted average.

$r_{\mathrm{trk}}^{\mathrm{subjet}}$ as a function of the parent jet p_{T} for calibrated subjets (with $R_{sub} = 0.4$). Calibration is performed using calibration constants derived for small jets ($R = 0.2 - 0.5$) using a simulation of the calorimeter energy response of jets by comparing the energy and pseudorapidity of a generator-level (small-R) jet to that of a matched calorimeter (small-R) jet (section 3.3.4.2). The imperfect knowledge of the material distribution in the tracking detector constitutes the dominating systematic uncertainty. It results in an additional uncertainty in R_{trk} of $\sim 2\%$ for $|\eta^{jet}| < 1.4$ and $\sim 3\%$ for $1.4 < |\eta^{jet}| < 2.1$, although it does not introduce a measurable shift[1].

Altogether these results indicate that subjets within a large-R jet, can be treated similarly than standard small-R jets in terms of calibration and uncertainty determination, and their performance is equally robust, a strong basis for *composite* jets used for the SUSY search (see section 4.4).

4.2.3.3 Ghost association of particles

A point of particular relevance in equations 4.6 and 4.7 is the association of tracks to a particular subjet (or jet).

Cone matching consists in selecting tracks if they lay within a given distance from the

[1]The subjet p_{T} systematic uncertainty is taken to be the absolute deviation of the central weighted-average R_{trk} from unity, with the shifts introduced by the systematic variations added in quadrature.

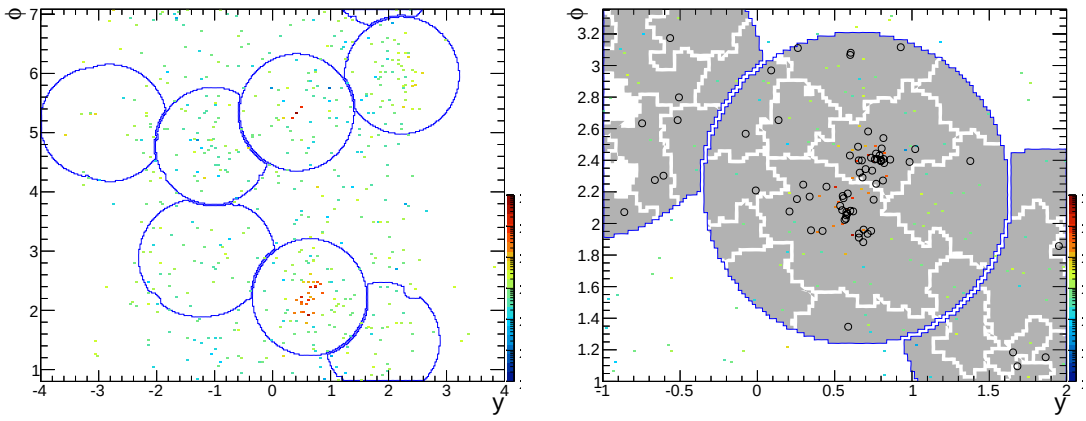

(a) Dijet event

(b) Zoom to the lead jet

Figure 4.7: (a) Display of a simulated dijet event projected to the rapidity-azimuth plane. Jets (shown in blue) having $p_{\mathrm{T}} \geq 30$ GeV are represented using the active area [115]. Jet constituents are shown in color scale. (b) Substructure of the lead jet ($p_{\mathrm{T}} = 1.57$ TeV). k_t ($R_{sub} = 0.3$) subjets within anti-k_t ($R = 1.0$) jets are shown in light gray. Tracks form the primary vertex falling in side the jet are shown (open circles). Dijet event simulated with PYTHIA, and displayed using the JetAnalysisDisplay tool [150].

subjet axis: $(y_{trk} - y_{subjet})^2 + (\phi_{trk} - \phi_{subjet})^2 \leq R_{sub}$. This association implicitly assumes a cone-like boundary and an area of πR_{sub}^2 for all subjets, and that all tracks within this area belong to the subjet. This assumption generally works well in the case of an isolated anti-k_t (sub)jet. Conversely, k_t, C/A, and even anti-k_t subjets in high-multiplicity environments begin to suffer from the proximity of neighbour subjets. For example, figure 4.7(b) shows the subjets of the lead p_{T} jet from a simulated dijet event, together with the tracks originating at the primary vertex. The irregular boundaries of subjets is evident and the question of which tracks to associate becomes more difficult to answer.

Ghost matching [95,115] provides a much more appropriate association of the tracks to the calorimeter subjets for this scenario. In this technique, tracks are treated as infinitesimally soft, low-p_{T} particles by setting their p_{T} to less than 1 eV. These tracks are then added to the list of inputs for jet finding. The low scale means the tracks do not disrupt the reconstruction of jets, as the jet reconstruction algorithms are infrared safe. However, after jet finding, it is possible to identify which tracks are clustered into which subjets. This technique shows a more stable dependence of the ratio $r_{\mathrm{trk}}^{\mathrm{subjet}}$ on the angular separation between subjets. Generally, this approach facilitates the measurement of the effective area of a jet, or the so-called *active catchment area* [115]. In this case instead of tracks, a uniform, fixed density (usually one per $\Delta y \times \Delta\phi = 0.01 \times 0.01$) of infinitesimally soft particles is distributed within the event and are allowed to participate in the jet clustering algorithm. Instead of identifying tracks associated with the resulting jets, the number of such ghost particles present in the jet after reconstruction defines the effective area of that jet.

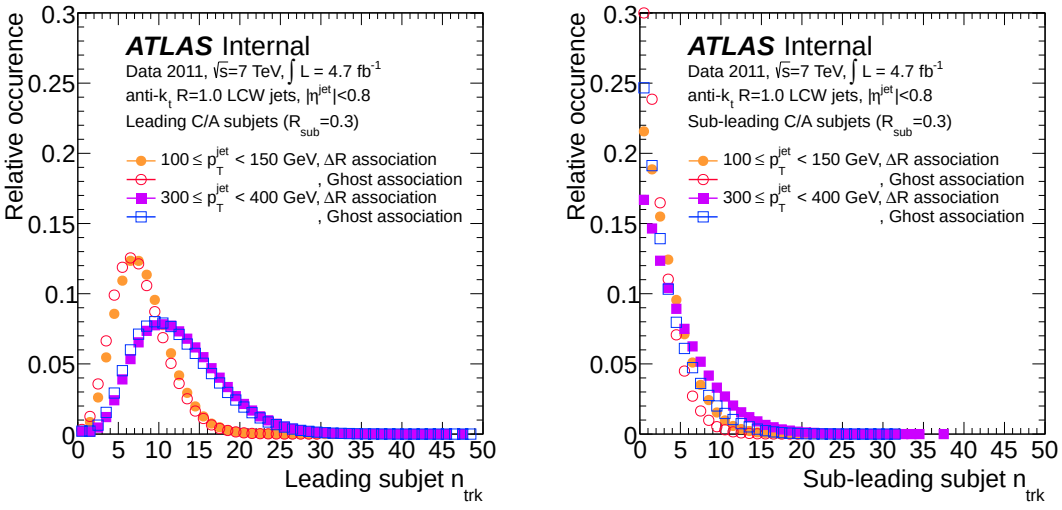

(a) leading subjet (b) second leading subjet

Figure 4.8: Track multiplicity (n_{trk}) associated to calorimeter subjets. Tracks are matched using $\Delta R-$ (cone) and ghost association schemes.

In general, the mean number of tracks associated to each subjet is not very sensitive to the choice of the track matching scheme, albeit slightly more tracks per subjet are associated by the cone matching, as shown in figure 4.8. With that method tracks laying close to the boundary of subjets are assigned twice, once for each of the subjets in contact (double counting).

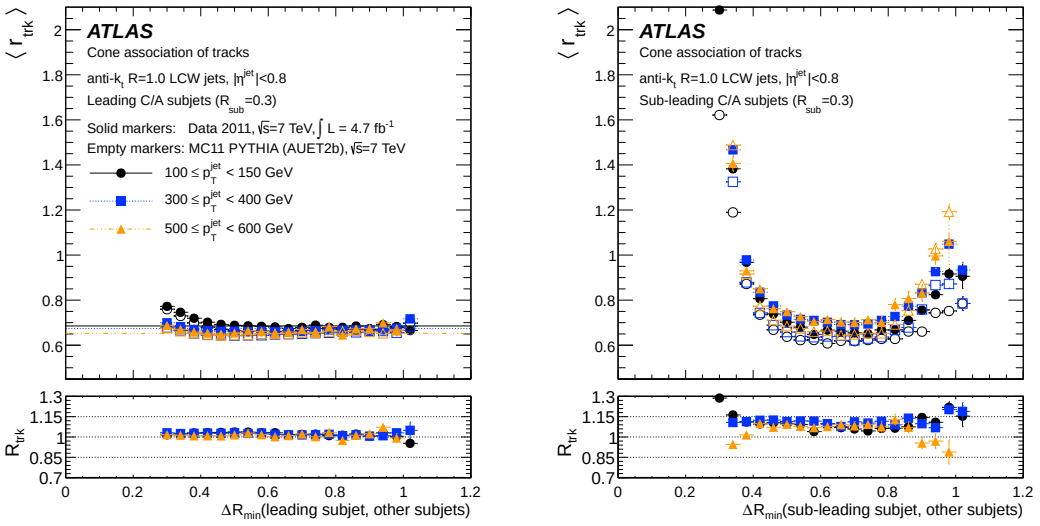

(a) Lead subjets (b) Second lead subjets

Figure 4.9: Mean ratio of calorimeter p_{T} to track p_{T} for leading (a) and second-leading (b) subjets as a function of the distance of the subjet to the nearest subjet within the jet. The horizontal lines in (a) indicate the p_{T} ratio for jets containing only one subjet, i.e. absolutely isolated subjets. Bottom panel shows the double ratio R_{trk}. Tracks are associated to subjets using cone matching.

This problem is noticeable when comparing the plots of $r_{\text{trk}}^{\text{subjet}}$ between figures 4.5 and 4.9. A rise in $r_{\text{trk}}^{\text{subjet}}$ is observed for close-by subjets with $\Delta R_{\text{min}} \leq 2 \times R_{sub}$. The rise is most notable for the softer subjets (figure 4.9(b)), in which case the ratio $r_{\text{trk}}^{\text{subjet}}$ is a factor of two smaller at $\Delta R_{\text{min}} = 0.6$ than at $\Delta R_{\text{min}} = 0.3$, the smallest separation between subjets.

As a final remark, it is worth noting that the same rationale presented here for tracks and subjets applies to constrain other objects within the jets. For instance, truth particles like partons, leptons or stable hadrons in the case of MC simulations can be associated to jets using this method. In fact, ATLAS is incorporating this procedure for the labelling of b jets using truth information (B-hadron labelling).

4.3 Jet grooming

The high luminosity and short bunch crossing separation ($50\,ns$ for year 2012) for pp collisions at the LHC promote multiple parton interactions (MPI) and event pile-up that, in addition to initial state radiation (ISR), contaminate the final state. Grooming algorithms [121,135,136] selectively remove portions of the jet supposedly associated to contamination or that are irrelevant or detrimental to resolve the product of the hard scattering (recent reviews and comparisons of these techniques, see for example refs. [133, 134, 139]). They are designed to retain the characteristic substructure within jets while reducing the impact of the fluctuations of the parton shower and the underlying event, thereby improving the mass resolution and mitigating the influence of pile-up. These features have only recently begun to be studied experimentally and have been exploited heavily in recent studies of the phenomenological implications of such tools in searches for new physics [33,121,151].

This section shows that the application of jet grooming can increase the robustness of non-standard large-R jets, reduce sensitivity to the intense environment of the high luminosity at the LHC, and improve the physics potential of searches for heavy boosted objects (most of these results form part of ref. [117]).

4.3.1 Jet grooming definitions

Two jet grooming procedures, trimming and pruning, are described and performance measurements related to each are defined. These procedures differ from others, like mass drop [121], in that they don't assume a specific hard substructure for the large-R jet, and may therefore improve the reconstruction of jets arising from the showering and fragmentation of ∼massles partons (light quarks and gluons) as well as from heavy particles.

Unless otherwise specified, the jets are reconstructed using the anti-k_t algorithm with $R = 1.0$, and the p_{T} reported for a groomed jet is that which is calculated after the grooming algorithm is applied to the original jet.

Trimming: The trimming algorithm [136] takes advantage of the fact that contamination from pile-up/MPI/ISR in the reconstructed jet is often much softer than the outgoing partons associated with the hard-scatter and their final-state radiation (FSR). The ratio of the p_{T} of the constituents to that of the jet is used as a selection criterion. Although there is some spatial overlap, removing the softer components from the final jet preferentially removes radiation from pile-up, MPI, and ISR while discarding only a small part of the hard-scatter decay products and FSR. Since the primary effect of pile-up in the detector is additional low-energy deposits in clusters of calorimeter cells, as opposed to additional energy being added to already existing clusters produced by particles originating from the hard scattering process, this allows a relatively simple jet energy offset correction for smaller radius jets ($R = 0.4,\ 0.6$) as a function of the number of primary reconstructed vertices [152].

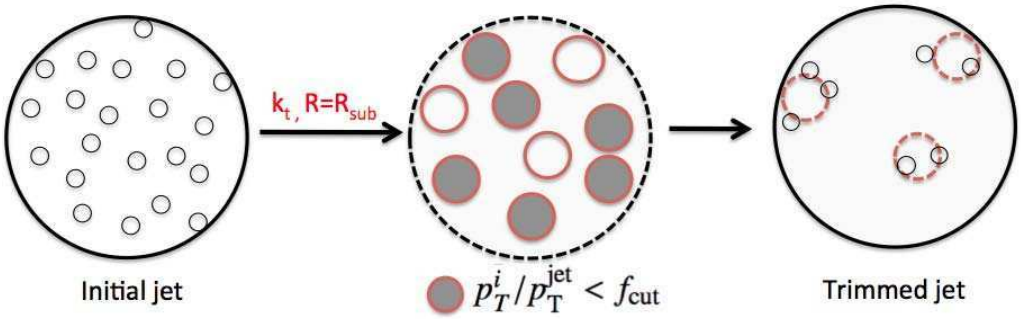

Figure 4.10: Diagram depicting the jet trimming procedure [117].

The trimming procedure uses a k_t algorithm to create subjets of size R_{sub} from the constituents of a jet. Any subjets with $p_{\mathrm{Ti}} < f_{\mathrm{cut}} \times p_{\mathrm{T}}^{\mathrm{jet}}$ are removed, where p_{Ti} is the transverse momentum of the i^{th} subjet, and f_{cut} is a parameter of the method, which is typically a few percent. The remaining constituents form the trimmed jet. This procedure is illustrated in figure 4.10. In this procedure, softness is therefore established via a cut on subjet p_{T} rather than for example restricting the number of subjets. Low-mass jets ($m_{\mathrm{jet}}^{R=1.0} < 100$ GeV) from a light-quark or gluon lose typically 30–50% of their mass in the trimming procedure, while jets containing the decay products of a boosted object lose less of their mass, with most of the reduction due to the removal of pile-up or UE (see, for example, figure 4.13). The fraction removed increases with the number of pp interactions in the event.

Pruning: The pruning algorithm [135, 153] is similar to trimming in that it removes constituents with a small relative p_{T}, but it additionally applies a veto on wide-angle radiation. The pruning procedure is invoked at each successive recombination step of the jet algorithm (either C/A or k_t). It is based on a decision at each step of the jet reconstruction whether or not to add the constituent being considered. As such, it does not require the reconstruction of subjets. For all plots shown here, the k_t algorithm is used for the pruning procedure. This results in definitions of the terms *wide-angle* or *soft* that are not directly related to the original jet but rather to the proto-jets formed in the process of rebuilding the pruned jet.

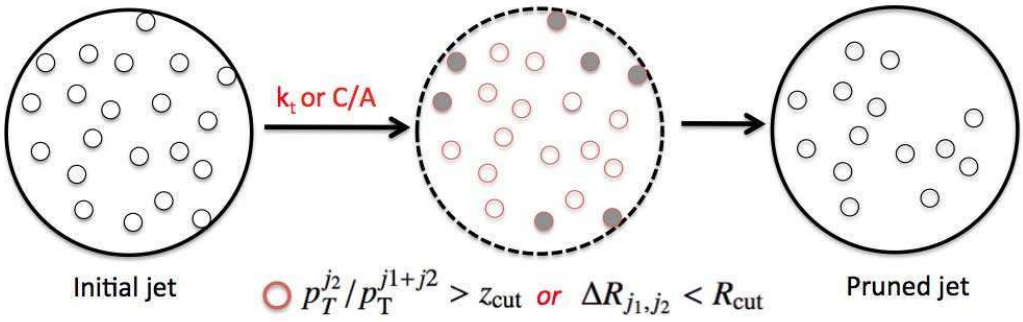

Figure 4.11: Diagram illustrating the pruning procedure [117].

The procedure is as follows:

- The C/A or k_t recombination jet algorithm is run on the constituents, which were found by any jet finding algorithm.
- At each recombination step of constituents j_1 and j_2 (where $p_{\mathrm{T}}^{j_1} > p_{\mathrm{T}}^{j_2}$), either $p_{\mathrm{T}}^{j_2}/p_{\mathrm{T}}^{j_1+j_2} > z_{\mathrm{cut}}$ or $\Delta R_{j_1,j_2} < R_{\mathrm{cut}} \times (2m^{\mathrm{jet}}/p_{\mathrm{T}}^{\mathrm{jet}})$ must be satisfied. Here, z_{cut} and R_{cut} are parameters of the algorithm which are studied in this paper.
- j_2 with j_1 are merged if one or both of the above criteria are met, otherwise, j_2 is discarded and the algorithm continues.

The pruning procedure is illustrated in figure 4.11.

4.3.2 Jet substructure and grooming in data and simulation

Comparisons between jets containing *signal-like* boosted objects and a light-quark or gluon jet background are presented. Boosted objects are divided into two categories depending on the event topology: *two-pronged*, such as hadronically decaying W or Z bosons, and *three-pronged*, such as the top quark decaying into a b-jet and a hadronically decaying W boson.

Previous studies conducted by ATLAS [140] and CMS [154] suggest that even complex jet-substructure observables are fairly well modelled by the MC simulations used by the LHC experiments.

Figure 4.12 presents a comparison of the jet invariant mass for ungroomed and trimmed jets in the range 600 GeV $\leq p_{\mathrm{T}}^{\mathrm{jet}} <$ 800 GeV and in the central calorimeter, $|\eta| < 0.8$. The description of both the ungroomed and trimmed anti-k_t jets with $R = 1.0$ provided by PYTHIA is poor for large masses. The descriptions provided by HERWIG++ as well as for the NLO generator POWHEG+PYTHIA are more accurate. PYTHIA tends to underestimate the fraction of high-mass large-R anti-k_t jets, whereas HERWIG++ and POWHEG+PYTHIA are accurate to within a few percent, even for very massive jets. The ungroomed anti-k_t, $R = 1.0$ jets are poorly described by all three MC simulations at

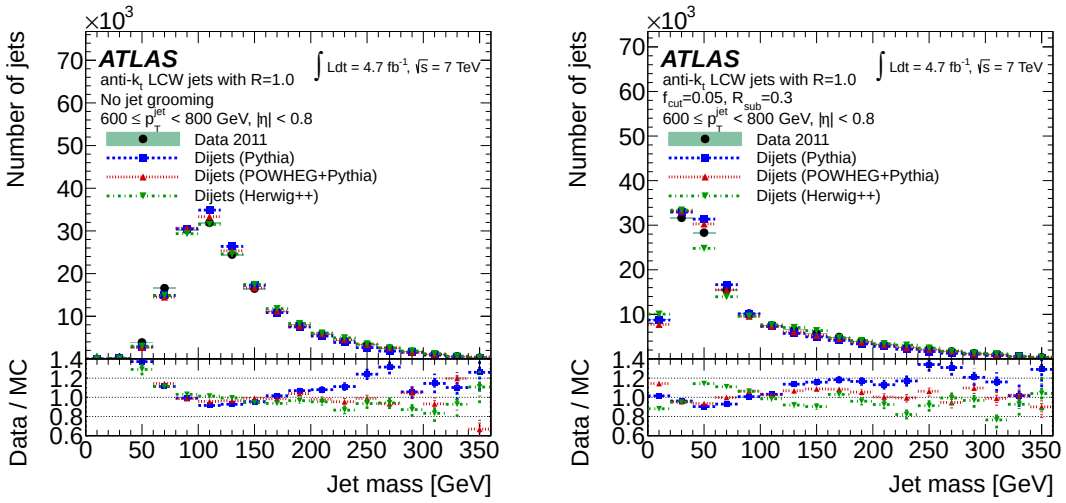

(a) anti-k_t, $R = 1.0$ (ungroomed)

(b) anti-k_t, $R = 1.0$ (trimmed)

Figure 4.12: Mass of jets in the range 600 GeV $\leq p_{\mathrm{T}}^{\mathrm{jet}} <$ 800 GeV and in the central calorimeter ($|\eta| < 0.8$). Shown are (a) ungroomed and (b) trimmed ($f_{\mathrm{cut}} = 0.05$, $R_{sub} = 0.3$) anti-k_t jets with $R = 1.0$. The ratios between data and MC distributions are shown in the lower section of each figure.

low mass; this could be due to non-perturbative and detector effects which increase the jet mass. This –generally soft– contribution is removed by grooming leaving hard components well described by simulation.

4.3.2.1 Jet mass resolution

Performance measurements are shown for simulated samples of $Z \to q\bar{q}$ (HERWIG+JIMMY), top quarks (from PYTHIA $Z' \to t\bar{t}$, $m_{Z'} = 1.6$ TeV) and dijet events (POWHEG+PYTHIA), as well as for data.

A groomed jet can be a powerful tool to discriminate between the often dominant multi-jet background and heavy-particle decays. Figure 4.13 demonstrates this by comparing the invariant mass distribution of the leading-p_{T} jet for jets in simulated signal and background events before and after the application trimming. Figures 4.13(a) and 4.13(b) show distributions for the two-pronged decay case ($Z \to q\bar{q}$) and for the three-pronged decay case (hadronically decaying top quarks from $Z' \to t\bar{t}$), respectively. In these figures, the ungroomed distributions are normalized to unit area, while the trimmed distributions have the efficiency with respect to the ungroomed large-R jets folded in for comparison. Prior to the application of grooming, no distinct features are present in the jet mass distribution between Z jets and QCD jets (figure 4.13(a)). The mass resolution of the simulated $Z \to q\bar{q}$ signal events dramatically improves after trimming. After trimming the mass peak corresponding to the Z boson is shifted to the correct mass. The small excess of signal events below 50 GeV is the result of one of the two quarks from the decay of the Z boson being

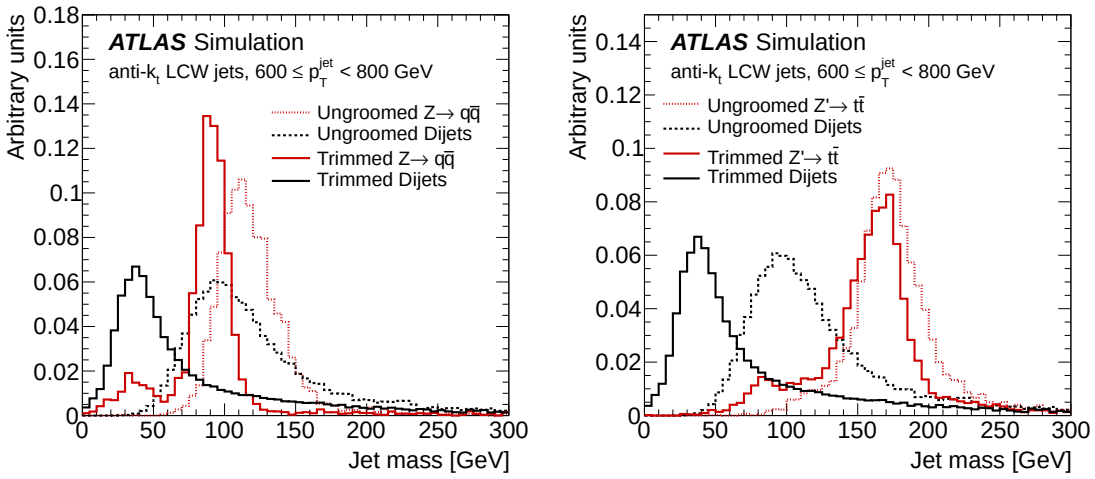

(a) $Z \to q\bar{q}$ vs. QCD (b) $Z' \to t\bar{t}$ vs. QCD

Figure 4.13: Leading-$p_{\mathrm{T}}^{\mathrm{jet}}$ jet mass for simulated $Z \to q\bar{q}$ signal events (a) and $Z' \to t\bar{t}$ ($m_{Z'} = 1.6$ TeV) signal events (b) is compared to dijet background events for jets in the range 600 GeV $\leq p_{\mathrm{T}}^{\mathrm{jet}} <$ 800 GeV. The dotted lines show the ungroomed jet distributions, whereas the solid lines show corresponding trimmed ($f_{\mathrm{cut}} = 0.05$ and $R_{sub} = 0.3$) jets. The groomed distributions are normalized with respect to the ungroomed distributions, which are themselves normalized to unity.

removed by the jet grooming, thus leaving only one quark reconstructed as the jet and making it indistinguishable from the background (see blue distribution in figure 4.19(a)). Note that the dijet background is pushed towards this mass range after trimming thus improving discrimination between signal and background.

The three-pronged hadronic top-jet mass distributions from $Z' \to t\bar{t}$ events are shown in figure 4.13(b), where the peak near the top-quark mass of approximately 175 GeV is relatively unshifted between trimmed and ungroomed jets. Again the mass resolution for the signal improves after grooming. A shoulder for the W-mass becomes discernible after trimming is applied. The enhancement of the W-mass peak is seen especially in jets with lower p_{T}, as the jet from the b-quark decay falls outside (splashes out) the radius of the large-R jet. Most important, the average separation between the mean jet mass for signal jets in the Z' sample and those in the dijet sample increases by nearly 60% after trimming, which increases signal sensitivity. These results are shown for jets containing highly boosted hadronically decaying Z bosons and top quarks in the range 600 $\leq p_{\mathrm{T}}^{\mathrm{jet}} <$ 800 GeV, but similar conclusions apply in all other p_{T} regions in the range $p_{\mathrm{T}}^{\mathrm{jet}} >$ 300 GeV, and $|\eta| < 2.1$.

The separation shown here is significant since the widths of the peaks of each of the distributions are also simultaneously narrowed by the grooming algorithm, as shown in figure 4.14. The fractional jet mass resolution is defined as the width of a Gaussian fit to the central part of the distribution that is generated by taking the difference between the

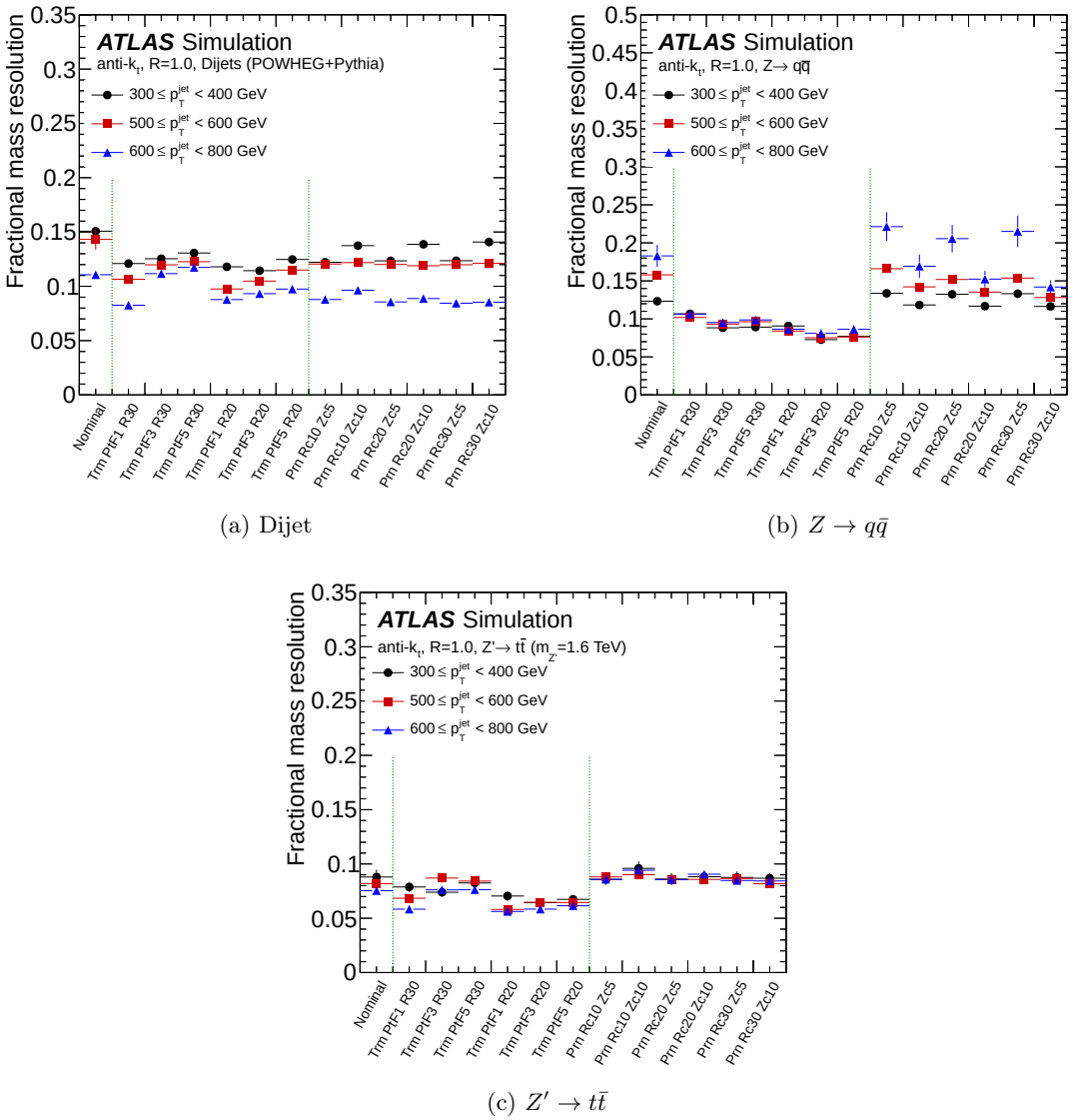

(a) Dijet

(b) $Z \to q\bar{q}$

(c) $Z' \to t\bar{t}$

Figure 4.14: (a) Fractional mass resolution comparing the various grooming algorithms for the leading-p_{T} jet in dijet simulated events. Here, *nominal* refers to jets before grooming is applied. Three ranges of the nominal jet $p_{\mathrm{T}}^{\mathrm{jet}}$ are shown. The uncertainty on the width of the Gaussian fit is indicated by the error bars. The abbreviations correspond to: Trm=trimming, Prn=pruned, PTF=f_{cut}, R=R_{sub}, Rc=R_{cut}, Zc=z_{cut}. (b) same as (a) for jet in $Z \to q\bar{q}$ simulated events. (c) same as (a) for jet in $Z' \to t\bar{t}$ ($m_{Z'} = 1.6$ TeV) simulated events.

generator-level jet mass and the reconstructed jet mass, divided by the same generator-level jet mass, $\sigma(m^{reco} - m^{truth})/\langle m^{truth} \rangle$. Figure 4.14 shows the fractional mass resolution for leading-p_{T} jets in the dijet, Z and Z' generated samples. In general, the groomed jets have better resolution than the ungroomed large-R jets, with improvements of up to ∼10% (absolute) in some cases. The trimmed and pruned jet resolution improves with increasing $p_{\mathrm{T}}^{\mathrm{jet}}$, where the calibrated jets gain $\sim 3-5\%$ over the range 300 GeV $\leq p_{\mathrm{T}}^{\mathrm{jet}} <$ 800 GeV. In the two-pronged 4.14(b) and three-pronged 4.14(b) configurations, the trimmed jets have

better fractional mass resolution ($\sim 5-10\%$) than the pruned jets. The pruning algorithm, especially with C/A jets, produces larger tails in the resolution distribution compared to the trimmed algorithm (not shown), worsening the overall fractional resolution in comparison.

4.3.2.2 Impact of pile-up on the jet mass scale and resolution

This section elaborates on the impact of pile-up on the jet mass, and the extent to which trimming and pruning are able to minimize these effects.

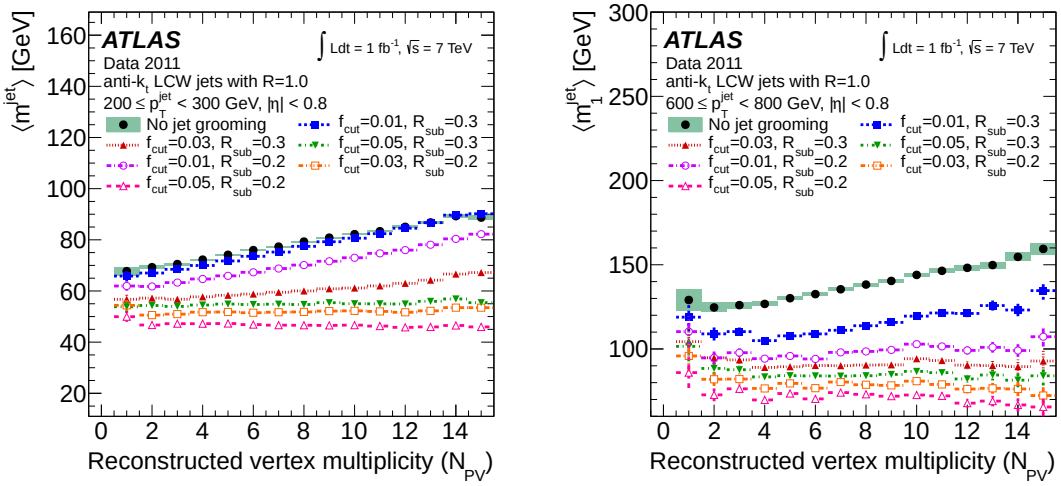

(a) Trimmed; 200 GeV $\leq p_{\mathrm{T}}^{\mathrm{jet}} <$ 300 GeV

(b) Trimmed; 600 GeV $\leq p_{\mathrm{T}}^{\mathrm{jet}} <$ 800 GeV

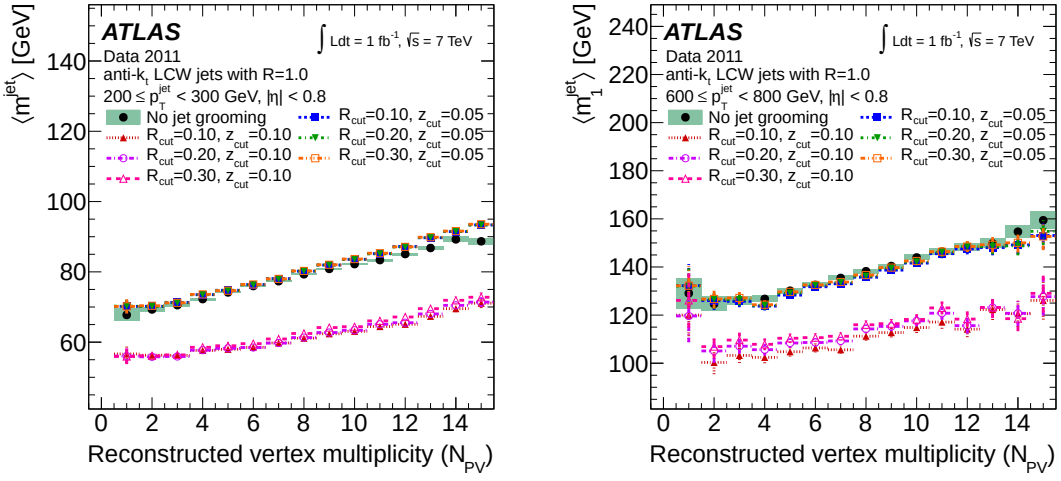

(c) Pruned; 200 GeV $\leq p_{\mathrm{T}}^{\mathrm{jet}} <$ 300 GeV

(d) Pruned; 600 GeV $\leq p_{\mathrm{T}}^{\mathrm{jet}} <$ 800 GeV

Figure 4.15: Evolution of the mean uncalibrated jet mass, $\langle m_{\mathrm{jet}}^{R=1.0} \rangle$, for jets in the central region $|\eta| < 0.8$ as a function of the reconstructed vertex multiplicity, N_{PV} for jets in the range 200 GeV $\leq p_{\mathrm{T}}^{\mathrm{jet}} <$ 300 GeV (left) and for leading-$p_{\mathrm{T}}^{\mathrm{jet}}$ jets ($\langle m_{\mathrm{jet}}^{R=1.0}{}_1 \rangle$) in the range 600 GeV $\leq p_{\mathrm{T}}^{\mathrm{jet}} <$ 800 GeV (right). (a)-(b) show trimmed anti-k_t jets with $R = 1.0$, (c)-(d) show pruned anti-k_t jets with $R = 1.0$. The error bars indicate the statistical uncertainty on the mean value in each bin.

The invariant mass of large-R jets is sensitive to the pile-up conditions. Figure 4.15 shows the dependence of the mean uncalibrated jet mass, $\langle m_{\text{jet}}^{R=1.0} \rangle$, on the number of reconstructed primary vertices, N_{PV}, for a variety of jet algorithms in the central region $|\eta| < 0.8$. N_{PV} is a measure of the MPI (section 2.1.2) and therefore an indication of the amount of additional activity that is deposited in the detector. This dependence is shown in two $p_{\text{T}}^{\text{jet}}$ ranges of interest for jets after trimming (figures 4.15(a)–4.15(b)) and pruning (figures 4.15(c)–4.15(d)). The lower range, 200 GeV $\leq p_{\text{T}}^{\text{jet}} <$ 300 GeV, represents the threshold for most hadronic boosted-object measurements and searches, whereas the range 600 GeV $\leq p_{\text{T}}^{\text{jet}} <$ 800 GeV is expected to contain top quarks for which the decay products are fully merged within an $R = 1.0$ jet nearly 100% of the time. In each figure, a large set of grooming algorithm parameter settings is included for comparison. Two values of the subjet radius, R_{sub}, are used for trimming, three R_{cut} factors for pruning are tested (using the k_t algorithm with the procedure in all cases). Trimming significantly reduces the rise with pile-up of $\langle m_{\text{jet}}^{R=1.0} \rangle$ seen for ungroomed jets, whereas pruning does not. For at least one of the configurations tested, trimming is able to essentially eliminate this dependence. The trimming configurations with large radius and largest fraction of removal $R_{sub} = 0.3, f_{\text{cut}} = 0.05$ exhibit good stability for both small and large $p_{\text{T}}^{\text{jet}}$.

The improvement of the jet mass resolution upon application of grooming is primarily due to the remotion of the jet mass sensitivity to N_{PV}. Beyond simply providing a pile-up-independent average jet mass as figure 4.15 demonstrates, trimming also renders the *full* jet mass spectrum insensitive to high instantaneous luminosity. Figure 4.16 demonstrates this by comparing the jet mass spectrum for leading-p_{T} ungroomed and trimmed anti-k_t jets for various values of N_{PV}. The inclusive jet sample obtained from data shows that a nearly identical trimmed $m_{\text{jet}}^{R=1.0}$ spectrum is obtained regardless of the original level of pile-up. The peak of the leading-p_{T} jet mass distribution for events with $N_{\text{PV}} \geq 12$ is shifted comparatively more due to trimming. Nonetheless, the resulting trimmed jet mass spectra exhibits no dependence on N_{PV}. The shape of this distribution for groomed jets is not merely a rigid shift of the ungroomed distribution, but includes an additional thinning. It is a combination of this shift plus narrowing that 'un-smear' the overall mass distribution and improve the resolution shown in figure 4.14.

In summary, the presence of pile-up represents a major experimental challenge as a decrease of the mass resolution may dramatically weaken sensitivity to new physics processes. With trimming, mass resolution and the signal discrimination can be enhanced, for a wide range of parameters, including large subjets ($R_{sub} = 0.3$) with 5% of the energy of the large-R jet. In addition, since the actual form of the spectrum is sensitive to the choice of the grooming parameters (see figure 38 in ref. [117]), so for any comparison between signal and background, the same configuration must be consistently applied for both.

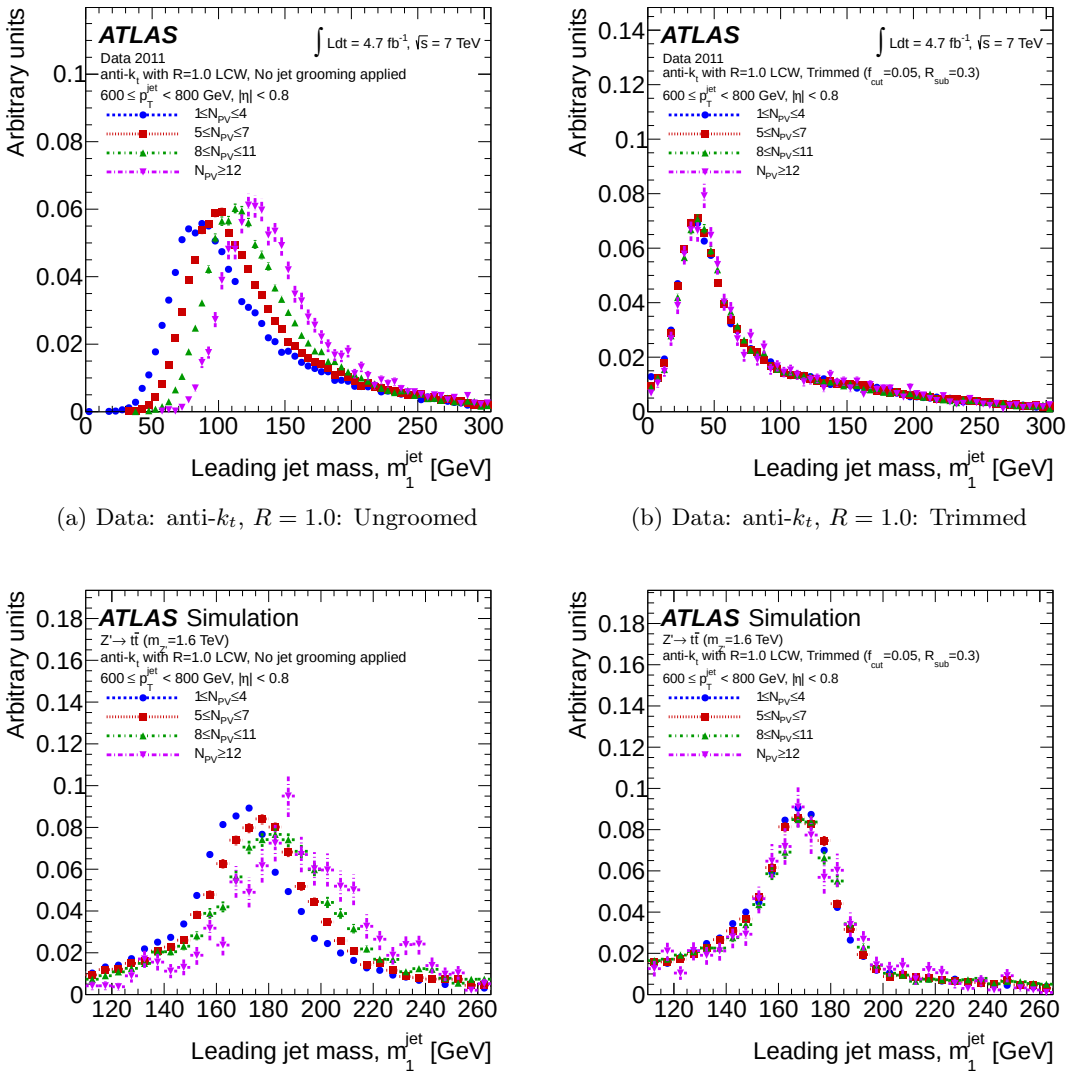

(a) Data: anti-k_t, $R = 1.0$: Ungroomed

(b) Data: anti-k_t, $R = 1.0$: Trimmed

(c) Z': anti-k_t, $R = 1.0$: Ungroomed

(d) Z': anti-k_t, $R = 1.0$: Trimmed

Figure 4.16: Jet mass spectra for four primary vertex multiplicity ranges for anti-k_t jets with $R = 1.0$ in the range 600 GeV $\leq p_{\mathrm{T}}^{\mathrm{jet}} <$ 800 GeV. Both untrimmed (left) and trimmed (right) anti-k_t jets are compared for the various N_{PV} ranges in data (top) and for a $Z' \to t\bar{t}$ Monte Carlo sample (bottom).

4.4 Composite Jets

In preceding sections, I have presented results of the performance of large-R jets with grooming. The general strategy of the multi-jet SUSY analysis motivated the usage of a slight variant of those definitions: the *composite* jets. Unlike standard large-R jets built from fine granularity constituents (calorimeter clusters or truth stable particles), composite jets are built using as components other jets reconstructed with a smaller R parameter. The reason for taking this approach in the analysis is because the topological clusters needed to build 'standard' large-R jets were not available in the SUSY dataset files centrally

produced by ATLAS. As will be shown here, this alternative approach performs equally well in relevant aspects such as the jet mass reconstruction and sensitiveness to pile-up.

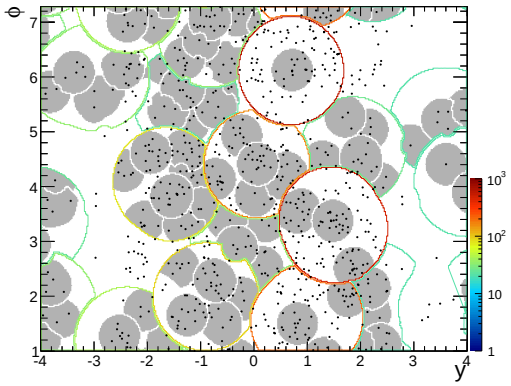

(a) Large-R jet, trimmed

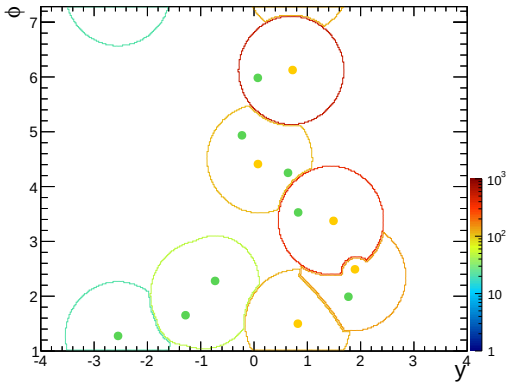

(b) Composite jet

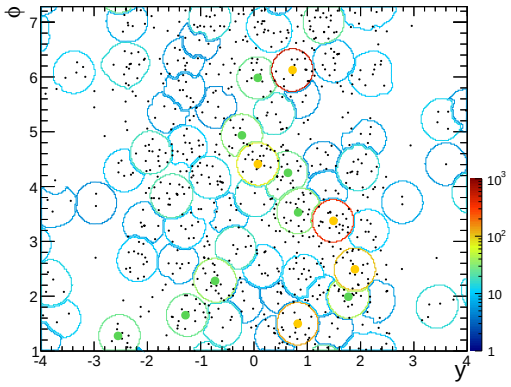

(c) Small-R jets

Figure 4.17: (a) Anti-k_t (R=1.0) jets are built from calorimeter topological clusters (black circles). Soft anti-k_t ($R_{sub} = 0.4$) subjets are removed using the trimming procedure (with $f_{\text{cut}} = 0.05$). Kept subjets are shown in light gray. (b) Composite anti-k_t (R=1.0) jets are built from small-R ($R = 0.4$) anti-k_t calorimeter jets. (c) The small-R jet are reconstructed from calorimeter clusters, and used to reconstruct composite jets if their $p_{\text{T}}^{R=0.4} \geq 20$ GeV. The axis of small-R jets is shown for clarity (green for $20 \leq p_{\text{T}}^{R=0.4} \leq 50$ GeV, and orange for $p_{\text{T}}^{R=0.4} \geq 50$ GeV). For illustrative purposes, large-R jets in (a) and (b) have a very low threshold $p_{\text{T}}^{R=1.0} \geq 20$ GeV. ATLAS simulation of a dijet event (Herwigg++). The p_{T} of the jets is codified by the vertical scale in GeV.

Figures 4.17 and 4.18 illustrate the comparison between trimmed large-R jets and composite jets. For these results small-R ($R = 0.4$) jets are selected by their transverse momentum ($p_{\text{T}}^{R=0.4}$ greater than 20–50 GeV) and their four-momenta are recombined using the anti-k_t algorithm with a large radius parameter ($R = 1.0$) to form the composite jets. The resemblance between these two classes is double. First, at the level of fat-jets, figures 4.17(a) and 4.17(b) show that both the location and the energy of the leading-p_{T} jets are similar among jet classes. Some differences exist though, as patches of the detector may have a reconstructed large-R jet that is not matched to any composite jet. This is expected since

composite jets are selected with two energy thresholds while large-R jets have just one. For example, the region $(y, \phi) \sim (-2, 4)$ in this event has diffuse energy that forms a large-R jet, but that is not concentrated within any small-R jet required to build the composite jet. Second, a similar correspondence applies when comparing the subjets of the large-R jet in figure 4.17(a) against the reconstructed small-R jets in figure 4.17(c). Clearly the hard elements of the event identified as energetic small-R jets show good correspondence to the subjets within the fatjets. Again, some differences may occur most notably for soft components that are below the $p_{\mathrm{T}}^{R=0.4}$ threshold of 20 GeV, or that not meet the trimming cut. This is the case for the fat jet at $(y, \phi) \sim (1, 6)$ that consists of two small-R jets in figure 4.17(b) while it is reconstructed as a one-prong jet according to figure 4.17(a) because the softer subjet is discarded by the 5% p_{T} cut of trimming.

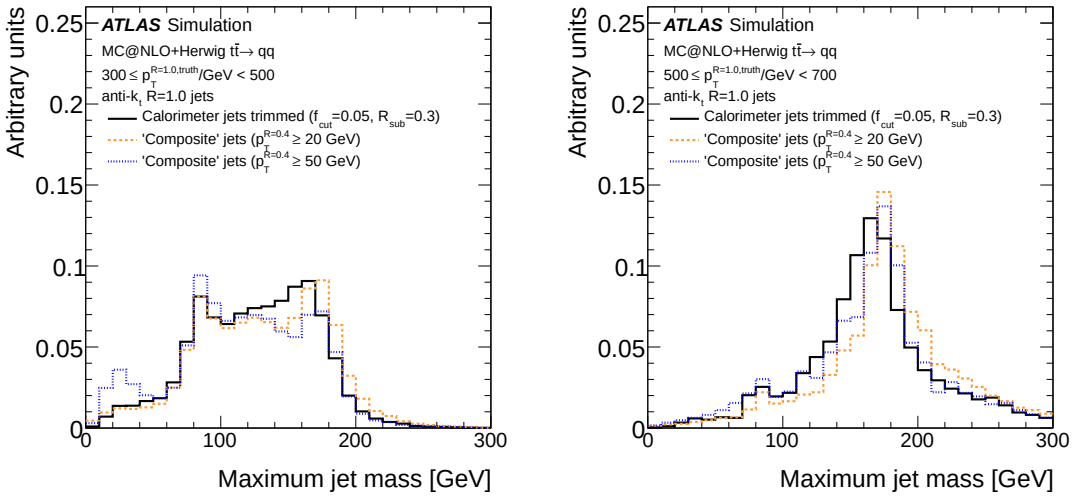

(a) $300 \leq {p_{\mathrm{T}}}^{R=1.0,truth}/\mathrm{GeV} \leq 500$ (b) $500 \leq {p_{\mathrm{T}}}^{R=1.0,truth}/\mathrm{GeV} \leq 700$

Figure 4.18: Performance of composite jets (formed by small-R jets with $p_{\mathrm{T}}^{R=0.4} \geq 20$ GeV) for different p_{T} thresholds for the small-R jets in simulated $t\bar{t}$ events. All distributions are normalized with respect to the trimmed distribution, which is itself normalized to 1. Bins of energy are defined at truth level jets to unfold biases associated to the energy reconstructed for different definitions.

Figure 4.18 shows the mass distribution of the most massive jet in hadronic $t\bar{t}$ events for composite and trimmed large-R jets. The effect of trimming is evident as it improves the mass resolution around the peaks of the top quark mass and the W mass (~ 80 GeV) for energies in the range 300–500 GeV (figure 4.18(a)). One determinant variable is the p_{T} of the $R = 0.4$ jets used to construct the composite large-R jets. For a low threshold of $p_{\mathrm{T}}^{R=0.4} \geq 20$ GeV composite jets reproduce the same peaks, with a slightly better mass resolution around the top quark mass. As the p_{T} of the $R = 0.4$ jets is increased up to $p_{\mathrm{T}}^{R=0.4} \geq 50$ GeV, the selection becomes more restrictive and less small-R jets are available to be clustered into the composite jets. Hence, the chance to fully reconstruct a top jet reduces with the p_{T} threshold, and simultaneously these partially reconstructed top jets

tend to populate the range around the mass of the W, suggesting that the 50 GeV energy cut is too aggressive. For more energetic jets in the range 500–700 GeV, all jet definitions have the same performance (figure 4.18(b)).

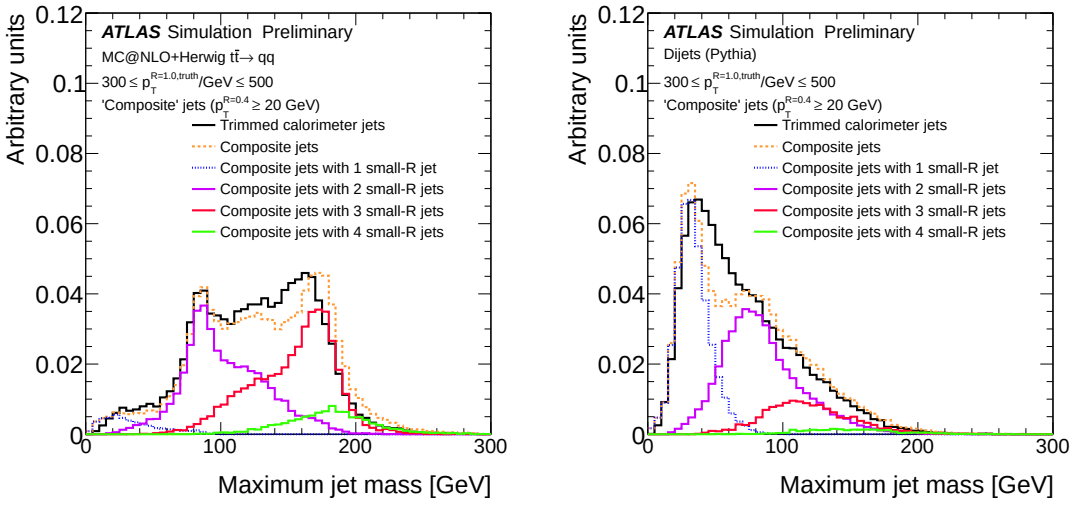

(a) full hadronic $t\bar{t}$ (b) dijet events

Figure 4.19: Substructure of composite jets. The mass spectrum of composite jets is split by the number of small-R jets that contain. All distributions are normalized with respect to the trimmed jet distribution, which is itself normalized to 1.

Also, for this high $p_{\mathrm{T}}^{R=0.4}$ threshold a third peak appears around $m_{R=1.0}$ ≈20–30 GeV which corresponds to mono-jets composed by a single $R = 0.4$ jet. This is demonstrated in figure 4.19. In general, composite jets with mass around 25 GeV are formed by one small-R jet, composite jets with masses around 80–90 GeV are predominantly formed by two $R = 0.4$ jets, and composite jets with masses around 150–200 GeV are dominantly constituted by three $R = 0.4$ jets. QCD jets tend to have smaller masses, although the tail is not negligible at the masses of the W boson and top quark due to the combinatoric effect of two and three constituents.

The bottom line of this chapter is that jets can be modified (from its very definition) according to the needs. To gain sensitivity of jet mass observables in the challenging high-pile-up LHC environment, complex jet algorithms with post processing provide a relative advantage over unprocessed jets. It is reasonable to accept that the jet substructure may be properly represented by any of these methods: **large-R jets+trimming** or **composite jets**. It is not the intention here to advocate in favor of one algorithm over the other, neither to perform an in-depth scrutiny of the similarities between these jets or for which cases their definitions differ. The performance of composite jets will be properly evaluated within the context of the physics analysis. In particular in the optimization of the signal regions section 5.5.

5
Analysis strategy

5.1 Motivation

In general terms, the final reach of a search for new particles relies on three main pillars. First, an intelligent definition of signal regions predominantly populated by the expected new particles and with low contamination from (background) Standard Model particles. Second, the size of uncertainties on the data measurements and simulated events. And finally the statistical treatment used to analyze those measurements. These matters are addressed in this and the next chapter.

In the context of R-parity-conserving supersymmetry (section 2.2.1), strongly interacting gluinos and squarks of the third generation (top-squark) could be pair-produced in the pp interactions at the LHC. Such particles are expected to decay in cascades that may include gluino decays to a stop and an anti-top quark,

$$\tilde{g} \;\rightarrow\; \tilde{t} + \bar{t} \tag{5.1a}$$

followed by the stop decay to a top quark and a neutralino LSP, $\tilde{\chi}_1^0$,

$$\tilde{t} \rightarrow t + \tilde{\chi}_1^0. \tag{5.1b}$$

Alternatively, if the top squark is heavier than the gluino, the three-body decay,

$$\tilde{g} \;\rightarrow\; t + \bar{t} + \tilde{\chi}_1^0 \tag{5.2}$$

may result[1]. A pair of cascade decays produces a large number of Standard Model particles, together with a pair of LSPs, one from the end of each cascade. The LSPs are assumed to be stable and only weakly interacting, and so escape undetected, resulting in missing transverse momentum.

Events are filtered at the trigger level and in the off-line selection requiring large jet multiplicities. With the large integrated luminosity collected during 2012 (L^{int}=20.3 fb^{-1}), it is possible to select final states with larger jet multiplicities than before [30–32]. Requiring a large jet multiplicity has the effect of increasing the sensitivity to models that predict

[1] Other possibilities include decays involving intermediate charginos, neutralinos, and/or squarks including bottom squarks.

many-body decays or sequential cascade decays of strongly interacting parent particles. Significant missing transverse momentum is also requested, to identify the signature of the weakly interacting LSP. The sensitivity of the search is further enhanced by analyzing the internal structure of jets. The structure of tracks associated to the jet are used to identify jets proceeding from (or containing) b-quarks (section 3.3.6). This provides better discrimination to signal models that predict either more or fewer number of b-jets than the Standard Model background. The calorimeter substructure of jets is used, by measuring the jet mass (section 4.2.2) of large-R ($R = 1.0$) composite jets which provide good mass resolution (section 4.4). An event variable formed by the sum of the masses of the composite jets gives additional discrimination in models with a large number of objects in the final state [33]. Events containing isolated, high transverse-momentum (p_{T}) electrons or muons are vetoed in order to reduce backgrounds involving leptonic W boson decays.

Searches of this type were confirmed to have good sensitivity to decays such as those in eqs. (5.1) and (5.2) [31], but they also provide sensitivity to any model resulting in final states with large jet multiplicity in association with missing transverse momentum. Such models include the pair production of gluinos, each of them decaying via

$$\tilde{g} \to \bar{q} + \tilde{q} \tag{5.3a}$$

followed by squark decay

$$\tilde{q} \to q' + \tilde{\chi}_1^{\pm} \to q' + W + \tilde{\chi}_1^0, \tag{5.3b}$$

or alternatively

$$\tilde{q} \to q' + \tilde{\chi}_1^{\pm} \to q' + W + \tilde{\chi}_2^0 \to q' + W + Z + \tilde{\chi}_1^0. \tag{5.3c}$$

Another possibility is the pair production of gluinos which decay as in eq. (5.1a) and the subsequent decay of the $\tilde{t}$-squark via

$$\tilde{t} \to b + \tilde{\chi}_1^{\pm},$$

or via the R-parity-violating decay

$$\tilde{t} \to \bar{b} + \bar{s}. \tag{5.4}$$

Several supersymmetric models are used to interpret the analysis results: simplified models that include decays such as those in eqs. (5.1)–(5.4), and an cMSSM model with parameters compatible with the observed Higgs boson mass at the LHC [1, 2].

This chapter describes the data (real and simulated) samples (section 5.2), object definitions (section 5.3), baseline event selection (section 5.4), and the subsequent event selection used to define the signal regions (together with the procedures for their optimization) (section 5.5). Finally, the statistical methods used to interpret the results are presented in section 5.7. The estimation of the dominant background processes and their uncertainties is deferred to chapter 6.

5.2 Data-set and Monte Carlo samples

5.2.1 Recorded data

The raw data sample used in this analysis was recorded by the ATLAS detector during the period from April to December 2012 with the LHC operating at a pp center-of-mass energy of $\sqrt{s} = 8$ TeV. Application of data-quality requirements (section 5.4.2) results in an integrated luminosity of $20.3 \pm 0.6\,\text{fb}^{-1}$. Over this period the peak instantaneous luminosity reach even higher values than during the previous years of data-taking (figure 3.2(a)) with up to $L = 7.7 \times 10^{33} cm^{-2} s^{-1}$ and the mean number of pp interactions per bunch crossing (μ) fluctuated between 5 and 40 (figure 3.3), which accounts for big variations of pile-up conditions.

5.2.2 Standard Model Monte Carlo

Monte Carlo simulations are used as part of the background determination and to assess the sensitivity to specific SUSY signal models during the optimization process and to set exclusion limits to particular signal models.

All Monte Carlo datasets were centrally produced by the ATLAS simulation framework [155] that considers the interaction of the generated shower of particles with a simulation of the detector using GEANT4 [156] or `AtlFast-II` [157]. These were produced with a pp $\sqrt{s} = 8$ TeV, and a variable number of pp interactions per bunch crossing to emulate different beam conditions and a realistic modeling of the pile-up conditions observed in the data. Monte Carlo events are reweighted to mimic the μ distribution of data as described in section 5.4.3.1. What follows is a description of the Monte Carlo generators used to simulate each of the different background processes, including the used cross section (all calculated for $\sqrt{s} = 8$ TeV).

Top pair production ($t\bar{t}$). Top pair events were generated using SHERPA-1.4.1 [158] with the CT10 [159] set of parton distribution functions (PDF), and up to four additional partons in the matrix element. Additional jets in these events are generated via parton showering. The choice for using a LO simulation is that this multi-leg generator is more accurate at modelling states with many jets than generators that rely entirely on parton shower to provide the additional jets. To account for higher-order terms which are not present in the SHERPA Monte Carlo simulation, the fraction of events initiated by gluon fusion, relative to other processes, is modified to improve the agreement with data in $t\bar{t}$-enriched validation regions as described in section 5.4.3.2. These samples can have up to nine jets in the matrix element (ME) if one of the W bosons decay to a hadronic τ. The $t\bar{t}$ cross section for pp collisions at $\sqrt{s} = 8$ TeV is $\sigma_{t\bar{t}} = 252.89^{+15.30}_{-16.12}$ pb, calculated at NNLO in QCD perturbative expansion including resummation of next-to-next-to-leading logarithmic (NNLL) soft gluon terms for a top quark mass of 172.5 GeV [160, 161]

Vector boson production in association with jets. Samples of $W + jets$ and $Z + jets$ were also generated using SHERPA, with up five additional partons in the matrix element, except for processes involving massive b-quarks for which up to four additional partons are included. Dedicated $W + jets$ samples with at least three (up to five), and at least four (up to five) additional partons were incorporated to increase the statistical power of these processes in the high multiplicity sector. Similarly, two samples were generated for $Z + jets$ processes: an inclusive sample with up to five additional partons, and a second sample filtered with only four and five additional partons. The $W + jets$ and $Z + jets$ backgrounds are normalised according to their inclusive theoretical cross sections [162, 163]. The cross-section times branching ratio at NNLO accuracy for these processes is $\sigma_{W\to\ell\nu} = 12185.6$ pb and $\sigma_{Z\to\ell^+\ell^-} = 1207.9$ pb per channel, and $\sigma_{Z\to\nu\nu} = 6521.4$ pb.

Single top production. Single top quark production in association with a W boson and trough the s-channel were generated using MC@NLO-4.06 [164–167] interfaced to HERWIG-6.520.2 [168] for fragmentation and hadronization and to JIMMY-4.31 [169] for the underlying event. Single top produced by the t-channel are simulated with AcerMC-3.8 [170] using the CTEQ6L1 [171] PDF set, and interfaced to PYTHIA-6.426 [172] for fragmentation and hadronization. The cross-section for the different channels calculated at NLO +NNLL are $\sigma_s = 5.61\pm0.22$ pb [173], $\sigma_t = 87.76^{+3.44}_{-1.91}$ pb [174], and $\sigma_{Wt} = 22.37\pm1.52$ pb [175].

Top pair production in association with vector bosons ($t\bar{t} + V$). Production of $t\bar{t}$ in association with a W or Z boson is simulated with MadGraph-5.1.4.8 [176] using the LO CTEQ6L1 PDF set, interfaced to PYTHIA-6.426. Although the cross sections are known to NLO [177, 178], the MC generation is performed at LO; the cross-section for the simulated processes are: $\sigma_{t\bar{t}W} = 0.199$ pb, $\sigma_{t\bar{t}Z} = 0.1528$ pb, both having a 22% symmetrical uncertainty [178].

Minor backgrounds. Di-boson production ($WW/ZZ/WZ$) [179] were simulated with SHERPA-1.4.1 using the CT10 PDF set. A sample of $t\bar{t}$ +Higgs was simulated with PYTHIA8 [180] using the CTEQ6L1 PDF set, assuming a Standard Model Higgs boson with mass at 125 GeV. The cross-section, calculated at NLO QCD perturbative expansion, is 0.1302 pb, and the branching ratio of Higgs to b-quarks is 0.577, according to the CERN Yellow Report [181].

5.2.3 Signal Models

Supersymmetric production processes are generated using HERWIG++ version 2.5.2 [182] and MadGraph-5.1.4.8 with the CTEQ6L1 PDF set. The cross sections are calculated to next-to-leading order in the strong coupling constant α_S, including the resummation of soft gluon emission at next-to-leading-logarithmic accuracy (NLO+NLL) [183–187].

For each process, the nominal cross section and its uncertainty are taken from an envelope of cross-section predictions using different PDF sets and factorisation and renormalisation scales, as described in ref. [188].

5.3 Definition of primary physics objects

Particle candidates are used in the event selection and to define all the different analysis regions. These are represented by objects reconstructed from calorimetric and tracking measurements as described in section 3.3. The specific selection used for this analysis is presented next.

Baseline jets are reconstructed using the anti-k_t jet algorithm [114] with four-momentum recombination and radius parameter $R = 0.4$ in $y - \phi$ (section 4.1) from LCW calorimeter clusters (section 3.3.4.1). These are calibrated and the contribution from pile-up is removed with a correction dependent on the jet area, as described in section 3.3.4.2. All jets passing a loose selection (see 'Non collision contributions to fake jets' in section 5.4) are considered when applying the object identification. Two jet acceptance cuts are required: $p_{\mathrm{T}} > 20$ GeV and $|\eta| < 2.8$. Higher p_{T} cuts are required for jets entering the final signal selection.

Large-R composite jets (section 4.4) are constructed reclustering anti-k_t ($R = 0.4$) jets into $R = 1.0$ anti-k_t jets using the FastJet v3.0.2 software [189]. As described in section 4.4, this approach was forced by the lack of appropriate data samples with which build large-R jets directly from calorimeter clusters (as its done for $R = 0.4$ jets). The inputs to the clustering algorithm are those $R = 0.4$ jets that have both $p_{\mathrm{T}} > 20$ GeV and $|\eta| < 2.8$, after all object and event cleaning and overlap removal (described later in this section). These small-R jets were chosen for several reasons. They show low sensitivity to pile-up conditions (figure 5.7). With these choice the resulting composite jets so formed have very nice properties like good resolution of the mass spectrum for different samples (figure 4.18), and provide good discrimination of signal events against background (figure 5.5). Those large-R jets which have $p_{\mathrm{T}} > 100$ GeV and $|\eta| < 1.5$ are used in the calculation of the selection variable M_{J}^{Σ} as it is further described in section 5.5.3.

Electrons. Two definitions for electrons are used in the analysis, as are summarized in table 3.2. *Baseline* electrons which is the definition used for electron veto 5.4.2. These electron candidates are also considered when resolving overlapping objects (see below). *Signal* electrons, that have additional criteria on the shower shape in the calorimeter and additional isolation criteria, are used for 'leptonic' control regions. Both are selected with $|\eta| < 2.47$. Baseline electrons must have $p_{\mathrm{T}} > 10$ GeV, and signal electrons must be harder, having $p_{\mathrm{T}} > 25$ GeV.

Muons. Similarly, there are two definitions of muons used in the analysis as described in section 3.3.3. *Baseline* muons are used in muon veto while *Signal* muons which satisfy

additional isolation and tracking requirements are used to create the 'leptonic' validation and control regions. Muons are reconstructed by the STACO algorithm which performs a combination of tracks reconstructed in the Muon Spectrometer with tracks measured in the Inner Detector. These muon candidates must fulfill a list of quality requirements as summarized in table 3.3. Furthermore, in Monte Carlo samples a smearing procedure must be applied to the muon p_{T} to mimic the resolution in data. The acceptance cuts of $p_{\mathrm{T}} > 10$ GeV and $|\eta| < 2.4$ are applied for the baseline muons; signal muons are harder with $p_{\mathrm{T}} > 25$ GeV.

Resolving overlapping objects Jet, electron and muon candidates passing their respective selection can overlap with each other, since algorithms that identify these objects are run in parallel independently. A classification is required to remove all but one of the overlapping objects. Rules to remove the overlap are based on simple cuts in the distance (in the η–ϕ plane, equation 3.5) between objects following this order:

1. If an electron and a jet are found within $\Delta R < 0.2$, the object is interpreted as an electron and the overlapping 'jet' is ignored.
2. If a muon and a jet are found within $\Delta R < 0.4$, the object is treated as a jet and the 'muon' is ignored, i.e. it is assumed that proceeds from the parton shower within the jet.
3. If an electron and a jet are found within $0.2 \leq \Delta R < 0.4$, the object is interpreted as a jet and the nearby 'electron' is ignored.

Except stated otherwise, overlap removal is done *before* all cleaning and selection cuts described in section 5.4.2, such that they be applied to the right object.

Heavy flavour tagging. Jets with heavy-flavour content are identified using the MV1 tagging algorithm that uses both impact parameter and secondary vertex information, as described in section 3.3.6. This b-tagging algorithm is applied to all jets that satisfy both $|\eta| < 2.5$ and $p_{\mathrm{T}} > 40$ GeV. The parameters of the algorithm are chosen such that 70% of b-jets are tagged and about 1% of light-flavour or gluon jets are mistagged in $t\bar{t}$ events in Monte Carlo simulations. Jets initiated by charm quarks are (mis)tagged as b-jets with about 16% efficiency [99].

Missing transverse momentum. As described in section 3.3.5, the $E_{\mathrm{T}}^{\mathrm{miss}}$ is computed as the p_{T} imbalance of the event. It uses the momentum of muons and of topological clusters/tracks associated to jets, electrons and photons, and the remaining clusters not belonging to such objects are included in the CellOut term (see equation 3.7).

5.4 Off-line event selection

5.4.1 Trigger

The off-line[1] event selection is designed to deliver good efficiency for all signal regions, starting from the choice of the triggers that the event had to satisfied in the on-line selection. The large jet multiplicity expected for SUSY phenomenology can be exploited at the trigger level by making an on-line selection based on multiple jets. The lowest threshold high-multiplicity jet triggers that remained un-prescaled (see section 3.2.7) throughout the data-taking period [190] were used to preselect multi-jet events in both data and simulation. These are named EF_5j55_a4tchad_L2FS and EF_6j45_a4tclcw_L2FS_5L2j15, were the compound name reflects the trigger signature. The final level of the trigger selection (EF for EventFilter) required either at least five jets[2] with $E_{\mathrm{T}} > 55$ GeV or at least six jets with $E_{\mathrm{T}} > 45$ GeV, where the jets must have $|\eta| < 3.2$. Pre-scaled multi-jet triggers `EF_5j45_a4tclcw_L2FS` and `EF_4j65_a4tchad_L2FS`, requiring lower jet multiplicities were used to estimate the multi-jet background. The integrated luminosity for these (after removal of events with low quality) is shown in table 5.1. Unprescaled single lepton triggers, `EF_e24vhi_medium1` and `EF_mu24i_tight`, requiring a well reconstructed isolated electron or muon with $E_{\mathrm{T}} > 24$ GeV were used in control regions to study non-multi-jet backgrounds.

Trigger	**Luminosity**
Signal regions	
EF_6j45_a4tclcw_L2FS_5L2j15	$20.3 \pm 0.6\,\mathrm{fb}^{-1}$
EF_5j55_a4tchad_L2FS	$20.3 \pm 0.6\,\mathrm{fb}^{-1}$
Control regions (multi-jet background)	
`EF_5j45_a4tclcw_L2FS`	$1.36\ \mathrm{fb}^{-1}$
`EF_4j65_a4tchad_L2FS`	$1.20\ \mathrm{fb}^{-1}$
Control regions (non multi-jet background)	
`EF_e24vhi_medium1`	$20.3 \pm 0.6\,\mathrm{fb}^{-1}$
`EF_mu24i_tight`	$20.3 \pm 0.6\,\mathrm{fb}^{-1}$

Table 5.1: The integrated luminosity (after removal of events with low quality) collected for the different triggers used in the analysis.

Due to trigger inefficiencies the probability that the trigger identifies n jets grows for samples containing more than n jets. The requirement of an off-line jet multiplicity at least larger in one than that used in the trigger is sufficient to achieve a large trigger

[1] Here, the term 'off-line' is used as a reference for any processing/cut/identification/etc. that is done to data saved on disk, in opposition to 'on-line' that corresponds to data that is being acquired.
[2] As in the off-line jet reconstruction, these 'on-line' jets are reconstructed from calorimeter cells combined into topological clusters (tc) and subsequently clustered using the anti-k_t jet algorithm with a cone size of 0.4 (a4). Calorimeter clusters are calibrated at the local cluster weighting (lcw) scale also referred to as hadronic scale (had).

efficiency. The cumulative trigger efficiency

$$\epsilon(p_{\mathrm{T}}^{i}|\mathrm{EF}) = \frac{\int_{0}^{p_{\mathrm{T}}^{\mathrm{i}}} dp_{\mathrm{T}}\, N(p_{\mathrm{T}} \text{ of i}^{th} \text{ jet}|\mathrm{EF})}{\int_{0}^{p_{\mathrm{T}}^{\mathrm{i}}} dp_{\mathrm{T}}\, N(p_{\mathrm{T}} \text{ of i}^{th} \text{ jet}|\mathrm{EF}_{\mathrm{ref}})} \tag{5.5}$$

where the numerator is the number of events selected by the trigger (EF) with the additional off-line condition that the i^{th} jet has $p_{\mathrm{T}} \geq p_{\mathrm{T}}^{i}$. The denominator is measured using a reference trigger, EF_{ref}, with lower energy threshold and/or lower requirement on jet multiplicity, such that is fully efficient for the signal trigger selection.

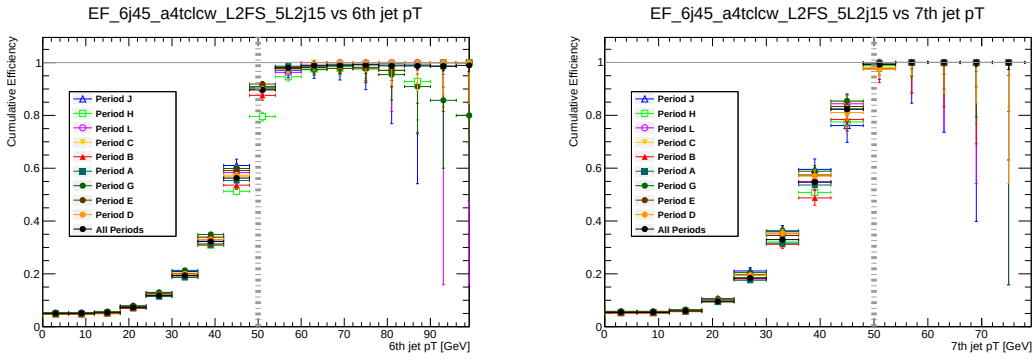

(a) Cumulative efficiency vs. 6^{th} jet p_{T} (b) Cumulaive efficiency vs. 7^{th} jet p_{T}

Figure 5.1: Comparison of trigger turn-on cumulative efficiency for all data periods (A-L) for `EF_6j45_a4tchad_L2FS_5L2j15`, using `EF_4j45_a4tchad_L2FS` as reference selection. Cumulative efficiency shown as functions of the calibrated p_{T} of the (a) 6^{th} and (b) 7^{th} jet.

In figure 5.1, these efficiencies are shown as a function of the calibrated jet p_{T} for the six jet trigger. The trigger efficiency remained stable along different data-taking periods and agree with the combined full-year behaviour. The EF_6j45_a4tclcw_L2FS_5L2j15 trigger selection reaches a $\sim 90\%$ of the plateau value if the 6^{th} jet is required to have ~ 50 GeV and is $> 98\%$ if the 7^{th} has ~ 50 GeV. The cumulative efficiency of multi-jet triggers for different off-line selections is shown in table 5.2.

Signal region trigger	off-line selection	Efficiency
EF_6j45_a4tclcw_L2FS_5L2j15	**6j50**: 6 or more jets with $p_{\mathrm{T}} > 50$ GeV	>90%
	7j50: 7 or more jets with $p_{\mathrm{T}} > 50$ GeV	>98%
	8j50: 8 or more jets with $p_{\mathrm{T}} > 50$ GeV	100%
EF_5j55_a4tchad_L2FS	**5j80**: 5 or more jets with $p_{\mathrm{T}} > 80$ GeV	>97%
	6j80: 6 or more jets with $p_{\mathrm{T}} > 80$ GeV	100%

Table 5.2: Summary of trigger cumulative efficiencies for the two signal triggers. Off-line regions with more jets than shown here are 100% efficient. The '5j80' and '6j50' selections are used in control regions, and the '6j80' and '7j50' selections are used in confirmation regions.

After off-line selection the resulting trigger efficiency is greater than 99% for all (high multi-

plicity) signal regions. Residual inefficiencies in control regions are evaluated as systematic uncertainties, as described in section 6.5.1.

5.4.2 Event cleaning

Before being used for the search, triggered events are subsequently filtered following a series of additional cuts, described here. Unless stated otherwise, all cuts are applied to events from both data and Monte Carlo simulations.

Data quality (data only). Data taking in ATLAS is very dynamic due to changes of the beam state, (sub-)detector(-s) or satellite infrastructure (e.g. trigger farms or data storage hardware). This dynamism requires frequent on-line adjustments of the experiment configuration, as for example an increase of the instantaneous luminosity may force to modify trigger pre-scales to prevent the loss of data. In order to group measurements taken under similar (beam and detector) conditions, data recording is segmented into luminosity blocks (LB) of about two minutes and a nearly constant luminosity. Data quality flags –defined to assess the beam stability, state of each sub-detector, noisy channels, trigger system and performance of object reconstruction– are stored for each LB and collected into a `GoodRunsList` (GRL) [191]. This analysis only considers events satisfying the GRL defined by the Data Quality team[1], that takes into account data-quality criteria for the inner detector, calorimeter and muon spectrometer, as well as the reconstructed objects.

Not all failures of the detector are so severe or longstanding that entire luminosity blocks must be vetoed with the `GoodRunsList`. Some additional defects are removed either from data only or both data and Monte Carlo on an event-level basis.

LAr and tile error veto (data only). Global noise bursts appear and disappear in the LAr calorimeter on a time scale smaller than a luminosity block. Events taken during improper function of the LAr and Tile calorimeters are rejected. The luminosities in Table 5.1 have been corrected for the small inefficiencies caused by this cut.

Corrupted tile data veto (data only). The Tile Calorimeter has suffered from frequent module trips since the $\sqrt{s} = 7$ TeV running began. These trips are considered a tolerable DQ defect as the energy in an unpowered module is extrapolated from its neighbors during off-line reconstruction [192, 193]. Unrelated to these tile trips, data corruption in a specific Tile channel was not always masked (due to non-optimal thresholds in the rejection algorithm), resulting in 400 GeV energy at (η=-0.15, ϕ=2.3), and therefore fake $E_{\mathrm{T}}^{\mathrm{miss}}$. Corrupted events are rejected on a LB-basis.

Incomplete data events (data only). In 2012 data-taking the TTC (Timing, Trigger and Control system) restart procedure was developed to recover certain detector busy

[1] For $20.3 \pm 0.6\,\mathrm{fb}^{-1}$, the following good run list was used: data12_8TeV.periodAllYear_DetStatus-v58-pro14-01_DQDefects-00-00-33_PHYS_StandardGRL_All_Good.xml.

conditions without the need for a full run-restart. LBs immediately after a TTC restart may contain incomplete data (where some detector information is missing from the event) and are rejected in and event-basis [194]. No luminosity correction following the veto is needed as the impact on the total number of events is small.

Non collision contributions to fake jets. Some jets measured with the calorimeter may not be produced by proton–proton collisions. These 'fake jets' arise from various sources like 'beam-gas' events (where one proton of the beam collided with the residual gas within the beam pipe), 'beam-halo' events (caused by interactions in the tertiary collimators in the beam-line far away from the ATLAS detector), cosmic ray muons overlapping in-time with collision events, and electronic noise of the calorimeter [195]. Most of the noise is identified and masked shortly after the data taking, yet a small fraction of calorimeter noise remains undetected and needs to be rejected by additional criteria. A very loose set of cleaning cuts (`Looser` in [196]) is applied to reduce the contribution from non-collision sources while retaining large efficiency. Variables used to veto fake jets are defined in table 5.3.

Fake jets induced by sporadic noise bursts in the liquid argon hadronic endcap calorimeter (HEC) have a large fraction of energy in the HEC (f_{hec}) and bad quality pulse shapes, $\langle Q \rangle$. These are identified by requiring: ($f_{hec} > 0.5$ `AND` $|f_Q^{hec}| > 0.5$ `AND` $\langle Q \rangle > 0.8$) `OR` ($|E_{neg}| > 60$ GeV); where cells with negative energy arise due to capacitive couplings between channels. Fake jets produced from coherent noise in the EM calorimeter have a large EM energy fraction and poor pulse shape quality: ($f_{em} > 0.95$ `AND` $|f_Q^{LAr}| > 0.8$ `AND` $\langle Q \rangle > 0.8$ `AND` $|\eta^{jet}| < 2.8$). Most real jets have a characteristic shower development and length, contain charged hadrons which are reconstructed in the tracking system and are produced in time with the beam collision. Fake jets are flagged as originating from cosmic rays or beam-induced background it satisfies any of the following criteria: ($f_{em} < 0.05$ `AND` $|\eta^{jet}| \geq 2$) `OR` ($f_{em} < 0.05$ `AND` $f_{ch} < 0.05$ `AND` $|\eta^{jet}| < 2$) `OR` ($f_{max} > 0.99$ `AND` $|\eta^{jet}| < 2$).

These cleaning criteria are applied to jets with $p_{\mathrm{T}}^{\mathrm{jet}} > 20$ GeV (calibrated) in any pseudo-rapidity (unless it is specified) *after* overlap removal in both data and MC. Events with at least one fake jet candidate are discarded for the analysis. In addition to this veto of fake jets, two additional requirements are applied to select good quality jets: the charge fraction of the leading two jets and a time cut, as described next.

Charge fraction of the leading two jets. In this analysis a jet 'charge fraction' cut is applied to only the two leading jets, rather than all identified jets. Provided that they have $p_{\mathrm{T}}^{\mathrm{jet}} > 100$ GeV and $|\eta^{jet}| < 2.0$ the two leading jets are required to have $f_{ch} > 0.02$ `OR` ($f_{ch} \geq 0.05$ `AND` $f_{em} > 0.9$), otherwise the event is rejected. This cut is very effective at rejecting events where the leading jets have not been generated by a hard interaction. Cutting on the charge fraction removes jets from non-collision events; the probability of having non-collision backgrounds in events with more than four jets is found to be negligible [197].

Energy weighted mean timing cut. This cut imposes time congruence among the leading jets of the event. If an event contains exactly 2, 3 or ≥ 4 jets with $p_{\mathrm{T}}^{\mathrm{jet}} > 40$ GeV

Variable	Description
f_{em}	Ratio of jet energy deposited in the EM calorimeter to the total jet energy.
f_{hec}	Ratio of jet energy deposited in the HEC calorimeter to the total jet energy.
f_{max}	Maximum energy fraction in any single calorimeter layer.
$\langle Q \rangle$	Jet pulse quality calculated as the mean quadratic difference between the pulses measured in the LAr calorimeter cells forming the jet and a pulse shape predicted for ionising signals. Is normalized such $0 < \langle Q \rangle < 1$.
f_Q^{LAr}	Fraction of energy in LAr calorimeter cells with poor signal shape quality.
f_Q^{hec}	Fraction of energy in HEC calorimeter cells with poor signal shape quality.
E_{neg}	Apparent negative energy of the cells contained in a jet.
f_{ch}	Charge fraction, is the ratio of the sum of the transverse momenta of tracks associated to a jet and originating at the primary vertex, to the jet calorimetric transverse momentum $\sum_{trk} \lvert p_{\mathrm{T}}^{trk} \rvert / p_{\mathrm{T}}^{\mathrm{jet}}$.
t^{jet}	Jet timing is energy-squared-weighted time of cells within a jet. Cell time is measured with respect to the time of the event recorded by the trigger.

Table 5.3: Calorimetric magnitudes used to reject fake jets. Calculation of these variables is done using the high-granularity information of calorimeter cells associated to the jet being evaluated.

and $|\eta| < 2.8$ then compute the energy weighted mean time with the leading 2, 3 or 4 jets respectively: $t = \sum E^{\mathrm{jet}} t^{jet} / \sum E^{\mathrm{jet}}$. Events are rejected if $|t| > 5$ ns.

Tile hotspot (data only). A *hot* Tile calorimeter cell affecting several runs in the beginning of 2012 (involving 0.27 fb^{-1}of data from periods B1 and B2) had not been masked in the reconstruction and has not been fixed in the reprocessing of data. Events from these runs are vetoed if any jet (after overlap removal) with $p_{\mathrm{T}}^{\mathrm{jet}} > 20$ GeV points to the hot cell ($-0.2 < \eta^{jet} < -0.1$ and $2.65 < \eta^{jet} < 2.75$) and deposited more than 60% of its energy in the affected layer of this sampling calorimeter.

Smart LAr hole veto. The presence of dead areas in the LAr affects the jet reconstruction, jet energy response and resolution and is a source of fake $E_{\mathrm{T}}^{\mathrm{miss}}$. This cut is used to reject events when a large amount of the $E_{\mathrm{T}}^{\mathrm{miss}}$ originates from jets pointing to these 'holes' by estimating the energy lost in these regions [198, 199] on an event by event basis. A simple veto of events having at least one jet pointing to the 'hole' would have a large impact in the signal acceptance given the large jet multiplicity involved [200]. The principle is to veto events containing any jet with (calibrated) $p_{\mathrm{T}}^{\mathrm{jet}} > 20$ GeV pointing to the direction of the $\vec{E}_{\mathrm{T}}^{\mathrm{miss}}$. The difference of energy of a jet due to energy lost in dead cells is calculated with:

$$E_{\mathrm{T}}^{\mathrm{miss}}(jet) = p_{\mathrm{T}}^{\mathrm{jet}} \times \frac{1 - B_{cell}}{1 - B_{jet}} - p_{\mathrm{T}}^{\mathrm{jet}} \times (1 - B_{cell}) \tag{5.6}$$

where B_{cell} is the fraction of energy deposited in *bad* channels as inferred from the average energy of neighboring cells, and B_{jet} is an independent estimation based on the shape of the energy deposits around the jet center[1]. The event is rejected if the contribution of any

[1] Calibrated jets are corrected with B_{cell} by default in the reconstruction, and therefore the factor $(1-B_{cell})$ reverts jet energy to its uncorrected value.

mismeasured jet to the $\vec{E}_{\mathrm{T}}^{\mathrm{miss}}$,

$$\Delta E_{\mathrm{T}}^{\mathrm{miss}} = E_{\mathrm{T}}^{\mathrm{miss}}(jet) \times \cos\left(\phi^{jet} - \phi^{\vec{E}_{\mathrm{T}}^{\mathrm{miss}}}\right), \tag{5.7}$$

is larger than 10 GeV, or if it represents more than 10% of the overall $E_{\mathrm{T}}^{\mathrm{miss}}$. This veto is the same as in previous versions of the analysis [201].

Dead tile veto. This cut again prevents fake $E_{\mathrm{T}}^{\mathrm{miss}}$ arising from non-operational cells in the Tile and the HEC calorimeters, but this time when the energy loss is $> 5\%$. An event is removed if it contains any jet (with $p_{\mathrm{T}}^{\mathrm{jet}} > 40$ GeV and $|\eta^{jet}| < 2.8$) pointing within 0.2 radians of the $\vec{E}_{\mathrm{T}}^{\mathrm{miss}}$, and has a fraction of energy in bad cells of $B_{cell} > 0.05$.

Cosmic muon veto. Events are vetoed for cosmic muon candidates if they contain a baseline muon with axial impact parameter $|z_0| > 1$ mm `OR` transverse impact parameter $|d_0| > 0.2$ mm. This cut is applied *after* overlap removal to avoid removal of muons from heavy flavor decays. Both of these impact parameters are computed relative to the reconstructed hard scatter vertex.

Muon cleaning. Events are rejected if they contain a baseline muon (**before** overlap removal) with a q/p fractional error > 0.2, where q/p is the charge-momentum ratio.

Although the core of the $\vec{E}_{\mathrm{T}}^{\mathrm{miss}}$ resolution is not much affected by the muon term, any muons which are not reconstructed, badly measured, or fake, can be a source of fake $\vec{E}_{\mathrm{T}}^{\mathrm{miss}}$ [96].

Primary vertex (PV) requirement. Multiple pp collisions –or pile-up– may result in several reconstructed primary vertices (PVs) per event. The hardest primary vertex, i.e. the vertex with the highest sum associated track momentum $\sum p_{\mathrm{T}}^2$, is of key importance for heavy flavor tagging (e.g. b-tagging) and proper object calibration. To reject non-collision beam backgrounds (e.g. cosmic rays), the hard scattering vertex of the event must be consistent with the LHC beamspot, and reconstructed from at least 5 tracks having transverse momenta $p_{\mathrm{T}}^{track} > 400$ MeV

Lepton veto. Events with baseline electrons 3.3.2 (muons 3.3.3) with $p_{\mathrm{T}} > 10$ GeV and $|\eta| < 2.47$ ($|\eta| < 2.4$) are rejected; this cut has to be employed *after* overlap removal. This is in fact the no-lepton selection of the analysis.

The relative impact of each of these cuts is illustrated in table 5.4 for data and a simulated signal events for comparison.

5.4.3 Monte Carlo re-weighting

5.4.3.1 Monte Carlo scale factors

Some discrepancies between events from data and simulation are corrected by the application of multiplicative *scale factors* to simulated events.

Cut	Data	$\tilde{g} \to t\tilde{t}$
Total number of events	1535671	19999
GRL + Trigger	17740	16505
LAr + Tile Error	17724	16505
Incomplete Data Events	17724	16505
Trigger Inefficiency Cut	17724	16505
Jet Cleaning	17685	16490
Tile Hotspot	17685	16490
Cosmic Muon Veto	17676	16386
Bad Muon Veto	17676	16386
Vertex Requirement	17669	16376
(# of events with electrons at this point)	(236)	(5731)
(# of events with muons at this point)	(30)	(4321)
Lepton Veto	17405	7594
Chf of leading two jets	17202	7526
'Smart' LAr hole Veto	17095	7504
Dead Tile Veto	17030	7481
$n_{\text{jet}} \geq 6$ ($p_{\text{T}}^{\text{jet}} > 50$ GeV and $\lvert\eta^{jet}\rvert < 2.8$)	8676	6933
Energy Weighted Mean Timing Cut	8675	6932

Table 5.4: The cut-flow for the series of vetoes described in section 5.4.2 for a day of early data-taking during 2012 ($\mathcal{L}^{int} = 36.9$ pb^{-1}), and simulated events from the $\tilde{g} \to t\tilde{t}$ process with $m_{\tilde{g}} = 900$ GeV, $m_{\tilde{t}} = 2.5$ TeV and $m_{\tilde{\chi}_1^0} = 150$ GeV. For this table, events are triggered by any of the multi-jet triggers from table 5.1.

Lepton Reconstruction and Trigger Efficiencies. η- and ϕ-dependent multiplicative scale factors are used to correct the signal electron and signal muon identification and reconstruction efficiencies in Monte Carlo. A similar reweighting based on η and E_T in the electron case and in the muon case as function of η, p_{T}, isolation, and type (combined or segment-tagged) is applied to account for differences in single-lepton trigger efficiency. The electron trigger scale factors also depend on which particular electron trigger is being used.

Flavor Tagging Efficiency. A weight is given to each jet considered for b-tagging (either if it is identified or not as a b-jet) from simulated events to correct for the tagging inefficiency and mistag rates of b, c, τ, or light flavor/gluon jets. An overall scale factor is applied to the event as the product of individual jet weights, since the probability of (not) having an event with bs is the compound probability that (none) at least one of the jets was tagged as a b-jet. Nominal ATLAS scaling factors come from combining measurements in data with the Monte Carlo efficiencies determined using a MC@NLO $t\bar{t}$ sample (showered using HERWIG). To account for differences in the showering and hadronization models with respect to the SHERPA simulations used for backgrounds in this analysis, additional SHERPA–to–MC@NLO scale factors were derived as the ratio of the tagging efficiency in SHERPA and MC@NLO samples (see appendix A of ref. [202] for a detailed description).

Pile-up re-weighting. ATLAS Monte Carlo simulations are produced before the actual data-taking occurs, assuming realistic but not the exact beam conditions that actual runs

ended up having. MC events are re-weighted such that the average number of interactions per bunch crossing match the distribution observed in the data sample (see figure 3.3).

5.4.3.2 NLO k-factors

Samples receive additional weights to incorporate the precision of higher order perturbative calculations.

$t\bar{t}$ samples. SHERPA $t\bar{t}$ cross sections are scaled to Next to Leading Order (NLO) calculations multiplying the Leading Order (LO) cross section by $\sigma_{\text{NLO}}(gg \to t\bar{t}) = k_{gg}\sigma_{\text{LO}}(t\bar{t})$, with $k_{gg} = 1.3705$ for gluon fusion ($gg \to t\bar{t}$), and $k_{qp} = 0.4505$ for the other two processes ($qq \to t\bar{t}$ and $qg \to t\bar{t}$) together. The use of two k-factors depending on the initial partonic state, rather than a single k-factor, correct for the different gg fraction between SHERPA and MC@NLO simulations, improving the agreement to data[1].

Z samples. Two types of SHERPA Z+jets Monte Carlo samples are used in this analysis: inclusive $Z \to ll$+light-jets (with $l = e, \mu, \tau$ and ν) and filtered to have 4 or more jets. To avoid overlap between samples, events from the inclusive sample are vetoed if they have at least 4 final state colored partons in the matrix element (this information is extracted from the truth record stored in the MC samples). Therefore, the two samples become orthogonal and cover the entire phase space. The four jet filtered samples don't have 0-jet contributions so don't benefit from the NLO normalisation. Therefore the cross-sections for the Z+4jets samples are normalized to the NLO cross section from the inclusive process, $\sigma_{\text{NLO}}(Z \to \ell^+\ell^-)$ or $\sigma_{\text{NLO}}(Z \to \nu\bar{\nu})$, multiplied by the fraction of events removed from the inclusive sample, i.e. ∼1.37% for $Z \to l^+l^-$ and ∼1.43% for $Z \to \nu\bar{\nu}$.

W samples. This background is treated similarly than Z samples, but is more convoluted. Four types of SHERPA W+jets Monte Carlo samples are used: inclusive $W \to \ell\nu$ +light-jets (with massless $b/\bar{b}$ quarks), filtered with 3 or more jets, filtered with 4 or more jets, and another inclusive in the number of jets but with massive $b/\bar{b}$ quarks. The fraction of b-jets for the inclusive W decays is taken from this last sample. These samples are made orthogonal to each other following this prescription:

- events from the inclusive b-massless sample are vetoed if they have 3 or more final state colored partons, or at least one b-jet (here, a b-jet has $p_{\text{T}} > 40$ GeV and is labeled at truth level as originating from a $b/\bar{b}$ quark);
- veto events from the W+3 jets sample if they have more than 3 final state coloured partons, or at least one b-jet;
- veto events from the W+4 jets if they have at least one b-jet;
- events from the b-massive sample are rejected if they have no b-jets;

[1] The k-factors change the gg fraction at LO, $f_{\text{LO}} = N(gg \to t\bar{t})/N$=59.73%, to match the NLO fraction, $f_{\text{NLO}} = k_{gg}N(gg \to t\bar{t})/N$=81.86%, such that the inclusive number of $t\bar{t}$ events remains constant: $N = N(gg \to t\bar{t}) + N(qq \text{ or } qg \to t\bar{t}) = k_{gg}N(gg \to t\bar{t}) + k_{qp}N(qq \text{ or } qg \to t\bar{t})$.

Consistently to this combination we need to scale the contribution from b-massless simulations by a factor f such that it takes into account the more reliable b-jet fraction from the b-massive simulation f_b, in spite of the b-jet fraction from the b-massless sample f_0: $\sigma(W) = [f\,(1 - f_0) + f_b]\,\sigma(W)$. The resulting cross section for each process is obtained by multiplying $\sigma(W)$ by different factors according to

- W+jets (b-massles): $f = (1 - f_b)/(1 - f_0) \approx (1 + f_0 - f_b)$, with f_b=0.11% and f_0=0.46% obtained from simulations;
- W+3 jets (b-massles): $f \times Br_3$, where Br_3 ∼4.5% is the ('brancing ratio') fraction of events from the inclusive sample with exactly 3 additional partons in the final state;
- W+4 jets (b-massles): $f \times Br_4$, with Br_4 ∼1.4%;
- W+jets (b-massive): no additional factor.

5.5 Signal regions

5.5.1 Inheritance

This analysis is built upon a series of previous ATLAS 0-lepton 'multijet' analyses [30–32]. There and here, the selection makes use of two multi-jet triggers as described in section 5.4.1. This initial requirement imposes the need of several reconstructed jets in the final state, at least one more jet than the number required by the respective trigger, such that events be in the trigger plateau (see figure 5.1 and table 5.2). This constraint is not detrimental for the search though, since the multi-jet sector *is* the target signature that motivated the choice of those triggers in the first place. For this analysis, we use a different analysis strategy in terms of observables and the statistical treatment used in constraining the model parameters.

Events containing no isolated electrons or muons, many jets and missing transverse momentum are analysed for novel physics in restricted sectors called Signal Regions (SRs). An extensive optimisation was performed varying many different cuts and introducing additional observables for the definitions of more selective SRs. The result of this is that no-lepton multi-jet events are further scrutinized in two complementary analysis *streams*, both of which require large jet multiplicities and significant $E_{\mathrm{T}}^{\mathrm{miss}}$ and exploit the substructure of jets. The rationale, optimization and definitions, as well as improvements with respect to previous multi-jet searches are described in subsequent sections.

5.5.2 The multi-jet + flavour stream

The high luminosity achieved during 2012 allows to form exclusive (orthogonal) SRs with exactly eight or exactly nine of such jets, further subdivided according to the number of the jets (0, 1 or ≥ 2) which satisfy the b-tagging criteria (section 5.3). The split into

b-jet multiplicity bins enhances the sensitivity to different signal models. For example, the $\tilde{g} \to t\tilde{t}$ process has at least two quarks b in the partonic final state, while simplified 1-step models have none b in the decay chain (section 2.2.3).

Multi-jet signal regions in this stream are defined by the number of anti-k_t (R=0.4) jets with $|\eta^{jet}| < 2$ and $p_{\mathrm{T}}^{\mathrm{jet}}$ above the threshold $p_{\mathrm{T}}^{\mathrm{min}} = 50$ GeV (and 80 GeV). Events with ten or more jets are scarce and therefore retained in a separate category without any further subdivision by the b-jet content. The b-tagged jets have $p_{\mathrm{T}} > 40$ GeV and are contained within the acceptance of the inner detector ($|\eta| < 2.5$) since the b-taggers rely on algorithms using tracks. The MV1 tagger is used at its 70% efficiency operating point. Since the optimal signal regions count jets within a narrower η acceptance and a tighter p_{T} cut (either 50 or 80 GeV), these jets and the b-jets defined and the set of jets used to count the jet multiplicity can be different (see section 5.5.4.1). A similar process is performed for the higher jet-p_{T} threshold of $p_{\mathrm{T}}^{\mathrm{min}} = 80$ GeV required for the EF_5j55_a4tchad_L2FS trigger. Signal regions are defined for events with exactly seven jets or at least eight jets. Both categories are again subdivided according to the number of jets (0, 1 or $\geq$2) that are b-tagged, as indicated in table 5.5.

In all cases the final selection variable is $E_{\mathrm{T}}^{\mathrm{miss}}/\sqrt{H_{\mathrm{T}}}$, the ratio of the $E_{\mathrm{T}}^{\mathrm{miss}}$ to the square root of the scalar sum H_{T} of the transverse momenta of all jets with $p_{\mathrm{T}}^{\mathrm{jet}} > 40$ GeV and $|\eta| < 2.8$. Each of these variables is suitable for discriminating signal events from Standard model background. Yet, cutting directly on H_{T} probing for the hadronic activity in the event, may bias the selection towards particular values of parton-parton center-of-mass energy $\sqrt{\hat{s}}$, while theabove mentioned ratio remains constant (on average) for a large range of values (see figure 15 in ref. [96]). This ratio is closely related to the significance of the $E_{\mathrm{T}}^{\mathrm{miss}}$ relative to the resolution due to stochastic variations in the measured jet energies [96], as described in section 6.1.1. The value of $E_{\mathrm{T}}^{\mathrm{miss}}/\sqrt{H_{\mathrm{T}}}$ is required to be larger than 4 GeV$^{1/2}$ for all signal regions.

The seven (six) orthogonal signal regions with $p_{\mathrm{T}}^{\mathrm{min}} = 50$ GeV (80 GeV) are used in a combined fit as described in section 5.7.

5.5.3 The multi-jet + $M_{\mathbf{J}}^{\Sigma}$ stream

In this analysis stream, only the EF_6j45_a4tclcw_L2FS_5L2j15 multi-jet trigger was used because the yield for the EF_5j55_a4tchad_L2FS trigger after all cuts resulted too small[1]. Six non-orthogonal signal regions (SRs) are defined in terms of the number of ($R = 0.4$) jets with p_{T} above $p_{\mathrm{T}}^{\mathrm{min}} = 50$ GeV and a larger pseudorapidity acceptance of $|\eta^{jet}| < 2.8$. Events with at least eight, at least nine or at least ten such jets are retained, and a category is created for each of those multiplicity thresholds.

[1] The jet p_{T} spectrum [203] follows a steeply falling power law $d\sigma/dp_{\mathrm{T}} \sim p_{\mathrm{T}}^{-4}$, meaning that any increase in $p_{\mathrm{T}}^{\mathrm{min}}$ reduces the event yield. Going from $p_{\mathrm{T}}^{\mathrm{min}} = 50$ to 80 GeV reduces the event count by a factor of $\sim$20 for 8-jet signal regions (see table 7.1).

The selection variable M_{J}^{Σ} is defined to be the sum of the masses $m_j^{R=1.0}$ of the composite jets

$$M_{\mathrm{J}}^{\Sigma} \equiv \sum_{\text{composite jets}} m_{jet}^{R=1.0} \tag{5.8}$$

where the sum is over the composite jets that satisfy $p_{\mathrm{T}}^{R=1.0} > 100$ GeV and $|\eta^{R=1.0}| < 1.5$. Signal regions are defined for two different M_{J}^{Σ} thresholds. Again the final selection requires that $E_{\mathrm{T}}^{\mathrm{miss}}/\sqrt{H_{\mathrm{T}}} > 4$ GeV$^{1/2}$.

Since the multi-jet SUSY search spans a wide area in the parameter space of masses the final state may be composed of different topologies including particles with transverse momenta that greatly exceed their rest mass, or particles decaying almost at rest. In the former case, decay products of boosted particles will tend to form a collimated pattern of energy deposits collected into large-R jets. In the latter case, the decay products of a massive particle that is only mildly boosted may be spread over a relatively large area of the detector. Yet, even in the absence of single boosted massive particle decays, events that exhibit high jet multiplicity can display a more spherical pattern (instead of a back-to-back pattern typical of di-jet events) which means that in high-multiplicity events near-coincident particles are more likely be gathered into jets leading to higher jet masses. This hypothesis requires that the signal is at least as jet-rich as background events, which it is for the list of models analysed (section 2.2.3).

M_{J}^{Σ} is sensitive to the signal both through boosted final state top quarks and other massive particles –these, in turn yield massive, large-radius jets– and through the event shape of signal events [33]. By applying an additional selection on M_{J}^{Σ}, rather than just on the number of jets, the reach of this analysis is improved, particularly at high gluino mass. This is illustrated in figure 5.2, where it can be seen that at a given jet multiplicity, the M_{J}^{Σ} distribution peaks at higher values for the signal than for the background. This, suggests that the high jet multiplicity and high M_{J}^{Σ} sector is dominated by signal. The effect should be maximal for high jet multiplicities (≥ 12 jets) but is currently inaccessible with the amount of data collected so far.

The particular choice for the variables used and the applied fiducial cuts are described in the following section 5.5.4.

5.5.4 Optimization

It should be noted that the whole optimization procedure was done with restricted access to data. A fraction of the data was used to assess the agreement with the simulation in the control regions[1], but only Monte Carlo simulations of SM and signal were used to adjust the definitions of signal regions. This prohibition, usually dubbed as 'blinding' the data, is

[1] During the optimization only 5.8 fb^{-1}of data were used. This corresponds to the first half of the year (out of the 20.3fb^{-1}for the whole 2012). This data was used for searches in previous studies [32].

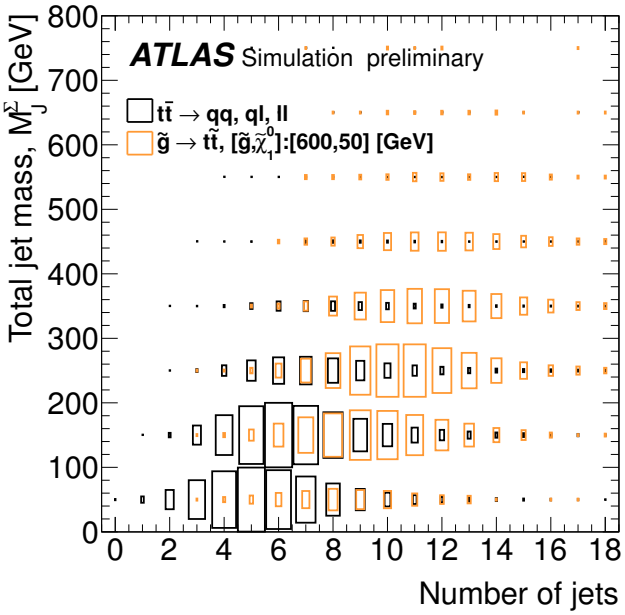

Figure 5.2: Two dimensional distributions of total jet mass and the number of jets for SM $t\bar{t}$ and $\tilde{g} \rightarrow t\tilde{t}$ simulated processes. Both distributions are normalized to the same area. The SUSY point corresponds to a gluino mass (600 GeV) already excluded by previus analysis. The size of each box is proportional to the cell content's value.

a common practice for search analyses that aims to prevent that the SRs be (involuntary) biased by the observation of the data. Once signal region definitions were 'freezed', data was un-blinded and the full statistical analysis performed, as described in section 5.7.

The analysis has been optimised for 21 fb^{-1}of luminosity according to two main strategies: an optimisation of the jet definition and the inclusion of b-jet requirements in the signal regions (see section 5.5.4.1); and the addition of cuts in the M_J^Σ variable (see section 5.5.4.2).

5.5.4.1 *b*-jet stream

The baseline definition for jet counts have improved the cuts in η^{jet} and $p_T^{\min}$. SUSY particles are more massive than the SM ones and are therefore created with smaller boost in the z-direction, which leads to more central topologies. Second, SUSY production is dominated by s-channel processes, while $t\bar{t}$ +ISR is predominantly produced through a t-channel process between $t\bar{t}$ and the ISR (e.g. [204]). Figure 5.3(c) shows the centrality of jets for $\tilde{g} \rightarrow t\tilde{t}$ and SM $t\bar{t}$ simulated events. The jets originating from gluino decay are in general more central than those in the Standard Model background, irrespective of the gluino and/or neutralino masses.

The signal jets are also typically more boosted than the background ones, as can be seen on figures 5.3(a) and 5.3(b). However, the peak in the p_T distribution of the signal jets decreases with jet multiplicity, and it is expected that in regions with a sufficiently con-

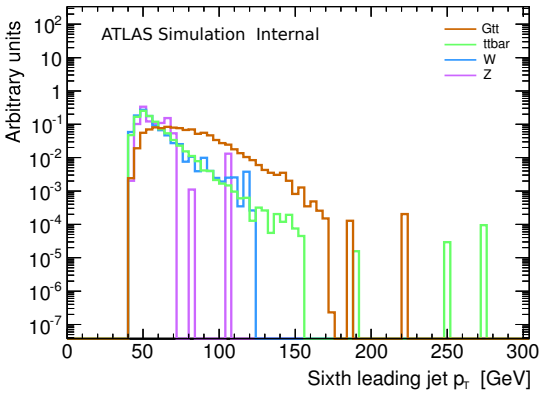

(a) p_{T} of the 6^{th} leading jet

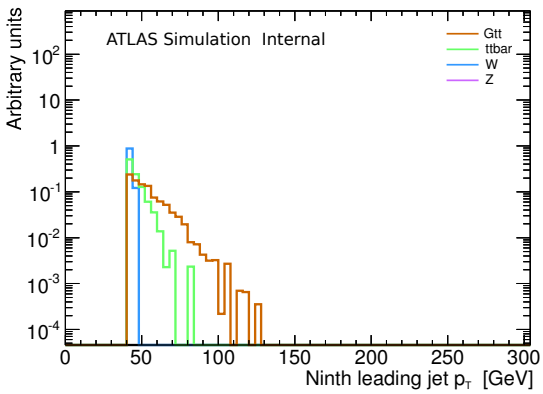

(b) p_{T} of the 9^{th}leading jet

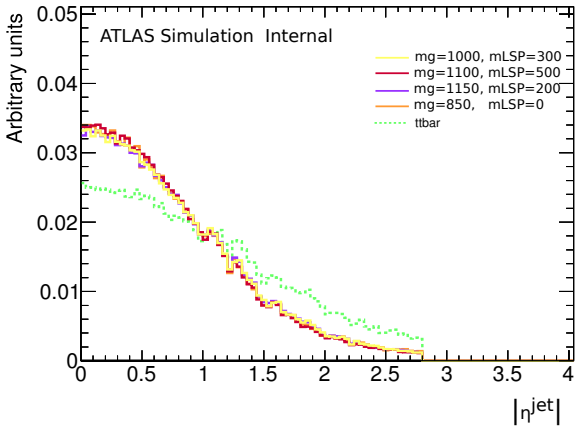

(c) $|\eta|$ all jets, $p_{\mathrm{T}} > 20$ GeV

Figure 5.3: p_{T} and $|\eta|$ distributions for three $\tilde{g} \to t\tilde{t}$ ($\tilde{t}$ off-shell) benchmark points, having different gluino and neutralino masses. The signal distributions are compared to a $t\bar{t}$ semileptonic sample. All events passed the trigger EF_6j45_a4tclcw_L2FS_5L2j15. All distributions are normalised to unity.

straining jet multiplicity, a tight p_{T} cut would reduce the significance (see figure 5.3(b)). The combination of these two changes (looser p_{T} cuts and tighter η cuts) leads to similar numbers of events in the different multiplicity bins from background processes but an increased fraction of signal.

The optimisation of the signal regions consisted on combining the η, $p_{\mathrm{T}}^{\mathrm{min}}$, jet multiplicity cuts and b-jet binning seeking for the highest sensitivity reach in the Gtt plane (gluino-LSP mass). In particular, the cuts tested were 2.8, 2.0 and 1.5 for $|\eta|$, 50 and 55 GeV for $p_{\mathrm{T}}^{\mathrm{min}}$, and 7, 8, 9 (or at least 9) and at least 10 jets respectively in jet multiplicity. In general, for low jet multiplicity ($n_{\mathrm{jet}} = 7, 8$) tighter cuts in $|\eta|$ increase the sensitivity, whereas for higher multiplicities the number of events is dramatically reduced if tight cuts are applied simultaneously. The idea underlying all the combinations is to exploit the statistical combination of exclusive signal regions to increase the significance, and therefore an independent full optimization for each jet multiplicity SR is futile. Several

sets combining all jet multiplicities were tested. The combinations considered are found on the legend of figure 5.4. Such choices were made to address the following questions:

- Gain in including a signal region with 10 jets (A vs B).
- Gain obtained by tightening η^{jet} (A vs C).
- Difference between 50 and 55 GeV cuts (with tighter η cuts) (A vs D).
- Gain in tightening eta for the same p_{T} cut (D vs E).
- Effect of increase in number of events in 10j by lowering the eta cut (D or E vs F).
- Gain obtained by fitting several regions against the reach of one jet multiplicity region (A vs G).

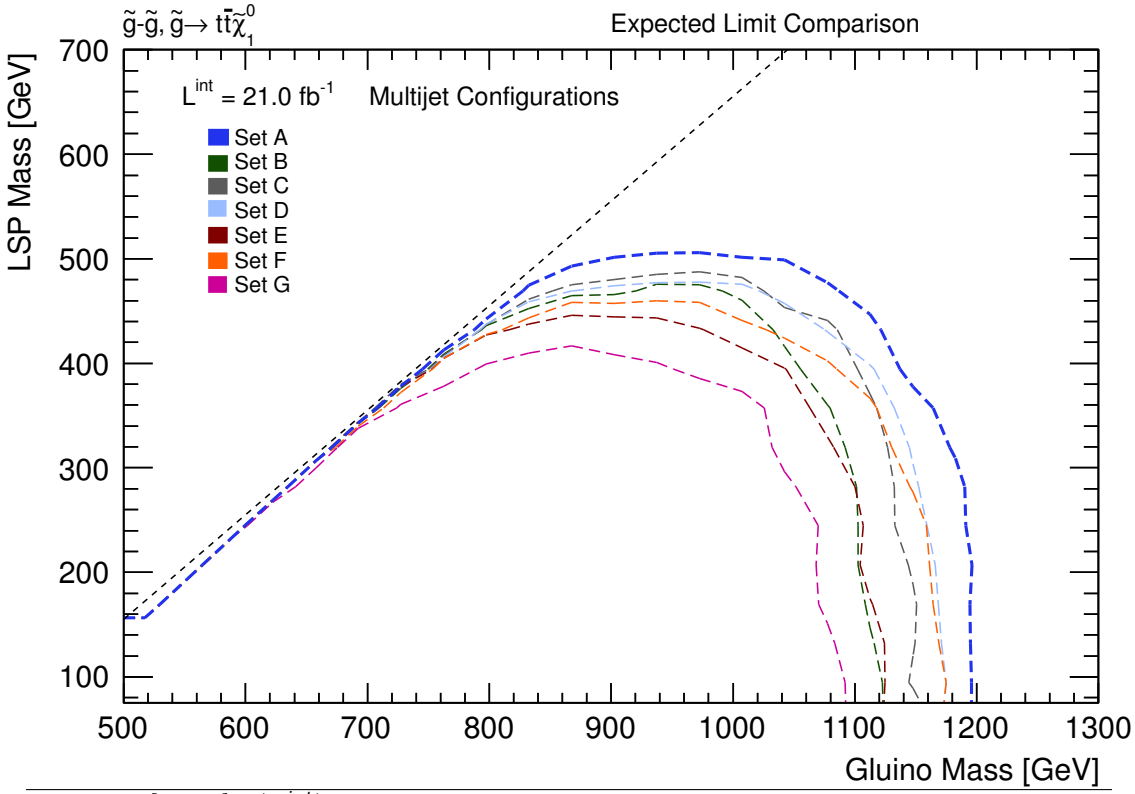

Set	p_{T} [GeV]	$\lvert\eta^{jet}\rvert$	**jet & b-jet binning**				
			zero, exactly one or at least 2 b-jets				b-jet blind
			7 jets	8 jets	9 jets	$\geq$ 9 jets	$\geq$ 10 jets
A	$\geq$ 50	$<$ 2.0	√	√	√	—	√
B	$\geq$ 50	$<$ 2.0	√	√	—	√	—
C	$\geq$ 50	$<$ 1.5	√	√	—	√	—
D	$\geq$ 55	$<$ 1.5	√	√	—	√	—
E	$\geq$ 55	$<$ 2.0	√	√	—	√	—
F	$\geq$ 55	$<$ 2.8	√	√	√	—	√
G	$\geq$ 55	$<$ 2.8	—	—	√	—	—

Figure 5.4: Optimization for b-jet signal regions. Exclusion limits for the Gtt grid by testing different combinations between $|\eta|$, p_{T} and jet and b-jet multiplicity as shown in the table.

Based on the overall optimization the baseline analysis has been changed to count jets

above p_{T} thresholds of 50 GeV and 80 GeV within a tighter η acceptance (rather than 55 GeV and 80 GeV and $|\eta| < 2.8$, as was the case in Ref. [201]). The final set of cuts correspond to the set A in figure 5.4, that improves significance while retaining signal acceptance.

Due to the large number of background events expected in the seven ($p_{\mathrm{T}}^{\mathrm{min}} = 50$ GeV) and six ($p_{\mathrm{T}}^{\mathrm{min}} = 80$ GeV) jet regions and the lack of signal observed in these regions in the previous analyses these are not expected to be sensitive to new physics so are now treated as 'confirmation' regions for the analysis, as defined in section 5.6.

5.5.4.2 M_{J}^{Σ} stream

A high multiplicity final state signature, such as that expected for the Gtt models, can benefit from the use of jet substructure observables. To discriminate against background the mass of large-R jets is used, i.e. the sum of the masses of large-R jets in the event, M_{J}^{Σ} as defined in equation 5.8. Preliminary studies indicated that this variable increased the discriminating power in combination with multi-jet signal regions.

M_{J}^{Σ} is the sum of the masses of large-R jets composed in turn by small-R jets (section 4.4). In this chain several variables can be subject of optimization: the p_{T} and η of the small-R jets counted to defined the multi-jet SRs, the $p_{\mathrm{T}}^{R=0.4}$ and $\eta^{R=0.4}$ of the small-R jets used to build the composite jets, the $p_{\mathrm{T}}^{R=1.0}$ and $\eta^{R=1.0}$ or number of composite jets used to calculate M_{J}^{Σ}, and finally the value of the cuts in M_{J}^{Σ}.

Jets used to defined multi-jet regions. In the original phenomenological study [33], a minimum number of large-R jets is required in addition to a cut in M_{J}^{Σ}. Here, in order to maintain the same multi-jet selection criteria throughout the study, the requirement on the jet multiplicity is applied not to large-R jets but to small-R ($R = 0.4$) jets, as is done for the flavour stream, section 5.5.2. The selection on M_{J}^{Σ} is very aggressive and therefore counting small-R jets within a tight $|\eta|$ region –as done in the flavour stream– would reject almost all events at high multiplicity. Therefore, multi-jet regions are defined by small-R jets having the maximum possible acceptance compatible with the trigger and the calorimeter η-range: $p_{\mathrm{T}}^{\mathrm{min}} = 50$ GeV and $|\eta^{jet}| < 2.8$. For the same reason, multi-jet regions are non-exclusive in the number of jets with eight or more, nine or more and ten or more $R = 0.4$ jets.

Acceptance of small-R jets used to construct composite jets. As shown in section 4.4, composite jets formed by small-R jets (dubbed 'component' for clarity) behave as large-R jets with a grooming applied. The level of removal of soft parts from the composite jets is determined by the minimum p_{T} of the component jets. A mild level of removal was chosen, $p_{\mathrm{T}}^{component} = 20$ GeV, as the mass spectrum breaks down for larger values as shown in figure 4.18.

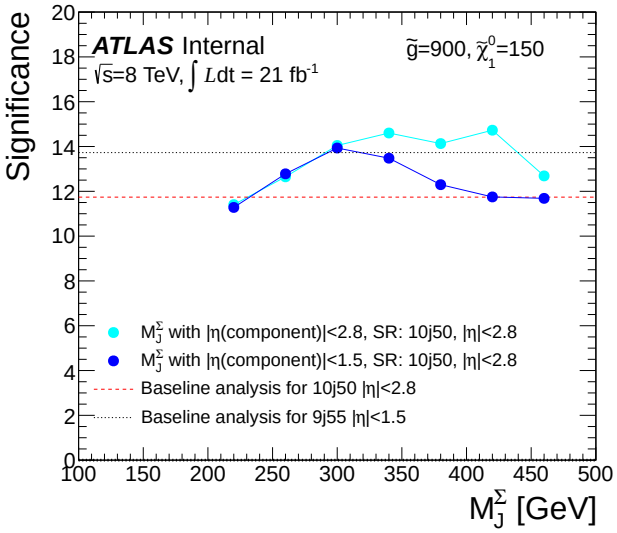

Figure 5.5: Significance vs different cuts in the total jet mass (M_{J}^{Σ}). The horizontal black line indicates the value of significance for the most promising SR without M_{J}^{Σ} cut: 9j55 ($|\eta| < 2.8$). In red is the baseline significance for 10j50 ($|\eta| < 2.8$), and in blue and light blue the improvement of significance after different M_{J}^{Σ} cuts. For these plots the sample of data used (a subset of periods A and B from the 2012 data taking) has $L = 4.8\mathrm{fb}^{-1}$ and is scaled to $L = 21.0\mathrm{fb}^{-1}$. The same performance was observed for other jet multiplicities.

Another determinant variable is the η of the $R = 0.4$ jets used for the construction of composite jets, $\eta^{component}$. For this test we measure the performance using an ad-hoc significance defined by the ratio of the signal expectation (S) and the uncertainty on the background (B):

$$Sig = S/\sqrt{B + 1.5 + 0.1 \times B^2} \tag{5.9}$$

where S (B) is the number of events from signal (background) after a given selection. The 1.5 cutoff in this formula prevents the optimization to favor selections that kill all background (a low expected event yield in some control/signal region would make the fit very sensitive to statistical fluctuations) and the quadratic term corresponds to a (conservative) $\sim 30\%$ prior for the systematic uncertainty added in quadrature to the statistical (poissonian) uncertainty. Figure 5.5 shows the significance for two choices of $\eta^{component}$: 1.5 and 2.8. The greater significance is achieved with compound jets built from $R = 0.4$ jets with $|\eta^{component}| < 2.8$ rather than $|\eta^{component}| < 1.5$. For signal regions defined with $|\eta^{component}| < 1.5$ the effect of any M_{J}^{Σ} cut is detrimental. The reason is that a baseline cut at $|\eta| < 1.5$ already removes a large amount of background so that any additional M_{J}^{Σ} cut can only remove a larger fraction of signal than background, reducing the significance rather than improving it.

Optimization of M_{J}^{Σ} definition and cuts. For the calculation of M_{J}^{Σ} (equation 5.8) only composite ($R = 1.0$) jets having $p_{\mathrm{T}}^{R=1.0} > 100$ GeV and $|\eta^{R=1.0}| < 1.5$ are used. Large-R jets with lower energy have a large uncertainty on their energy measurement (see equation 6.3). The η requirement was applied to be able to b-tag the large-R jets

(since b-tagging section 3.3.6 is possible only for jets within the acceptance of the tracking sub-detector, $|\eta| < 2.5$ section 3.2.2), an idea that was finally not exploited for the analysis.

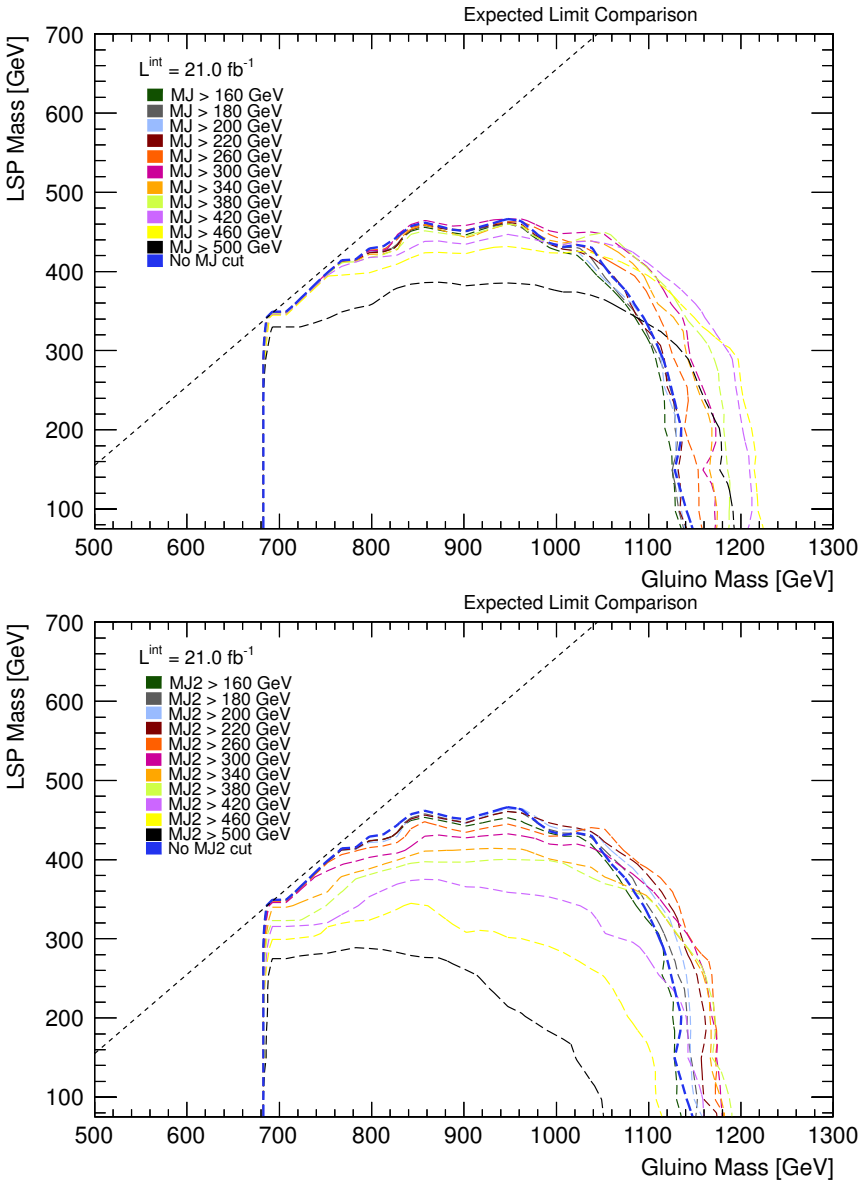

Figure 5.6: Expected exclusion limits for the ten jets signal regions ($p_{\mathrm{T}}^{\mathrm{min}} > 50$ GeV) and M_{J}^{Σ} or $M_{\mathrm{J},2}^{\Sigma}$ selections. The baseline analysis without any M_{J}^{Σ} cut is shown in blue for comparison.

Different cuts in M_{J}^{Σ} from 160 GeV to 500 GeV were evaluated, and it was also studied whether these selections benefit by restricting the number of composite jets entering in M_{J}^{Σ}. This benefit could occur if tops from $t\bar{t}$ and signal events are partially reconstructed into composite jets having then much smaller masses, in which case the addition of a third (or subsequent) leading jets may be detrimental for the search. For this, we compared two jet mass variables, the total jet mass (M_{J}^{Σ}) and the mass of the two leading composite jets ($M_{\mathrm{J},2}^{\Sigma}$), calculated with equation (5.8) but where the sum runs up to the second leading compound jet. The sensitivity has been checked with HistFitter [205, 206], as in

section 5.5.4.1. Figure 5.6 demonstrates the reach of the ten jet selection with different additional M_{J}^{Σ} and $M_{\mathrm{J},2}^{\Sigma}$ cuts. These plots suggest that $M_{\mathrm{J},2}^{\Sigma}$ is not a better option than M_{J}^{Σ}. A harder M_{J}^{Σ} cut is seen to reach further for light neutralino while a softer cut is preferred for higher neutralino masses. Therefore two different cuts are chosen for the final analysis; $M_{\mathrm{J}}^{\Sigma} > 340$ GeV and $M_{\mathrm{J}}^{\Sigma} > 420$ GeV. The first cut is also a reasonable value as backgrounds containing only two top quarks will have at most a total jet mass of $2 \times m_{top}$.

The final selection is summarized in table 5.5. The selections are non-exclusive, so the same events can be found in more than one signal region.

5.5.5 Sensitiveness to pile-up

During 2012, and especially the last half of it, the mean number of proton-proton interactions per bunch-crossing μ was rarely less than 10 and often as high as 25 or 30 as demonstrated in figure 3.3. Although the topocluster reconstruction (see section 3.3.4.1) achieve some amount of pile-up suppression, pile-up remains a potential source of background to any calorimeter-based reconstructed object, especially jets. For reconstructed jets the contribution of pile-up to the jet p_{T} is effectively removed through the 'Jet-Areas' corrections [94,95]. This correction subtracts jet-by-jet an amount of energy that is proportional to the event-by-event estimate of pile-up activity (obtained from low-p_{T} calorimeter deposits) and to the jet's *area* which is an estimate of the jet sensitivity to pile-up. However, variables such as the jet multiplicity or the selection variable M_{J}^{Σ} (section 5.5.3) may be further affected by the presence of local fluctuations in pile-up activity separate from the signal jets.

Figure 5.7 shows the mean reconstructed jet multiplicity as a function of the number of reconstructed primary vertices, requiring at least six or eight jets with $p_{\mathrm{T}} > 50$ GeV, and separately for a representative signal and the 2012 data triggered with a multi-jet trigger. Additionally, the mean jet multiplicity is evaluated both before and after requiring $M_{\mathrm{J}}^{\Sigma} > 340$ GeV. In all cases, the pile-up dependence is negligible. Figure 5.8 shows the equivalent plots for M_{J}^{Σ}, after several different cuts on the jet multiplicity, and separately for a representative signal and the 2012 data. In all these cases the pile-up dependence is small and therefore no further pile-up suppression for jets is used in the analysis.

Note then, that the performance of composite jets in response to pile-up is similar to that of the large-R jets to which grooming has been applied, as shown in figure 4.15.

Finally, although considered minor, in order to account for this small variations, the effects of pile-up are considered as a potential source for systematic uncertainty as described in section 6.5.2.1.

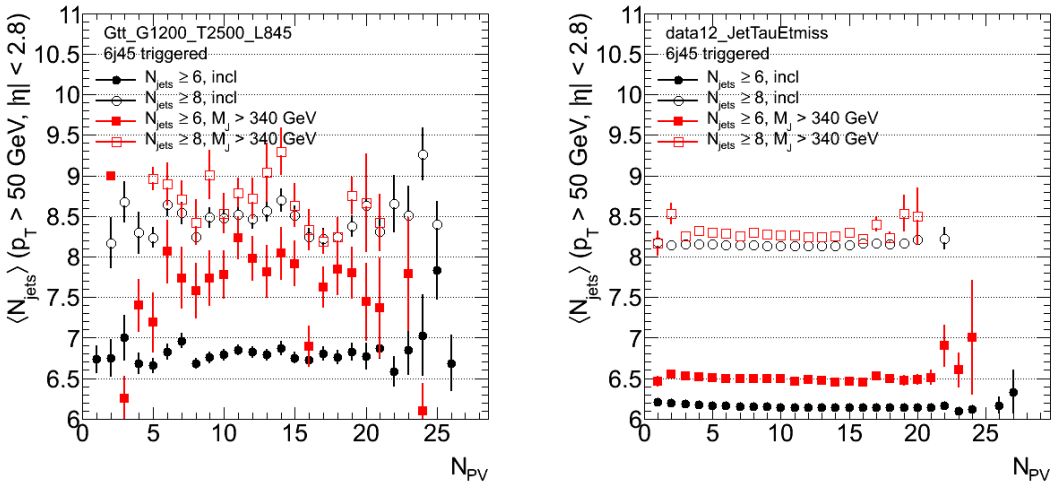

(a) (b)

Figure 5.7: The dependence of the mean jet multiplicity on the number of reconstructed primary vertices (formed from at least 2 tracks), requiring at least 6 or 8 jets with p_{T} > 50 GeV. The dependence is shown separately for a representative signal model (a), and data events selected with a multi-jet trigger (b), and evaluated both before and after requiring $M_{\mathrm{J}}^{\Sigma} > 340$ GeV.

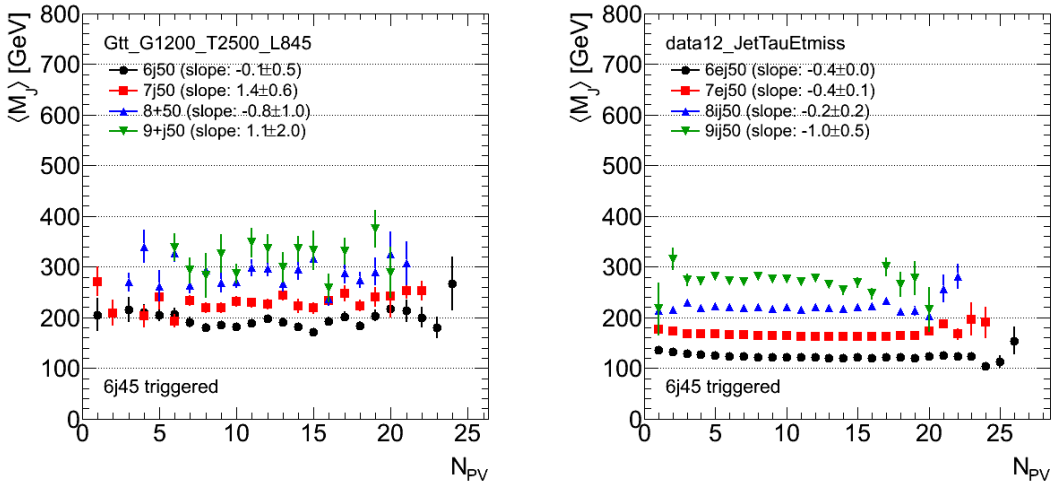

(a) (b)

Figure 5.8: The dependence of M_{J}^{Σ} on the number of reconstructed primary vertices with at least 2 tracks, after several different cuts on the jet multiplicity, and separately for a representative signal (a), and data events selected with a multi-jet trigger (b). The slope of each trend is always very small or consistent to zero, which indicates that there is very small or no dependency of M_{J}^{Σ} on the number of primary vertices.

5.5.6 Summary of signal regions

The selections of the two streams are verified to have good sensitivity to decays such as those in equations 5.1–5.4, but are kept generic to ensure sensitivity in a broad set of

models with large jet multiplicity and $E_{\mathrm{T}}^{\mathrm{miss}}$ in the final state.

Due to separation by jet energy threshold, jet multiplicity, b-jet count and M_{J}^{Σ} cuts there are a total of nineteen signal regions, as summarized in table 5.5. Within the multi-jet + flavour stream the seven signal regions defined with $p_{\mathrm{T}}^{\mathrm{min}} = 50$ GeV are mutually disjoint. The same is true for the six signal regions defined with the threshold of 80 GeV. However, the two sets of signal regions overlap; an event found in one of the $p_{\mathrm{T}}^{\mathrm{min}} = 80$ GeV signal regions may also be found in one of the $p_{\mathrm{T}}^{\mathrm{min}} = 50$ GeV signal regions. Each pool of orthogonal signal regions are combined into a single fit to address the background-only or signal hypotheses, as described in section 5.7. The multi-jet + M_{J}^{Σ} stream has six non-exclusive signal regions, then again an event may be found in more than one signal region. Being non-orthogonal, the background-only and signal hypotheses are assessed for each of these regions separately, and then the one providing the best exclusion is taken for the entire stream. Combination of among the streams is done using the best SR-principle, in which the overall exclusion is taken from the analysis stream providing the best exclusion.

Signal Regions	**Multijet + $M_{\mathbf{J}}^{\Sigma}$**			**Multijet + *b*-jet**								
Multi-jet trigger	EF_6j45_a4tclcw_L2FS_5L2j15						EF_5j55_a4tchad_L2FS					
SR name	**8+j50**	**9+j50**	**10+j50**	**8j50**		**9j50**		**10+j50**	**7j80**		**8+j80**	
Jet multiplicity (*)	≥ 8	≥ 9	≥ 10	8		9		≥ 10	7		≥ 8	
$p_{\mathrm{T}}^{\mathrm{min}}$ (*)	50 GeV								80 GeV			
$\lvert\eta^{jet}\rvert$ selection for jets (*)	< 2.8			< 2.0								
# b-jets	——			0	1	2+	0	1	2+	——	0	1	2+	0	1	2+
Total jet mass, M_{J}^{Σ}	> 340 and > 420 GeV			——								
$E_{\mathrm{T}}^{\mathrm{miss}}/\sqrt{H_{\mathrm{T}}}$	> 4 GeV$^{1/2}$											
Statistical treatment	Best SR-principle			Combined into one fit					Combined into one fit			
	Combination of analyses streams: best SR-principle											

Table 5.5: Signal region definitions. In all cases an additional final requirement of $E_{\mathrm{T}}^{\mathrm{miss}}/\sqrt{H_{\mathrm{T}}} > 4$ GeV$^{1/2}$ is applied. The selection variable $E_{\mathrm{T}}^{\mathrm{miss}}/\sqrt{H_{\mathrm{T}}}$ equals to the ratio of the magnitude of the missing transverse momentum to the square root of the scalar sum H_{T} of the transverse momenta of all jets with $p_{\mathrm{T}}^{\mathrm{jet}} > 40$ GeV and $\eta^{jet} < 2.8$. A long dash '——' indicates that no requirement is made. (*) These values correspond to anti-k_t jets with $R = 0.4$.

5.6 Glossary of phase space regions

Different types of event selection are defined using the following nomenclature: *control* region, *validation* region and *confirmation* region, in addition to the usual *signal* regions. The purpose for these is briefly summarized below and extensively discussed in the following sections of this chapter.

Control region (CR). An event selection used only for constraining the SM background; kinematically close (but orthogonal) to the signal regions. Good control samples should be as close as possible to the signal region, yet free of signal events. Control regions are used, for example, in the multi-jet template method for extracting the *closure* systematic uncertainty (section 6.5.1), and in the 'leptonic' backgrounds to normalise the Monte Carlo predictions. The usage of these regions reduce or even cancels uncertainties from the theory, the modeling and detector response (more details in section 5.7). It is a region with negligible signal contamination.

Validation region. An event selection used to validate the performance of Monte Carlo simulations before additional cuts are applied to create control regions. The validation regions are used to asses the agreement of 'leptonic' backgrounds simulations and data (section 6.2). It is a region with negligible signal contamination

Confirmation region. An event selection used to confirm the accuracy of the full background estimation. It is a region which has large background yields and small signal contamination (section 6.1).

Signal region (SR). This regions are designed to have a large content of (potential) signal relative to Standard Model events. All SM processes significantly populating these regions are considered as *background* and usually referred to as 'contamination'.

Table 5.6 aims to unfold the complexity of these definitions in terms of the phase space variables used to define them. Strict selections for the signal regions are summarized in table 5.5. Multi-jet control and confirmation regions are commented in section 6.1. 'Leptonic' regions used to validate the $t\bar{t}$ and W or Z backgrounds are detailed in tables 6.1 and 6.2, respectively.

5.7 Statistical methods

> *"The real world seldom fits exactly into the scheme provided by the ideal mathematical models."*
>
> – *[207]*

In general terms, a search is designed to answer –in the statistical sense– a set of primal questions: 'the result constitutes a discovery?' and depending on the answer it may respond

Jet multiplicity	$\mathcal{S}_{\mathrm{T}}^{\mathrm{miss}}$ [GeV$^{1/2}$]	
	< 3.5	> 4.0
No lepton		
6		
7		
8 (or 8+ for M_{J}^{Σ})		
9 (or 9+ for M_{J}^{Σ})		
10+		
One lepton (one muon or one electron)		
Any		
Same as for SR, (emulate leptons as jets)		
Two leptons of same flavor (either two muons or two electrons)		
Any		
Same as for SR (emulate leptons as neutrinos)		

Table 5.6: Summary of the different regions used for this analysis. Multi-jet *control* regions are shown in green. Non-multi-jet background *control* regions are shown in gray. In red are shown the *signal* regions and in yellow the *confirmation* regions used to test the validity of the template method. 'Leptonic' *validation* regions in blue. These regions are in turn subdivided into bins of b-jet multiplicity (zero, exactly one, and two or more b-jets, except the $n_{\mathrm{jet}} \geq 10$ region that is blind to the number of b-jets) or M_{J}^{Σ} ($\geq$ 340 GeV, $\geq$ 420 GeV). Multi-jet control regions have an additional subdivision with M_{J}^{Σ} $\geq$ 260 GeV to assess the performance of the template method. For clarity the $p_{\mathrm{T}}^{\mathrm{jet}} > 80$ GeV regions are omitted.

'how well does the alternate model describe the discovery?' or 'what limits can be imposed to the alternate model?' in case we were not that lucky as to unveil a discovery. These *human* questions must be encoded into precise hypotheses before they can be evaluated using appropriate statistical tools.

A robust interpretation of experimental results cannot be accomplished without recurring to the mathematical construct of hypothesis testing. Hypothesis testing may be outlined by two general rules. First, a function of the sample variables $\{x_i\}$ and known parameters $\{\theta_i\}$ is chosen as the test statistic $t(x_1 \ldots x_n | \theta_1 \, \theta_2 \ldots)$ and its probability density function $f_t(t|\mathrm{H}_0)$ is calculated under the assumption that the null hypothesis H_0 is true; the null hypothesis imposes conditions upon f_t by stipulating the values of the parameters θ_i or the form of the underlying distribution for $\{x_i\}$. At last, a decision is taken based on a (e.g., one-sided) p-value

$$p = \int_{t_{obs}}^{\infty} f_t(t|\mathrm{H}_0) dt \tag{5.10}$$

that quantifies how probable is that the statistic for the observed data be compatible to H_0: if the p-value is smaller than a preassigned probability α (in general the significance is set to $\alpha = 0.05$ corresponding to 3 standard deviations of a gaussian) then the hypothesis H_0 is rejected.

At Atlas, the chosen test statistic is the CL_s prescription [208] based on the *profile*

likelihood ratio [209, 210] a variant of the Feldman & Cousins method [211]. Before giving a precise definition of this variable (in section 5.7.2), for clarity it is preferable to present progressively the formalization and some technicalities with particular emphasis put on providing a transparent correspondence to the elements of the analysis.

5.7.1 Profile likelihood function (PLL)

The test statistic is built from the likelihood of the experimental model, which will be described in this section. Let's consider first the simplest possible working case of one signal and one background source, a unique signal region and no systematic uncertainties. The probability of measuring n events in this region under the 'background only' null hypothesis

> H_0: physics is described solely by the Standard Model

or the 'signal+background' null hypothesis

> H_0: physics is described by the Standard Model plus some additional processes not contained in the SM

can be formally condensed into a single distribution $P_n(n|\mu S + B)$, where S and B are the expected event yields for a signal model and for SM processes, respectively. The inclusion of a special parameter μ, called *signal strength*, allows to apply the same machinery for the background-only (μ=0) and for the signal+background (μ=1) hypotheses or for setting limits on the signal. This establishes a qualitative difference between μ and any other parameter in the model, because as we will see, the likelihood is left solely as a function (*profile*) of μ.

In a realistic analysis most samples (for signals and backgrounds) are subject to variations due to statistical/systematic/theoretical uncertainties (section 6.5) which in turn may or may not be correlated among different backgrounds samples and regions. To cover for these effects, the model can be improved by including in it additional *nuisance* parameters ν_p, that are not of intrinsic interest but provide a more accurate modeling of the problem: $P_n(n|\mu S(\nu_p)+B(\nu_p);\mu,\nu_p)$. The additional flexibility introduced to parametrize systematic effects will result in increased statistical uncertainty for the parameter of interest μ. To reduce the impact of nuisance parameters their values are constrained, whenever possible, by measurements in control regions $\{n_j\}$. The joint model for measurements in signal and control regions is given by the likelihood

$$L(\mu,\nu_p) = P_n(n|\mu S(\nu_p) + B(\nu_p);\mu,\nu_p) P_{n_j}(n_j|B(\nu_p);\nu_p) \tag{5.11}$$

where the second factor is independent of the signal (and therefore of μ) in the control regions. Using all the parameters (μ,ν_p) to find the statistical errors in the paramter of

interest μ is equivalent to using the *profile likelihood* [7]

$$L_p(\mu) = L(\mu, \hat{\hat{\nu}}_p(\mu)) \tag{5.12}$$

where the quantity $\hat{\hat{\nu}}_p(\mu)$ indicates the *profiled* values of the nuisance parameters, defined as the values that maximize L for the specified μ. By now the non-profiled likelihood will be used, and this 'marginalization' will be used later for the test statistic (section 5.7.2).

Measurements over several control and/or signal regions receiving contributions from many background processes and uncertainties affecting mean expectations for these backgrounds are pieces of information that can be combined into a single binned likelihood as the product of Poisson probabilities for all mutually exclusive signal and control regions

$$\begin{aligned} L(\mu, \nu_p, L^{\text{int}}) = & \left[\prod_{c \in \textit{channels}} \text{Pois}(n_c | \mu S_c + B_c; \mu, \nu_p, L^{\text{int}}) \right] \times \left[\prod_p G(m_p | \nu_p, 1) \right] \times \\ & \times G(L_0^{\text{int}} | L^{\text{int}}, \Delta L^{\text{int}}) \end{aligned} \tag{5.13}$$

where poisson likelihood functions are used for event counts in signal and control regions, and G are gaussian penalty terms describing auxiliary measurements m_p (like the luminosity L_0^{int}) that constrain the nuisance parameters ν_p (see section 5.7.1.1). Therefore, the full likelihood (5.13) is a function of the strength parameter μ, and a series of nuisance parameters ν_p, L^{int}, etc.

The formula still needs further explanation, naturally. The first factor is, as usual for a likelihood, the joint conditional probability for obtaining the measurements $\{n_i\}$ in the respective channels[1]. The factorization into independent poissonian distributions is a consequence of the orthogonality (and therefore statistical independence) among channels; for example all the 'j50' signal regions in the b-jet stream ('8j50' 0-b-jets, '8j50' 1-b-jet, '8j50' $\geq$2-b-jets, '9j50' 0-b-jets, '9j50' 1-b-jet, '9j50' $\geq$2-b-jets and the '10+j50', see table 5.5), together with the corresponding leptonic control regions form a set of non-overlapping selections that can coexist in the factorization. The inclusion of the various exclusive signal/control regions has the effect of evaluating the shape of the jet multiplicity distribution, constraining the background in the control regions and reducing the impact of their uncertainties in the signal regions.

The total number of expected events for channel c is composed by three types of additive samples: the signal model, multi-jet background events, and leptonic backgrounds (some of which are constrained by the maximization of the likelihood in the 'leptonic' control regions). Formally the expected number of events for the sample s (in a given decay

[1] In this context a 'channel' means a region of the data defined by an event selection (not to be confused with a scattering process), either a signal or a 'leptonic' control region.

process) for the channel c is expressed as

$$n_{s,c}^{\text{expected}} = \sigma_s \times BR \times \epsilon_c \times \mathcal{A}_c \times L^{\text{int}} \tag{5.14}$$

where the rate of the process for a given decay mode (BR, stands for branching ratio) is multiplied by the nominal acceptance of the selection $\mathcal{A}$ and the detection efficiency ϵ for the channel. Within the statistical model it is convenient a rather different form that takes into account the correlations among samples and channels:

$$n_{s,c}^{\text{expected}} = \lambda_{s,c} \times \gamma_c \times \phi_{s,c} \times \eta_{s,c}(\underline{\nu}) \times \sigma_{s,c} \tag{5.15}$$

where the parameters have the following meaning

- $\lambda_{s,c}$ is the nuisance parameter associated to the luminosity for a given channel and sample. Within a given channel this parameter is a common luminosity parameter for all the samples that include luminosity uncertainty. Backgrounds that don't have this uncertainty have $\lambda_{s,c}$ fixed at the nominal luminosity L_0^{int}.
- γ_c, is the nuisance parameter associated to the statistical uncertainty in the channel; for computational convenience γ_c is the same for all the samples in the channel. Data-driven samples that don't have this systematic have γ=1.
- $\phi_{s,c}$ is the unconstrained normalization factor for a given sample within a given channel. This parameter is free to move to adjust the sample normalization in a control region.
- $\eta_{s,c}(\underline{\nu})$ are normalization factors (around 1) that are parametrized in the nuisance parameters. These factors are constrained by the uncertainties during the LLP fit. The underline notation indicates a n-tuple of values: $\underline{\nu} = (\nu_1\, \nu_2 \ldots)$.
- $\sigma_{s,c}$ is the rate of predicted events for a given sample within a given channel.

All calculations including maximization of the likelihood and hypothesis testing are performed using the HistFitter package [205, 206], a wrapper for the RooFit framework [212].

5.7.1.1 Incorporating systematic uncertainties

Uncertainties are treated within the classical frequentist paradigm by the inclusion of nuisance parameters ν_p into the likelihood [213]. For instance, the jet energy scale systematic is considered as having a true (but unknown) value, in contrast to the bayesian approach in which the uncertainty itself is interpreted as a variable subject to fluctuations. The nuisance parameters ν_p introduced in the statistical model are not of relevance by themselves, and therefore their numerical values are arbitrary. By convenience a value ν_p=0 corresponds to the nominal value of the quantity while $\nu_p = \pm 1$ maps to an upward/downward shift by 1σ on the uncertainty [205, 206]. To set the concept, consider a jet p_{T} uncer-

tainty of 10%, then, a jet having 30 GeV at the nominal energy scale (ν_p=0), has 33 GeV (27 GeV) if the energy scale is shifted upwards $+1\sigma$ (downwards -1σ) by its uncertainty which corresponds to ν_p=+1 (ν_p=-1). The claimed 10% systematic is not the true value of the uncertainty but a given measurement of it. The measurement m_p of the nuisance parameter ν_p fluctuates with a gaussian distribution of width 1: $G(m_p|\nu_p, 1)$. This p.d.f. is included in the likelihood (equation 5.13) for each systematic. When generating (toy) Monte Carlo experiments the value of m_p is allowed to move between -5 and +5.

Here we must distinguish between the *source* of the uncertainty and its *effect* on the event yield (which is sample and channel dependent). As will be clear in section 6.5, the effect of a given uncertainty is known at three points: at the nominal prediction ν^0 for the nominal scale, and the predictions $\nu^{\pm}$ upon application of '$\pm1\sigma$' variations of the scale about the nominal. To model the effect on the event yield for an arbitrary variation, a continuous parametrization $\eta(\nu_p)$ in equation 5.15 is formed by a polynomial interpolation (and linear extrapolation) of these three measurements such that $\eta(0)$=1 and $\eta(\pm1) = \nu^{\pm}/\nu^0$.

5.7.1.2 Incorporating statistical uncertainties

Statistical uncertainties for Monte Carlo based background predictions are treated slightly different. One nuisance parameter γ, is employed to model the overall statistical uncertainty in each channel:

$$\text{Pois}\left(n_c|B_c^{\text{multi-jet}}(\underline{\nu}) + \gamma_c\left(\mu S_c(\underline{\nu}) + B_c^{\text{'leptonic'}}\right)\right)\text{Pois}\left(m_c|\gamma_c\tau_c\right) \tag{5.16}$$

where $B_c^{\text{multi-jet}}(\underline{\nu})$ is the number of events expected for the channel c where Monte Carlo statistical uncertainties need not be included (because the background is data driven) and

$$\mu S_c(\underline{\nu}) + \sum_{j\,\in\,\text{'leptonic'}} B_{j,c}(\underline{\nu}) \tag{5.17}$$

is the number of events predicted for signal and all the 'leptonic' backgrounds ($j = t\bar{t}$, $W + jets$, W+b-jets, $Z + jets$, Wt, $t\bar{t}$ $+V$) where the statistical uncertainty needs to be taken into account. The factor γ_c is the nuisance parameter reflecting that the true rate may differ from the Monte Carlo estimate ν_c^{MC} by some amount. The constraint for the nuisance parameter γ_c is modeled through a Poisson distribution[1], with mean $\gamma_c\left(\delta_c/MC_c\right)^2$.

[1] If the total statistical uncertainty is δ_c then the relative statistical uncertainty is given by δ_c/ν_c^{MC}. This corresponds to a total Monte Carlo sample of size $m_b = \left(\delta_c/\nu_c^{MC}\right)^2$. Treating the Monte Carlo estimate as an auxiliary measurement, we arrive at a Poisson constraint term Pois($m_c|\gamma_c\tau_c$), where m_c would fluctuate about $\gamma_c\tau_c$ if we generated a new Monte Carlo sample. Since we have scaled γ to be a factor about 1, then we also have $\tau_c = \left(\delta_c/MC_c\right)^2$; τ_c is treated as a fixed constant and does not fluctuate when generating ensembles of pseudo-experiments.

5.7.1.3 Analysis specificities

Correlations between processes and regions (i.e. channels) are fully taken into account, and described next.

Channels considered for the likelihood. As mentioned before, all non-overlapping regions are included in the same likelihood of equation 5.13. This establishes a fundamental difference between the two analysis streams since multi-jet + M_{J}^{Σ} signal regions are inclusive in the jet multiplicity and in the M_{J}^{Σ} cut, whereas the seven $p_{\mathrm{T}}^{\mathrm{min}} = 50$ GeV signal regions (and similarly the six $p_{\mathrm{T}}^{\mathrm{min}} = 80$ GeV regions) are orthogonal among each other (see table 5.5). This implies that a single PLL is formed gathering all the seven 'j50' (or all the six 'j80') signal regions from the flavour stream, while for the M_{J}^{Σ} stream the PLL includes just one signal region per fit. Control regions for the dominant 'leptonic' backgrounds (section 6.5.2) are also taken into account as active channels in the PLL if they have at least two expected events (electron and muon channels are combined into a single leptonic control region). These additional channels are included to normalise the background MC to data in regions where signal is expected to have very low rates. For the multi-jet + M_{J}^{Σ} stream the ≥ 2 event cut turns out to be too stringent such that a control region is only available for the (less sensitive) '8j50' signal regions. Altogether, this results in that the multi-jet + flavour stream favours from a simultaneous fit of many signal and control regions together, which reduces MC uncertainties more than for the multi-jet + M_{J}^{Σ} stream.

Sample correlations. Backgrounds are treated as independent components in the likelihood.

- $t\bar{t}$ and $W + jets$. One control region is defined for each signal region. If these control regions are included in the likelihood (i.e. have ≥ 2 predicted events) then the background component is allowed to vary freely in the fit ($\phi_{s,c}$ and $\eta_{s,c}$ are adjusted in the fit). If the control regions have less than two events, the MC predictions are individually allowed to vary within their uncertainties ($\eta_{s,c}$ is adjusted in the fit, but $\phi_{s,c}$ is fixed at 1).
- Less significant backgrounds ($Z + jets$, $t\bar{t} + W$, $t\bar{t} + Z$, and single top) are determined using Monte Carlo simulations. These are individually allowed to vary within their uncertainties ($\eta_{s,c}$ is adjusted in the fit, but $\phi_{s,c}$ is fixed at 1).
- Being data-driven the multi-jet background is not constrained in the fit by any control region ($\phi_{s,c}$ is fixed at 1) and is not subject to statistical fluctuations, but is constrained in the signal regions by its uncertainties ($\eta_{s,c}$).

Each of these background categories is considered as correlated between all the channels used for the statistical fit. The rough idea behind background adjustment and normalization is that for each channel (either a signal or control region) the total expected number

of events is roughly: $\mu S_c + B_c^{\text{multi-jet}}(\underline{\nu}) + \sum_{j \in \text{'leptonic'}} B_{j,c}(\underline{\nu})$, but the relative rate for multi-jet and 'leptonic' backgrounds is different at signal and control regions. Therefore, although a simultaneous fit is done across all these regions together, $t\bar{t}$ Monte Carlo (for instance) will almost only be adjusted by the measured data in its respective control region where this background is dominant and the remaining ones are negligible.

Uncertainty correlations. In both analysis streams, the signal and background uncertainties are considered as uncorrelated except for the jet energy scale, jet energy resolution, b-tagging, pile-up and luminosity uncertainties (other detector uncertainties are negligible on the signal samples). The fit framework [205] splits the source of an uncertainty from its effect on the event yield as described before. When toy pseudo-experiments are generated to emulate auxiliary measurements, the constraint upon the nuisance parameter ν_p is propagated to all samples/channels that depend on that uncertainty through $\eta_{s,c}(\underline{\nu})$.

Large uncertainties that predominantly affect the 'leptonic' background expectation are treated as correlated, but the different sources must be kept separated[1]. For instance, if the efficiency of tagging b-jets is incorrect in some p_{T} and η range, it is likely incorrect for both the signal and background samples, and across all background samples equally, since there is no strong reason for these b-jets to differ. Therefore, such uncertainties should be correlated. However, lumping all three uncertainties together would be incorrect.

Correlations for template method uncertainties (e.g. closure uncertainty, subtraction of the 'leptonic' component, etc.) are more difficult to obtain. Statistical uncertainties in the template determination are fully correlated across all bins.

For the signal, the dominant systematic effects are included in the fit; these are the jet energy scale and resolution uncertainties, the b-tagging efficiency uncertainties, and the theoretical uncertainties.

5.7.2 Profile likelihood test statistic

As mentioned before in this chapter, the purpose of the statistic t, is to provide an objective procedure to establish discovery (or exclusion limits), which in this context means to test hypothetical values of the strength parameter μ. Either μ=0 for the background-only hypothesis or the maximum μ compatible with data for setting limits. A solid description of the experimental reality forced to include additional nuisance parameters ν_p, that end up as additional arguments of the p-value in equation 5.10. In the strict frequentist approach, the μ-hypothesis is rejected only if the p-value is less than α for all possible values of the nuisance parameters, that is impossible to corroborate in practice. The difficulty described above is effectively solved if the statistic is defined such that its distribution $f_t(t|\mu)$ is independent of the nuisance parameters. An approximate independence is found using the

[1] In principle, these uncertainties may also affect the QCD multi-jet background templates, but their effect is small and are already partially comprised in the 'Leptonic-like background subtraction' (section 6.5.1).

profile likelihood ratio [209, 211] given by

$$Q(\mu) = \frac{L(\mu, \hat{\underline{\nu}}(\mu))}{L(\hat{\mu}, \hat{\underline{\nu}})} \tag{5.18}$$

where the denominator is the value of the likelihood at its maximum, that is, $\hat{\mu}$ and $\hat{\nu}_p$ are the maximum likelihood estimators for μ and ν_p, and the numerator is the profiled likelihood defined above with the double hat notation indicating the values of ν_p that maximize the likelihood for a given μ. The ratio so defined, is obviously non-negative, and since the maximum of L for a particular μ cannot exceed the maximum value over the entire (μ, ν_p) space, $Q(\mu)$ must be a quantity between 0 and 1. If Q turns out to be in the neighborhood of 1, the numerator will be close the maximum likelihood, and the μ-hypothesis will have large probability of being true. On the other hand, a small Q will indicate that $L(\mu, \hat{\underline{\nu}}(\mu))$ is much smaller than the maximum L and that the value of μ is unlikely for the observed data.

Instead of this ratio, however, is convenient to take $-2\ln Q(\mu)$, since the distribution for this statistic is analytically known in the (large sample) asymptotic limit [209, 210]. There is one final modification to this statistic introduced in ref. [210]. Under the assumption that the presence of a new signal can only increase the mean event rate beyond what is expected from background rates[1], the signal processes must necessarily have $\mu \geq 0$. To take this into account an alternative test statistic t_μ that does not allow the signal strength to become negative is used

$$t_\mu = -2\ln \tilde{Q}(\mu), \quad \text{with} \quad \tilde{Q}(\mu) = \begin{cases} \dfrac{L(\mu, \hat{\underline{\nu}}(\mu))}{L(\hat{\mu}, \hat{\underline{\nu}})}, & \hat{\mu} \geq 0, \\ \dfrac{L(\mu, \hat{\underline{\nu}}(\mu))}{L(0, \hat{\underline{\nu}}(0))}, & \hat{\mu} < 0, \\ 1, & \mu < \hat{\mu}. \end{cases} \tag{5.19}$$

With this conversion, unlikely values of μ now correspond to large and positive values of t_μ, and therefore the one-side p-value from equation 5.10 reads

$$p_\mu = \int_{t_{\mu,n_i}}^{\infty} f(t_\mu | \mu, \hat{\underline{\nu}}(\mu, n_i)) dt_\mu \tag{5.20}$$

where t_{μ,n_i} is the value of the statistic t_μ corresponding to a set of (observed or simulated) measurements $\{n_i\}$ and $f(t_\mu|\mu, \hat{\underline{\nu}}(\mu, x_i))$ is the p.d.f. of t_μ under the assumption of the signal strength μ, for the profiled nuisance parameters. Alternatively, the p-value is converted into an equivalent significance, $\mathcal{Z}$, defined as the distance to the mean of a normal gaussian such that the upper tail starting at $\mathcal{Z}$ has a probability p: $\int_{\mathcal{Z}}^{\infty} G(x|1,0)dx = p$,

[1] This is not the general case, though, as for example in pure neutrino beams, mass oscillations decrease of the yield of the initial flavor.

5.7.3 Discovery significance and exclusion limits

The p.d.f in equation 5.20 needed to evaluate the integral is constructed with the aid of toy Monte Carlo pseudo-experiments. The likelihood in equation 5.13 depends on the real measurements $\{n_i, L_0^{\rm int}\}$, auxiliary measurements m_p, and the parameters $\{\mu, \nu_p, L\}$, where the nuisance parameters include the factors of equation 5.15, all of which play a role in the toy Monte Carlo.

Observed limits. To build the p.d.f, values are toss for the auxiliary measurements $\{\mathcal{L}_0'^{\rm int}, m_p'\}$ taken randomly from their gaussian distributions $G(\mathcal{L}_0'^{\rm int}|\hat{\hat{L}}(\mu, \text{obs}), \Delta L^{\rm int})$ and $G(m_p'|\hat{\hat{\nu}}_p(\mu, \text{obs}), 1)$ (see equation 5.13). Note that the auxiliary measurements fluctuate around the profiled parameters for the *observed* data. These values are then used to generate a pseudo-experiment of random measurements $\{n_i'\}$ according to their poissonian distribution (given μ and$\{\mathcal{L}_0'^{\rm int}, m_p'\}$). The unconditional maximum likelihood estimators $\hat{\mu}$ and the nuisance $\hat{\nu}_p$ are fitted by maximizing the likelihood, and the test statistic is calculated from equation 5.19 for each ensemble of pseudo-data. With the p.d.f. thus built, the probability that the observed data is not compatible with the μ hypothesis is

$$p_\mu = \int_{t_{\mu,\text{obs}}}^{\infty} f(t_\mu|\mu, \hat{\underline{\nu}}(\mu, \text{obs}))dt_\mu \tag{5.21}$$

whereas the probability that the observed data is incompatible with the background only hypothesis is

$$p_b = \int_{-\infty}^{t_{0,\text{obs}}} f(t_0|0, \hat{\underline{\nu}}(0, \text{obs}))dt_0 \tag{5.22}$$

Note that in this case pseudo-data is used only to obtain the shape of the p.d.f., but the p-values depend on the observed data through the limits of the integrals [214].

Expected limits. Expected upper-limits are computed from background-only pseudo experiments. Toy background-only experiments $\{data'\}$ are simulated using the likelihood of equation 5.13, with $\mu = 0$ and the nuisance at their profile estimators for the observed data: $\hat{\hat{\nu}}_p(\mu = 0, \text{obs})$. Using the toy sample $\{data'\}$, the expected upper limits are found exactly as before but with the replacement obs $\rightarrow$ data': $p_\mu = \int_{t_{\mu,\text{data'}}}^{\infty} f(t_\mu|\mu, \hat{\underline{\nu}}(\mu, \text{data'}))dt_\mu$, instead of equation 5.21.

Discovery fit. A *discovery* is claimed if the observed data has an excess with respect to the background only hypothesis; in probability language if the p-value for the observed data (i.e. μ=0 in equation 5.21) is equal or less than the critical area of size α at the tail of the p.d.f. distribution. A p_0-value is obtained that quantifies the consistency of the background-only hypothesis with the observed data. If $p_0 > \alpha$, the background only hypothesis is not ruled out, and upper limits are imposed to physics beyond the standard model (BSM).

Model independent upper limits. For both cases, the *observed* and *expected* limits a fit evaluates the μ-hypothesis with $S = 1$ in equation 5.13 for each signal region (one at a time), along with all control regions. *Model-independent* upper limits on non-Standard-Model production (visible cross-section limits) are determined with this fit, if we understand that the total number of events in the channel is: $N_{BSM} + B = \mu \times 1 + B$. The upper-limit on μ is the highest value of μ not excluded (at 95% confidence level), in practice found by solving $p_\mu = \alpha$ for μ. In this case the upper limit on μ, provides an upper limit on the number of events from BSM, $N^{95\%}_{\text{BSM}}$, not excluded at the 95% confidence level. In order to ensure that these limits and p_0-values are model-independent, no shape information is taken into account in this fit, i.e. no more than a single signal region is used for a signal region at a time. For these limits, possible signal contamination in the control regions is neglected.

As fits are being performed, special care is taken when evaluating the strength of profiling of nuisance parameters. Some profiling of certain systematic uncertainties should be expected (that is a reduction of their uncertainty after the fit), but strong profiling may point to problems in the fit as events with significantly different topologies and characteristics must not be allowed to significantly constrain one another. No strong profiling was found for any of the nuisance parameters in any of the fits.

Model dependent upper limits, CL_s. When evaluating a supersymmetric signal model for exclusion, any signal contamination in the control regions is taken into account (yet, signal contamination is in all cases within the statistical uncertainty of the number of events in the control region). One may carry out the statistical test of the signal hypothesis based on the p_μ statistic, such that a value μ is excluded with a $1 - \alpha = 95\%$ confidence level (CL) if $p_\mu < \alpha$. Yet there is a problem with it for some regions in the parameter space of the signal model where the predictions for data are almost indistinguishable from those of the background-only model: $\mu S \ll B$. In these regions with no experimental sensitivity, the $\mu \neq 0$ hypotheses may be disfavored and rejected, simply because the observed statistic $t_{\mu,\text{obs}}$ falls in the rejection tail in $\sim \alpha$ (i.e. 5%) percent of the cases just by chance. Given that many tests are carried out for different signal models, it is not desirable that one out of $1/\alpha = 20$ searches where there is no sensitivity result in exclusion. To mitigate the problem, the p_μ is penalized by dividing by $1 - p_b$

$$\text{CL}_s(\mu) = \frac{p_\mu}{1 - p_b} \tag{5.23}$$

such that a point in a model's parameter space is excluded if $\text{CL}_s(\mu) < \alpha$ [208]. If the experimental sensitivity to a given value of μ is very low, then one finds that as p_μ decreases, so does the denominator $1 - p_b$, and thus the condition $\text{CL}_s \leq \alpha$ is effectively prevented from being satisfied. This statistic has the double benefit that it prevents the rejection of signal hypotheses where the background is much more dominant ($p_b \approx 1$), and also avoids the undesired fact that for experiments with the same efficiency and observations the one

having the largest expected background can quote strongest limits, as it happens if the p_μ test alone is used.

By iteration, the 95% confidence level upper-limit for μ is found by solving $\mathrm{CL}_s(\mu_{up}) = 0.05$. A given point in the model parameter space (see e.g. figure 7.4) is excluded if the $\mu_{up} \leq 1$.

6
Background estimation

A *search* in high energy physics can be understood as the seek for new particles by studying specific regions in the phase space of final states. The high center-of-mass energy achieved at the LHC is one natural 'coordinate' of this phase space, and a great effort is made within ATLAS to understand the Standard Model (SM) physics in this new regime (see figure 6.1). Beyond its value *per se*, a proper understanding of the SM is fundamental in the context of a search since any excess of data with respect to already known processes may hint to new physics.

Although Monte Carlo simulations of SM processes are continuously constrained by new precision measurements, it is not expected *a priori* that these simulations may provide a reliable description for all the possible kinematics, in particular for 'corners' of the phase space as is the case for signal regions. The same premises of the search prevent us from adjusting the SM simulations to agree with data in those regions, since that may mask the existence of new physics. In addition, the inaccuracy of the SM simulation in the signal regions cannot be directly quantified as a difference with respect to data, since that would imply that no other physics is expected at those regions, again in contradiction with the search premises. Because of all this, the estimation of a background and its uncertainties is not straightforward.

SM *background* processes are by definition those that contaminate the signal regions. These include processes that have similar signatures than signal models (i.e., many jets, $E_{\mathrm{T}}^{\mathrm{miss}}$ and no leptons), or processes that have different true signatures (for example processes with leptons in the final state) but because of imperfections in the event selection can also contribute to the signal regions. Signal regions in this analysis are characterized by many jets, the presence of missing energy and no leptons. Relevant SM processes populating the signal regions are multi-jet QCD events, top pair production in association with jets or a vector boson, W and Z boson + jets and single top.

The number of events for these backgrounds is determined using similar methods as in ref. [201] and proceeds along two general paths. Background processes for which the MC simulations are not trusted at high jet multiplicity are estimated from data (data-driven) in control regions at low multiplicity and then are 'extrapolated' to the signal regions (section 6.1). For physics processes that are reliably predicted by MC, the estimation is taken directly from simulations but constrained by comparisons to data in regions where the signal hypothesis has been excluded by previous analyses (section 6.2); the level of

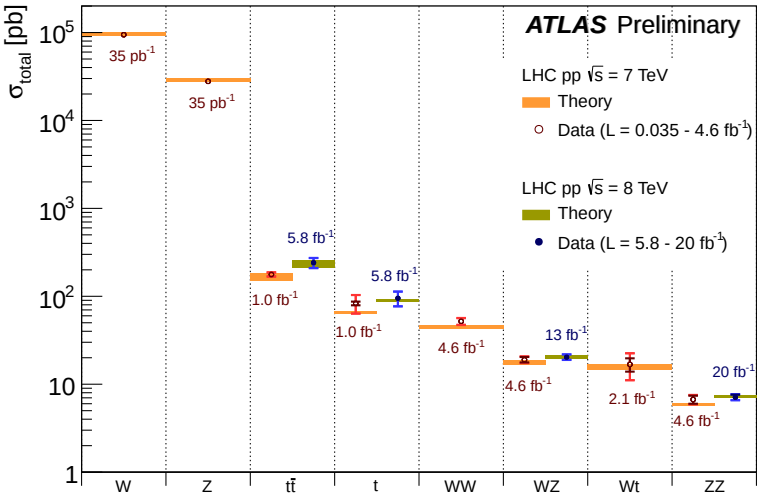

(a) Atlas

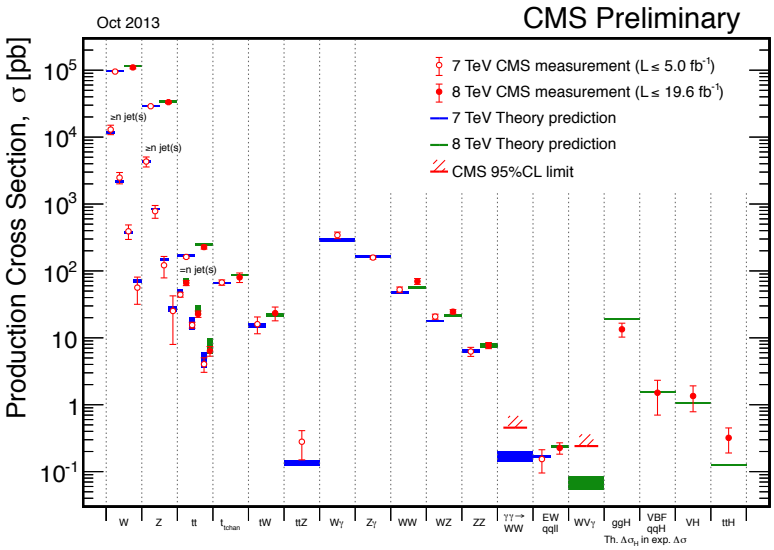

(b) Cms

Figure 6.1: Summary of several Standard Model total production cross section measurements, compared to the corresponding theoretical expectations. (a) The dark-color error bar represents the statistical uncertainly. The lighter-color error bar represents the full uncertainty, including systematics and luminosity uncertainties. All theoretical expectations were calculated at NLO or higher. (b) Total experimental uncertainties are shown as error bars. Vertical extent of the theory predictions indicates the theoretical uncertainty. See [215, 216] and references therein.

agreement is used to extract the background uncertainties (general remarks about these regions are described in section 5.6). The specific procedures used in this analysis are described in the next sections.

6.1 Multi-Jet production

Final states with high jet multiplicity produced from parton scattering processes and from hadronically decaying $t\bar{t}$ events (multi-jet background for brevity) contaminate signal regions (SRs) when the mismeasurement of jets induce momentum imbalance and hence fake $E_{\mathrm{T}}^{\mathrm{miss}}$. This is the dominant background at intermediate values of $E_{\mathrm{T}}^{\mathrm{miss}}$. Multi-jet production from purely strong scattering processes cannot be reliably predicted from available Monte Carlo simulations. Therefore, multi-jet contamination is estimated using a data-driven method, as described in the next section.

6.1.1 Template method

The ABCD method. As has just been said, MC simulations do not provide an accurate description of the QCD phenomenology for corners of the phase space with many jets. Because of that, a data-driven 'ABCD' method is used to determine the QCD multi-jet background. The basic idea behind it is schematized in figure 6.2. The shape of any

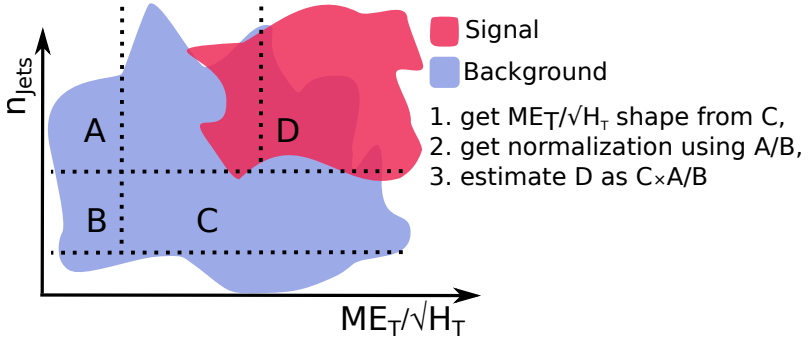

Figure 6.2: Sketch of the data-driven ABCD method used to estimate the QCD background in the signal region (D) from a template measured and normalized in the control regions (A, B, C).

distribution for the multi-jet background in the signal region D cannot be reliably taken from MC and cannot be taken either from measurements in that regions (since is in conflict with the signal hypothesis that needs to be evaluated). Therefore it must be estimated from the real measurements at neighboring regions (A, B, C). The shape of the distribution is taken from a low jet multiplicity (n_{jet}) control region C, and normalized to the large multiplicity signal region using the ratio of event counts in A and B:

$$\text{Shape in } D \longleftarrow \text{Shape in } C \times \frac{\#\text{events in } A}{\#\text{events in } B} \tag{6.1}$$

In principle A, B and C don't need to be orthogonal regions among each other, but do need to be orthogonal to the signal region D [1]. Also, the different factors in equation 6.1

[1] In this context, a pair of 'orthogonal' regions means that an event belonging to one of the regions cannot belong to the other, and viceversa.

are not only measurements of real data, but can also include MC prediction of processes which provide credible counts at the signal regions. A mandatory condition of the *shape* being templated is that it must be invariant as we go from low to large jet multiplicity.

The '$E_{\mathrm{T}}^{\mathrm{miss}}$ significance' template. Here, the shape of the $E_{\mathrm{T}}^{\mathrm{miss}}$ significance (to be defined later) is used to estimate the QCD background, as it has proven to be stable across different jet multiplicities [197]. The missing transverse momentum is measured from the momentum imbalance of electrons, photons, jets, and muons (and unmatched tracks and calorimeter cells) as was defined in equation 3.7, and therefore the resolution of $E_{\mathrm{T}}^{\mathrm{miss}}$ is affected by energy fluctuations of these objects. The effect is dominant for jets since the energy of electrons, photons and muons can be determined with better resolution, e.g. ∼1.2% for electrons [89] and 5–12% for jets [217]. From equation 3.7 this implies that the uncertainty of the $E_{\mathrm{T}}^{\mathrm{miss}}$ is at first order the uncertainty of the jet term, that (together with equation 3.6) reads approximately:

$$\sigma\left(E_{\mathrm{x(y)}}^{\mathrm{miss}}\right) \approx \sigma\left(E_{\mathrm{x(y)}}^{\mathrm{miss,jets}}\right) \approx \sigma\left(\sum_{i=jets} \vec{p}_{\mathrm{T}}^{\,i}\right) \approx \sqrt{\sum_{i=jets} \sigma^2\left(\vec{p}_{\mathrm{T}}^{\,i}\right)} \tag{6.2}$$

Thus, the actual form of the $E_{\mathrm{T}}^{\mathrm{miss}}$ resolution relies on the form of the jet energy resolution $\sigma\left(p_{\mathrm{T}}\right)$. Due to the sampling nature of ATLAS calorimeters, the jet p_{T} resolution $\sigma(p_{\mathrm{T}}^{\mathrm{jet}})$ is approximately proportional to $\sqrt{p_{\mathrm{T}}}$ of the jet being measured [217]

$$\sigma(p_{\mathrm{T}}^{\mathrm{jet}}) = N \oplus S \times \sqrt{p_{\mathrm{T}}^{\mathrm{jet}}} \oplus C \times p_{\mathrm{T}}^{\mathrm{jet}} \tag{6.3}$$

where the noise term (N) is due to external noise contributions that are not (or only weakly) dependent on the jet p_{T}, and include the electronics and detector noise, and contributions from pile-up. It is expected to be significant in the low p_{T} region, below ∼30 GeV. The constant term (C) encompasses the fluctuations that are a constant fraction of the jet p_{T}, due mainly to a fraction of the integrated signal being lost in un-instrumented regions of the detector. It is expected to dominate the high p_{T} region, above 400 GeV. In the intermediate region the Poissonian fluctuations, represented by the stochastic term (S), become the limiting factor in the jet resolution.

With this form the uncertainty of the $E_{\mathrm{T}}^{\mathrm{miss}}$ component associated to jets is the sum in quadrature of the momentum uncertainty of individual jets (6.2), which is dominated by the stochastic term in this energy regime: $\sigma(E_{\mathrm{T}}^{\mathrm{miss}}) = S \cdot \sqrt{\sum p_{\mathrm{T}}^{\mathrm{jet}}}$. This functional dependence is consistent with real data as shown in figure 6.3. The radicand is commonly known as H_{T}, the visible energy of the event. Under the assumption that this is the only contribution to the $E_{\mathrm{T}}^{\mathrm{miss}}$ uncertainty (a hypothesis that turns out to be slightly imperfect as shown in section 6.1.2), the $E_{\mathrm{T}}^{\mathrm{miss}}$ significance is defined as the inverse of the fractional

resolution[1]

$$\mathcal{S}_{\mathrm{T}}^{\mathrm{miss}} = \left(\frac{\sigma(E_{\mathrm{T}}^{\mathrm{miss}})}{E_{\mathrm{T}}^{\mathrm{miss}}} \right)^{-1} \sim E_{\mathrm{T}}^{\mathrm{miss}} / \sqrt{H_{\mathrm{T}}}. \tag{6.4}$$

where H_{T} is the scalar sum of the transverse momenta of all ($R = 0.4$) jets with $p_{\mathrm{T}}^{\mathrm{jet}} > 40$ GeV and $|\eta^{jet}| < 2.8$.

Since in QCD events with well separated high p_{T} jets the $E_{\mathrm{T}}^{\mathrm{miss}}$ is dominated by independent jet mismeasurement, the cut of $\mathcal{S}_{\mathrm{T}}^{\mathrm{miss}}$ is expected to be almost invariant under changes in jet multiplicity and also under changes in the H_{T} of the event. This allows to make an accurate prediction of the QCD background using the ABCD method as follows.

A "template" is formed from the shape of the measured $\mathcal{S}_{\mathrm{T}}^{\mathrm{miss}}$ distribution subtracting the expected contribution from backgrounds with prompt neutrinos, hence *real* $E_{\mathrm{T}}^{\mathrm{miss}}$. Based on Monte Carlo predictions, relevant SM background processes are non hadronic $t\bar{t}$, $W \to \ell\nu$, Z, $t\bar{t} + V$ and single top (but not b or c) decays, referred as 'leptonic' backgrounds for convenience (section 6.2). Thus defined,

$$N\left(\mathcal{S}_{\mathrm{T}}^{\mathrm{miss}}, n_{\mathrm{jet}}\right) = N_{data}\left(\mathcal{S}_{\mathrm{T}}^{\mathrm{miss}}, n_{\mathrm{jet}}; \text{X as in SR}\right) - N_{MC,\text{'leptonic'}}\left(\mathcal{S}_{\mathrm{T}}^{\mathrm{miss}}, n_{\mathrm{jet}}; \text{X as in SR}\right) \tag{6.5}$$

the 'leptonic'-background-subtracted distribution provides the number of events in bins of $\mathcal{S}_{\mathrm{T}}^{\mathrm{miss}}$ and jet multiplicity for events dominated by fake $E_{\mathrm{T}}^{\mathrm{miss}}$. The template is constructed from low jet multiplicity events –where the background is well understood and under control– and then used to predict the number of multi-jet events for the signal regions, after normalizing it to data in the background-dominated region with $\mathcal{S}_{\mathrm{T}}^{\mathrm{miss}} < 1.5$ GeV$^{1/2}$:

$$\underbrace{N(\mathcal{S}_{\mathrm{T}}^{\mathrm{miss}}, n_{\mathrm{jet}} \text{ as in } SR)}_{\text{Multi-jet prediction}} = \underbrace{N\left(\mathcal{S}_{\mathrm{T}}^{\mathrm{miss}}, n_{\mathrm{jet}} \text{ as in CR}\right)}_{\text{Template}} \times \underbrace{\frac{N\left(\mathcal{S}_{\mathrm{T}}^{\mathrm{miss}} < 1.5, n_{\mathrm{jet}} \text{ as in SR}\right)}{N\left(\mathcal{S}_{\mathrm{T}}^{\mathrm{miss}} < 1.5, n_{\mathrm{jet}} \text{ as in CR}\right)}}_{\text{Normalization to high } n_{\mathrm{jet}}} \tag{6.6}$$

which is of the form equation 6.1. The assumption that the control region at small $E_{\mathrm{T}}^{\mathrm{miss}}/\sqrt{H_{\mathrm{T}}}$ is dominated by Standard Model processes is supported by the agreement between measurements and Standard Model predictions of multi-jet cross-sections and distributions up to jet multiplicities of six [203].

To mitigate variations among different regions in the phase space, dedicated templates for each signal region are created applying the same criteria in both. For example, the multi-jet prediction for the signal region with exactly 9 jets and one b-jet is estimated from a template built from exactly 6 jets and one b-jet. This is what 'X as in SR' in equation 6.5 refers to, where 'X' stands either for the number of b-jets or a M_{J}^{Σ} cut.

[1] The stochastic factor S is dropped from this formula since any global scaling of the $E_{\mathrm{T}}^{\mathrm{miss}}$ significance is irrelevant for the purpose of the background estimation.

6.1.2 SoftTerm $E_{\mathrm{T}}^{\mathrm{miss}}$ correction

Precise measurements of the $\vec{E}_{\mathrm{T}}^{\mathrm{miss}}$ resolution indicate that its x and y components grow with the total transverse energy, defined as the sum of the transverse energy of all the cells in the detector: $\sum E_{\mathrm{T}} = \sum_{cells} E_i \cos\theta_i$, as shown in figure 6.3.

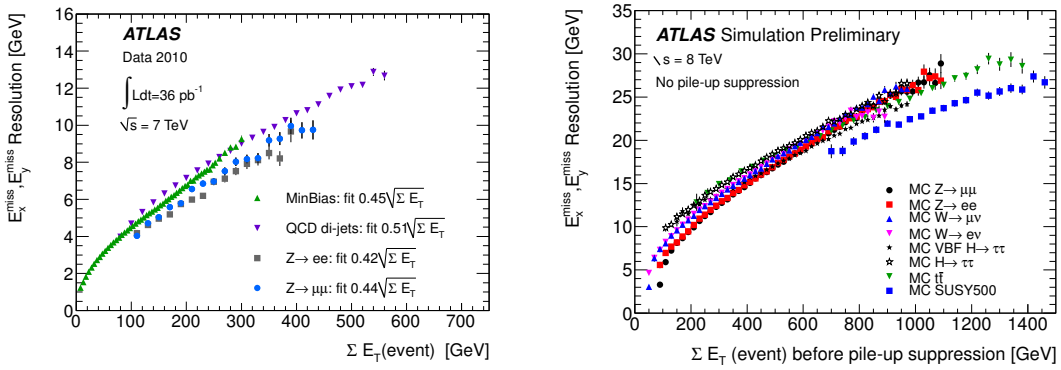

(a) (b)

Figure 6.3: $E_{\mathrm{T}}^{\mathrm{miss,x}}$ and $E_{\mathrm{T}}^{\mathrm{miss,y}}$ resolution as a function of the total transverse energy in the event calculated by summing the p_{T} of muons and the total transverse energy in the calorimeter in data at $\sqrt{s} = 7$ TeV (a) and MC at $\sqrt{s} = 8$ TeV (b). Note the worst resolution for 2012, due to additional pile-up events (see figure 3.3). In (a) the resolution of the two $\vec{E}_{\mathrm{T}}^{\mathrm{miss}}$ components is fitted with a function $\sigma = c \cdot \sqrt{\Sigma E_{\mathrm{T}}}$ and the fitted values of the parameter c (expressed in $\mathrm{GeV}^{1/2}$) are reported in the figure. [96, 218].

By splitting the total transverse energy into a hard (defined as the H_{T} scale) and a soft (the remnants) term it is found that the $E_{\mathrm{T}}^{\mathrm{miss}}$ significance defined in equation 6.4 is re-written as the hard part corrected by a function of $E_{\mathrm{T}}^{\mathrm{Soft}}/H_{\mathrm{T}}$:

$$\frac{E_{\mathrm{T}}^{\mathrm{miss}}}{\sigma(E_{\mathrm{T}}^{\mathrm{miss}})} = \frac{E_{\mathrm{T}}^{\mathrm{miss}}}{\sqrt{H_{\mathrm{T}} + E_{\mathrm{T}}^{\mathrm{Soft}}}} = \frac{E_{\mathrm{T}}^{\mathrm{miss}}}{\sqrt{H_{\mathrm{T}}}} \times f(E_{\mathrm{T}}^{\mathrm{Soft}}/H_{\mathrm{T}}) \tag{6.7}$$

This significance accounts for the residual dependence of the $E_{\mathrm{T}}^{\mathrm{miss}}$ on the soft energy in the event, from calorimeter clusters not associated with jets or other physics objects, part of which originates from pile-up and underlying events (see equation 3.7). This soft component[1], $E_{\mathrm{T}}^{\mathrm{CellOut}}$, is almost insensitive to jet multiplicity but is not included in the H_{T} calculation so can disrupt the invariance of $E_{\mathrm{T}}^{\mathrm{miss}}/\sqrt{H_{\mathrm{T}}}$ between different multiplicities.

To correct for this effect, a relative weight is calculated from the normalized distributions of the dimensionless variable $E_{\mathrm{T}}^{\mathrm{CellOut}}/H_{\mathrm{T}}$, in the region $\mathcal{S}_{\mathrm{T}}^{\mathrm{miss}} < 1.5$ $\mathrm{GeV}^{1/2}$ as (see appendix

[1] $E_{\mathrm{T}}^{\mathrm{CellOut}}$ is the scalar sum of $E\sin(\theta)$ over all jets with $p_{\mathrm{T}} < 20$ GeV and all clusters of calorimeter cells not associated with tracks, or jets or electron or muon candidates [96]. Jets with p_{T} between 20 GeV and 40 GeV that contribute to the soft component are not used for the SoftTerm correction. The impact of this is absorbed in the uncertainty associated to the closure of the template method (section 6.5.1).

A in ref. [201])

$$\omega(E_{\mathrm{T}}^{\mathrm{CellOut}}/H_{\mathrm{T}}) = \frac{N_{data}\left(\mathcal{S}_{\mathrm{T}}^{\mathrm{miss}} < 1.5, n_{\mathrm{jet}} \text{ as in SR, X as in SR}, E_{\mathrm{T}}^{\mathrm{CellOut}}/H_{\mathrm{T}}\right)}{N_{data}\left(\mathcal{S}_{\mathrm{T}}^{\mathrm{miss}} < 1.5, n_{\mathrm{jet}} \text{ as in CR, X as in SR}, E_{\mathrm{T}}^{\mathrm{CellOut}}/H_{\mathrm{T}}\right)} \tag{6.8}$$

Note that this event-by-event weight is applied only to events in the low n_{jet} CR regions, from equation 6.6:

$$N(\mathcal{S}_{\mathrm{T}}^{\mathrm{miss}}, X \text{ as in } SR) = N^{\omega}\left(\mathcal{S}_{\mathrm{T}}^{\mathrm{miss}}, \text{X as in CR}\right) \times \frac{N\left(\mathcal{S}_{\mathrm{T}}^{\mathrm{miss}} < 1.5, \text{X as in SR}\right)}{N^{\omega}\left(\mathcal{S}_{\mathrm{T}}^{\mathrm{miss}} < 1.5, \text{X as in CR}\right)} \tag{6.9}$$

By this, the reshaped template N^{ω}, is such that its underlying soft energy content mimics that of data at large jet multiplicities.

The cuts of this analysis were designed such that the multi-jet background would be predictable under the assumption that this process is dominant in the control regions. These hypotheses have been confirmed by previous versions of the analysis [30–32] and strengthened in this analysis with an increased luminosity.

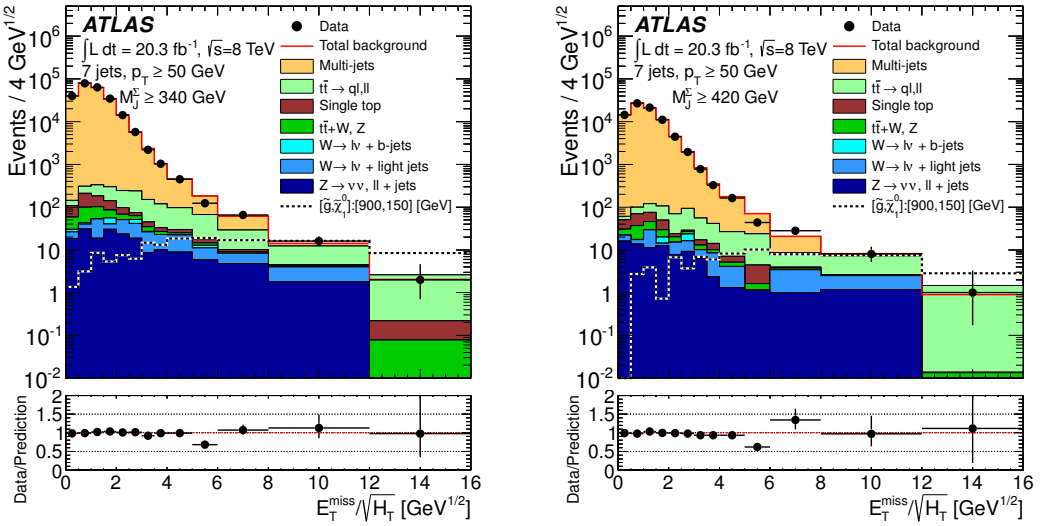

(a) $M_{\mathrm{J}}^{\Sigma} > 340$ GeV (b) $M_{\mathrm{J}}^{\Sigma} > 420$ GeV

Figure 6.4: Distribution of $\mathcal{S}_{\mathrm{T}}^{\mathrm{miss}} = E_{\mathrm{T}}^{\mathrm{miss}}/\sqrt{H_{\mathrm{T}}}$, for different *confimation* regions with exactly seven jets and $p_{\mathrm{T}} \geq 50$ GeV, and two cuts in M_{J}^{Σ}. The multi-jet prediction is determined from an $E_{\mathrm{T}}^{\mathrm{miss}}/\sqrt{H_{\mathrm{T}}}$ template obtained from events with exactly six jets. It is normalised to the data in the region $\mathcal{S}_{\mathrm{T}}^{\mathrm{miss}} < 1.5$ GeV$^{1/2}$ after subtraction of the 'leptonic' backgrounds. The most important leptonic backgrounds are also shown, based on Monte Carlo simulations. Variable bin sizes are used with bin widths (in units of GeV$^{1/2}$) of 0.5 (up to $\mathcal{S}_{\mathrm{T}}^{\mathrm{miss}} = 4$ GeV$^{1/2}$), 1 (from 4 to 6), 2 (from 6 to 8) and 4 thereafter. For reference and comparison, the distribution for a supersymmetric model is also included where gluinos of mass 900 GeV are pair produced and each decay as in equation 5.2 to a $t\bar{t}$ pair and a $\tilde{\chi}_1^0$with a mass of 150 GeV. The model is referred to as '$[\tilde{g}, \tilde{\chi}_1^0]$: [900, 150] [GeV]'. Signal regions defined in bins of the number of b-tagged jets show a similar good agreement.

Prior to the un-blinding of the 2012 dataset the validity of this procedure was tested in *confirmation* regions orthogonal to the control and signal regions involved in the calculation of the template. These regions have the same $E_{\mathrm{T}}^{\mathrm{miss}}$ significance than signal regions but lower jet multiplicity (see table 5.6), and were used to evaluate the degree of understanding of the multi-jet background before the unblinding. Figure 6.4 shows Monte Carlo predictions of 'leptonic' background for seven jets. On top of these is a template taken from a lower jet multiplicity (exactly six jets) where the leptonic contributions have been subtracted as described above. It is evident that multi-jet is the dominant background up to $\mathcal{S}_{\mathrm{T}}^{\mathrm{miss}} \sim 5$, being non-full hadronic $t\bar{t}$ the subdominant process. The overall agreement with data is very good. Deviations are quantified as a systematic error associated to the template method as described in section 6.5.1.

6.2 'Leptonic' backgrounds

Signal regions in this analysis require no isolated leptons in the final state. Processes with leptons in the final state that may contaminate the signal regions include non-hadronic decay of top quark, W and Z may if they are produced in conjunction with additional jets (which greatly reduces the production rate, figure 6.1(b) or [219]). The production of $Z \to \nu\bar{\nu}$ + jets contributes to the signal regions since it produces jets in association with $E_{\mathrm{T}}^{\mathrm{miss}}$. Leptonic top and W decays contribute to the signal regions when hadronic τ decays allow them to evade the lepton veto, as for example $W \to \tau\nu_\tau \to (qq')\nu_\tau$. A smaller contribution from these decays occurs when electrons or muons are produced but are not reconstructed or identified, for example if $W \to e\nu$ is seen as jet+$E_{\mathrm{T}}^{\mathrm{miss}}$. This later contribution is only marginal due to the high efficiency of electron ($> 91\%$ for 'baseline' electrons with $p_{\mathrm{T}} > 10$ GeV [220]) and muon (> 98 % for 'baseline' muons with $p_{\mathrm{T}} > 20$ GeV [91]) identification in ATLAS. Top quarks and vector bosons can be produced at the LHC and detected by ATLAS from different processes. Non negligible backgrounds processes include non-fully-hadronic (i.e. semi-leptonic or di-leptonic) $t\bar{t}$, $W \to \ell\nu$, $Z \to \nu\bar{\nu}$, $t\bar{t} + V$ or single top production (see figure 6.1). These processes with prompt neutrinos leading to real $E_{\mathrm{T}}^{\mathrm{miss}}$ are collectively referred to as 'leptonic' backgrounds within the context of this thesis, in accordance with the literature [30,31]. Other standard model backgrounds with many jets and $E_{\mathrm{T}}^{\mathrm{miss}}$ in the final state like di-boson (WW, WZ and ZZ) are not produced with a significant rate and therefore their contribution was negligible during 2012, as described in section 6.3.

'Leptonic' yields being under- or overestimated in the signal regions may lead to wrong conclusions when evaluating signal hypotheses. Therefore the 'normalization' of these backgrounds is fundamental. The event yield of minor backgrounds is taken directly from the prediction at the signal regions. For dominant backgrounds a more sophisticated approach is taken. First, *validation* regions –rich in these backgrounds– are formed using general cuts. In these validation regions the kinematic distributions are studied seeking

for good agreement between data an MC events. Having validated the performance of the Monte Carlo, additional cuts are applied to form 'leptonic' *control* regions that mimic as much as possible the signal regions. The purpose of having such 'signal-like' control regions is to compare Monte Carlo to data for the (almost) same topology as occurs in true signal regions, and to scale (i.e. 'normalise') the Monte Carlo to mitigate any difference if exists.

Ideally, Monte Carlo should be normalized to data in control regions enriched for $t \to b(\tau\nu_\tau)$ and $Z \to \nu\bar{\nu}$. Yet, experimental limitations suggest otherwise. Identification of Z bosons in $Z \to \nu\bar{\nu}$ processes is hindered since its invariant mass cannot be fully reconstructed from the invisible neutrino decays. Because of the large mass difference between the Z boson and e, μ, τ, ν, all leptons originating from Z decays have roughly similar *ultrarelativistic* kinematics. This characteristic is exploited to form '$Z \to \nu\bar{\nu}$' control regions from $Z \to \ell^+\ell^-$ processes, with the following recipe

- In di-lepton control regions, leptons are used to emulate neutrinos in the case of $Z \to \nu\bar{\nu}$ from $Z \to \ell^+\ell^-$. $E_{\mathrm{T}}^{\mathrm{miss}}$ is modified to include these additional 'neutrinos'.

It is therefore preferable to trigger events for light-leptons (e or μ) with high efficiency and purity, reconstruct Z bosons from the di-lepton invariant mass, and use these equivalent processes (from the kinematic point of view) to normalize the real $Z \to \nu\bar{\nu}$ background.

Similarly, identification of $t \to b(\tau\nu_\tau)$ is much difficult than for leptonic decays (into electrons and muons) because of the small the reconstruction efficiency for hadronically decaying taus ($\sim$ 70% for 'baseline' taus with $p_{\mathrm{T}} > 20$ GeV [221]). The experimental challenge to identify hadronic taus is mainly due to its decays that are predominantly seen as light-jets which are immersed in a sea of other light-jets (from QCD radiation). In this case, it is again preferable to trigger on visible leptons (e or μ), and use these processes to normalize the background of interest. Control regions for top and W consist of applying the same cuts as for signal regions but with this important modification:

- In one-lepton control regions, leptons are used to emulate additional jets in the event (i.e. the τ decays as actually seen in the detector). Thus, the lepton is considered for the count of jets and for the calculation of H_{T} which in turn impacts $E_{\mathrm{T}}^{\mathrm{miss}}/\sqrt{H_{\mathrm{T}}}$. Events selected with this prescription allows the estimation of signal contamination by backgrounds containing hadronic τ decays from tops and Ws.

Different 'leptonic' control regions are designed to enhance the sensitivity to particular background processes as described in sections 6.2.1 and 6.2.2. A simultaneous fit across signal and dedicated control regions is used to normalize the dominant 'leptonic' backgrounds, as fully described in section 5.7.

6.2.1 Selection of $t\bar{t}$ and W+jets enriched background

These processes are normalised in regions where a single isolated lepton (electron or muon) is required. The lowest unprescaled single lepton triggers are used and the reconstructed lepton is required to have $p_{\mathrm{T}} > 25$ GeV (such that the triggers are fully efficient). For muon triggered events, it is also required that the muon that triggered the event to be also reconstructed off-line (muon-trigger match: ΔR (on-line muon,off-line muon) < 0.15). Both leptons have to pass the 'signal' isolation criteria, and electrons must satisfy also shower shape criteria for electrons section 3.3.2). To ensure for the correct reconstruction of the $E_{\mathrm{T}}^{\mathrm{miss}}$, events with mismeasured jets or unreliable data are vetoed. These vetoes are the same as the applied for the no-lepton signal regions described in section 5.4.2, except naturally for the lepton veto.

A validation region is defined with a minimal selection of a single isolated electron or muon, no additional 'baseline' leptons, $E_{\mathrm{T}}^{\mathrm{miss}} > 30$ GeV, $E_{\mathrm{T}}^{\mathrm{miss}}/\sqrt{H_{\mathrm{T}}} > 2$ GeV$^{1/2}$ and transverse mass[1], $m_{\mathrm{T}} < 120$ GeV. $E_{\mathrm{T}}^{\mathrm{miss}}$ and $E_{\mathrm{T}}^{\mathrm{miss}}/\sqrt{H_{\mathrm{T}}}$ cuts reject unwanted multi-jet backgrounds with fake leptons that may contaminate these one-lepton regions. Multi-jet contamination affects, most notably, the electron channel as indicated in figure 6.5. The small amount of residual fake lepton background is seen at very low values of $E_{\mathrm{T}}^{\mathrm{miss}}$ and $E_{\mathrm{T}}^{\mathrm{miss}}/\sqrt{H_{\mathrm{T}}}$ such that after the control region cut, this background is negligible. An upper m_{T} cut of 120 GeV is applied to complete the validation region selection as this will reduce signal contamination in this region such that the accuracy of the modeling of the SM backgrounds can be studied.

In addition, to selectively enhance the sample purity in $t\bar{t}$ or W events, control regions are subdivided according to the number of b-jets (70% b-tag operating point). For the b-jet stream, the same splitting is done as for the signal regions, that is: no b-tagged, one and two or more b-jets. For the stream of the analysis which selects on M_{J}^{Σ}, the regions are also split into those with no b-tagged jets (for W determination) and $\geq$1 b-tagged jets (for W determination). In this case, the isolated lepton is also included as an additional input to the 'compound' jet to emulate a hadronic object.

The agreement of data and Monte Carlo in these *validation* regions was evaluated by the inspection of many distributions, that included: $E_{\mathrm{T}}^{\mathrm{miss}}$, H_{T}, $E_{\mathrm{T}}^{\mathrm{miss}}/\sqrt{H_{\mathrm{T}}}$, m_{T}, the lepton p_{T} spectrums, $E_{\mathrm{T}}^{\mathrm{CellOut}}$, the jet multiplicity, the total jet mass (M_{J}^{Σ}) and the (large-R) 'compound' jet p_{T} spectrums.

In general, good agreement was found between the MC and the data, indicating minimal contamination from QCD and confirming the signal-free assumption for these regions.

[1] The transverse mass is defined as the transverse mass between the lepton and the $E_{\mathrm{T}}^{\mathrm{miss}}$ assuming the lepton is massless,

$$m_{\mathrm{T}} = \sqrt{2\left(|\boldsymbol{p}_{\mathrm{T}}^{\mathrm{miss}}||\mathbf{p}_{\mathrm{T}}^{\ell}| - \boldsymbol{p}_{\mathrm{T}}^{\mathrm{miss}} \cdot \mathbf{p}_{\mathrm{T}}^{\ell}\right)},$$

where $\mathbf{p}_{\mathrm{T}}^{\ell}$ is the transverse momentum vector of the lepton.

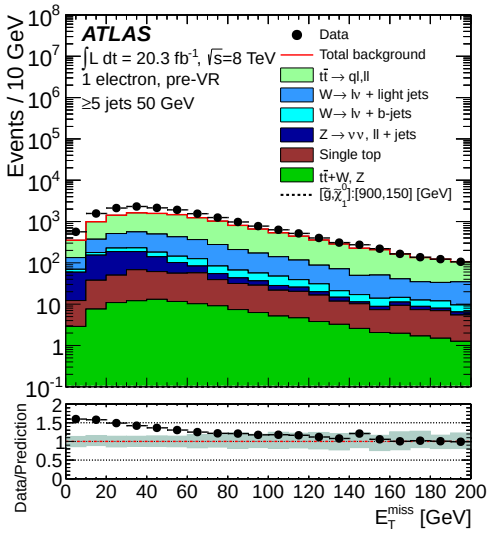

(a) $E_{\mathrm{T}}^{\mathrm{miss}}$, electron channel

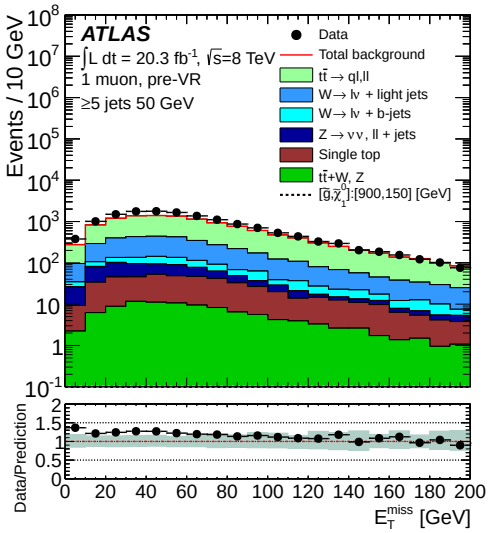

(b) $E_{\mathrm{T}}^{\mathrm{miss}}$, muon channel

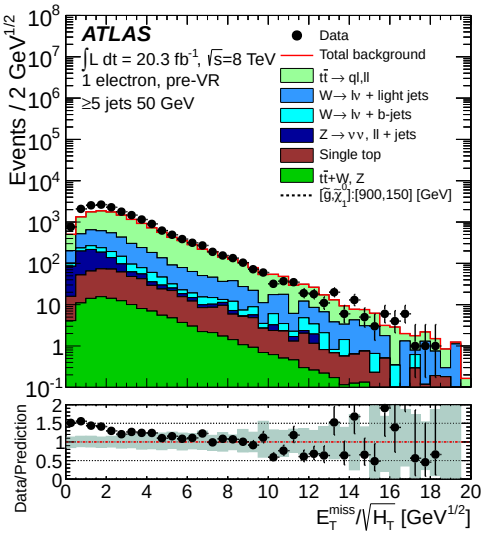

(c) $E_{\mathrm{T}}^{\mathrm{miss}}/\sqrt{H_{\mathrm{T}}}$, electron channel

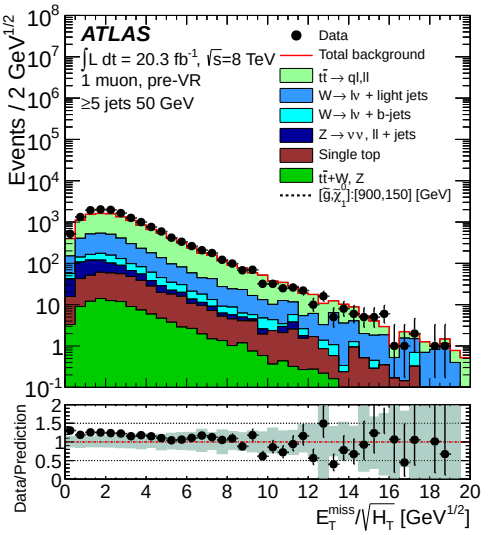

(d) $E_{\mathrm{T}}^{\mathrm{miss}}/\sqrt{H_{\mathrm{T}}}$, muon channel

Figure 6.5: Distributions of $E_{\mathrm{T}}^{\mathrm{miss}}$ and $E_{\mathrm{T}}^{\mathrm{miss}}/\sqrt{H_{\mathrm{T}}}$ for the one lepton selections. Unaccounted multi-jet background contaminates the low $E_{\mathrm{T}}^{\mathrm{miss}}$ and low $E_{\mathrm{T}}^{\mathrm{miss}}/\sqrt{H_{\mathrm{T}}}$ regions. *Pre*-validation regions (cuts #1-#4 in table 6.1) used to define validation regions. The band in the ratio plot indicates the experimental uncertainties on the Monte Carlo simulation prediction and also includes the Monte Carlo simulation statistical uncertainty. Additional theoretical uncertainties are not shown.

Figure 6.6 shows the distribution of the total large-R jet mass (M_{J}^{Σ}) and the leading jet p_{T} for the one lepton validation region. Moderate disagreement occurs at the soft part of the spectrums, specially for the $t\bar{t}$ enriched samples figures 6.6(b) and 6.6(d). This occurs at low M_{J}^{Σ}, well below the values used for the control regions (340 GeV). At large mass, MC central values exceed those of data for both leptonic channels, as seen in figure 6.6(b). The impact of this discrepancy was evaluated by re-weighting the MC distributions to data[1]

[1] Scale factors derived from the lead p_{T} spectrum in the lepton channel at the low jet multiplicity sector,

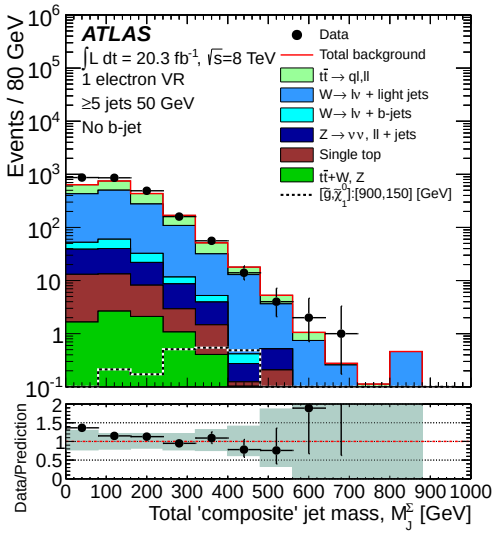

(a) M_{J}^{Σ}, b-jet veto

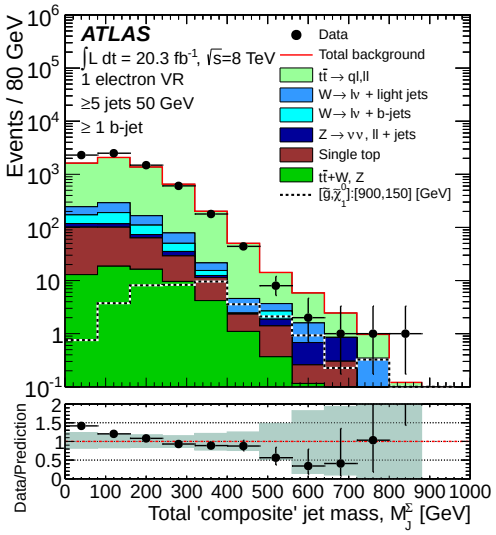

(b) M_{J}^{Σ}, ≥ 1 b-jets

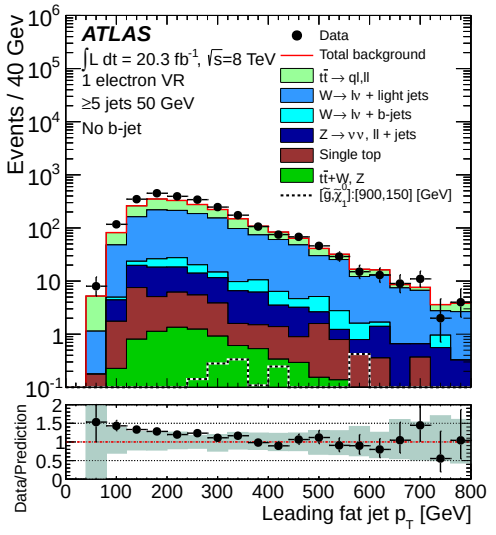

(c) lead p_{T}, b-jet veto

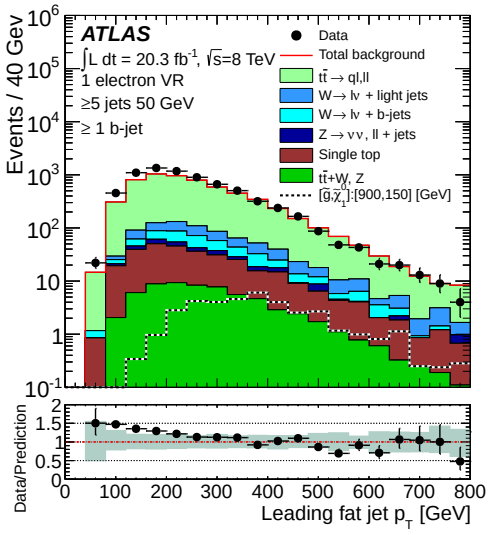

(d) lead p_{T}, ≥ 1 b-jets

Figure 6.6: Distribution of M_{J}^{Σ} and the leading large-R jet p_{T} for the one lepton validation region (one-electron is only shown).Distributions are split in bins of the number of b-tagged jets, to selectively enhance W (b-jet veto) or tops (≥ 1 b-jet). Other details are as for figure 6.5.

and was found to be less than 20% in the signal regions, smaller than the prescribed errors; also, tails of the distributions remained unaffected since the weights are close to unity, as the leading jet p_{T} is well described at large p_{T}. Because of this, no re-weight was used in the default analysis.

Control regions are then formed on top of these validation regions with additional criteria to better emulate the signal region selection. These are based around the fact that the

$SF = [N_{data}(n_{\mathrm{jet}} \geq 4, \text{lead } p_{\mathrm{T}})/N_{prediction}(n_{\mathrm{jet}} \geq 4, \text{lead } p_{\mathrm{T}})]^{-1}$, were applied to MC events in the signal regions, i.e. no-lepton channel and high jet multiplicity.

Cut	Value
	Validation regions
1. Trigger	Lowest unprescaled single muon trigger, `EF_mu24i_tight`, or lowest unprescaled single electron trigger, `EF_e24vhi_medium1`
2. Event cleaning	Same as for 0-lepton signal regions (section 5.4.2)
3. Off-line lepton	Exactly one 'signal' electron or muon, and no 'baseline' lepton of the other flavor
4. Lepton p_{T}	> 25 GeV
5. $E_{\mathrm{T}}^{\mathrm{miss}}$	> 30 GeV
6. $E_{\mathrm{T}}^{\mathrm{miss}}/\sqrt{H_{\mathrm{T}}}$	> 2.0 GeV$^{1/2}$, not including lepton in H_{T}
7. Transverse mass, m_{T}	< 120 GeV
8. b-jet binning	b-jet stream: b-veto, 1 or ≥ 2 b-jets (same as signal regions) M_{J}^{Σ} stream: b-veto or ≥ 1 b-jets
9. M_{J}^{Σ}	Include lepton as jet to build large-R jet
	Control regions (additional criteria)
10. Jet Count	Include lepton in jet count if it passes jet selection cuts
11. $E_{\mathrm{T}}^{\mathrm{miss}}/\sqrt{H_{\mathrm{T}}+p_{\mathrm{T}}^{l}}$	> 4.0 GeV$^{1/2}$ (including the lepton as an additional jet)

Table 6.1: The selection criteria for the validation and control regions for $t\bar{t}$ and W enriched backgrounds.

background entering the signal region primarily comes from hadronically decaying taus such that what is observed as an isolated lepton in the control region is observed as a jet in the signal region, as was described at the beggining of this section. Firstly the lepton is included in the jet count if it has sufficient p_{T}, and passes the jet counting and $|\eta|$ criteria. Secondly, a cut on the $E_{\mathrm{T}}^{\mathrm{miss}}/\sqrt{H_{\mathrm{T}}}$ is applied to emulate the cut that is applied to the signal region, $E_{\mathrm{T}}^{\mathrm{miss}}/\sqrt{H_{\mathrm{T}}} > 4$ GeV$^{1/2}$, where in the definition of $E_{\mathrm{T}}^{\mathrm{miss}}/\sqrt{H_{\mathrm{T}}}$ the lepton is included for the computation of H_{T}. The validation and control region criteria are summarised in table 6.1.

Distributions of jet multiplicity for the leptonic control regions can be found in figure 6.7. The contamination of QCD in these distributions was omited from start, but it is indeed small for jet multiplicity above two. Excellent agreement is found for all these control regions, except for $t\bar{t}$-enriched samples at low jet multiplicity and large M_{J}^{Σ} (figure 6.7(b)). This discrepancy is due to mismodeling of M_{J}^{Σ} for $t\bar{t}$ events as the same difference is seen for selection with ≥ 1 b-jet and no M_{J}^{Σ} cut (figure 6.6(b)), but not in samples with $M_{\mathrm{J}}^{\Sigma} >$ 340 GeV and blind to the number of b-jets (not shown).

6.2.2 Selection of Z+jets enriched events

Similarly to the $t\bar{t}$ and $W + jets$ backgrounds, control regions are used where expected event counts are sufficient. The validation and control region criteria are summarised in table 6.2. The Z control regions require two leptons of the same flavor which have an

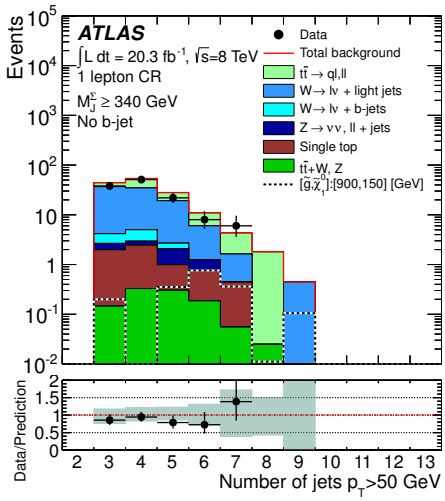

(a) $M_J^{\Sigma} > 340$ GeV, no b-jets

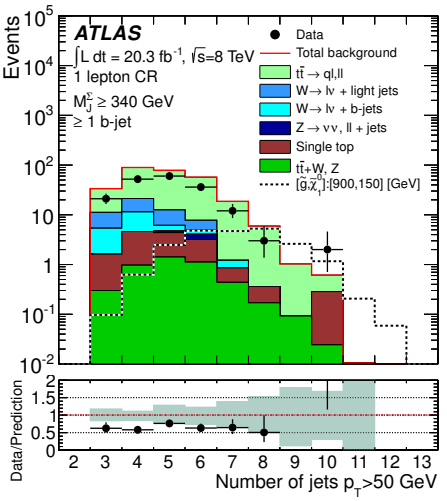

(b) $M_J^{\Sigma} > 340$ GeV, $\geq$1 b-jets

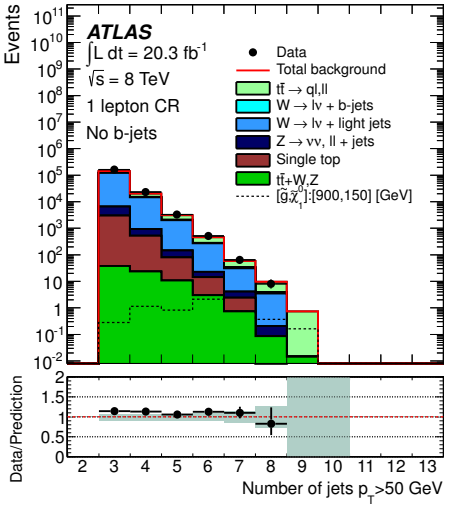

(c) No b-jets

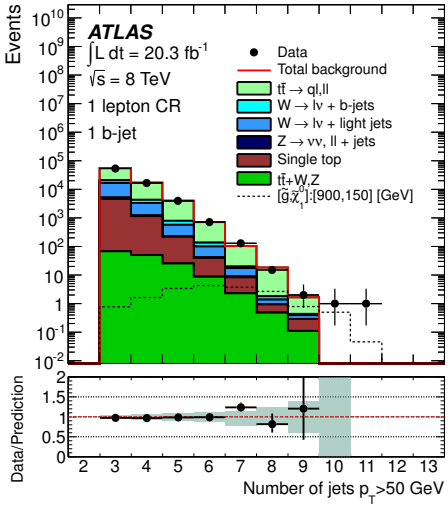

(d) Exactly one b-jet

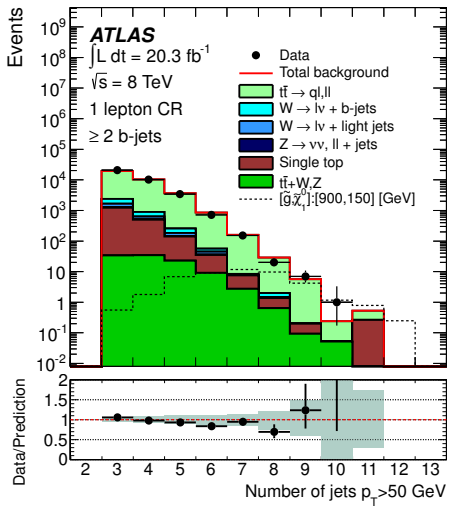

(e) $\geq$2 b-jets

Figure 6.7: Jet multiplicity distributions for p_{T}^{min} =50 GeV jets in the one-lepton $t\bar{t}$ and W +jets control regions for different b-jet multiplicities. Monte Carlo simulation predictions are before fitting to data. Other details are as for figure 6.5.

	Cut	Value
		Validation regions
1.	Trigger	Lowest unprescaled single muon trigger, `EF_mu24i_tight`, or lowest unprescaled single electron trigger, `EF_e24vhi_medium1`
2.	Event cleaning	Same as for 0-lepton signal regions (section 5.4.2)
3.	Off-line lepton	Exactly two 'signal' electrons or muons (no 'baseline' lepton of the other flavor)
4.	Lead lepton p_{T}	> 25 GeV
5.	Subleading lepton p_{T}	> 10 GeV
6.	Di-lepton mass, m_{ll}	80 GeV to 110 GeV
7.	$E_{\mathrm{T}}^{\mathrm{miss}}/\sqrt{H_{\mathrm{T}}}$	< 4.0 GeV$^{1/2}$, not including leptons in $E_{\mathrm{T}}^{\mathrm{miss}}$
8.	b-jet binning	b-jet stream: b-veto, 1 or ≥ 2 b-jets (same as signal regions) M_{J}^{Σ} stream: no b-jet requirement (b-jet blind)
		Control regions (additional criteria)
9.	Jet Count	Not include lepton in jet count
10.	$\lvert\boldsymbol{p}_{\mathrm{T}}^{\mathrm{miss}}+\boldsymbol{p}_{\mathrm{T}}^{\mathrm{l_1}}+\boldsymbol{p}_{\mathrm{T}}^{\mathrm{l_2}}\rvert/\sqrt{H_{\mathrm{T}}}$	> 4.0 GeV$^{1/2}$, including leptons (as 'neutrinos') in $E_{\mathrm{T}}^{\mathrm{miss}}$

Table 6.2: The selection criteria for the validation and control regions for Z enriched backgrounds. For this sample, leptons are used to emulate *true* neutrinos.

invariant mass

$$m_{\mathrm{ll}} = \sqrt{2p_{\mathrm{T}}^{\ell_1}p_{\mathrm{T}}^{\ell_2}\left[\cosh\left(\eta^{\ell_1}-\eta^{\ell_2}\right)-\cos\left(\phi^{\ell_1}-\phi^{\ell_2}\right)\right]} \tag{6.10}$$

lying in the range $80 < m_{\mathrm{ll}} < 110$ GeV. This provides a high purity sample enriched in Z as shown in figure 6.8. In that figure it is clear that the contributon of multi-jet background at low m_{ll}.

To create control regions that emulate the signal regions the lepton transverse momenta are added to the missing momentum two-vector and the requirement $E_{\mathrm{T}}^{\mathrm{miss}}/\sqrt{H_{\mathrm{T}}} > 4\mathrm{GeV}^{1/2}$ is then applied. This emulates the situation of a $Z \to \nu\bar{\nu}$ background.

For the b-jet stream, the same splitting is done as for the signal regions, that is: no b-tagged, one and two or more b-jets. For the stream of the analysis which selects on M_{J}^{Σ}, the regions have no b-tagged jet requirement.

For the b-jet analysis stream there are no control region plots produced at this point as the expected background is below 1 event in most signal regions. For the M_{J}^{Σ} analysis stream, the control region plots are shown in figure 6.9.

6.2.3 $t\bar{t}$+(W,Z) and single tops

The rest of the significant SM processes, $t\bar{t}$ +W, $t\bar{t}$ +Z and single top, considered as (very small) backgrounds in this analysis are extracted directly from Monte Carlo predictions in the signal regions. For the single top production we studied the t-, Wt- and s-channels separately and found that the Wt is the dominant one in the control and signal regions, as demonstrated in figure 6.10. In this figure the main processes are split into different

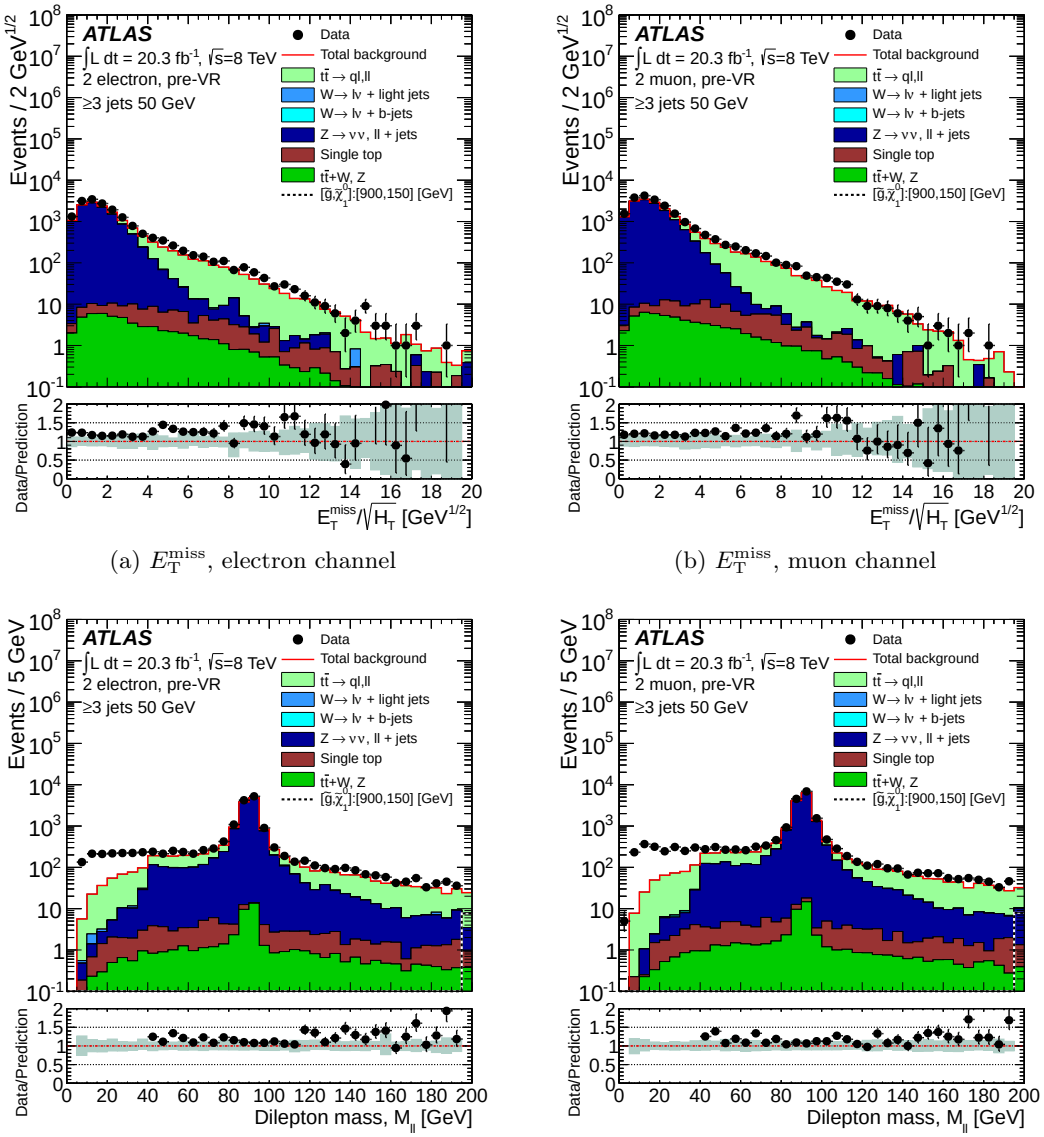

(a) $E_{\mathrm{T}}^{\mathrm{miss}}$, electron channel

(b) $E_{\mathrm{T}}^{\mathrm{miss}}$, muon channel

(c) m_{ll}, electron channel

(d) m_{ll}, muon channel

Figure 6.8: Distributions of $E_{\mathrm{T}}^{\mathrm{miss}}$ and m_{ll} for the two lepton selections. Unaccounted multi-jet background contaminates the low $E_{\mathrm{T}}^{\mathrm{miss}}$ and m_{ll} regions. *Pre*-validation regions (cuts #1-#5 from table 6.2) used to define validation regions. The error band indicates systematic uncertainties only.

channels to illustrate this point. Note that there are very few events at the jet multiplicities requested for the signal regions (8 or more), which are even less if additional cuts are applied (like a minimum M_{J}^{Σ}). This precludes the use of control regions in many fits for the multi-jet + M_{J}^{Σ} stream.

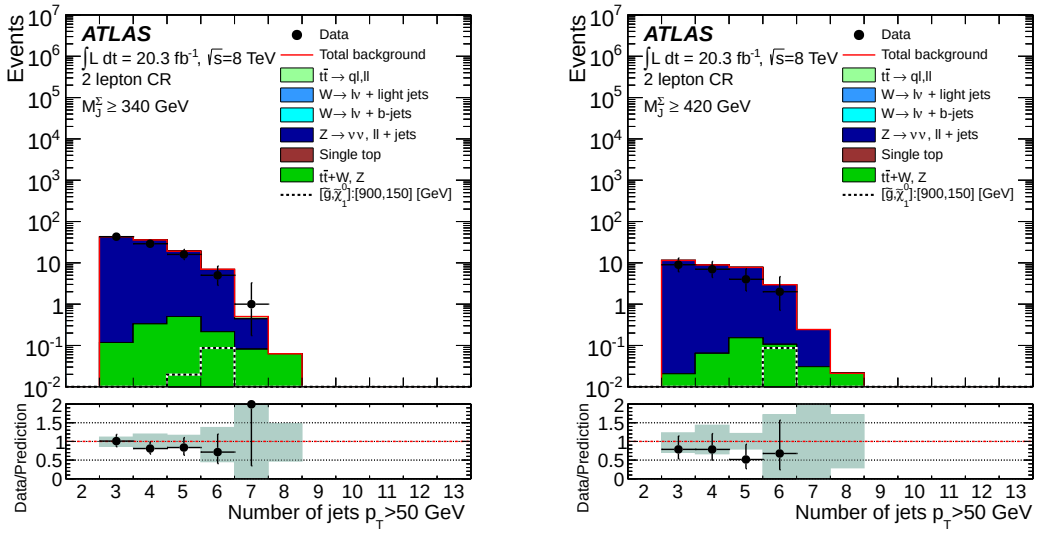

(a) $E_{\mathrm{T}}^{\mathrm{miss}}$, electron channel

(b) $E_{\mathrm{T}}^{\mathrm{miss}}$, muon channel

Figure 6.9: Jet multiplicity distributions for p_{T}^{min} =50 GeV jets in the two-lepton Z control regions for the M_{J}^{Σ} stream. The error band indicates systematic uncertainties only.

6.3 Other Standard Model processes

There are some other Standard Model processes which produce a significant number of jets but whose cross-sections are too small to contribute to the analysis. This is the case of the di-boson background (WW, WZ and ZZ) and the associated $t\bar{t}$ +Higgs production. For both samples, the number of events predicted for 20.3 fb^{-1} was < 1 in all the control and signal regions in the b-jet stream of the analysis. Given this result, it is also expected that the contribution from tri-boson processes will be $\sim$0.

6.4 Summary of central background values

Table 6.3 summarizes the predictions of background processes in confirmation and signal regions.

Provided the expected number of Standard Model events in the corresponding control region is greater than two, the number of observed events in that control region is used in a fit to determine the Standard Model background, as described in section 5.7. For these fits, electron and muon channels are added in to a single 'leptonic' channel. In both streams of the analysis (flavour and M_{J}^{Σ}), if insufficient event counts are expected in the appropriate control regions then the prediction is taken from Monte Carlo. This has the disadvantage that without the fit it is not possible to factorise the detector uncertainties in the ratio (equation 5.19). It should be noted that other than $t\bar{t}$ the yield from other background sources are very small such that their contributions to the control regions are

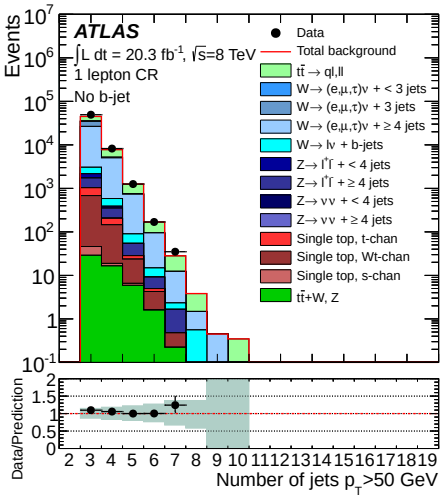

(a) W control region (b-jet veto)

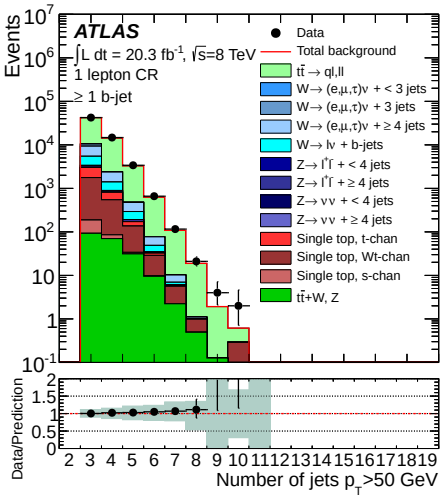

(b) $t\bar{t}$ control region (≥ 1 b-jet)

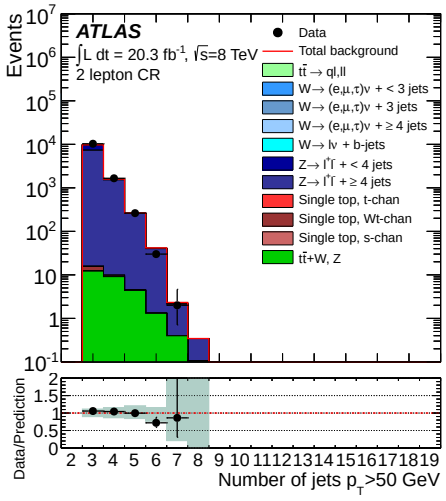

(c) Z control region

Figure 6.10: Jet multiplicity distributions for $t\bar{t}$, W and Z control regions (same as control regions but without the cut in M_{J}^{Σ}). Here the different processes are separated into several channels to appreciate the relative contribution of each subprocess. Note that in (c) many processes (almost all containing W bosons) have a negligible contribution (i.e. < 0.1 predicted events). The error band indicates systematic uncertainties only.

Multijet + b-jet Signal Regions										
	Confirmation Regions			**Signal Regions**						
Process	**7j50**			**8j50**			**9j50**			**10+j50**
	0 bs	1 b	$\geq$2 bs	0 bs	1 b	$\geq$2 bs	0 bs	1 b	$\geq$2 bs	
Multi-jets	260.69	230.50	168.44	27.14	30.10	26.00	2.95	4.00	4.44	1.23
$t\bar{t} \to q\ell, \ell\ell$	27.82	104.34	187.33	3.46	15.48	29.75	0.41	1.85	4.01	0.08
W + jets	26.91	8.37	1.82	2.92	0.93	0.29	0	0.36	0	0
$W + b/\bar{b}/b\bar{b}$ + jets	2.35	3.09	3.95	1.16	0	0	0	0	0.19	0
Z + jets	7.34	4.08	3.09	0.56	0.08	0	0	0	0	0
$t\bar{t} + V$	1.42	3.66	5.15	0.26	0.77	1.06	0.03	0.17	0.11	0.08
Single Top	1.09	6.89	6.55	0.37	0.90	1.75	0	0.17	0.10	0
Total SM	327.62	360.93	376.33	35.87	48.26	58.85	3.39	6.55	8.85	1.39
	6j80			**7j80**			**8+j80**			
	0 bs	1 b	$\geq$2 bs	0 bs	1 b	$\geq$2 bs	0 bs	1 b	$\geq$2 bs	
Multi-jets	111.68	111.34	83.53	9.07	10.72	10.19	0.75	1.18	1.44	
$t\bar{t} \to q\ell, \ell\ell$	10.50	43.67	67.66	0.34	4.34	10.03	0.07	0.64	1.48	
W + jets	14.66	6.34	0.47	0.46	0.29	0	0	0	0	
$W + b/\bar{b}/b\bar{b}$ + jets	1.27	1.54	2.41	0.68	0	1.05	0	0	0.19	
Z + jets	6.37	3.35	1.29	0.41	0.19	0.65	0	0	0	
$t\bar{t} + V$	0.45	1.56	1.97	0.07	0.19	0.38	0.02	0.02	0.03	
Single Top	1.12	2.80	3.23	0.64	0.50	0.92	0	0	0.13	
Total SM	146.04	170.59	160.55	11.67	16.24	23.22	0.84	1.84	3.27	

Multijet + M_J^{Σ} Signal Regions								
	7j50		**8+j50**		**9+j50**		**10+j50**	
	M_J^{Σ}/GeV>340	>420	>340	> 420	>340	>420	>340	>420
Multi-jets	134.5	55.4	52.4	26.5	11.8	7.0	2.3	1.6
$t\bar{t} \to q\ell, \ell\ell$	49.4	18.7	26.9	14.2	4.7	3.4	0.8	0.6
W + jets	9.4	3.2	0.8	0.4	0.0	0.0	0.0	0.0
$W + b/\bar{b}/b\bar{b}$ + jets	0.4	0.0	0.3	0.3	0.0	0.0	0.0	0.0
Z + jets	8.3	2.3	2.3	1.4	0.1	0.0	0.0	0.0
$t\bar{t} + V$	1.9	0.7	1.2	0.6	0.3	0.1	0.1	0.1
Single Top	3.0	1.3	1.3	0.4	0.3	0.3	0.0	0.0
Total SM	206.9	81.6	85.3	43.8	17.0	10.8	3.1	2.2

Table 6.3: Number of events predicted for the background contributions and the total SM prediction. All predictions, except for the multi-jets, come from MC. These are the input to the fit described in section 5.7.

small. This is in part a consequence of that the signal region cuts (which are also applied to the control regions) are designed to remove such backgrounds.

6.5 Background uncertainties

Every measurement of a physical observable is accompanied by an uncertainty. Theoretical or phenomenological predictions also have uncertainties, either because calculations can only be carried out up to a certain order in perturbation theory, or ultimately because the parameters and tunnings they rely on are based on data which was also measured with a finite precision instrument. In this section I will describe the instrumental (i.e. experimental) and theoretical uncertainties associated to the determination of SM backgrounds. These, in addition to statistical uncertainties, are determinant for the search since they degrade the discriminant power of the analysis.

6.5.1 Multi-jet background uncertainties

Multi-jet background is derived using a data-driven method in which templates formed from events with low jet multiplicity are used to predict the multi-jet content at large jet multiplicity events, as described in section 6.1. Therefore there is no JES and JER uncertainty associated to it (these uncertainties are only applied to MC simulated events).

Uncertainties evaluated for this background are described next.

Closure. The dominant systematic uncertainty on the multi-jet background is the template method itself. It is quantified from the degree of agreement to data measured events in a large number of control regions where few signal events are expected. The method is similar to the one used in ref. [31], but adapted to the signal regions used here. These multi-jet control regions either have low multiplicity or have large multiplicity and low $E_{\mathrm{T}}^{\mathrm{miss}}/\sqrt{H_{\mathrm{T}}}$, being then orthogonal to the signal regions and also to the regions were the template is taken (see sketch in table 5.6), as defined in table 6.4. For the '6j50' and '5j80' control regions the template is formed from events selected with prescaled multijet triggers (see table 5.1) that require one lower in jet multiplicity: five jets of $p_{\mathrm{T}} > 50$ GeV or four jets with $p_{\mathrm{T}} > 80$ GeV, respectively.

Jet multiplicity	$p_{\mathrm{T}}^{\mathrm{min}}$	$E_{\mathrm{T}}^{\mathrm{miss}}/\sqrt{H_{\mathrm{T}}}$ bins	b-jet or M_{J}^{Σ} bins
		'Flavor' analysis stream	
exactly 6	50 GeV	(1.5;2.0], (2.0;2.5], (2.5;3.5], (4.0;∞)	0, 1, 2+ b-jets
exactly 7	50 GeV	(1.5;2.0], (2.0;2.5], (2.5;3.5]	0, 1, 2+ b-jets
exactly 8	50 GeV	(1.5;2.0], (2.0;2.5], (2.5;3.5]	0, 1, 2+ b-jets
exactly 9	50 GeV	(1.5;2.0], (2.0;2.5], (2.5;3.5]	0, 1, 2+ b-jets
10 or more	50 GeV	(1.5;2.0], (2.0;2.5], (2.5;3.5]	b-jet blind
exactly 5	80 GeV	(1.5;2.0], (2.0;2.5], (2.5;3.5], (4.0;∞)	0, 1, 2+ b-jets
exactly 6	80 GeV	(1.5;2.0], (2.0;2.5], (2.5;3.5]	0, 1, 2+ b-jets
exactly 7	80 GeV	(1.5;2.0], (2.0;2.5], (2.5;3.5]	0, 1, 2+ b-jets
8 or more	80 GeV	(1.5;2.0], (2.0;2.5], (2.5;3.5]	b-jet blind
		'M_{J}^{Σ}' analysis stream	
exactly 6	50 GeV	(1.5;2.0], (2.0;2.5], (2.5;3.5], (4.0;∞)	$M_{\mathrm{J}}^{\Sigma} \geq 340$, 420 GeV
exactly 7	50 GeV	(1.5;2.0], (2.0;2.5], (2.5;3.5]	$M_{\mathrm{J}}^{\Sigma} \geq 340$, 420 GeV
8 or more	50 GeV	(1.5;2.0], (2.0;2.5], (2.5;3.5]	$M_{\mathrm{J}}^{\Sigma} \geq 340$, 420 GeV
9 or more	50 GeV	(1.5;2.0], (2.0;2.5], (2.5;3.5]	$M_{\mathrm{J}}^{\Sigma} \geq 340$, 420 GeV
10 or more	50 GeV	(1.5;2.0], (2.0;2.5], (2.5;3.5]	$M_{\mathrm{J}}^{\Sigma} \geq 340$, 420 GeV

Table 6.4: Multi-jet control regions used to asses the degree of agreement between measurements and the template prediction. The third column indicates the $E_{\mathrm{T}}^{\mathrm{miss}}/\sqrt{H_{\mathrm{T}}}$ range, in units of $\mathrm{GeV}^{1/2}$, for which the measurements in data and simulation are done.

The (symmetrical) systematic uncertainty on any signal region is given by the maximal deviation (between data and background prediction) in any of the closure regions of the same jet multiplicity or lower, for the same b-tagging requirements. For example, the systematic on the signal region '9j50-0bjets' is given by all the '6j50-0bjets', '7j50-0bjets',

'8j50-0bjets', and '9j50-0bjets' but not the ≥1 b-tagged samples or the '10j50' regions. A similar conservative approach is applied for the M_{J}^{Σ} stream, where the uncertainty is taken as the maximal deviation in any of the closure regions of the same jet multiplicity or lower and the same M_{J}^{Σ} cut. For example, the systematic on the signal region '8+j50-MJ420' is given by all the '6j50-MJ420', '7j50-MJ420', and '8+j50-MJ420' but not the $M_{\mathrm{J}}^{\Sigma} >$ 340 GeV samples or the '9+j50' regions. In general a closure in the range 5% to 15% is observed where large numbers of events are available, yet the uncertainty can grow large in statistically limited bins (up to ∼52% uncertainty was found for the most stringent '10j50' and $M_{\mathrm{J}}^{\Sigma} > 420$ GeV control region).

Heavy Flavour Content. The main source for the missing energy in the multi-jet background is the mismeasurement of jets (section 6.1.1). There is yet a residue of *true* missing energy due to the presence of neutrinos produced in the decay of hadrons containing bottom or charm quarks (if the associated W boson decays leptonically). This $E_{\mathrm{T}}^{\mathrm{miss}}$ is not invariant with the number of jets since the fraction of events with b-jets increases from $\sim 1/3$ to $\sim 1/2$ across the multiplicity range – an increase of $\sim 1/6$. This affects the template invariance because the $E_{\mathrm{T}}^{\mathrm{miss}}$ derived at low jet multiplicity underestimates the true $E_{\mathrm{T}}^{\mathrm{miss}}$ at large multiplicity. The treatment of this uncertainty is complex and differs depending on the signal region being considered, as described below.

- The 0-b-tag flavour-stream signal regions are populated with events that either don't have b-jets, or do have them but are not tagged as such. Events from the later class are the source of true $E_{\mathrm{T}}^{\mathrm{miss}}$ so the uncertainty is associated to the inefficiency of tagging b-jets. The b-tagger is used at its 70% operating point so the probability of an event with a b-jet failing to be b-tagged is ∼0.3. To account for the relative increase from $\sim 1/3$ to $\sim 1/2$ in the fraction of b-jets, a template is formed with a mixture of 10% of b-tagged and 90% of b-veto events[1] to overcompensating the content of b-jets. The event yield predicted in the signal regions using this template is compared to the default (that depends on a template formed by 100% b-veto events) and the difference is taken as a systematic uncertainty.

- The 1-b-tag and ≥2-b-tag flavour-stream regions. These bins have small fake b-tagged background in either the control regions or signal regions. However the assumption that the template holds in the presence of b-jets is less trivial. The degree of closure is addressed numerically using a fully hadronic $t\bar{t}$ sample. The direct prediction of events at large jet multiplicity (i.e. how many events have 8 jets) is compared to the template extrapolation, and the difference taken as the systematic. This is the dominant component being ∼ 25%.

- For the 10j50 flavour-stream signal region where there is no splitting by the number of b-jets (see table 5.5) the template is formed by the sum of templates formed with 0, 1 and ≥2 b-jets. In this case, the systematic comes from forming a template without

[1] The 10% proceeds from $2 \cdot 1/6 0.3$, where '2' is a conservative safety factor

any splitting by number of b-tags (b-jet blind).

- The multi-jet + M_{J}^{Σ} signal regions make no b-tagging requirements, so the b-jet systematic is computed by comparing the default prediction with the sum of predictions from two separate templates requesting: 0 b-jets and $\geq$1 b-jets.

Soft Energy. This systematic evaluates the disturbance of soft energy deposits by two contributions. First, the data-to-Monte Carlo agreement was measured for all control regions (table 6.4) under different pile-up conditions in bins of the number of primary vertices (N_{PV}): $0 \leq N_{\mathrm{PV}} < 8$, $8 \leq N_{\mathrm{PV}} < 14$, $N_{\mathrm{PV}} \geq 14$. Deviations are encompassed by the closure systematic, so no separate uncertainty is used for this effect. Second, the stability of the template following SoftTerm re-shaping (section 6.1.2) is assessed by including soft jets (between 20 and 30 GeV) to the $E_{\mathrm{T}}^{\mathrm{CellOut}}$ spectrum; this is done in equation 6.8 by the substitution: $E_{\mathrm{T}}^{\mathrm{CellOut}}/H_{\mathrm{T}} \rightarrow \left(E_{\mathrm{T}}^{\mathrm{CellOut}} + p_{\mathrm{T}}^{\text{soft-jets}}\right)/H_{\mathrm{T}}$. The difference between templates formed with and without the inclusion of soft jets impact the background determination with an uncertainty 3–15%.

Trigger Inefficiency. As documented earlier in table 5.2 there is a small inefficiency in the trigger for the low jet multiplicity events used to build the templates. Over the trigger turn-on the acceptance changes abruptly and then even small discrepancies between data and MC can be strongly amplified and impact the relative event yield. To evaluate how much this affects the template, the weight of events where the 6^{th} jet has a transverse momentum between 50 (the actual $p_{\mathrm{T}}^{\min}$ for the control region) and 55 GeV is increased by $1/\epsilon$, where $\epsilon = 0.83$ is the trigger efficiency estimated from figure 5.1. The difference between the re-weighted and standard templates is taken as a systematic uncertainty, which is <1% for all selections.

Leptonic-like background subtraction The multijet background is derived from data upon subtraction of contributions from simulated $t\bar{t}$, W and Z processes. Therefore, theoretical and experimental uncertainties on these samples (see section 6.5.2) are propagated to the multi-jet prediction in the signal regions. This side-effect is evaluated by scaling up and down the leptonic contribution used to form the template, from equation 6.5:

$$N'\left(\mathcal{S}_{\mathrm{T}}^{\mathrm{miss}}, n_{\mathrm{jet}}\right) = N_{data}\left(\mathcal{S}_{\mathrm{T}}^{\mathrm{miss}}, n_{\mathrm{jet}}\right) - (1 \pm C_l)\, N_{MC,\text{`leptonic'}}\left(\mathcal{S}_{\mathrm{T}}^{\mathrm{miss}}, n_{\mathrm{jet}}\right) \tag{6.11}$$

where C_l is measured form the closure observed in the leptonic control regions (figures 6.7–6.10). A conservative value of C_l=0.3, results in a (asymmetrical) uncertainty between 5% and 20%, depending on the signal region.

6.5.2 Non-multi-jet background uncertainties

The 'leptonic' background predictions employ the Monte Carlo simulations described in section 5.2.2. When predictions are taken directly from the Monte Carlo simulations,

event yields are subject to experimental and theoretical uncertainties. Uncertainties arise due to imperfect modelling of the proton beams state, the parton scattering, shower and hadronization processes, the interactions of those particles with the detector, the description (geometry and/or materials) of the detector, and/or the detector signal response to those interactions. These are generally split in two categories: 'theoretical' uncertainties gathering the incomplete knowledge from the proton-proton collision to the particle hadronization, and 'detector' uncertainties collecting the remaining ones. Systematic experimental and theoretical uncertainties associated with the 'leptonic' backgrounds are described in sections 6.5.2.1 and 6.5.2.2 respectively.

6.5.2.1 Detector Uncertainties

From the point where signals in the detector are simulated, the ATLAS software machinery is applied equally to data from real collisions and from Monte Carlo simulations, including the trigger selection, object reconstruction, identification and calibration. Although the true sources of experimental uncertainties are prior to these stages, their effect in this analysis is evaluated at the level of the final observables. For example, a miss-modeling of the thickness of the lead absorber plates in the electromagnetic calorimeter will be (implicitly) described by an ulterior systematic: the jet energy scale uncertainty. The dominant experimental uncertainties for this analysis are described next.

The values of all the systematics for all backgrounds in all signal regions is given in appendix B.

Jet energy scale (JES). The JES uncertainty [92,222] encompasses uncertainties arising from in-situ analyses (Z +jet balance, gamma+jet balance and multijet balance), MC non-closure, pile-up, the unknown flavour composition and from flavour response [223]. The JES uncertainty is paramatrized in terms of the jet p_{T}, η, the distance to the closest jet (having $p_{\mathrm{T}} > 7$ GeV) and the number of primary vertices. The overall fractional JES uncertainty is in general <4% for central jets above 20 GeV, grows for larger η and decreases for higher p_{T}. The yields for a given region are recalculated by rerunning the analysis with all jet momentum shifted up (down) by one standard deviation of the jet energy scale as recommended by the ATLAS Jet/Etmiss group [224]; the same is done for the close-by uncertainty. The differences in event yield between the 'shifted' runs and the 'nominal' run quantify the systematic uncertainty for the region. 'Up' and 'down' variations are kept separate as two asymmetric errors. The JES uncertainty is in general <20% (<40%) for top pair ($W + jets$) backgrounds but can be as large as 50% for some regions.

Jet energy resolution (JER). Variations of the jet energy within the bounds of the energy resolution [217] are a source of $E_{\mathrm{T}}^{\mathrm{miss}}$ as described in section 6.1.1. The JER uncertainty introduces fluctuations into this bound and therefore modifies the $E_{\mathrm{T}}^{\mathrm{miss}}$. The impact of this uncertainty is evaluated using standard ATLAS JER tools provided by the

Jet/ETmiss group [225,226]. For each jet its energy is scaled by a random factor taken from a Gaussian distribution with unit mean and a width equal to the resolution function; the resolution is in turn parametrized as a function of the p_{T} and η of the jet being 'smeared' (actually individual jets are not 'smeared', although is common language). The analysis is run shifting randomly the p_{T} of all jets, and the difference with respect to the 'nominal' run is taken as a one-side (symmetrical) uncertainty. This uncertainty is in general less than 1% but some backgrounds with very few events have up to 20% in some regions. This variation is also propagated to the $E_{\mathrm{T}}^{\mathrm{miss}}$ but the impact is very small.

This and the JES uncertainties have a dual role on signal regions that cut on the total jet mass M_{J}^{Σ}. They disturb the jet counting for signal regions (as it happens for the 'flavour' stream) and the energy of the jets forming the composite jets, that in turn propagate to M_{J}^{Σ}. Therefore, no specific uncertainty is designed for M_{J}^{Σ}.

Pile-up re-weighting As described in section 5.4.3.1 simulated events receive a weight to acquire the same distribution of μ (number of proton-proton collisions per bunch crossing) than data. A one-sided (symmetrical) uncertainty is generated by scaling up the weight by 10% and measuring the difference with respect to 'nominal' numbers. This uncertainty is typically a few percent but can reach to 20% for some backgrounds in some regions.

Heavy flavour tagging efficiency The systematic uncertainties of the efficiency and mistag of heavy flavour tagging impact the b-jet stream, as events may migrate from signal regions vetoing b-jets to signal regions requesting with one or more b-jets, and viceversa. The event scale factor is shifted up (down) by shifting up (down) the scale factor of individual jets

$$\mathcal{F}_{\substack{up\\down}} = \prod_{jets} \mathcal{F}_j \left(1 \pm \Delta F_j\right) \tag{6.12}$$

where both the nominal jet scale factor, $\mathcal{F}_j$ and its error $\Delta\mathcal{F}_j$ are function of the jet p_{T}, η the jet true flavour (b-, c/τ- or light-jets), and the tagger decision (the tagger decision defines if $\mathcal{F}$ corresponds to tagging inefficiency or mistag of fakes). Uncertainties for each flavour are kept separate. For example a systematic for c-tag is done shifting the scale factors for all true c-jets of the event, leaving the scale factors at their nominal values for other jet falvours. Again, the differences in event yield between the 'shifted' run and the 'nominal' run quantify the systematic uncertainty. 'Up' and 'down' variations are taken as asymmetric errors.

$E_{\mathrm{T}}^{\mathrm{miss}}$ **soft terms.** For this uncertainty the soft component of the $E_{\mathrm{T}}^{\mathrm{miss}}$, that is $E_{\mathrm{T}}^{\mathrm{CellOut}}$, is scaled up and down, and the events in the signal regions are measured for the two values of the $E_{\mathrm{T}}^{\mathrm{miss}}$. The difference of each variation with respect to the (unchanged) 'nominal' results provides two-sided uncertainty. It is almost always negligible relative to other uncertainties.

6.5.2.2 Theoretical Uncertainties

The event selection described in section 5.5 reduces the yield of most Standard Model backgrounds in the signal regions. Events surviving this selection must exhibit particular features, like large jet multiplicities, some of which may not be accurately described by the simulation. Theoretical uncertainties from different sources –e.g. the dependence on the generator, parton showering method, hadronization model and tunes– are evaluated by comparing the baseline Monte Carlo samples used for the analysis to other simulations. Some of the comparisons (of the most important uncertainties) are computed using samples with full (or AtlasFast-II) simulation and comparing observables at the detector level, whereas for others, the comparison is done at truth level using objects reconstructed with the stable particles of the simulation (instead of signals at the detector).

The overall cross-section for $t\bar{t}$, W and Z are reasonably well known ($\bar{t}$ is largest and is $\sim$10%). For the other minor processes of single top and $t\bar{t}+V$ the cross-section uncertainty is significant and is included separately.

The treatment of the systematics for different backgrounds follow the recommendations of the ATLAS SUSY working group ([227]), as described next

$t\bar{t}$ Systematics. The default generator for the $t\bar{t}$ process used is SHERPA with up to four additional partons in the ME.

- Variations due to the use of other **generators** are studied using ALPGEN showered with HERWIG (with underlying event provided by JIMMY). Up to 4 additional partons are present in the ME calculation of these samples. The full difference between the prediction of the two samples at detector level is taken as a symmetrical uncertainty. This systematic uncertainty is considered redundant to the scale variations, and therefore will not be considered.
- The effect of the **PDF** on this background is checked applying an event weight to the baseline samples (that use the NLO CT10 set of PDFs) to resemble the LO equivalent CTEQ6L1 PDF set. For this the ATLAS PDFTool [228] is used. Again the difference between the two is taken as a symmetrical uncertainty ($\lesssim$ 15%).
- All Monte Carlo events are generated at a specific scale (for renormalization and factorization), which is process and generator dependent. The **factorisation scale** uncertainty is evaluated at true level using SHERPA samples produced with the factorisation scale increased and decreased by a factor 2 [229]. The difference between the prediction from the two samples is taken as a symmetrical systematic ($\lesssim$ 10–50%).
- SHERPA samples with shift in the **scale of the additional parton splitting** were not available at the time of the analysis (see appendix B in ref. [230]). ALPGEN samples with this scale shifted up and down are compared to the baseline ALPGEN sample at truth level; the same uncertainty is assumed to apply to SHERPA as it is

at the same order (20–30%)

- SHERPA samples produced with up to three additional partons and with the **CKKW matching scale** [231] shifted up and down by 10 GeV (the default is 30 GeV), are compared at truth level to the nominal sample. Half the difference between the prediction of the two shifted sets is taken as a symmetrical systematic uncertainty. It is checked that the sample with the nominal scale and up to three additional partons in the ME lie approximately half way between these two samples 1–25%).
- The yield dependence on the **number of partons in the ME** is measured using SHERPA samples with up to three additional jets. The difference against the nominal values at truth level is taken as a symmetric uncertainty (10–50%). The reduction in the number of partons implies a greater dependence on the parton shower to meet the high multiplicity required by signal regions.
- The two k-factor re-weighting procedure that is used to improve the agreement of Monte Carlo with the data (see section 5.4.3.2) is not a full NLO calculation. Therefore the difference between the weighted and unweighted samples is taken as a symmetric systematic for the **re-weighting** uncertainty (20–40%).
- Traditionally a **parton shower systematic** on $t\bar{t}$ backgrounds is found by comparing PowHeg samples showered with PYTHIA versus samples showered with HERWIG/JIMMY. However, as these two genetarors do not contain additional ME partons the systematic would be largely overestimated with this comparison in the high multiplicity regions. A parton shower systematic was already considered when reducing the number of partons in the ME calculation as more jets are required to come from the parton shower to meet the high multiplicity requirement of signal regions. Therefore no systematic is added to cover explicitly for this effect.

Comparing the shape differences between the control and signal region selections it can be seen that there is some cancellation of uncertainties for signal regions having sufficient statistics in the corresponding control region (see section 5.7.)

W+jets Systematics. The default generator for this background is SHERPA using the CT10 PDF set.

- A large statistics sample of ALPGEN interfaced with PYTHIA (with the Perugia 2011 C tune) containing up to five additional partons in the ME is used to test an **alternative generator**. This PYTHIA showered sample is recommended by the ATLAS Jet/Etmiss group as it reproduces better the jet shapes. The difference between this and the baseline sample at truth level is taken as a symmetric systematic.
- The effect of the **PDF** is checked as for $t\bar{t}$ background re-weighting events to the LO equivalent PDF CTEQ6L1 using the ATLAS PDFTool. The difference between the two is taken as a symmetrical uncertainty for the PDF.

- The nominal generator has up to five added partons in the ME in a massless five flavour scheme. Then parton shower is responsible for the production of additional jets at all signal regions. The **parton shower** systematic is assessed with a comparison at particle level between samples generated with the multi-leg ALPGEN generator interfaced to two different showering schemes: PYTHIA and HERWIG
- Dedicated SHERPA (with the CT10 PDF set) produced with three and four, or exactly four additional partons in the ME are compared at truth level to obtain a systematic on the **number of partons in the ME**.

The PDF uncertainty is found to be small ($< 20\%$) with larger contributions coming from the different generator (30–100%), parton shower (30–100%) and number of partons (25–100%). Quite good factorisation of these is also seen between the signal and control regions. In the tightest regions (where the vector boson backgrounds are very small) large statistical uncertainties due to the finite size of the samples become dominant.

$W + b/\bar{b}/b\bar{b}$**+jets Systematics.** The default generator for this process is SHERPA with massive b-quark treatment and up to 4 partons in the ME. The $W+b$ cross-section has been measured to a precision of $\sim 24\%$. This value is added in quadrature to the systematic uncertainty for $W + jets$.

$Z \to \nu\nu$**+jets Systematics.** The default generator for this process is SHERPA with up to five additional partons in the ME calculation. There do not exist large samples for the evaluation of all the different systematics however as this is a very similar process to $W + jets$, some of the systematic uncertainties for the $Z + jets$ are estimated from $W + jets$ other than the degree of agreement in the control regions where the dedicated Z validation regions are used.

Single Top Systematics. The Wt production dominates both the signal and control regions over the other single top channels (almost 100%), then systematics are computed only for this process. No multi-leg generators are available for this process so the reliability of additional jets in the final state comes from parton shower.

- Samples generated using POWHEG interfaced to PYTHIA are compared to the nominal sample (simulated using MC@NLO +HERWIG) and the difference is taken as a systematic for **alternative generator** (10–80%).
- Two PowHeg simulations (both with DR, see below), one interfaced to PYTHIA and the other interfaced to HERWIG are compared to between each other to quantify the uncertainty due to **parton shower**. There is a good agreement between these simulations (10–100%).
- The dominant systematic for this background is due to the **interference with** $t\bar{t}$. At NLO the Wt channel receives large corrections due to diagrams that can be interpreted as top pair production, followed by the decay of the antitop [167]. PowHeg

samples have been produced with diagram subtraction (DS) and diagram removal (DR) [1]. The difference between them is taken as a one-sided systematic that measures the interference between Wt and $t\bar{t}$ production (50–100%).

$t\bar{t}$ +W/Z Systematics. The predictions of these processes using the baseline MadGraph are compared with two ALPGEN samples (with up to 2 and up to 3 additional partons in the matrix element) to check the generator systematic. The uncertainty ranges between 10–40% for the generator and 20–100% for the number of partons. The uncertainty in the cross-section is 22%.

6.5.3 Other experimental uncertainties

On top of the uncertainties in the backgrounds described above, a flat 0.6% luminosity uncertainty is applied for the entire 2012 dataset. Uncertainties associated to lepton reconstruction and identification are considered negligible when compared to the uncertainties already described, and are not included in the analysis.

[1] In DR all diagrams containing an intermediate $t\bar{t}$ pair are removed at the amplitude level, completely eradicating the interference with $t\bar{t}$. In DS the differential cross-section is modified with a local subtraction term which removes the resonant top pair contribution, but leaves the effect of the interference in the amplitude.

7
Results & Interpretations

7.1 Results

Figures 7.1–7.3 show the $E_{\mathrm{T}}^{\mathrm{miss}}/\sqrt{H_{\mathrm{T}}}$ distributions for all the signal regions of both analysis streams. No apparent excess is seen for any of the signal regions. In order to check the consistency of the data with the background-only and signal hypotheses, a simultaneous profile maximum likelihood fit is performed in the control and signal regions, for each of the analysis streams separately as desribed in section 5.7.

Tables 7.1–7.2 summarise the fit results; the number of events observed in each of the signal regions, as well as their Standard Model background expectations, are reported before and after the fit to the control regions. In each of the signal regions, agreement is found between the Standard Model prediction and the data. The fit results are checked for stability and consistency with the background modelling based on the predictions described in sections 6.1 and 6.2. There is no indication of a systematic mis-modelling of any of the major backgrounds; the fitted values are in all cases consistent with the Monte Carlo simulation predictions.

In addition to the event yields, the probability (p_0-value) that a background-only pseudo-experiment is more signal-like than the observed data is given for each individual signal region. To obtain these p_0-values, the fit in the signal region proceeds in the same way as the control-region-only fit, except that the number of events observed in the signal region is included as an input to the fit. Then, an additional parameter for the non-Standard-Model signal strength, constrained to be non-negative, is fitted. The significance ($\mathcal{Z}$) of the agreement between data and the Standard Model prediction is given. No significant deviations from the Standard Model prediction are found. The 95% confidence level (CL) upper limit on the number of events ($N_{\mathrm{BSM}}^{95\%}$) and the cross section times acceptance times efficiency ($\sigma_{\mathrm{BSM,max}}^{95\%} \cdot \mathcal{A} \cdot \epsilon$) from non-Standard-Model production are also provided, neglecting in the fit possible signal contamination in the control regions.

7.2 Model interpretations

In the absence of significant discrepancies, exclusion limits at 95% CL are set in the context of several simplified supersymmetric models and the cMssm model, all described

	Signal region												
	8j50			**9j50**			**10j50**	**7j80**			**8j80**		
b-jets	0	1	≥ 2	0	1	≥ 2	—	0	1	≥ 2	0	1	≥ 2
Observed events	40	44	44	5	8	7	3	12	17	13	2	1	3
Total events after fit	35 ± 4	40 ± 10	50 ± 10	3.3 ± 0.7	6.1 ± 1.7	8.0 ± 2.7	1.37 ± 0.35	11.0 ± 2.2	17 ± 6	25 ± 10	0.9 ± 0.6	1.5 ± 0.9	3.3 ± 2.2
Fitted $t\bar{t}$	2.7 ± 0.9	11.8 ± 3.0	23.0 ± 5.0	0.36 ± 0.18	1.5 ± 0.5	3.2 ± 1.1	$0.06^{+0.09}_{-0.06}$	$0.00^{+0.26}_{-0.00}$	5.0 ± 4.0	12 ± 9	$0.10^{+0.14}_{-0.10}$	$0.32^{+0.67}_{-0.32}$	$1.5^{+1.9}_{-1.5}$
Fitted W+jets	$2.0^{+2.6}_{-2.0}$	$0.62^{+0.81}_{-0.62}$	$0.20^{+0.28}_{-0.20}$	–	$0.24^{+0.65}_{-0.24}$	–	–	$0.07^{+0.38}_{-0.07}$	$0.29^{+0.37}_{-0.29}$	–	–	–	–
Fitted others	$2.9^{+1.8}_{-1.8}$	$1.7^{+1.5}_{-1.2}$	$2.8^{+2.3}_{-2.0}$	0.03 ± 0.03	0.38 ± 0.25	$0.40^{+0.60}_{-0.24}$	0.08 ± 0.08	$1.9^{+1.1}_{-0.9}$	$0.71^{+0.31}_{-0.25}$	$2.6^{+1.7}_{-1.1}$	0.02 ± 0.02	0.02 ± 0.02	$0.32^{+0.36}_{-0.21}$
Total events before fit	36	48	59	3.4	6.6	8.9	1.39	11.7	16	23	0.8	1.8	3.3
$t\bar{t}$ before fit	3.5	15	30	0.41	1.8	4	0.08	0.34	4	10	0.08	0.6	1.5
W+jets before fit	2.9	1.0	0.29	–	0.40	–	–	0.46	0.29	–	–	–	–
Others before fit	2.4	1.8	2.8	0.03	0.34	0.4	0.08	1.8	0.89	3.0	0.02	0.02	0.35
Multi-jets	27 ± 3	30 ± 10	26 ± 10	3.0 ± 0.6	4.0 ± 1.4	4.4 ± 2.2	1.23 ± 0.32	9.1 ± 1.6	11 ± 4	10 ± 4	0.75 ± 0.56	1.2 ± 0.5	1.4 ± 1.0
$N^{95\%}_{\mathrm{BSM}}$ (exp)	16	23	26	5	7	8	4	10	17	14	4	4	6
$N^{95\%}_{\mathrm{BSM}}$ (obs)	20	23	22	7	9	7	6	10	16	12	5	3.5	6
$\sigma^{95\%}_{\mathrm{BSM,max}} \cdot \mathcal{A} \cdot \epsilon$ (exp) [fb]	0.8	1.2	1.3	0.26	0.36	0.40	0.19	0.5	0.8	0.7	0.18	0.18	0.31
$\sigma^{95\%}_{\mathrm{BSM,max}} \cdot \mathcal{A} \cdot \epsilon$ (obs) [fb]	0.97	1.1	1.1	0.34	0.43	0.37	0.29	0.5	0.8	0.6	0.24	0.17	0.31
p_0	0.24	0.5	0.7	0.21	0.28	0.6	0.13	0.5	0.6	0.8	0.19	0.6	0.5
Significance ($\mathcal{Z}$)	0.7	-0.02	-0.6	0.8	0.6	-0.28	1.14	0.05	-0.14	-1.0	0.9	-0.28	-0.06

Table 7.1: Number of observed and expected (fitted) events for the seven $p_{\mathrm{T}}^{\mathrm{min}} = 50$ and 80 GeV signal regions of the multi-jet + flavour stream. The category indicated by 'others' includes the contributions from $Z + jets$, $t\bar{t}$+W, $t\bar{t}$ +Z, and single top. The table also contains for each signal region the probability, p_0, that a background-only pseudo-experiment is more signal-like than the observed data; the significance, $\mathcal{Z}$, of the agreement between data and the Standard Model prediction; the 95% CL upper limit on the number of events, $N^{95\%}_{\mathrm{BSM}}$, originating from sources other than the Standard Model (rounded to no decimal places); and the corresponding cross section times acceptance times efficiency, $\sigma^{95\%}_{\mathrm{BSM,max}} \cdot \mathcal{A} \cdot \epsilon$. They are simply related by $N^{95\%}_{\mathrm{BSM}} = \sigma^{95\%}_{\mathrm{BSM,max}} \cdot \mathcal{A} \cdot \epsilon \times \mathrm{L}_0^{\mathrm{int}}$.

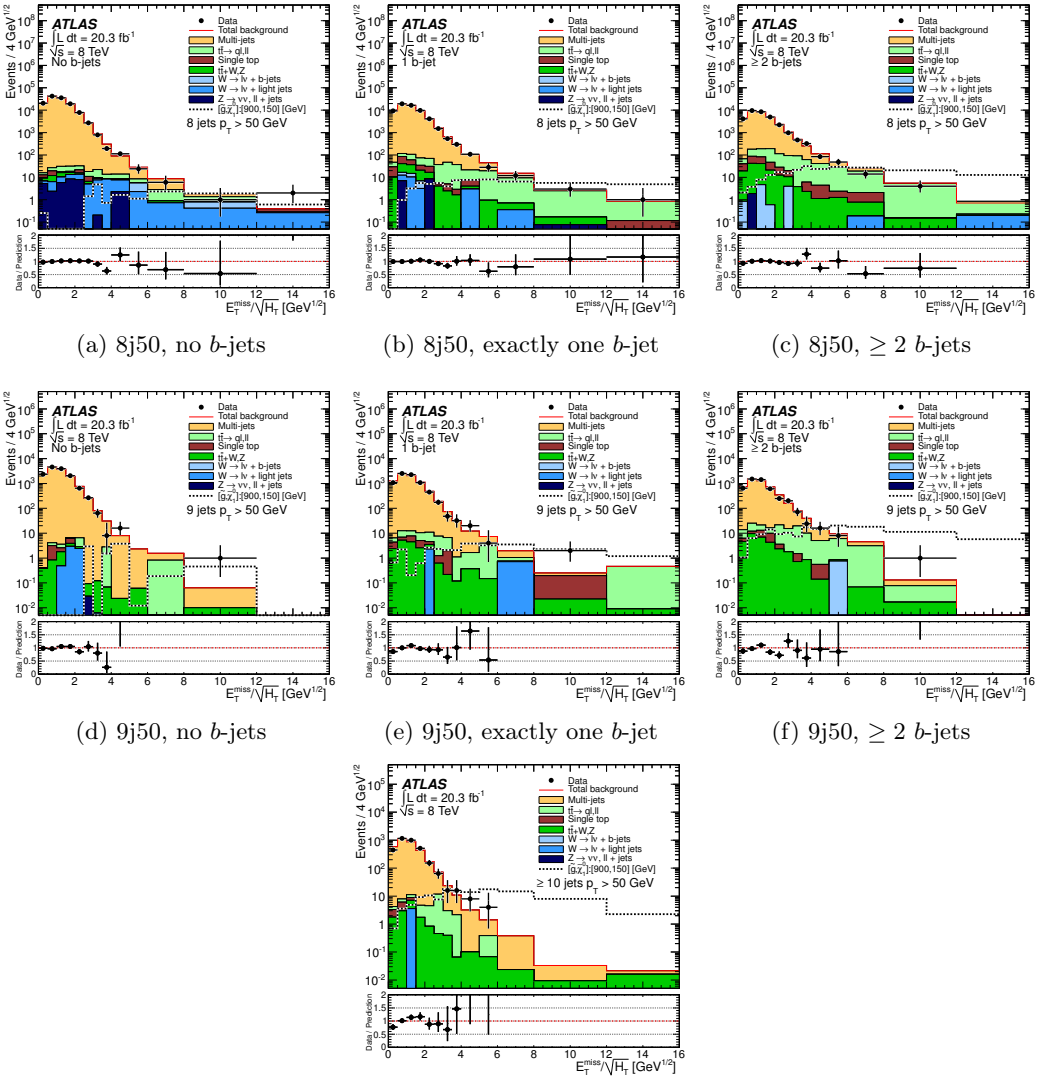

(a) 8j50, no b-jets (b) 8j50, exactly one b-jet (c) 8j50, ≥ 2 b-jets

(d) 9j50, no b-jets (e) 9j50, exactly one b-jet (f) 9j50, ≥ 2 b-jets

Figure 7.1: $E_{\mathrm{T}}^{\mathrm{miss}}/\sqrt{H_{\mathrm{T}}}$ distributions for the multi-jet + flavour stream with $p_{\mathrm{T}}^{\mathrm{min}} = 50$ GeV, and either exactly eight jets, exactly nine jets or ten or more jets with the signal region selection, other than that on $E_{\mathrm{T}}^{\mathrm{miss}}/\sqrt{H_{\mathrm{T}}}$ itself. The b-jet multiplicity increases from no b-jets (left) to exactly one b-jet (center) to at least two b-jets (right). Other details are as for figure 6.4.

in section 2.2.3. Theoretical uncertainties on the SUSY signals are estimated as described in section 6.5.2.2. Combined experimental systematic uncertainties on the signal yield from the jet energy scale, resolution, and b-tagging efficiency in the case of the flavour stream, range from 15% to 25%. Acceptance and efficiency values, uncertainties and other information per signal region are tabulated in HepData [232].

The limit for each signal region is obtained by comparing the observed event count with that expected from Standard Model background plus SUSY signal processes. The resulting exclusion regions are obtained using the CL_s prescription [208]. For the multi-jet + flavour stream a simultaneous fit is performed in all the signal regions for each of the two values of $p_{\mathrm{T}}^{\mathrm{min}}$, and the two fit results are combined using the better expected limit per point in the

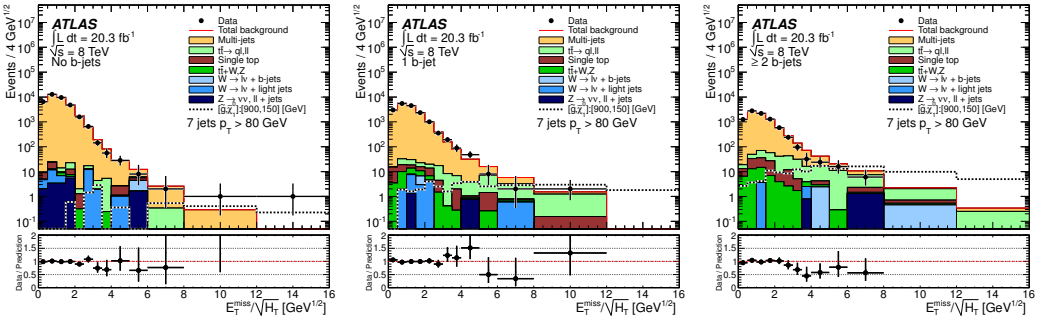

(a) 7j80, no b-jets (b) 7j80, exactly one b-jet (c) 7j80, ≥ 2 b-jets

(d) 8j80, no b-jets (e) 8j80, exactly one b-jet (f) 8j80, ≥ 2 b-jets

Figure 7.2: $E_{\mathrm{T}}^{\mathrm{miss}}/\sqrt{H_{\mathrm{T}}}$ distributions for the multi-jet + flavour stream with $p_{\mathrm{T}}^{\mathrm{min}}$ =80 GeV. The complete signal region selections were applied, other than the final $E_{\mathrm{T}}^{\mathrm{miss}}/\sqrt{H_{\mathrm{T}}}$ requirement. Other details are as for figure 6.4.

parameter space, as described in section 5.7.1.3. For the multi-jet + M_{J}^{Σ} stream the signal region with the best expected limit at each point in parameter space is used. The stream with the better expected limit at each point in parameter space is chosen when combining the two streams. The multi-jet + flavour stream typically has stronger expected exclusion limits than the multi-jet + M_{J}^{Σ} stream. However, in models with large numbers of objects in the final state, and more so in boosted topologies, the multi-jet + M_{J}^{Σ} stream becomes competitive. Limits on sparticle masses quoted in the text are those from the lower edge of the 1σ signal cross-section band rather than the central value of the observed limit.

As shown in the rest of this section, the analysis substantially extends previous published exclusion limits on various models, from Atlas [31, 233] and Cms [234, 235].

‘Gluino–stop (off-shell)’ model

The analysis result is interpreted in a simplified model that contains only a gluino octet and a neutralino $\tilde{\chi}_1^0$ within kinematic reach, and decaying with unit probability according to Eq. 5.2, via an off-shell $\tilde{t}$-squark. The results are presented in the $(m_{\tilde{g}}, m_{\tilde{\chi}_1^0})$ plane in figure 7.4, which shows the combined exclusion. Within the context of this simplified model, the 95% CL exclusion bound on the gluino mass is 1.1 TeV for the lightest neutralino mass up to 350 GeV.

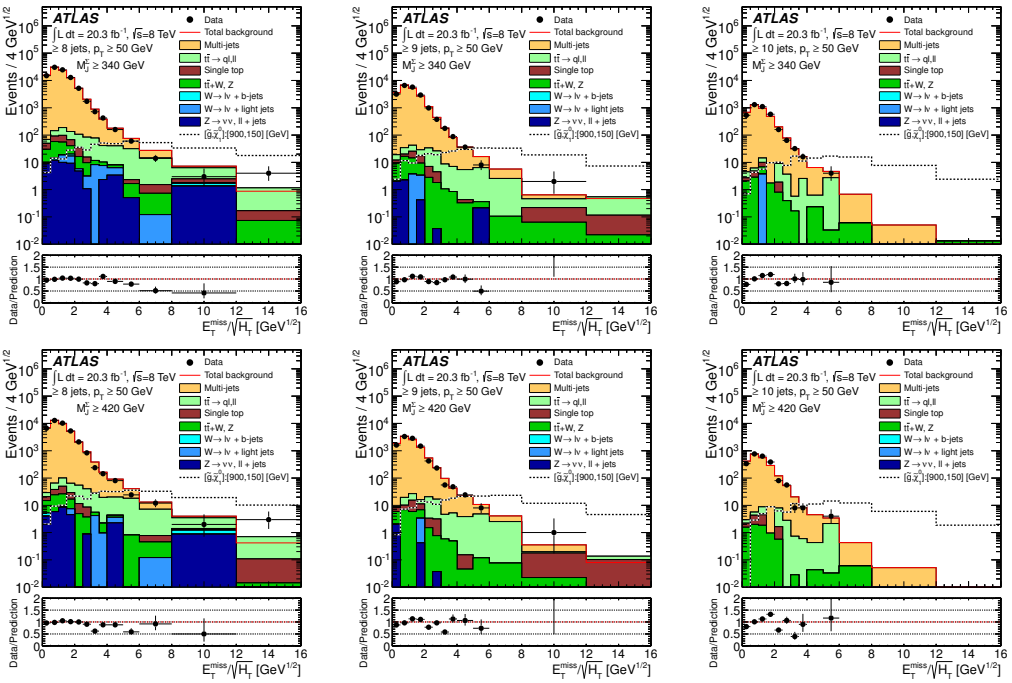

Figure 7.3: $E_{\mathrm{T}}^{\mathrm{miss}}/\sqrt{H_{\mathrm{T}}}$ distributions for the multi-jet + M_{J}^{Σ} stream with the signal region selection, other than the final $E_{\mathrm{T}}^{\mathrm{miss}}/\sqrt{H_{\mathrm{T}}}$ requirement. The figures on the left are for events with $M_{\mathrm{J}}^{\Sigma} > 340$ GeV, while those on the right are for $M_{\mathrm{J}}^{\Sigma} > 420$ GeV. The minimum multiplicity requirement for $p_{\mathrm{T}}^{\mathrm{min}} = 50$ GeV, $R = 0.4$ jets increases from eight (left) to nine (center) and finally to ten jets (left). Other details are as for figure 6.4.

'Gluino–stop (on-shell)' model

In this simplified model, each gluino of a pair decays as $\tilde{g} \rightarrow \tilde{t}+\bar{t}$; $\tilde{t} \rightarrow \tilde{\chi}_1^0+t$. The mass of $\tilde{\chi}_1^0$ is fixed to 60 GeV. The results are presented in the $(m_{\tilde{g}}, m_{\tilde{t}})$ plane in figure 7.5 which shows the combined exclusion limits. Within the context of this simplified model, the 95% CL exclusion bound on the gluino mass is 1.15 TeV for stop masses up to 750 GeV.

'Gluino–squark (via $\tilde{\chi}_1^{\pm}$)' model

In this simplified model, each gluino of a pair decays as $\tilde{g} \rightarrow q + \tilde{q}$ and the squark as $\tilde{q} \rightarrow q' + \tilde{\chi}_1^{\pm} \rightarrow q' + W + \tilde{\chi}_1^0$. Two versions of this model are evaluated, and the combined exclusion results are shown in figure 7.6. In figure 7.6a, the fractional mass splitting, x, defined as $\mathrm{x} = (\mathrm{m}_{\tilde{\chi}_1^{\pm}} - \mathrm{m}_{\tilde{\chi}_1^0})/(\mathrm{m}_{\tilde{\mathrm{g}}} - \mathrm{m}_{\tilde{\chi}_1^0})$, is set to 1/2, while the $\tilde{\chi}_1^0$ mass varies, and the results are shown in the $(m_{\tilde{g}}, m_{\tilde{\chi}_1^0})$ plane. In the second case, the $\tilde{\chi}_1^0$ mass is fixed to 60 GeV while x varies, and the results are presented in the $(m_{\tilde{g}}, \mathrm{x})$ plane. Gluino masses are excluded below 1 TeV at 95% CL, for $\tilde{\chi}_1^0$ masses below 200 GeV, in the case of $\mathrm{x} = 1/2$.

Signal region	**8j50**		**9j50**		**10j50**	
M_J^Σ [GeV]	340	420	340	420	340	420
Observed events	69	37	13	9	1	1
Total events after fit	75 ± 19	45 ± 14	17 ± 7	11 ± 5	$3.2^{+3.7}_{-3.2}$	2.2 ± 2.0
Fitted $t\bar{t}$	17 ± 11	16 ± 13	5 ± 4	$3.4^{+3.6}_{-3.4}$	$0.8^{+0.8}_{-0.8}$	$0.6^{+0.9}_{-0.6}$
Fitted W+jets	$0.8^{+1.3}_{-0.8}$	$0.4^{+0.7}_{-0.4}$	–	–	–	–
Fitted others	$5.2^{+4.0}_{-2.5}$	$2.8^{+2.9}_{-1.6}$	$0.58^{+0.54}_{-0.33}$	$0.39^{+0.32}_{-0.30}$	0.12 ± 0.12	0.06 ± 0.06
Total events before fit	85	44				
$t\bar{t}$ before fit	27	14				
W+jets before fit	0.8	0.4				
Others before fit	5	2.8				
Multi-jets	52 ± 15	27 ± 7	12 ± 4	7.0 ± 2.3	$2.3^{+3.6}_{-2.3}$	$1.6^{+1.8}_{-1.6}$
$N_{\mathrm{BSM}}^{95\%}$ (exp)	40	23	13	11	5	5
$N_{\mathrm{BSM}}^{95\%}$ (obs)	35	20	11	10	4	4
$\sigma_{\mathrm{BSM,max}}^{95\%} \cdot \mathcal{A} \cdot \epsilon$ (exp) [fb]	1.9	1.1	0.7	0.5	0.23	0.23
$\sigma_{\mathrm{BSM,max}}^{95\%} \cdot \mathcal{A} \cdot \epsilon$(obs) [fb]	1.7	1.0	0.5	0.5	0.2	0.2
p_0	0.60	0.7	0.7	0.6	0.8	0.7
Significance ($\mathcal{Z}$)	-0.27	-0.6	-0.6	-0.34	-0.8	-0.6

Table 7.2: As for table 7.1 but for the signal regions in the multi-jet + M_J^Σ stream. For the '8j50' regions the number of events in the control regions allowed background determination using a fit, whereas for the '9j50' and the '10j50' regions the number of events in the control regions did not allow background determination using a fit and therefore the leptonic background is extracted directly from Monte Carlo simulations.

'Gluino–squark (via $\tilde{\chi}_1^\pm$ and $\tilde{\chi}_2^0$)' model

In this simplified model, each gluino of a pair decays as $\tilde{g} \to q + \tilde{q}$ and the squark as $\tilde{q} \to q + \tilde{\chi}_1^\pm \to q' + W + \tilde{\chi}_2^0 \to q' + W + Z + \tilde{\chi}_1^0$. The intermediate particle masses, $m_{\tilde{\chi}_1^\pm}$ and $m_{\tilde{\chi}_2^0}$, are set to $(m_{\tilde{g}} + m_{\tilde{\chi}_1^0})/2$ and $(m_{\tilde{\chi}_1^\pm} + m_{\tilde{\chi}_1^0})/2$, respectively. The results are presented in the $(m_{\tilde{g}}, m_{\tilde{\chi}_1^0})$ plane in figure 7.7, which shows the combined exclusion limits for this model. Gluino masses are excluded below 1.1 TeV at 95% CL, for $\tilde{\chi}_1^0$ masses below 300 GeV.

cMssm

An cMssm model with parameters $\tan\beta = 30$, $A_0 = -2m_0$ and $\mu > 0$ is also used to interpret the analysis results. The exclusion limits are presented in the $(m_0, m_{1/2})$ plane in figure 7.8. For large universal scalar mass m_0, gluino masses smaller than 1.1 TeV are excluded at 95% CL.

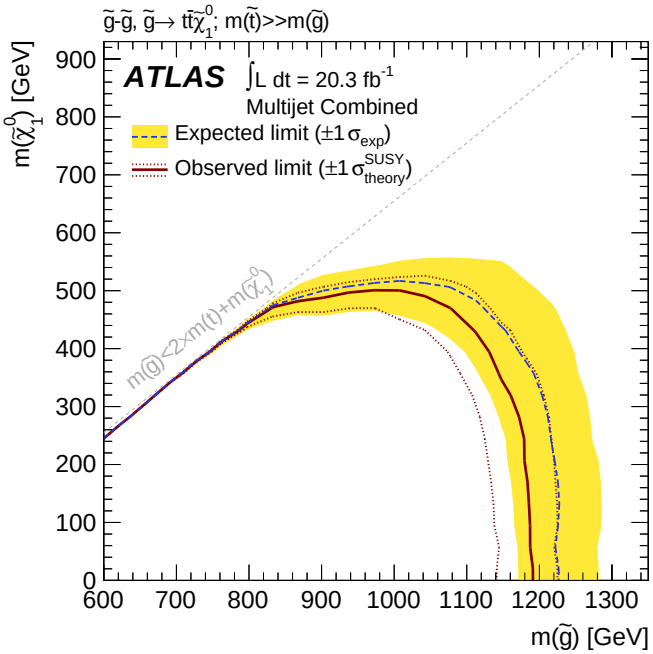

Figure 7.4: 95% CL exclusion curve for the simplified gluino–stop (off-shell) model. The dashed grey and solid red curves show the 95% CL expected and observed limits, respectively, including all uncertainties except the theoretical signal cross-section uncertainty (PDF and scale). The shaded yellow band around the expected limit shows the $\pm 1\sigma$ result. The $\pm 1\sigma$ lines around the observed limit represent the result produced when moving the signal cross section by $\pm 1\sigma$ (as defined by the PDF and scale uncertainties). The diagonal dashed line is the kinematic limit for this decay channel.

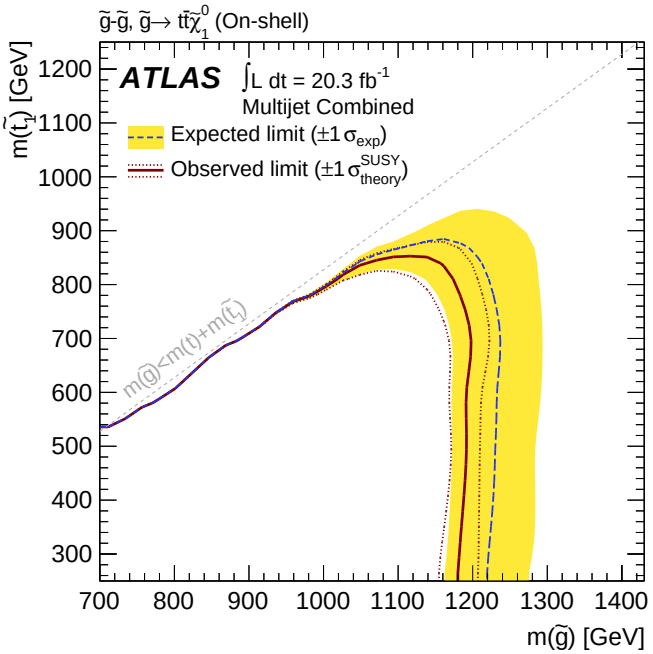

Figure 7.5: 95% CL exclusion curve for the simplified gluino–stop (on-shell) model, where the gluino decays as $\tilde{g} \rightarrow \tilde{t} + \bar{t}$ and the stop as $\tilde{t} \rightarrow \tilde{\chi}_1^0 + t$, with $m_{\tilde{\chi}_1^0} = 60$ GeV. Other details are as in figure 7.4.

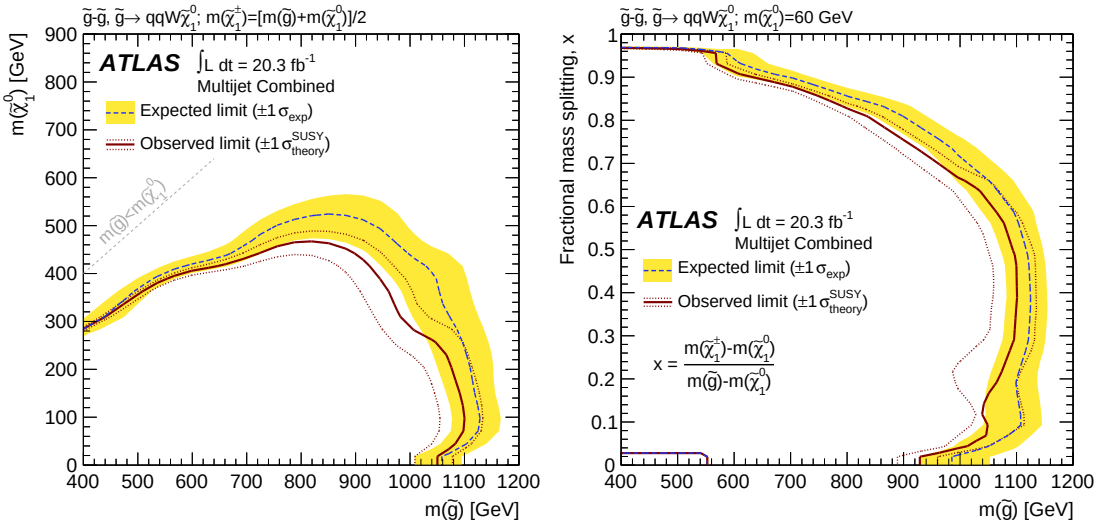

(a)x = 1/2 (b)$m_{\tilde{\chi}_1^0} = 60$ GeV

Figure 7.6: 95% CL exclusion curve for the simplified gluino–squark (via $\tilde{\chi}_1^{\pm}$) model, for the two versions on the model; fixed x = 1/2, where x = $(m_{\tilde{\chi}_1^{\pm}} - m_{\tilde{\chi}_1^0})/(m_{\tilde{g}} - m_{\tilde{\chi}_1^0})$, and varying $\tilde{\chi}_1^0$mass on the left, and $\tilde{\chi}_1^0$mass fixed to 60 GeV and varying x on the right. The region with gluino masses between 400 GeV and 550 GeV at small x has no signal Monte Carlo simulation. Other details are as in figure 7.4.

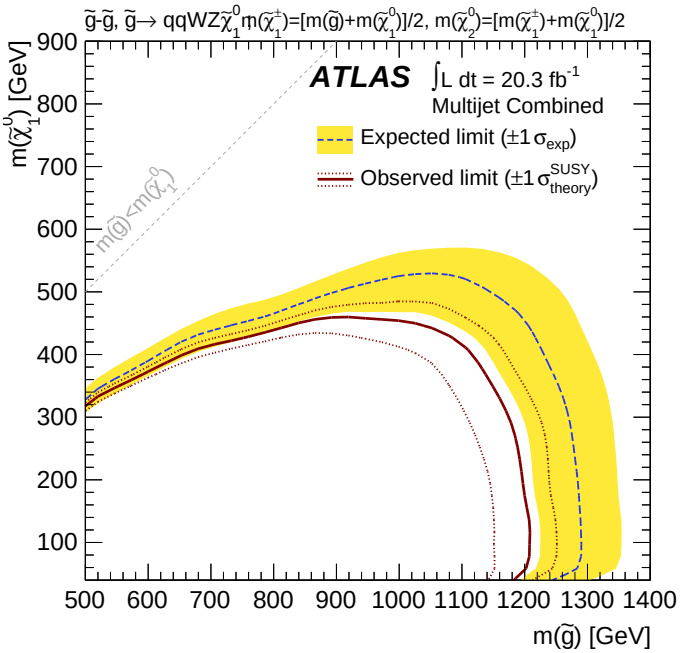

Figure 7.7: 95% CL exclusion curve for the simplified gluino–squark (via $\tilde{\chi}_1^{\pm}$ and $\tilde{\chi}_2^0$) model. Other details are as in figure 7.4.

'Gluino–stop (RPV)' model

In this simplified model, each gluino of a pair decays as $\tilde{g} \rightarrow \tilde{t} + \bar{t}$; and the $\tilde{t}$-squark decays via the R-parity- and baryon-number-violating decay $\tilde{t} \rightarrow s + b$. The results are

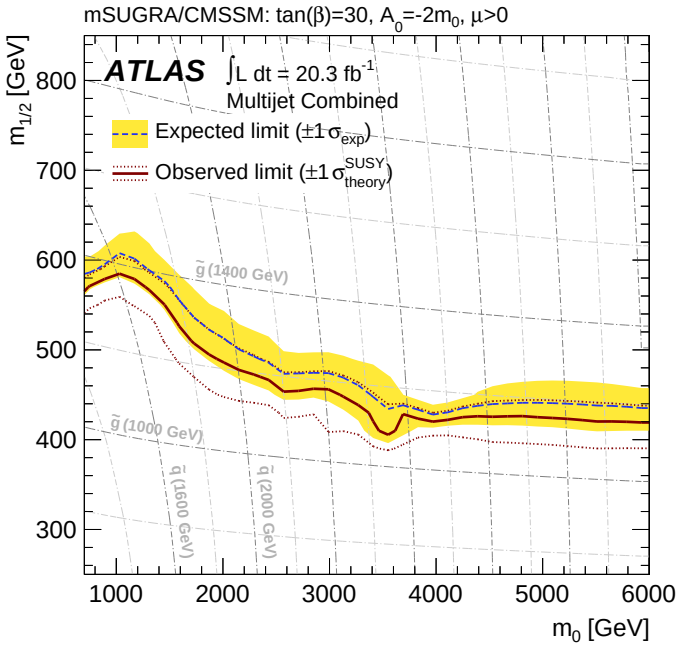

Figure 7.8: 95% CL exclusion curve for the cMSSM model, generated with parameters $\tan\beta = 30$, $A_0 = -2m_0$ and $\mu > 0$. Other details are as in figure 7.4.

presented in the $(m_{\tilde{g}}, m_{\tilde{t}})$ plane in figure 7.9. Within the context of this simplified model, the 95% CL exclusion bound on the gluino mass is 900 GeV for $\tilde{t}$-squark masses ranging from 400 GeV to 1 TeV.

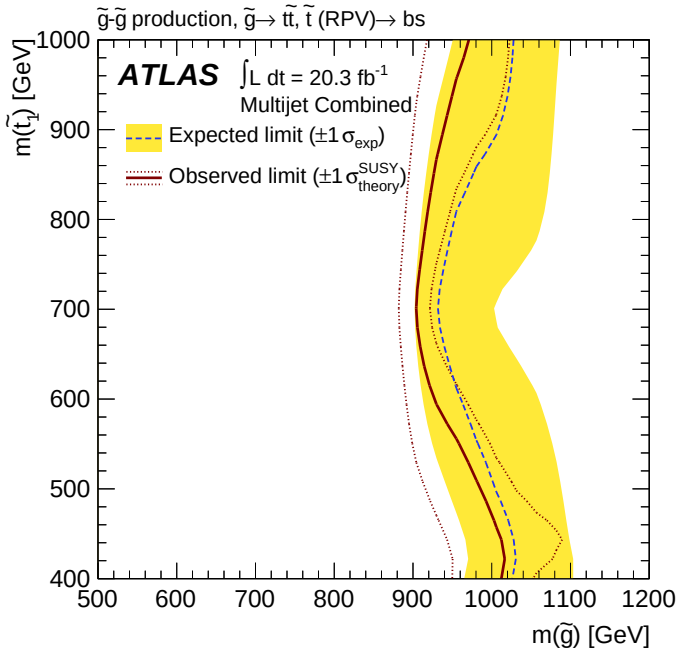

Figure 7.9: 95% CL exclusion curve for the simplified gluino–stop (RPV) model. Other details are as in figure 7.4.

8
Summary & Conclusions

A search is presented for new phenomena with large jet multiplicities (from 7 to 10 or more) and missing transverse momentum in the absence of isolated electrons or muons using 20.3 $\text{fb}^{-1}$of $\sqrt{s} = 8$ TeV pp collision data collected by the ATLAS experiment at the Large Hadron Collider [29]. The results are interpreted in the context of an cMSSM model and various simplified models resulting in final states with large jet multiplicity and $E_{\text{T}}^{\text{miss}}$.

The strategy developed for this analysis improves the reach with respect to a plain multi-jet $+E_{\text{T}}^{\text{miss}}$ selection as was done previously [30–32], as is showed by the optimization studies (section 5.5.4). The sensitivity to new physics is mainly enhanced by the combination of several signal regions into a sophisticated statistical fit (section 5.7), and by the inclusion of properties associated to the substructure of jets. That is, the number of b-tagged jets as defined by the tracking information associated to jets and the scalar sum of masses of radius $R = 1.0$ jets in the event. To provide a reliable measure of the jet mass a novel approach for jet reconstruction was implemented and validated (section 4.4). This definition was shown to be consistent with some of the benefits provided by modern post-processing techniques for jets (grooming) commonly used to refine the jet mass resolution and improve the jet robustness for environments with high pile-up.

Searches for new phenomena in final states with large jet multiplicities –requiring from at least six to at least nine jets– and missing transverse momentum have previously been reported by the ATLAS collaboration using LHC pp collision data corresponding to 1.34 fb^{-1} [30] and to 4.7 fb^{-1} [31] at $\sqrt{s} = 7$ TeV. Searches with explicit tagging of jets from bottom quarks (b-jets) in multi-jet events were also performed by ATLAS [233] and CMS [234, 236, 237]. These searches found no significant excess over the Standard Model expectation and provide limits on various supersymmetric models, including decays such as that in eq. (5.2) and an cMSSM [27, 28] model that includes strong production processes. The analysis presented here extends previous analyses by reaching higher jet multiplicities, by utilizing new sensitive variables and taking advantage of the increased accumulated luminosity. For example, in a model where both of the pair-produced gluinos decay via $\tilde{g} \to t + \bar{t} + \tilde{\chi}_1^0$, gluino masses smaller than 1.1 TeV are excluded for neutralino masses below 350 GeV.

These limits to supersymmetric particles were the first results from $\sqrt{s} = 8$ TeV pp collisions recorded by ATLAS to be published. Since then, other searches have extended the limits of some these models to even heavier masses as shown in figure 8.1 for the Gtt and cMSSM

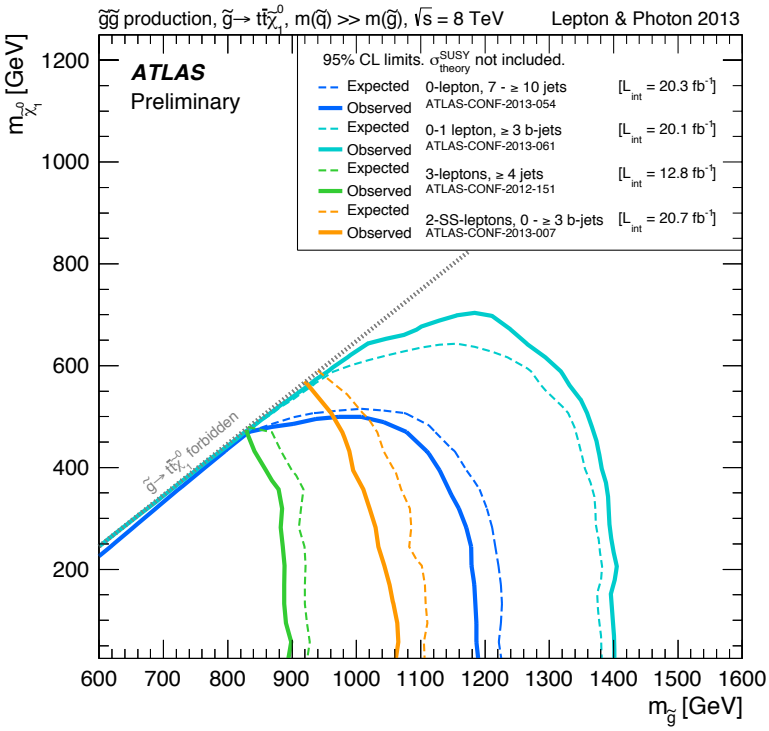

(a) Gtt

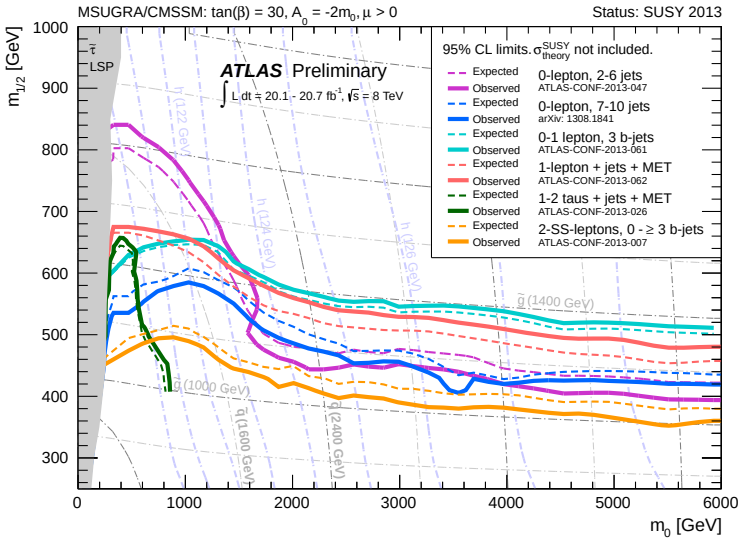

(b) cMSSM

Figure 8.1: (a) Exclusion limits at 95% CL for 8 TeV analyses in the $(m_{\tilde{g}}, m_{\tilde{\chi}_1^0})$ plane for the Gtt simplified model where a pair of gluinos decays promptly via off-shell stop to four top quarks and two lightest neutralinos (LSP). (b) Exclusion limits at 95% CL for 8 TeV analyses in the $(m_0, m_{1/2})$ plane for the cMSSM model with the remaining parameters set to $\tan(\beta) = 30$, $A_0 = -2m_0$, $\mu > 0$. Part of the model plane accommodates a lightest neutral scalar Higgs boson mass of 125 GeV.

models, in particular by the '3-b-jet analysis' [238] which was particularly designed to target the Gtt signal model (equation 5.2). It should be remarked however, that independent studies target different topologies, and therefore the relative effectiveness to exclude a specific signal model cannot be considered as the rule for other signal models. For instance, in spite of the clear outreach of (for example) the 3-b-jet analysis with respect to the multi-jet search in the Gtt grid (figure 8.1(a)), the upper limits on the $N^{95\%}_{\mathrm{BSM,max}}$ are similar between these two analyses.

Future multi-jet Susy searches will probably benefit from jet substructure techniques, by the inclusion of tagging boosted objects (W-tag and *top*-tags), the requirement of higher number of b-jets, softer cuts in M_{J}^{Σ} and alternative ways to count jets by looking into subjets within large-R jets [239].

The LHC was built with the purpose of extending the limits of our understanding of the microscopic world. The discovery of a spin 0 particle compatible with the SM Higgs boson has been an incredible payoff for the first years of operation[1]. The work of this thesis aimed at providing a further insight within the context of supersymmetric searches conducted in Atlas. Unfortunately, no experimental hint of Susy has been observed neither here nor in any other analysis so far. Therefore, whether supersymmetry is or is not a symmetry of Nature at high energy is still a matter of theoretical speculation. Upon reactivation in 2015 the LHC will produce pp collisions at even higher energies than before (probably at $\sqrt{s}$ =13–14 TeV). Until then, the discovery of new evidence of Susy will be probably on hold.

[1] The LHC physics program is more vast than pp collisions. Results from heavy ions collisions about the quark-gluon plasma or the spectra of anti-hydrogen atoms also provide fundamental information about the quantum world.

Bibliography

[1] ATLAS Collaboration, G. Aad et al., *Observation of a new particle in the search for the Standard Model Higgs boson with the ATLAS detector at the LHC*, Phys.Lett. **B716** (2012) 1–29, arXiv:1207.7214 [hep-ex] (2012). [Page 1, 12, 25, 92]

[2] CMS Collaboration, S. Chatrchyan et al., *Observation of a new boson with mass near 125 GeV in pp collisions at $\sqrt{s}$ = 7 and 8 TeV*, JHEP **1306** (2013) 081, arXiv:1303.4571 [hep-ex] (2013). [Page 1, 12, 25, 92]

[3] ATLAS Collaboration, G. Aad et al., *Evidence for the spin-0 nature of the Higgs boson using ATLAS data*, Phys.Lett. **B726** (2013) 120–144, arXiv:1307.1432 [hep-ex] (2013). [Page 1, 12]

[4] Englert, F. and Brout, R. , *Broken Symmetry and the Mass of Gauge Vector Mesons*, Phys. Rev. Lett. **13, 9** (Aug, 1964) 321–323. [Page 1, 5, 6, 7]

[5] P. Higgs, *Broken symmetries, massless particles and gauge fields*, Physics Letters **12** (1964) no. 2, 132–133. [Page 1, 5, 6, 7]

[6] G. S. Guralnik, C. R. Hagen, and T. W. B. Kibble, *Global Conservation Laws and Massless Particles*, Phys. Rev. Lett. **13, 20** (Nov, 1964) 585–587. [Page 1, 5, 6, 7]

[7] Particle Data Group Collaboration, J. Beringer et al., *Review of Particle Physics (RPP)*, Phys. Rev. **D 86** (2012) 010001. [Page 1, 5, 6, 12, 13, 22, 121]

[8] G. Bertone, D. Hooper, and J. Silk, *Particle dark matter: Evidence, candidates and constraints*, Phys.Rept. **405** (2005) 279–390, arXiv:hep-ph/0404175 [hep-ph] (2005). [Page 1, 11]

[9] A. Sakharov, *Violation of CP Invariance, c Asymmetry, and Baryon Asymmetry of the Universe*, Pisma Zh.Eksp.Teor.Fiz. **5** (1967) 32–35. [Page 1]

[10] L. Evans, (ed.) and P. Bryant, (ed.), *LHC Machine*, JINST **3** (2008) S08001. [Page 1, 31]

[11] ATLAS Collaboration, G. Aad et al., *The ATLAS Experiment at the CERN Large Hadron Collider*, JINST **3** (2008) S08003. [Page 1, 33, 38, 43, 44, 51]

[12] CMS Collaboration, *The CMS experiment at the CERN LHC*, JINST **3** (2008) no. 08, S08004. [Page 1, 33]

[13] ALICE Collaboration, *The ALICE experiment at the CERN LHC*, JINST **3** (2008) no. 08, S08002. [Page 1, 33]

[14] LHCb Collaboration, *The LHCb Detector at the LHC*, JINST **3** (2008) no. 08,

S08005. [Page 1, 33]

[15] Ellis, J., *The superstring - Theory of everything, or of nothing?*, Nature **323** (oct, 1986) 595–598. [Page 1, 11]

[16] P. Fayet and S. Ferrara, *Supersymmetry*, Physics Reports **32** (1977) no. 5, 249 – 334. [Page 1, 15]

[17] I. Aitchison, *Supersymmetry in Particle Physics: An Elementary Introduction*. Cambridge University Press, 2007. http://books.google.com.ar/books?id=x3QVeJhPBeUC. [Page 1, 15, 16, 19]

[18] J. Wess and J. Bagger, *Supersymmetry and Supergravity*. Princeton series in physics. Princeton University Press, 1992. http://books.google.com.ar/books?id=4QrQZ_Rjq4UC. [Page 1, 15, 16, 21]

[19] S. P. Martin, *A Supersymmetry primer*, arXiv:hep-ph/9709356v6 [hep-ph] (1997). [Page 1, 14, 15, 16, 17, 19, 21, 23, 25]

[20] M. E. Peskin, *Supersymmetry in Elementary Particle Physics*, arXiv:0801.1928 [hep-ph] (2008). [Page 1, 12, 15, 18]

[21] R. Haag, J. T. Lopuszański, and M. Sohnius, *All possible generators of supersymmetries of the S-matrix*, Nuclear Physics B **88** (1975) no. 2, 257 – 274. [Page 1, 15, 16]

[22] P. Fayet, *Supersymmetry and Weak, Electromagnetic and Strong Interactions*, Phys.Lett. **B64** (1976) 159. [Page 1]

[23] P. Fayet, *Spontaneously Broken Supersymmetric Theories of Weak, Electromagnetic and Strong Interactions*, Phys.Lett. **B69** (1977) 489. [Page 1]

[24] G. R. Farrar and P. Fayet, *Phenomenology of the Production, Decay, and Detection of New Hadronic States Associated with Supersymmetry*, Phys.Lett. **B76** (1978) 575–579. [Page 1]

[25] P. Fayet, *Relations Between the Masses of the Superpartners of Leptons and Quarks, the Goldstino Couplings and the Neutral Currents*, Phys.Lett. **B84** (1979) 416. [Page 1]

[26] S. Dimopoulos and H. Georgi, *Softly Broken Supersymmetry and SU(5)*, Nucl.Phys. **B193** (1981) 150. [Page 1]

[27] G. R. Farrar and P. Fayet, *Phenomenology of the production, decay, and detection of new hadronic states associated with supersymmetry*, Physics Letters B **76** (1978) no. 5, 575 – 579. [Page 1, 17, 22, 169]

[28] G. L. Kane, C. F. Kolda, L. Roszkowski, and J. D. Wells, *Study of constrained minimal supersymmetry*, Phys.Rev. **D49** (1994) 6173–6210,

arXiv:hep-ph/9312272 (1994). [Page 1, 169]

[29] Aad, G. and others, *Search for new phenomena in final states with large jet multiplicities and missing transverse momentum at $\sqrt{s}$=8 TeV proton-proton collisions using the ATLAS experiment*, Journal of High Energy Physics **2013** (2013) no. 10, 1–50. [Page 2, 169]

[30] ATLAS Collaboration, G. Aad et al., *Search for new phenomena in final states with large jet multiplicities and missing transverse momentum using $\sqrt{s} = 7$ TeV pp collisions with the ATLAS detector*, JHEP **11** (2011) 099, arXiv:1110.2299 [hep-ex] (2011). [Page 2, 91, 105, 137, 138, 169]

[31] ATLAS Collaboration, G. Aad et al., *Hunt for new phenomena using large jet multiplicities and missing transverse momentum with ATLAS in $4.7 fb^{-1}$ of $\sqrt{s} = 7$ TeV proton-proton collisions*, JHEP **1207** (2012) 167, arXiv:1206.1760 [hep-ex] (2012). [Page 2, 91, 92, 105, 137, 138, 150, 162, 169]

[32] ATLAS Collaboration, *Search for new phenomena using large jet multiplicities and missing transverse momentum with ATLAS in 5.8 fb^{-1} of $\sqrt{s} = 8$ TeV proton-proton collisions*, Tech. Rep. ATLAS-CONF-2012-103, ATLAS-COM-CONF-2012-142, CERN, Geneva, Aug, 2012. https://cds.cern.ch/record/1472672. [Page 2, 91, 105, 107, 137, 169]

[33] A. Hook, E. Izaguirre, M. Lisanti, and J. G. Wacker, *High Multiplicity Searches at the LHC Using Jet Masses*, Phys. Rev. **D 85** (2012) 055029, arXiv:1202.0558 [hep-ph] (2012). [Page 2, 70, 71, 79, 92, 107, 111]

[34] M. Gell-Mann, *A schematic model of baryons and mesons*, Physics Letters **8** (1964) no. 3, 214–215. [Page 5, 6]

[35] G. Zweig, *An SU_3 model for strong interaction symmetry and its breaking; Version 1*, Tech. Rep. CERN-TH-401, CERN, Geneva, Jan, 1964. [Page 5, 6]

[36] S. L. Glashow, *Partial-symmetries of weak interactions*, Nuclear Physics **22** (1961) no. 4, 579 – 588. [Page 5, 6]

[37] S. Weinberg, *A Model of Leptons*, Phys.Rev.Lett. **19** (1967) 1264–1266. [Page 5, 6]

[38] A. Salam, *Elementary Particle Theory*, p. 367. Stockholm, 1969. [Page 5, 6]

[39] F. Halzen and A. D. Martin, *Quarks and Leptons: An Introductory Course in Modern Particle Physics*. john Wiley & Sons, 1984. [Page 5, 13]

[40] M. E. Peskin and D. V. Schroeder, *An Introduction to quantum field theory*. Addison-Wesley, 1995. [Page 5]

[41] L. Ryder, *Quantum field Theory*. Cambridge, 1985. [Page 5]

[42] N. Cabibbo, *Unitary Symmetry and Leptonic Decays*, Phys. Rev. Lett. **10** (Jun,

1963) 531–533. [Page 7]

[43] M. Kobayashi and T. Maskawa, *CP-Violation in the Renormalizable Theory of Weak Interaction*, Progress of Theoretical Physics **49** (1973) no. 2, 652–657. [Page 7]

[44] http://indico.cern.ch/event/197461/ (Jul, 2012). [Page 7]

[45] http://www.nobelprize.org/nobel_prizes/physics/laureates/2013/ . [Page 7]

[46] ATLAS Collaboration, G. Aad et al., *Measurements of Higgs boson production and couplings in diboson final states with the ATLAS detector at the LHC*, Phys.Lett. **B726** (2013) 88–119, arXiv:1307.1427 [hep-ex] (2013). [Page 8]

[47] ATLAS Collaboration, G. Aad et al., *Search for the Standard Model Higgs boson in the H to $\tau^+\tau^-$ decay mode in $\sqrt{s} = 7$ TeV pp collisions with ATLAS*, JHEP **1209** (2012) 070, arXiv:1206.5971 [hep-ex] (2012). [Page 8]

[48] R. P. Feynman, *Very High-Energy Collisions of Hadrons*, Phys. Rev. Lett. **23** (Dec, 1969) 1415–1417. [Page 9]

[49] R. P. Feynman, *The Behavior of Hadron Collisions at Extreme Energies, in High Energy Collisions*. Proceedings of the Third Topical Conference on High Energy Collisions of Hadrons, Stony Brook, New York, 1969. [Page 9]

[50] E. D. Bloom, D. H. Coward, H. DeStaebler, J. Drees, G. Miller, L. W. Mo, R. E. Taylor, M. Breidenbach, J. I. Friedman, G. C. Hartmann, and H. W. Kendall, *High-Energy Inelastic e-p Scattering at 6° and 10°*, Phys. Rev. Lett. **23** (Oct, 1969) 930–934. [Page 9]

[51] J. D. Bjorken and E. A. Paschos, *Inelastic Electron-Proton and γ-Proton Scattering and the Structure of the Nucleon*, Phys. Rev. **185** (Sep, 1969) 1975–1982. [Page 9]

[52] D. J. Gross and F. Wilczek, *Ultraviolet Behavior of Non-Abelian Gauge Theories*, Phys. Rev. Lett. **30, 26** (Jun, 1973) 1343–1346. [Page 9]

[53] H. D. Politzer, *Reliable Perturbative Results for Strong Interactions?*, Phys. Rev. Lett. **30, 26** (Jun, 1973) 1346–1349. [Page 9]

[54] L. Susskind, *Dynamics of spontaneous symmetry breaking in the Weinberg-Salam theory*, Phys. Rev. D **20** (Nov, 1979) 2619–2625. [Page 12]

[55] J. R. Ellis, *Beyond the standard model for hill walkers*, arXiv:hep-ph/9812235 [hep-ph] (1998). [Page 12]

[56] H. Georgi, H. R. Quinn, and S. Weinberg, *Hierarchy of Interactions in Unified Gauge Theories*, Phys. Rev. Lett. **33** (Aug, 1974) 451–454. [Page 13, 17]

[57] J. Ellis, *Beyond the standard model with the LHC*, Nature **448** (July, 2007) 297–301. [Page 13]

[58] I. H. Lee and S. D. Drell, *Fermion masses in the Standard Model*, . [Page 14]

[59] C. T. Hill and E. H. Simmons, *Strong dynamics and electroweak symmetry breaking*, Phys.Rept. **381** (2003) 235–402, arXiv:hep-ph/0203079 [hep-ph] (2003). [Page 14]

[60] M. Carena, L. Da Rold, and E. Ponton, *Minimal Composite Higgs Models at the LHC*, arXiv:1402.2987 [hep-ph] (2014). [Page 14]

[61] L. Ryder, *Quantum Field Theory*. Cambridge University Press, 1996. http://books.google.com.ar/books?id=nnuW_kVJ500C. [Page 15, 16]

[62] J. Wess and B. Zumino, *A lagrangian model invariant under supergauge transformations*, Physics Letters B **49** (1974) no. 1, 52 – 54. [Page 15]

[63] S. Coleman and J. Mandula, *All Possible Symmetries of the S-Matrix*, Phys. Rev. **159** (Jul, 1967) 1251–1256. [Page 15]

[64] B. Claude Cohen-Tannoudji, *Quantum Mechanics Volume 1*. Hermann. http://books.google.com.ar/books?id=e_Ec0IlSbMMC. [Page 16]

[65] H. Georgi and S. L. Glashow, *Unity of All Elementary-Particle Forces*, Phys. Rev. Lett. **32** (Feb, 1974) 438–441. [Page 17]

[66] A. Buras, J. Ellis, M. Gaillard, and D. Nanopoulos, *Aspects of the grand unification of strong, weak and electromagnetic interactions*, Nuclear Physics B **135** (1978) no. 1, 66 – 92. [Page 17]

[67] J. R. Ellis, *Limits of the standard model*, arXiv:hep-ph/0211168 [hep-ph] (2002). [Page 18]

[68] D. Chung, L. Everett, G. Kane, S. King, J. Lykken, and L.-T. Wang, *The soft supersymmetry-breaking Lagrangian: theory and applications*, Physics Reports **407** (2005) no. 1-3, 1 – 203. [Page 19, 21]

[69] L. Girardello and M. Grisaru, *Soft breaking of supersymmetry*, Nuclear Physics B **194** (1982) no. 1, 65 – 76. [Page 20]

[70] H. Primakoff and S. P. Rosen, *Baryon Number and Lepton Number Conservation Laws*, Annual Review of Nuclear and Particle Science **31** (1981) no. 1, 145–192, http://www.annualreviews.org/doi/pdf/10.1146/annurev.ns.31.120181.001045 (1981). [Page 22]

[71] G. 't Hooft, *Symmetry Breaking through Bell-Jackiw Anomalies*, Phys. Rev. Lett. **37** (Jul, 1976) 8–11. [Page 22]

[72] A. Bartl, S. Hesselbach, K. Hidaka, T. Kernreiter, and W. Porod, *Top squarks and bottom squarks in the minimal supersymmetric standard model with complex parameters*, Phys. Rev. D **70** (Aug, 2004) 035003. [Page 24]

[73] LHC New Physics Working Group Collaboration, D. Alves et al., *Simplified Models for LHC New Physics Searches*, J.Phys. **G39** (2012) 105005, arXiv:1105.2838 [hep-ph] (2012). [Page 26, 30]

[74] J. Alwall, P. Schuster, and N. Toro, *Simplified Models for a First Characterization of New Physics at the LHC*, Phys. Rev. **D79** (2009) , arXiv:hep-ph/0810.3921 (2009). [Page 26]

[75] A. Barr, C. Lester, M. A. Parker, B. Allanach, and P. Richardson, *Discovering anomaly mediated supersymmetry at the LHC*, JHEP **0303** (2003) 045, arXiv:hep-ph/0208214 [hep-ph] (2003). [Page 27]

[76] D. S. Alves, E. Izaguirre, and J. G. Wacker, *Where the Sidewalk Ends: Jets and Missing Energy Search Strategies for the 7 TeV LHC*, JHEP **1110** (2011) 012, arXiv:1102.5338 [hep-ph] (2011). [Page 27]

[77] http://pauli.uni-muenster.de/~akule_01/nllwiki/index.php/NLL-fast . [Page 28]

[78] B. Fuks, M. Klasen, D. R. Lamprea, and M. Rothering, *Revisiting slepton pair production at the Large Hadron Collider*, arXiv:1310.2621 [hep-ph] (2013). [Page 28]

[79] ATLAS Collaboration, *Luminosity Determination in pp Collisions at $\sqrt{s}$=7 TeV Using the ATLAS Detector at the LHC*, Eur. Phys. J. **C71** (2011) 1630, arXiv:1101.2185 (2011). [Page 36]

[80] M. Lamont, *Status of the LHC*, Journal of Physics: Conference Series **455** (2013) no. 1, 012001. [Page 36]

[81] S. van der Meer, *Calibration of the effective beam height in the ISR*, Tech. Rep. CERN-ISR-PO-68-31. ISR-PO-68-31, CERN, Geneva, 1968. [Page 36]

[82] ATLAS Collaboration, *ATLAS Policy on Radiation Tolerant Electronics: ATLAS Radiation Tolerance Criteria*, . [Page 38]

[83] ATLAS Collaboration, G. Aad et al., *Expected performance of the ATLAS experiment - detector, trigger and physics*, arXiv:0901.0512 (2009). [Page 46, 48, 51, 55, 58]

[84] T. Cornelissen, M. Elsing, S. Fleischmann, W. Liebig, E. Moyse, and A. Salzburger, *Concepts, Design and Implementation of the ATLAS New Tracking (NEWT)*, Tech. Rep. ATL-SOFT-PUB-2007-007. ATL-COM-SOFT-2007-002, CERN, Geneva, Mar, 2007. [Page 51]

[85] ATLAS Collaboration, *ATLAS inner detector: Technical Design Report, 1.* Technical Design Report ATLAS. CERN, Geneva, 1997. [Page 51]

[86] R. Fruhwirth, W. Waltenberger, and P. Vanlaer, *Adaptive vertex fitting*, J.Phys.

G34 (2007) N343. [Page 52]

[87] *Performance of primary vertex reconstruction in proton-proton collisions at* $\sqrt{s}$ *=7 TeV in the ATLAS experiment*, Tech. Rep. ATLAS-CONF-2010-069, CERN, Geneva, Jul, 2010. https://cdsweb.cern.ch/record/1281344. [Page 52]

[88] *Expected electron performance in the ATLAS experiment*, Tech. Rep. ATL-PHYS-PUB-2011-006, CERN, Geneva, Apr, 2011. [Page 53]

[89] ATLAS Collaboration, G. Aad et al., *Electron performance measurements with the ATLAS detector using the 2010 LHC proton-proton collision data*, Eur.Phys.J. **C72** (2012) 1909, arXiv:1110.3174 [hep-ex] (2012). [Page 53, 54, 134]

[90] W. Lampl, S. Laplace, D. Lelas, P. Loch, H. Ma, S. Menke, S. Rajagopalan, D. Rousseau, S. Snyder, and G. Unal, *Calorimeter Clustering Algorithms: Description and Performance*, Tech. Rep. ATL-LARG-PUB-2008-002. ATL-COM-LARG-2008-003, CERN, Geneva, Apr, 2008. http://cdsweb.cern.ch/record/1099735. [Page 53, 58, 59]

[91] ATLAS Collaboration, *Preliminary results on the muon reconstruction efficiency, momentum resolution, and momentum scale in ATLAS 2012 pp collision data*, Tech. Rep. ATLAS-CONF-2013-088, CERN, Geneva, August, 2013. [Page 55, 138]

[92] ATLAS Collaboration, G. Aad et al., *Jet energy measurement with the ATLAS detector in proton-proton collisions at* $\sqrt{s}$ *= 7 TeV*, arXiv:1112.6426 [hep-ex] (2011). [Page 58, 153]

[93] T. Barillari et al., *Local Hadronic Calibration*, Tech. Rep. ATL-LARG-PUB-2009-001-2. ATL-COM-LARG-2008-006. ATL-LARG-PUB-2009-001, CERN, Geneva, Jun, 2008. Due to a report-number conflict with another document, the report-number ATL-LARG-PUB-2009-001-2 has been assigned. [Page 59]

[94] ATLAS Collaboration, *Pile-up corrections for jets from proton-proton collisions at* $\sqrt{s} = 7$ *TeV in* ATLAS *in 2011*, . [Page 60, 114]

[95] M. Cacciari and G. P. Salam, *Pileup subtraction using jet areas*, Phys. Lett. **B 659** (2008) 119, arXiv:0707.1378 [hep-ph] (2008). [Page 60, 67, 77, 114]

[96] ATLAS Collaboration, G. Aad et al., *Performance of Missing Transverse Momentum Reconstruction in Proton-Proton Collisions at 7 TeV with ATLAS*, Eur.Phys.J. **C72** (2012) 1844, arXiv:1108.5602 [hep-ex] (2012). [Page 60, 102, 106, 136]

[97] ATLAS Collaboration, *Electron and photon reconstruction and identification in ATLAS: expected performance at high energy and results at 900 GeV*, Tech. Rep. ATLAS-CONF-2010-005, CERN, Geneva, Jun, 2010. [Page 61]

[98] *Performance of shower deconstruction in ATLAS*, Tech. Rep. ATLAS-CONF-2014-003, CERN, Geneva, Feb, 2014. [Page 62]

[99] ATLAS Collaboration, *Measurement of the b-tag Efficiency in a Sample of Jets Containing Muons with 5 fbâĹŠ1 of Data from the ATLAS Detector*, Tech. Rep. ATLAS-CONF-2012-043, CERN, Geneva, Mar, 2012. [Page 62, 96]

[100] ATLAS Collaboration, *Commissioning of the ATLAS high-performance b-tagging algorithms in the 7 TeV collision data*, Tech. Rep. ATLAS-CONF-2011-102, CERN, Geneva, Jul, 2011. [Page 62]

[101] G. Piacquadio and C. Weiser, *A new inclusive secondary vertex algorithm for b-jet tagging in ATLAS*, Journal of Physics: Conference Series **119** (2008) no. 3, 032032. [Page 62, 63]

[102] B. C. Buttler, *Searches for Natural Supersymmetry in Hadronic Final States with Heavy Flavor at ATLAS*. text, Stanford University, 2012. [Page 64]

[103] Maarten Ballintijn and Rene Brun and Fons Rademakers and Gunther Roland. [Page 64]

[104] R. Brun and F. Rademakers, *ROOT: An object oriented data analysis framework*, Nucl.Instrum.Meth. **A389** (1997) 81–86. [Page 64]

[105] I. Antcheva et al., *ROOT âĂŤ A C++ framework for petabyte data storage, statistical analysis and visualization*, Comput. Phys. Commun. **180** (2009) no. 12, 2499–2512. [Page 64]

[106] ATLAS Collaboration, Asquith, Brelier, et al., *Performance of Jet Algorithms in the ATLAS Detector*, Tech. Rep. ATL-PHYS-INT-2010-129, CERN, Geneva, Dec, 2010. https://cds.cern.ch/record/1311867/files/ATL-PHYS-INT-2010-129.pdf. [Page 65, 66, 67]

[107] S. D. Ellis, *On defining the undefinable: jets*, Journal of Physics G: Nuclear and Particle Physics **17** (1991) no. 10, 1552. [Page 65]

[108] J. E. Huth, N. Wainer, K. Meier, N. Hadley, F. Aversa, et al., *Toward a standardization of jet definitions*, . [Page 66]

[109] S. Catani, Y. L. Dokshitzer, M. Seymour, and B. Webber, *Longitudinally invariant K_t clustering algorithms for hadron hadron collisions*, Nucl.Phys. **B406** (1993) 187–224. [Page 66, 67, 69]

[110] Y. L. Dokshitzer, G. Leder, S. Moretti, and B. Webber, *Better jet clustering algorithms*, JHEP **08** (1997) 001, arXiv:hep-ph/9707323 [hep-ph] (1997). [Page 66, 67]

[111] M. Wobisch and T. Wengler, *Hadronization corrections to jet cross sections in*

deep- inelastic scattering, arXiv:hep-ph/9907280 [hep-ph] (1998). [Page 66, 67]

[112] C. Buttar, J. D'Hondt, M. Kramer, G. Salam, M. Wobisch, et al., *Standard Model Handles and Candles Working Group: Tools and Jets Summary Report*, arXiv:0803.0678 [hep-ph] (2008). [Page 66, 67]

[113] S. D. Ellis and D. E. Soper, *Successive combination jet algorithm for hadron collisions*, Phys. Rev. D **48, 7** (Oct, 1993) 3160–3166. [Page 66, 67]

[114] M. Cacciari, G. P. Salam, and G. Soyez, *The anti-k_t jet clustering algorithm*, JHEP **04** (2008) 063, arXiv:0802.1189 [hep-ph] (2008). [Page 67, 95]

[115] M. Cacciari, G. P. Salam, and G. Soyez, *The Catchment Area of Jets*, JHEP **04** (2008) 005, arXiv:0802.1188 [hep-ph] (2008). [Page 67, 77]

[116] M. Dasgupta, L. Magnea, and G. P. Salam, *Non-perturbative QCD effects in jets at hadron colliders*, JHEP **0802** (2008) 055, arXiv:0712.3014 [hep-ph] (2008). [Page 67]

[117] ATLAS Collaboration, G. Aad et al., *Performance of jet substructure techniques for large-R jets in proton-proton collisions at $\sqrt{s}$ = 7 TeV using the ATLAS detector*, JHEP **1309** (2013) no. 9, 076, arXiv:1306.4945 [hep-ex] (2013). [Page 67, 68, 79, 80, 81, 86]

[118] Y. Cui, Z. Han, and M. D. Schwartz, *W-jet Tagging: Optimizing the Identification of Boosted Hadronically-Decaying W Bosons*, Phys. Rev. **D 83** (2011) 074023, arXiv:1012.2077 [hep-ph] (2011). [Page 68, 70]

[119] J. Thaler and L.-T. Wang, *Strategies to Identify Boosted Tops*, JHEP **07** (2008) 092, arXiv:0806.0023 [hep-ph] (2008). [Page 68]

[120] L. G. Almeida, S. J. Lee, G. Perez, I. Sung, and J. Virzi, *Top Jets at the LHC*, Phys. Rev. **D 79** (2009) 074012, arXiv:0810.0934 [hep-ph] (2009). [Page 68]

[121] J. M. Butterworth et al., *Jet substructure as a new Higgs search channel at the LHC*, Phys. Rev. Lett. **100** (2008) 242001, arXiv:0802.2470 [hep-ph] (2008). [Page 68, 70, 71, 73, 79]

[122] T. Sjostrand, S. Mrenna, and P. Z. Skands, *PYTHIA 6.4 Physics and Manual*, JHEP **0605** (2006) 026, arXiv:hep-ph/0603175 [hep-ph] (2006). [Page 68]

[123] E. Richter-Was, D. Froideveaux, and L. Poggioli, *ATLFAST 2.0 a fast simulation package for ATLAS*, ATLAS Note **ATL-PHYS-98-131** (1998) . [Page 69]

[124] ATLAS Collaboration, *Prospects for top anti-top resonance searches using early ATLAS data.*, Tech. Rep. ATL-PHYS-PUB-2010-008, CERN, Geneva, Jul, 2010. [Page 69]

[125] J. Thaler and K. Van Tilburg, *Identifying Boosted Objects with N-subjettiness*,

JHEP **03** (2011) 015, arXiv:1011.2268 [hep-ph] (2011). [Page 70]

[126] T. Plehn, M. Spannowsky, M. Takeuchi, and D. Zerwas, *Stop Reconstruction with Tagged Tops*, JHEP **10** (2010) 078, arXiv:1006.2833 [hep-ph] (2010). [Page 70, 71, 73]

[127] M. Jankowiak and A. J. Larkoski, *Jet Substructure Without Trees*, JHEP **06** (2011) 057, arXiv:1104.1646 [hep-ph] (2011). [Page 70]

[128] D. E. Soper and M. Spannowsky, *Finding physics signals with shower deconstruction*, Phys.Rev. **D84** (2011) 074002, arXiv:1102.3480 [hep-ph] (2011). [Page 70, 71]

[129] C. Chen, *New approach to identifying boosted hadronically-decaying particle using jet substructure in its center-of-mass frame*, Phys. Rev. **D 85** (2012) 034007, arXiv:1112.2567 [hep-ph] (2012). [Page 70]

[130] OPAL Collaboration, *Experimental properties of gluon and quark jets from a point source*, Eur. Phys. J. **C 11** (1999) 217, arXiv:hep-ex/9903027 [hep-ex] (1999). [Page 70]

[131] J. Gallicchio and M. D. Schwartz, *Quark and Gluon Tagging at the LHC*, Phys. Rev. Lett. **107** (2011) 172001, arXiv:1106.3076 [hep-ph] (2011). [Page 70]

[132] ATLAS Collaboration, *Study of Jet Shapes in Inclusive Jet Production in pp Collisions at $\sqrt{s} = 7$ TeV using the ATLAS Detector*, Phys. Rev. **D 83** (2011) 052003, arXiv:1101.0070 [hep-ex] (2011). [Page 70, 72]

[133] A. Altheimer et al., *Jet Substructure at the Tevatron and LHC: New results, new tools, new benchmarks*, J. Phys. **G 39** (2012) 063001, arXiv:1201.0008 [hep-ph] (2012). [Page 70, 79]

[134] A. Altheimer, A. Arce, L. Asquith, J. Backus Mayes, E. Bergeaas Kuutmann, et al., *Boosted objects and jet substructure at the LHC*, arXiv:1311.2708 [hep-ex] (2013). [Page 70, 79]

[135] S. D. Ellis, C. K. Vermilion, and J. R. Walsh, *Techniques for improved heavy particle searches with jet substructure*, Phys. Rev. **D 80** (2009) 051501, arXiv:0903.5081 [hep-ph] (2009). [Page 70, 79, 80]

[136] D. Krohn, J. Thaler, and L.-T. Wang, *Jet Trimming*, JHEP **02** (2010) 084, arXiv:0912.1342 [hep-ph] (2010). [Page 70, 71, 73, 79, 80]

[137] M. Seymour, *Searches for new particles using cone and cluster jet algorithms: a comparative study*, Zeitschrift für Physik C Particles and Fields **62** (1994) no. 1, 127–138. [Page 70]

[138] T. Plehn and M. Spannowsky, *Top Tagging*, J.Phys. **G39** (2012) 083001,

arXiv:1112.4441 [hep-ph] (2012). [Page 70]

[139] A. Abdesselam et al., *Boosted objects: A Probe of beyond the Standard Model physics*, Eur. Phys. J. **C71** (2011) 1661, arXiv:1012.5412 [hep-ph] (2011). [Page 70, 79]

[140] ATLAS Collaboration, ATLAS, *Jet mass and substructure of inclusive jets in* $\sqrt{s} = 7$ *TeV pp collisions with the ATLAS experiment*, JHEP **05** (2012) 128, arXiv:1203.4606 [hep-ex] (2012). [Page 70, 74, 81]

[141] ATLAS Collaboration, *ATLAS measurements of the properties of jets for boosted particle searches*, Phys. Rev. **D 86** (2012) 072006, arXiv:1206.5369 [hep-ex] (2012). [Page 70]

[142] M. Jankowiak and A. J. Larkoski, *Jet Substructure Without Trees*, JHEP **1106** (2011) 057, arXiv:1104.1646 [hep-ph] (2011). [Page 70]

[143] J. Gallicchio and M. D. Schwartz, *Seeing in Color: Jet Superstructure*, Phys.Rev.Lett. **105** (2010) 022001, arXiv:1001.5027 [hep-ph] (2010). [Page 70]

[144] S. Ellis, J. Huston, K. Hatakeyama, P. Loch, and M. Tonnesmann, *Jets in hadron-hadron collisions*, Prog.Part.Nucl.Phys. **60** (2008) 484–551, arXiv:0712.2447 [hep-ph] (2008). [Page 71]

[145] G. P. Salam, *Towards Jetography*, Eur.Phys.J. **C67** (2010) 637–686, arXiv:0906.1833 [hep-ph] (2010). [Page 71]

[146] G. Corcella et al., *HERWIG 6.5 release note*, arXiv:0210213 [hep-ph] (2002). [Page 72]

[147] J. M. Butterworth, J. R. Forshaw, and M. H. Seymour, *Multiparton interactions in photoproduction at HERA*, Z. Phys. C **72** (1996) 637, arXiv:9601371 [hep-ph] (1996). [Page 72]

[148] ATLAS Collaboration, G. Aad et al., *Improved luminosity determination in pp collisions at* $\sqrt{s} = 7$ *TeV using the ATLAS detector at the LHC*, Eur.Phys.J. **C73** (2013) no. CERN-PH-EP-2013-026, 2518, arXiv:1302.4393 [hep-ex] (2013). [Page 73]

[149] ATLAS Collaboration, *Measurement of dijet azimuthal decorrelations in pp collisions at* $\sqrt{s} = 7$ *TeV*, Phys. Rev. Lett. **106** (2011) 172002, arXiv:1102.2696 [hep-ex] (2011). [Page 74]

[150] ATLAS. [Page 77]

[151] D. E. Soper and M. Spannowsky, *Combining subjet algorithms to enhance ZH detection at the LHC*, JHEP **08** (2010) 029, arXiv:1005.0417 [hep-ph] (2010). [Page 79]

[152] ATLAS Collaboration, *Jet energy measurement with the ATLAS detector in proton-proton collisions at* $\sqrt{s} = 7$ *TeV*, Eur. Phys. J. **C 73** (2013) 2304, arXiv:1112.6426 [hep-ex] (2013). [Page 80]

[153] S. D. Ellis, C. K. Vermilion, and J. R. Walsh, *Recombination Algorithms and Jet Substructure: Pruning as a Tool for Heavy Particle Searches*, Phys. Rev. **D 81** (2010) 094023, arXiv:0912.0033 [hep-ph] (2010). [Page 80]

[154] CMS Collaboration, *Search for anomalous* $t\bar{t}$ *production in the highly-boosted all-hadronic final state*, JHEP **09** (2012) 029, arXiv:1204.2488 [hep-ex] (2012). [Page 81]

[155] ATLAS Collaboration, G. Aad et al., *The ATLAS Simulation Infrastructure*, Eur.Phys.J. **C70** (2010) 823–874, arXiv:1005.4568 [physics.ins-det] (2010). [Page 93]

[156] GEANT4 Collaboration, S. Agostinelli et al., *GEANT4: A simulation toolkit*, Nucl. Instrum. Meth. **A 506** (2003) 250. [Page 93]

[157] W. Lukas, *Fast Simulation for ATLAS: Atlfast-II and ISF*, Journal of Physics: Conference Series **396** (2012) no. 2, 022031. [Page 93]

[158] T. Gleisberg, S. Hoeche, F. Krauss, M. Schonherr, S. Schumann, et al., *Event generation with SHERPA 1.1*, JHEP **0902** (2009) 007, arXiv:0811.4622 [hep-ph] (2009). [Page 93]

[159] H.-L. Lai, M. Guzzi, J. Huston, Z. Li, P. M. Nadolsky, et al., *New parton distributions for collider physics*, Phys.Rev. **D82** (2010) 074024, arXiv:1007.2241 [hep-ph] (2010). [Page 93]

[160] M. Cacciari, M. Czakon, M. Mangano, A. Mitov, and P. Nason, *Top-pair production at hadron colliders with next-to-next-to-leading logarithmic soft-gluon resummation*, Phys.Lett. **B710** (2012) 612–622, arXiv:1111.5869 [hep-ph] (2012). [Page 93]

[161] M. Czakon and A. Mitov, *NNLO corrections to top-pair production at hadron colliders: the all-fermionic scattering channels*, JHEP **1212** (2012) 054, arXiv:1207.0236 [hep-ph] (2012). [Page 93]

[162] M. Aliev, H. Lacker, U. Langenfeld, S. Moch, P. Uwer, et al., *HATHOR: HAdronic Top and Heavy quarks crOss section calculatoR*, Comput. Phys. Commun. **182** (2011) 1034–1046, arXiv:1007.1327 [hep-ph] (2011). [Page 94]

[163] S. Catani, L. Cieri, G. Ferrera, D. de Florian, and M. Grazzini, *Vector boson production at hadron colliders: A Fully exclusive QCD calculation at NNLO*, Phys. Rev. Lett. **103** (2009) 082001, arXiv:0903.2120 [hep-ph] (2009). [Page 94]

[164] S. Frixione and B. R. Webber, *Matching NLO QCD computations and parton shower simulations*, JHEP **06** (2002) 029, arXiv:hep-ph/0204244 (2002). [Page

94]

[165] S. Frixione, F. Stoeckli, P. Torrielli, B. R. Webber, and C. D. White, *The MCaNLO 4.0 Event Generator*, arXiv:1010.0819 [hep-ph] (2010). [Page 94]

[166] S. Frixione, E. Laenen, P. Motylinski, and B. R. Webber, *Single-top production in MC@NLO*, JHEP **03** (2006) 092, arXiv:hep-ph/0512250 [hep-ph] (2006). [Page 94]

[167] S. Frixione, E. Laenen, P. Motylinski, B. R. Webber, and C. D. White, *Single-top hadroproduction in association with a W boson*, JHEP **07** (2008) 029, arXiv:0805.3067 [hep-ph] (2008). [Page 94, 157]

[168] G. Corcella, I. Knowles, G. Marchesini, S. Moretti, K. Odagiri, et al., *HERWIG 6.5 release note*, arXiv:hep-ph/0210213 [hep-ph] (2002). [Page 94]

[169] J. M. Butterworth, J. R. Forshaw, and M. H. Seymour, *Multiparton interactions in photoproduction at HERA*, Z. Phys. **C72** (1996) 637–646, arXiv:hep-ph/9601371 (1996). [Page 94]

[170] B. P. Kersevan and E. Richter-Was, *The Monte Carlo Event Generator AcerMC versions 2.0 to 3.8 with interfaces to PYTHIA 6.4, HERWIG 6.5 and ARIADNE 4.1*, arXiv:hep-ph/0405247v3 [hep-ph] (2004). [Page 94]

[171] J. Pumplin et al., *New generation of parton distributions with uncertainties from global QCD analysis*, JHEP **07** (2002) 012, arXiv:hep-ph/0201195 (2002). [Page 94]

[172] T. Sjöstrand, S. Mrenna, and P. Z. Skands, *PYTHIA 6.4 physics and manual*, JHEP **05** (2006) 026, arXiv:hep-ph/0603175 (2006). [Page 94]

[173] N. Kidonakis, *NNLL resummation for s-channel single top quark production*, Phys.Rev. **D81** (2010) 054028, arXiv:1001.5034 [hep-ph] (2010). [Page 94]

[174] N. Kidonakis, *Next-to-next-to-leading-order collinear and soft gluon corrections for t-channel single top quark production*, Phys.Rev. **D83** (2011) 091503, arXiv:1103.2792 [hep-ph] (2011). [Page 94]

[175] N. Kidonakis, *Two-loop soft anomalous dimensions for single top quark associated production with a W- or H-*, Phys.Rev. **D82** (2010) 054018, arXiv:1005.4451 [hep-ph] (2010). [Page 94]

[176] J. Alwall, M. Herquet, F. Maltoni, O. Mattelaer, and T. Stelzer, *MadGraph 5 : Going Beyond*, JHEP **06** (2011) 128, arXiv:1106.0522 [hep-ph] (2011). [Page 94]

[177] J. M. Campbell and R. K. Ellis, $t\bar{t}W^{+-}$ *production and decay at NLO*, JHEP **1207** (2012) 052, arXiv:1204.5678 [hep-ph] (2012). [Page 94]

[178] M. Garzelli, A. Kardos, C. Papadopoulos, and Z. Trocsanyi, *$t\bar{t}\,W^{+-}$ and $t\bar{t}\,Z$ Hadroproduction at NLO accuracy in QCD with Parton Shower and Hadronization effects*, JHEP **1211** (2012) 056, arXiv:1208.2665 [hep-ph] (2012). [Page 94]

[179] J. Butterworth, E. Dobson, U. Klein, B. Mellado Garcia, T. Nunnemann, J. Qian, D. Rebuzzi, and R. Tanaka, *Single Boson and Diboson Production Cross Sections in pp Collisions at sqrts=7 TeV*, Tech. Rep. ATL-COM-PHYS-2010-695, CERN, Geneva, Aug, 2010. [Page 94]

[180] T. Sjostrand, S. Mrenna, and P. Z. Skands, *A Brief Introduction to PYTHIA 8.1*, Comput. Phys. Commun. **178** (2008) 852–867, arXiv:0710.3820 [hep-ph] (2008). [Page 94]

[181] ATLAS Collaboration. [Page 94]

[182] M. Bahr et al., *Herwig++ physics and manual*, Eur. Phys. J. **C58** (2008) 639–707, arXiv:0803.0883 (2008). [Page 94]

[183] W. Beenakker, R. Hopker, M. Spira, and P. M. Zerwas, *Squark and gluino production at hadron colliders*, Nucl. Phys. **B492** (1997) 51–103, arXiv:hep-ph/9610490 (1997). [Page 94]

[184] A. Kulesza and L. Motyka, *Threshold resummation for squark-antisquark and gluino-pair production at the LHC*, Phys.Rev.Lett. **102** (2009) 111802, arXiv:0807.2405 [hep-ph] (2009). [Page 94]

[185] A. Kulesza and L. Motyka, *Soft gluon resummation for the production of gluino-gluino and squark-antisquark pairs at the LHC*, Phys.Rev. **D80** (2009) 095004, arXiv:0905.4749 [hep-ph] (2009). [Page 94]

[186] W. Beenakker, S. Brensing, M. Kramer, A. Kulesza, E. Laenen, et al., *Soft-gluon resummation for squark and gluino hadroproduction*, JHEP **0912** (2009) 041, arXiv:0909.4418 [hep-ph] (2009). [Page 94]

[187] W. Beenakker, S. Brensing, M. Kramer, A. Kulesza, E. Laenen, et al., *Squark and gluino hadroproduction*, Int.J.Mod.Phys. **A26** (2011) 2637–2664, arXiv:1105.1110 [hep-ph] (2011). [Page 94]

[188] M. Kramer, A. Kulesza, R. van der Leeuw, M. Mangano, S. Padhi, et al., *Supersymmetry production cross sections in pp collisions at $\sqrt{s} = 7$ TeV*, arXiv:1206.2892 [hep-ph] (2012). [Page 95]

[189] M. Cacciari and G. P. Salam, *Dispelling the N^3 myth for the k_t jet-finder*, Phys. Lett. **B641** (2006) 57–61, arXiv:hep-ph/0512210 (2006). [Page 95]

[190] ATLAS Collaboration, https://twiki.cern.ch/twiki/bin/viewauth/Atlas/LowestUnprescaled . [Page 97]

[191] ATLAS Collaboration. [Page 99]

[192] ATLAS Collaboration, https://twiki.cern.ch/twiki/bin/viewauth/Atlas/TileTripReader . [Page 99]

[193] ATLAS Collaboration, https://twiki.cern.ch/twiki/bin/viewauth/Atlas/TileOverflowAnalysis#Problematic_events . [Page 99]

[194] ATLAS Collaboration. [Page 100]

[195] ATLAS Collaboration, https://twiki.cern.ch/twiki/bin/viewauth/AtlasProtected/HowToCleanJets2012 . [Page 100]

[196] ATLAS Collaboration, *Selection of jets produced in proton-proton collisions with the ATLAS detector using 2011 data*, ATLAS-CONF-2012-020. [Page 100]

[197] A. J. Barr, E. Duchovni, M. J. Flowerdew, M. Hodgkinson, T. J. Khoo, I. Roth, A. Sfyrla, F. Siegert, K. Suruliz, A. Tua, and C. J. S. Young, *Search for squarks and gluinos in multi-jet final state with the ATLAS experiment in sqrts=7TeV proton-proton collisions: Supporting Documentation*, Tech. Rep. ATL-COM-PHYS-2011-984, CERN, Geneva, Jul, 2011. [Page 100, 134]

[198] ATLAS Collaboration, https://twiki.cern.ch/twiki/bin/viewauth/AtlasProtected/FakeMetEstimator . [Page 101]

[199] ATLAS Collaboration, https://twiki.cern.ch/twiki/bin/viewauth/AtlasProtected/JetMomentsForBadCells#BCH_CORR_CELL_from_JetBadChanCor . [Page 101]

[200] ATLAS Collaboration, ATL-COM-PHYS-2011-507 (2011). [Page 101]

[201] ATLAS Collaboration, A. Barr et al., *Search for new phenomena using large jet multiplicities and missing transverse momentum with ATLAS in 5.8 fb^{-1} of $\sqrt{s}$ = 8 TeV proton-proton collisions – supporting documentation*, Tech. Rep. ATL-COM-PHYS-2012-964, CERN, Geneva, Jun, 2012. https://cdsweb.cern.ch/record/1369836. [Page 102, 111, 131, 137]

[202] A. Barr et al., *Quest for new phenomena using large jet multiplicities and missing transverse momentum with ATLAS in 20.3/fb of 8 TeV proton-proton collisions: Supporting documentation*, Tech. Rep. ATL-COM-PHYS-2012-1814, CERN, Geneva, Dec, 2012. https://cds.cern.ch/record/1514200/. [Page 103]

[203] ATLAS Collaboration, G. Aad et al., *Measurement of multi-jet cross sections in proton-proton collisions at a 7 TeV center-of-mass energy*, Eur.Phys.J. **C71** (2011) 1763, arXiv:1107.2092 [hep-ex] (2011). [Page 106, 135]

[204] S. Dittmaier, P. Uwer, and S. Weinzierl, *Hadronic top-quark pair production in association with a hard jet at next-to-leading order QCD: Phenomenological studies for the Tevatron and the LHC*, Eur.Phys.J. **C59** (2009) 625–646, arXiv:0810.0452 [hep-ph] (2009). [Page 108]

[205] Atlas Collaboration, http://twiki.cern.ch/twiki/bin/viewauth/AtlasProtected/SusyFitter . [Page 113, 122, 125]

[206] ROOT Collaboration Collaboration, K. Cranmer, G. Lewis, L. Moneta, A. Shibata, and W. Verkerke, *HistFactory: A tool for creating statistical models for use with RooFit and RooStats*, Tech. Rep. CERN-OPEN-2012-016, New York U., New York, Jan, 2012. https://cdsweb.cern.ch/record/1456844. [Page 113, 122]

[207] A. G. Frodesen, O. Skjeggestad, and H. Tofte, *Probability and Statistics in Particle Physics* . Universitetsforlaget, 1979. [Page 118]

[208] A. Read, *Presentation of search results: the CL_s technique*, Journal of Physics G: Nucl. Part. Phys. **28** (2002) 2693–2704. [Page 119, 128, 161]

[209] A. Stuart and K. Ord, *Kendall's advanced theory of statistics*, vol. 2, Classical Inference and Relationship. fifth ed., March, 1991. [Page 120, 126]

[210] G. Cowan, K. Cranmer, E. Gross, and O. Vitells, *Asymptotic formulae for likelihood-based tests of new physics*, Eur. Phys. J. **C71** (2011) 1554, arXiv:1007.1727 (2011). [Page 120, 126]

[211] Gary J. Feldman and Robert D. Cousins, Phys.Rev.D57:3873-3889,1998 (1997). [Page 120, 126]

[212] ROOT Collaboration Collaboration, http://root.cern.ch/drupal/content/roofit . [Page 122]

[213] R. Cousins and V. Highland, *Incorporating systematic uncertainties into an upper limit*, Nucl. Instrum. Meth. **A320** (1992) 331. [Page 122]

[214] CERN Collaboration, E. Gross, *Frequentist Limit Recommendation*, tech. rep., Feb, 2011. http://indico.cern.ch/event/126652/contribution/0/material/2/0.pdf. [Page 127]

[215] ATLAS Collaboration, *ATLAS Standard Model Results*, tech. rep., CERN, Geneva, January, 2014. [Page 132]

[216] CMS Collaboration, *Summaries of CMS cross section measurements*, tech. rep., CERN, Geneva, January, 2014. [Page 132]

[217] ATLAS Collaboration, G. Aad et al., *Jet energy resolution in proton-proton collisions at $\sqrt{s} = 7$ TeV recorded in 2010 with the ATLAS detector*, Eur.Phys.J.

C73 (2013) 2306, arXiv:1210.6210 [hep-ex] (2013). [Page 134, 153]

[218] ATLAS Collaboration, *Performance of Missing Transverse Momentum Reconstruction in ATLAS studied in Proton-Proton Collisions recorded in 2012 at 8 TeV*, tech. rep., 2013. https://cds.cern.ch/record/1570993. [Page 136]

[219] A. Tricoli, *Measurements of inclusive and associated jet W and Z production with the ATLAS detector*, Tech. Rep. ATL-PHYS-PROC-2013-233, CERN, Geneva, Sep, 2013. [Page 138]

[220] ATLAS Collaboration, *Electron Efficiency Measurements for 2012 and 2011 Data*, Tech. Rep. ATL-COM-PHYS-2013-1287, CERN, Geneva, September, 2013. [Page 138]

[221] ATLAS Collaboration, *Identification of the Hadronic Decays of Tau Leptons in 2012 Data with the ATLAS Detector*, Tech. Rep. ATLAS-CONF-2013-064, CERN, Geneva, July, 2013. [Page 139]

[222] ATLAS Collaboration. https://twiki.cern.ch/twiki/bin/view/AtlasPublic/JetEtmissApproved2013JESUncertainty. [Page 153]

[223] ATLAS Collaboration, *Light-quark and Gluon Jets: Calorimeter Response, Jet Energy Scale Systematics and Properties*, Tech. Rep. ATLAS-CONF-2012-138, CERN, Geneva, Sep, 2012. http://cds.cern.ch/record/1480629. [Page 153]

[224] ATLAS Collaboration, https://twiki.cern.ch/twiki/bin/viewauth/AtlasProtected/JetUncertainties2012 . [Page 153]

[225] ATLAS Collaboration, https://twiki.cern.ch/twiki/bin/viewauth/AtlasProtected/JetEnergyResolutionProvider2012 . [Page 154]

[226] ATLAS Collaboration, https://twiki.cern.ch/twiki/bin/viewauth/AtlasProtected/ApplyJetResolutionSmearing . [Page 154]

[227] ATLAS Collaboration, https://twiki.cern.ch/twiki/bin/viewauth/AtlasProtected/SUSYSystematicUncertainties2012 . [Page 155]

[228] ATLAS Collaboration, https://twiki.cern.ch/twiki/bin/viewauth/AtlasProtected/PDFReweight . [Page 155]

[229] M. Hohlfeld, *Scale uncertainties for W+jets and ttbar+jets events using Alpgen at 8 TeV*, Tech. Rep. ATL-COM-PHYS-2012-1525, CERN, Geneva, Oct, 2012. [Page 155]

[230] ATLAS Collaboration, *Search for squarks and gluinos using final states with jets*

and missing transverse momentum with the ATLAS experiment in sqrt(s) = 8 TeV proton-proton collisions: supporting documentation, Tech. Rep. ATL-PHYS-INT-2012-063, CERN, Geneva, Sep, 2012. [Page 155]

[231] S. Catani, F. Krauss, R. Kuhn, and B. Webber, *QCD matrix elements + parton showers*, JHEP **0111** (2001) 063, arXiv:hep-ph/0109231 [hep-ph] (2001). [Page 156]

[232] HepData: http://hepdata.cedar.ac.uk/view/red6095 . [Page 161]

[233] ATLAS Collaboration, *Search for top and bottom squarks from gluino pair production in final states with missing transverse energy and at least three b jets with the ATLAS detector*, Eur. Phys. J. **C72** (2012) 2174, arXiv:1207.4686 [hep-ex] (2012). [Page 162, 169]

[234] CMS Collaboration, S. Chatrchyan et al., *Search for supersymmetry in hadronic final states with missing transverse energy using the variables AlphaT and b-quark multiplicity in pp collisions at 8 TeV*, Eur.Phys.J. **C73** (2013) 2568, arXiv:1303.2985 [hep-ex] (2013). [Page 162, 169]

[235] CMS Collaboration, *Interpretation of searches for supersymmetry with simplified models*, arXiv:1301.2175 [hep-ex] (2013). [Page 162]

[236] CMS Collaboration, S. Chatrchyan et al., *Inclusive search for supersymmetry using the razor variables in pp collisions at* $\sqrt{s} = 7$ *TeV*, Phys.Rev.Lett. **111** (2013) 081802, arXiv:1212.6961 [hep-ex] (2013). [Page 169]

[237] CMS Collaboration, S. Chatrchyan et al., *Search for new physics in the multijet and missing transverse momentum final state in proton-proton collisions at* $\sqrt{s} = 7$ *TeV*, Phys.Rev.Lett. **109** (2012) 171803, arXiv:1207.1898 [hep-ex] (2012). [Page 169]

[238] ATLAS Collaboration, *Search for strong production of supersymmetric particles in final states with missing transverse momentum and at least three b-jets using 20.1* fb^{-1} *of pp collisions at sqrt(s) = 8 TeV with the ATLAS Detector.*, Tech. Rep. ATLAS-CONF-2013-061, CERN, Geneva, Jun, 2013. [Page 171]

[239] S. El Hedri, A. Hook, M. Jankowiak, and J. G. Wacker, *Learning How to Count: A High Multiplicity Search for the LHC*, JHEP **1308** (2013) 136, arXiv:1302.1870 (2013). [Page 171]

A
Event displays

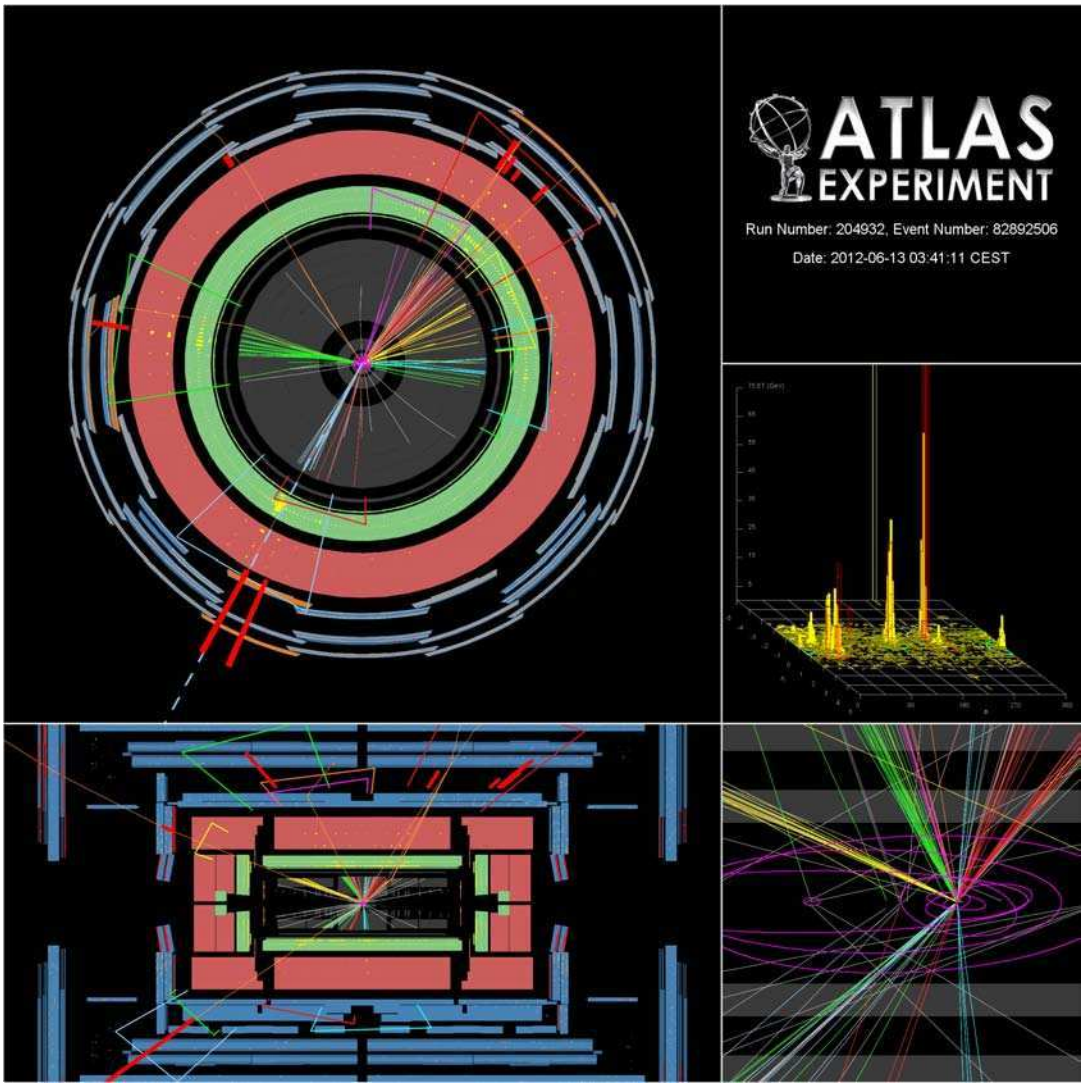

Figure A.1: ATLAS event display of a high multiplicity event that passes the criteria for the 9j50 + MJ420 signal region and the 9j50+$\geq 2b$-jets and 8j80 signal regions. The total jet mass of this event is M_{J}^{Σ} =800 GeV. It has $\mathcal{S}_{\mathrm{T}}^{\mathrm{miss}}$ =8.8GeV$^{1/2}$ and $E_{\mathrm{T}}^{\mathrm{miss}}$ =413 GeV. The event has four b-jets is identified using the MV1 b-tagger (section 3.3.6). The view in the transverse plane is not at scale, the size of the inner detector is exaggeratedly enlarged to facilitate the path of the tracks. The image at bottom-right is a zoom of the central part of the detector showing the reconstructed tracks and vertices (magenta.

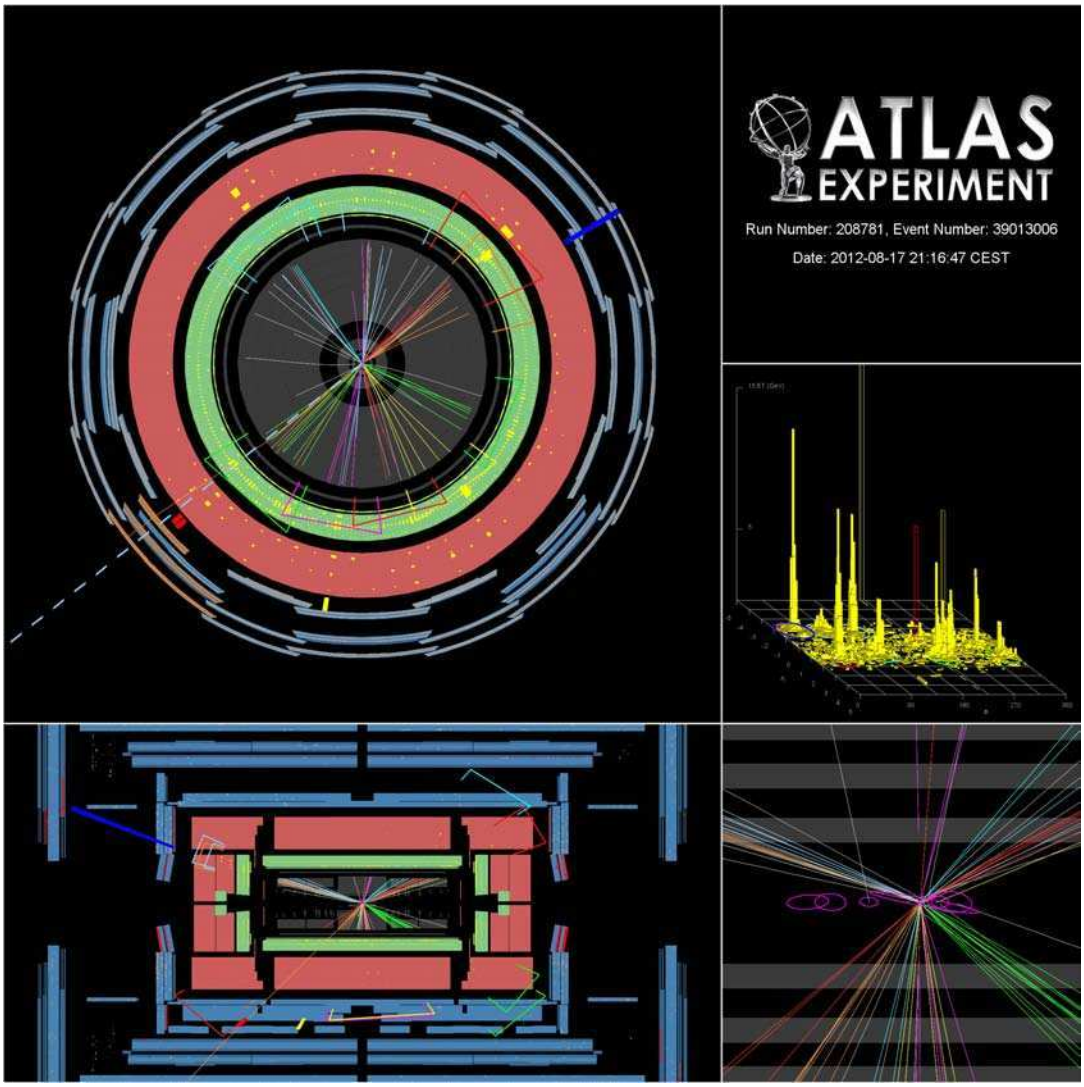

Figure A.2: ATLAS event display of a high multiplicity event that passes the criteria for the 10j50 signal region. The event has one b-jet, $\mathcal{S}_{\mathrm{T}}^{\mathrm{miss}}$ =4.1GeV$^{1/2}$ and $E_{\mathrm{T}}^{\mathrm{miss}}$ =118 GeV. See legend in figure A.1 for more details.

B
Details of systematic uncertainties for the backgrounds

Tables B.1 and B.2 summarize the experimental uncertainties on the 'leptonic' background predictions for all the signal regions. Table B.3 summarizes the experimental uncertainties on the multi-jet background predictions for all the signal regions.

Multijet + M_J^Σ Signal Regions							
Process	**Source**	**8+j50**		**9+j50**		**10+j50**	
		MJ340	MJ420	MJ340	MJ420	MJ340	MJ420
$t\bar{t}$	JES	$^{+21.9}_{-21.4}$	$^{+23.7}_{-18.8}$	$^{+56.7}_{-10.7}$	$^{+30.4}_{-20.7}$	$^{+1.1}_{-10.3}$	$^{+1.4}_{-12.7}$
	Close-by	$^{+40.8}_{-31.6}$	$^{+40.4}_{-29.6}$	$^{+90.4}_{-36.9}$	$^{+62.1}_{-28.6}$	$^{+43.8}_{-22.8}$	$^{+54.1}_{-28.2}$
	JER	-0.8	-8.8	2.5	-10.9	-4.5	-6.2
	Soft MET term	$^{+2.6}_{-0.0}$	$^{+3.4}_{-0.0}$	$^{+15.4}_{-0.0}$	$^{+14.0}_{-0.0}$	$^{+31.2}_{-0.0}$	0.0
	Pile-up	-2.8	-2.6	-4.7	-5.3	-21.0	-19.9
	B-tag	0.0	0.0	0.0	0.0	0.0	0.0
	C-tag	0.0	0.0	0.0	0.0	0.0	0.0
	L-tag	0.0	0.0	0.0	0.0	0.0	0.0
	Statistical	9.1	12.7	23.4	28.0	63.2	74.5
W+jets	JES	$^{+15.4}_{-26.8}$	$^{+0.0}_{-15.4}$	0.0	0.0	0.0	0.0
	Close-by	$^{+135.8}_{-26.8}$	$^{+134.1}_{-15.4}$	0.0	0.0	0.0	0.0
	JER	-4.0	-15.4	0.0	0.0	0.0	0.0
	Soft MET term	0.0	0.0	0.0	0.0	0.0	0.0
	Pile-up	32.8	23.7	0.0	0.0	0.0	0.0
	B-tag	0.0	0.0	0.0	0.0	0.0	0.0
	C-tag	0.0	0.0	0.0	0.0	0.0	0.0
	L-tag	0.0	0.0	0.0	0.0	0.0	0.0
	Statistical	55.8	86.0	0.0	0.0	0.0	0.0
W+b	JES	$^{+0.0}_{-100.0}$	$^{+0.0}_{-100.0}$	0.0	0.0	0.0	0.0
	Close-by	$^{+0.0}_{-100.0}$	$^{+0.0}_{-100.0}$	0.0	0.0	0.0	0.0
	JER	-100.0	-100.0	0.0	0.0	0.0	0.0
	Soft MET term	0.0	0.0	0.0	0.0	0.0	0.0
	Pile-up	1.1	1.1	0.0	0.0	0.0	0.0
	B-tag	0.0	0.0	0.0	0.0	0.0	0.0
	C-tag	0.0	0.0	0.0	0.0	0.0	0.0
	L-tag	0.0	0.0	0.0	0.0	0.0	0.0
	Statistical	100	100	0.0	0.0	0.0	0.0
Z+jets	JES	$^{+36.8}_{-44.0}$	$^{+20.0}_{-38.1}$	0.0	0.0	0.0	0.0
	Close-by	$^{+49.5}_{-23.6}$	$^{+46.7}_{-38.1}$	0.0	0.0	0.0	0.0
	JER	-19.7	-19.4	0.0	0.0	0.0	0.0
	Soft MET term	0.0	0.0	0.0	0.0	0.0	0.0
	Pile-up	1.6	-0.2	156.5	0.0	0.0	0.0
	B-tag	0.0	0.0	0.0	0.0	0.0	0.0
	C-tag	0.0	0.0	0.0	0.0	0.0	0.0
	L-tag	0.0	0.0	0.0	0.0	0.0	0.0
	Statistical	36.7	44.8	100	0.0	0.0	0.0
$t\bar{t}+V$	JES	$^{+25.0}_{-22.6}$	$^{+16.3}_{-21.6}$	$^{+49.4}_{-25.6}$	$^{+30.7}_{-18.9}$	$^{+28.8}_{-24.7}$	$^{+28.0}_{-21.4}$
	Close-by	$^{+47.0}_{-37.8}$	$^{+46.4}_{-35.6}$	$^{+85.6}_{-29.9}$	$^{+105.4}_{-31.2}$	$^{+36.3}_{-50.0}$	$^{+44.4}_{-37.3}$
	JER	2.9	-2.3	0.3	23.5	-15.3	-1.1
	Soft MET term	$^{+0.5}_{-0.8}$	$^{+0.3}_{-0.7}$	$^{+1.6}_{-0.0}$	$^{+0.0}_{-3.8}$	0.0	0.0
	Pile-up	-2.5	0.1	-1.7	6.3	-8.5	0.6
	B-tag	0.0	0.0	0.0	0.0	0.0	0.0
	C-tag	0.0	0.0	0.0	0.0	0.0	0.0
	L-tag	0.0	0.0	0.0	0.0	0.0	0.0
	Statistical	8.6	12.3	18.7	27.5	28.4	39.5
Single top	JES	$^{+21.0}_{-7.9}$	$^{+33.3}_{-21.4}$	$^{+0.0}_{-33.5}$	$^{+33.9}_{-0.6}$	0.0	0.0
	Close-by	$^{+50.1}_{-38.9}$	$^{+182.5}_{-6.1}$	$^{+46.4}_{-43.2}$	$^{+43.6}_{-0.5}$	0.0	0.0
	JER	9.9	-9.3	-33.5	-33.9	0.0	0.0
	Soft MET term	0.0	0.0	0.0	0.0	0.0	0.0
	Pile-up	-7.2	8.7	17.1	19.0	0.0	0.0
	B-tag	0.0	0.0	0.0	0.0	0.0	0.0
	C-tag	0.0	0.0	0.0	0.0	0.0	0.0
	L-tag	0.0	0.0	0.0	0.0	0.0	0.0
	Statistical	36.4	55.9	67.0	66.5	0.0	0.0

Table B.1: 'Leptonic' background uncertainties (in %) for the M_J^Σ signal regions.

Process	Source	Multijet + b-jet Signal Regions												
		8j50			9j50			10+j50	7j80			8+j80		
		0 bs	1 b	≥2 bs	0 bs	1 b	≥2 bs	——	0 bs	1 b	≥2 bs	0 bs	1 b	≥2 bs
$t\bar{t}$	JES	$^{30.08}_{-20.55}$	$^{22.82}_{-23.14}$	$^{21.28}_{-22.11}$	$^{82.49}_{-0.00}$	$^{37.99}_{-31.34}$	$^{28.17}_{-2.26}$	$^{10.93}_{-100.00}$	$^{23.63}_{11.59}$	$^{12.11}_{-20.16}$	$^{21.47}_{-14.28}$	$^{0.71}_{-0.70}$	$^{35.53}_{-53.37}$	$^{12.33}_{-24.59}$
	Close-by	$^{30.85}_{-53.51}$	$^{37.74}_{-25.67}$	$^{37.45}_{-37.27}$	$^{87.66}_{-0.08}$	$^{155.19}_{-39.22}$	$^{33.08}_{-19.62}$	$^{385.30}_{-100.00}$	$^{195.36}_{123.12}$	$^{27.35}_{-23.31}$	$^{40.15}_{-33.92}$	$^{-3.37}_{-100.00}$	$^{106.59}_{-53.45}$	$^{48.78}_{-27.85}$
	JER	19.49	15.26	2.83	−0.04	0.34	3.25	37.94	76.77	2.49	−2.54	−0.32	−0.03	−16.20
	Soft MET term	0.00	$^{0.24}_{0.80}$	$^{3.55}_{-0.79}$	$^{0.29}_{82.45}$	0.00	$^{0.00}_{2.46}$	$^{304.15}_{0.00}$	0.00	$^{0.18}_{0.00}$	$^{1.52}_{-1.24}$	0.00	0.00	0.00
	Pile-up	−0.37	−2.09	−2.34	−18.97	−18.08	−7.05	1.13	49.96	−1.42	−0.62	7.79	−21.39	−9.09
	B-tag	$^{-20.05}_{22.48}$	$^{-8.08}_{7.40}$	$^{5.06}_{-5.45}$	$^{-31.10}_{38.37}$	$^{-12.43}_{12.17}$	$^{-8.90}_{9.91}$	0.00	$^{-20.53}_{21.59}$	$^{-14.17}_{13.35}$	$^{-0.68}_{0.42}$	$^{-32.53}_{37.64}$	$^{-1.55}_{-1.69}$	$^{0.64}_{-3.55}$
	C-tag	$^{-7.17}_{7.60}$	$^{-4.25}_{4.44}$	$^{4.37}_{-4.15}$	0.00	$^{-5.83}_{5.16}$	$^{4.41}_{-4.93}$	0.00	$^{-5.82}_{6.19}$	$^{-3.00}_{2.95}$	$^{8.22}_{-7.75}$	$^{-10.64}_{11.15}$	$^{-6.04}_{6.05}$	$^{2.68}_{-2.94}$
	L-tag	$^{-0.90}_{0.91}$	$^{-0.87}_{0.88}$	$^{0.57}_{-0.53}$	$^{-1.23}_{1.24}$	$^{-0.05}_{0.05}$	$^{0.95}_{-0.98}$	0.00	$^{-1.02}_{1.02}$	$^{-0.68}_{0.68}$	$^{0.36}_{-0.30}$	$^{-0.85}_{0.86}$	$^{-1.08}_{1.09}$	$^{0.62}_{-0.63}$
	Statistical	24.74	12.36	9.11	72.11	36.83	32.46	100.00	42.95	22.62	18.32	100.00	67.58	48.33
W+**jets**	JES	$^{-0.02}_{-23.92}$	$^{0.17}_{19.38}$	$^{0.09}_{-0.42}$	0.00	$^{0.14}_{-100.00}$	0.00	0.00	$^{23.07}_{0.01}$	$^{0.00}_{-0.01}$	0.00	$^{25.33}_{0.00}$	0.00	0.00
	Close-by	$^{4.93}_{-26.44}$	$^{6.92}_{-8.51}$	$^{1.32}_{-0.61}$	0.00	$^{-0.01}_{-100.00}$	0.00	0.00	$^{34.85}_{-0.01}$	$^{77.91}_{-0.01}$	$^{78.61}_{0.00}$	$^{52.81}_{0.00}$	0.00	0.00
	JER	−12.00	−15.55	−32.12	33.15	0.10	0.00	0.00	91.72	−0.01	0.00	0.00	0.00	0.00
	Soft MET term	0.00	0.00	0.00	0.00	0.00	0.00	0.00	0.00	0.00	0.00	0.00	0.00	0.00
	Pile-up	−11.90	0.62	56.96	0.00	−2.66	0.00	0.00	−7.64	−14.39	0.00	0.00	0.00	0.00
	B-tag	0.00	0.00	0.00	0.00	0.00	0.00	0.00	0.00	0.00	0.00	0.00	0.00	0.00
	C-tag	$^{-7.98}_{8.47}$	$^{3.10}_{-3.89}$	$^{17.10}_{-17.03}$	0.00	$^{17.85}_{-17.85}$	0.00	0.00	$^{-8.44}_{8.82}$	$^{-6.34}_{6.34}$	0.00	0.00	0.00	0.00
	L-tag	$^{-1.18}_{1.19}$	$^{7.55}_{-7.74}$	$^{10.87}_{-9.23}$	0.00	$^{-1.45}_{1.47}$	0.00	0.00	$^{-1.07}_{1.08}$	$^{18.59}_{-18.91}$	0.00	0.00	0.00	0.00
	Statistical	33.11	50.87	75.10	0.00	100.00	0.00	0.00	71.04	100.00	0.00	0.00	0.00	0.00
W+$b/b\bar{b}$+**jets**	JES	$^{0.10}_{-100.00}$	0.00	0.00	0.00	0.00	$^{0.06}_{-3.35}$	0.00	$^{-0.05}_{-100.00}$	0.00	$^{-0.00}_{-57.03}$	0.00	0.00	$^{0.06}_{-3.35}$
	Close-by	$^{-0.02}_{-100.00}$	0.00	$^{0.85}_{0.00}$	0.00	0.00	$^{-2.67}_{-1.72}$	0.00	$^{-0.36}_{-100.00}$	0.00	$^{-57.76}_{0.02}$	0.00	0.00	$^{-2.67}_{-1.72}$
	JER	−100.00	58.62	60.22	0.00	0.00	−1.44	0.00	0.09	0.00	0.06	0.00	0.00	−1.44
	Soft MET term	0.00	0.00	0.00	0.00	0.00	0.00	0.00	0.00	0.00	$^{-57.05}_{0.00}$	0.00	0.00	0.00
	Pile-up	−11.38	0.00	0.00	0.00	0.00	−57.74	0.00	−8.94	0.00	−30.24	0.00	0.00	−57.75
	B-tag	$^{-18.60}_{18.60}$	0.00	0.00	0.00	0.00	$^{-2.38}_{0.62}$	0.00	$^{-38.67}_{47.83}$	0.00	$^{23.72}_{-20.67}$	0.00	0.00	$^{-2.38}_{0.62}$
	C-tag	$^{-8.98}_{9.50}$	0.00	0.00	0.00	0.00	$^{5.42}_{-6.27}$	0.00	0.00	0.00	$^{-0.16}_{-0.47}$	0.00	0.00	$^{5.42}_{-6.27}$
	L-tag	$^{-1.08}_{1.09}$	0.00	0.00	0.00	0.00	$^{-1.08}_{1.08}$	0.00	$^{-0.77}_{0.77}$	0.00	$^{-0.60}_{0.60}$	0.00	0.00	$^{-1.08}_{1.08}$
	Statistical	75.65	0.00	0.00	0.00	0.00	100.00	0.00	100.00	0.00	71.41	0.00	0.00	100.00
Z+**jets**	JES	$^{52.90}_{-100.00}$	$^{682.51}_{-66.12}$	$^{0.00}_{0.00}$	0.00	0.00	$^{0.00}_{-100.00}$	0.00	$^{0.00}_{0.00}$	$^{129.47}_{0.01}$	$^{5.53}_{0.00}$	0.00	0.00	0.00
	Close-by	$^{56.83}_{-100.00}$	$^{998.31}_{-66.68}$	$^{67.14}_{0.00}$	0.00	0.00	$^{-100.00}_{0.00}$	0.00	$^{54.82}_{0.00}$	$^{142.51}_{0.01}$	$^{3.52}_{0.19}$	0.00	0.00	0.00
	JER	−51.83	316.91	63.68	0.00	0.00	0.00	0.00	−0.00	129.47	−1.82	0.00	0.00	0.00
	Soft MET term	0.00	0.00	0.00	0.00	0.00	0.00	0.00	0.00	0.00	0.00	0.00	0.00	0.00
	Pile-up	4.52	164.50	0.00	0.00	0.00	0.00	0.00	−52.30	38.91	−47.21	0.00	0.00	0.00
	B-tag	0.00	0.00	0.00	0.00	0.00	0.00	0.00	0.00	0.00	0.00	0.00	0.00	0.00
	C-tag	$^{-2.45}_{2.51}$	$^{-4.35}_{3.32}$	0.00	0.00	0.00	$^{50.00}_{-50.00}$	0.00	0.00	$^{11.30}_{-11.30}$	$^{23.39}_{-22.51}$	0.00	0.00	0.00
	L-tag	$^{-1.14}_{1.15}$	$^{9.96}_{-10.21}$	0.00	0.00	0.00	0.00	0.00	$^{-1.34}_{1.36}$	$^{-1.06}_{1.08}$	$^{-0.88}_{0.88}$	0.00	0.00	0.00
	Statistical	70.76	74.26	0.00	0.00	0.00	100.00	0.00	100.00	100.00	100.00	0.00	0.00	0.00
$t\bar{t}$ +**V**	JES	$^{17.29}_{-10.98}$	$^{22.02}_{-21.80}$	$^{26.47}_{-15.74}$	$^{120.20}_{0.32}$	$^{-7.38}_{-49.30}$	$^{70.75}_{-34.60}$	$^{51.48}_{-15.80}$	$^{38.26}_{-19.98}$	$^{32.39}_{-21.28}$	$^{35.93}_{-23.34}$	$^{0.00}_{0.53}$	$^{4.98}_{-49.30}$	$^{0.00}_{-24.91}$
	Close-by	$^{8.26}_{3.80}$	$^{28.83}_{-37.36}$	$^{41.04}_{-28.56}$	$^{132.18}_{0.45}$	$^{8.74}_{-54.24}$	$^{69.98}_{-5.64}$	$^{37.43}_{-45.71}$	$^{60.07}_{-28.80}$	$^{80.58}_{-43.97}$	$^{50.16}_{-25.85}$	$^{-65.80}_{0.66}$	$^{9.29}_{-65.11}$	$^{89.42}_{-24.69}$
	JER	33.32	9.02	14.72	18.39	−37.40	13.43	13.62	−2.20	−9.37	4.18	0.53	23.83	−12.34
	Soft MET term	0.00	$^{1.05}_{0.86}$	$^{0.80}_{0.28}$	0.00	$^{0.00}_{-3.87}$	$^{4.37}_{19.32}$	0.00	0.00	$^{0.00}_{-3.60}$	$^{0.00}_{5.61}$	0.00	0.00	0.00
	Pile-up	−2.09	−1.50	2.89	17.77	−12.44	6.32	3.90	−6.59	3.63	1.80	35.46	−5.02	29.85
	B-tag	$^{-21.29}_{23.51}$	$^{-8.97}_{8.36}$	$^{4.86}_{-4.97}$	$^{-24.12}_{26.19}$	$^{-6.70}_{6.24}$	$^{6.21}_{-6.22}$	0.00	$^{-17.30}_{19.68}$	$^{-4.59}_{3.55}$	$^{3.56}_{-4.88}$	$^{-26.36}_{30.54}$	$^{-12.03}_{12.34}$	$^{17.12}_{-15.61}$
	C-tag	$^{-6.41}_{6.86}$	$^{-3.02}_{3.13}$	$^{2.41}_{-2.72}$	$^{-6.77}_{7.02}$	$^{-4.02}_{4.33}$	$^{3.51}_{-3.79}$	0.00	$^{-5.49}_{5.58}$	$^{-4.55}_{4.72}$	$^{1.92}_{-2.04}$	$^{-2.72}_{2.85}$	$^{9.07}_{-8.90}$	$^{-1.76}_{0.90}$
	L-tag	$^{-0.97}_{0.97}$	$^{-0.41}_{0.40}$	$^{1.39}_{-1.32}$	$^{-1.10}_{1.17}$	$^{-1.04}_{1.05}$	$^{3.44}_{-3.50}$	0.00	$^{-0.96}_{0.97}$	$^{0.17}_{-0.18}$	$^{-0.35}_{0.35}$	$^{-1.33}_{1.39}$	$^{-0.97}_{0.97}$	$^{9.59}_{-9.71}$
	Statistical	20.97	11.89	9.20	60.68	23.11	28.17	84.21	42.34	21.16	14.99	74.15	61.65	113.62
Single top	JES	$^{0.02}_{-29.41}$	$^{48.35}_{-30.21}$	$^{2.49}_{-24.29}$	0.00	$^{0.02}_{0.01}$	$^{245.42}_{1.56}$	0.00	$^{4.40}_{-0.09}$	$^{83.37}_{0.03}$	$^{34.34}_{-5.41}$	0.00	0.00	$^{-0.01}_{-3.23}$
	Close-by	$^{74.54}_{-29.44}$	$^{15.84}_{-87.71}$	$^{-8.12}_{-28.96}$	0.00	$^{-0.17}_{0.01}$	$^{245.56}_{1.56}$	0.00	$^{4.94}_{-42.37}$	$^{22.16}_{61.50}$	$^{2.57}_{-12.12}$	0.00	0.00	$^{94.16}_{-3.23}$
	JER	−17.87	48.81	−13.67	0.00	0.02	246.93	0.00	3.90	3.68	7.12	0.00	0.00	−2.70
	Soft MET term	0.00	$^{1.42}_{0.00}$	$^{-5.80}_{0.00}$	0.00	0.00	0.00	0.00	0.00	0.00	0.00	0.00	0.00	0.00
	Pile-up	2.60	−32.23	−0.38	0.00	−9.47	−7.72	0.00	−17.20	−6.13	−3.31	0.00	0.00	−8.95
	B-tag	$^{-29.58}_{35.33}$	$^{-32.36}_{41.21}$	$^{6.86}_{-8.10}$	0.00	$^{-11.03}_{3.70}$	$^{11.57}_{-10.95}$	0.00	$^{-31.92}_{37.55}$	$^{-11.03}_{4.00}$	$^{2.19}_{-5.17}$	0.00	0.00	$^{20.75}_{-19.40}$
	C-tag	$^{-1.01}_{1.01}$	$^{6.22}_{-7.29}$	$^{-0.87}_{0.59}$	0.00	$^{-7.11}_{7.12}$	$^{-7.45}_{7.45}$	0.00	$^{-3.70}_{3.70}$	$^{-0.51}_{0.51}$	$^{-1.74}_{1.54}$	0.00	0.00	$^{6.66}_{-7.61}$
	L-tag	$^{-0.95}_{0.96}$	$^{-0.72}_{0.72}$	$^{1.52}_{-1.54}$	0.00	$^{-0.96}_{0.97}$	$^{-1.23}_{1.25}$	0.00	$^{-0.75}_{0.75}$	$^{-0.79}_{0.79}$	$^{5.21}_{-5.25}$	0.00	0.00	$^{-0.84}_{0.84}$
	Statistical	76.47	76.31	33.60	0.00	100.00	101.57	0.00	71.52	65.22	47.06	0.00	0.00	100.00

Table B.2: 'Leptonic' background uncertainties (in %) for the b-jet signal regions.

Source	**Signal Regions**																		
	Multi-jet + b-jet													**Multi-jet + M_{J}^{Σ}**					
	8j50			**9j50**		**10+j50**		**7j80**			**8+j80**			**8+j50**		**9+j50**		**10+j50**	
	0 bs	1 b	$\geq$2 bs	0 bs	1 b	$\geq$2 bs	——	0 bs	1 b	$\geq$2 bs	0 bs	1 b	$\geq$2 bs	MJ340	MJ420	MJ340	MJ420	MJ340	MJ420
Closure	2.40	10.80	12.70	14.70	15.00	28.60	16.90	10.20	25.00	20.10	72.70	25.80	54.40	23.4	34.8	23.4	34.8	24.6	51.4
Heavy Flavour	6.99	−25.20	−25.20	11.11	−25.20	−25.20	8.88	8.67	−25.20	−25.20	14.81	−25.20	−25.20	5.4	6.0	11.6	14.0	13.5	17.4
Trigger ineff.	−0.28	−0.31	−0.83	−0.64	−0.34	−1.13	0.00	−0.33	−0.10	−0.39	−0.44	−0.12	−0.28	-0.7	-0.1	-0.6	0.1	-0.4	0.2
Leptonic bkg.	$^{-5.26}_{5.25}$	$^{-9.82}_{9.80}$	$^{-20.23}_{20.14}$	5.40	$^{-9.44}_{9.42}$	$^{-18.62}_{18.54}$	9.10	4.73	$^{-7.45}_{7.44}$	$^{-13.34}_{13.28}$	4.44	$^{-6.52}_{6.51}$	$^{-11.74}_{11.69}$	$^{+14.3}_{-14.2}$	12.1	13.8	11.7	$^{+13.6}_{-13.5}$	11.9
CellOut rwgt.	−2.77	−6.73	−17.91	−4.66	−11.22	−21.35	−14.11	−4.38	−6.64	−14.29	−5.15	−4.86	−16.67	0.6	-0.1	0.9	1.1	1.4	1.4

Table B.3: Multi-jet background uncertainties (in %) for all signal regions and all backgrounds.